Development of a Novel Low Inertia Exoskeleton Device for Characterizing the Neuromuscular Properties of the Human Shoulder

by

Justin Hunt

A Dissertation Presented in Partial Fulfillment
of the Requirement for the Degree
Doctor of Philosophy

Approved September 2020 by the
Graduate Supervisory Committee:

Hyunglae Lee, Chair
Panagiotis Artemiadis
Thomas Sugar
Sze Zheng Yong
Hamid Marvi

ARIZONA STATE UNIVERSITY

December 2020

ABSTRACT

The human shoulder plays an integral role in upper limb motor function. As the basis of arm motion, its performance is vital to the accomplishment of daily tasks. Impaired motor control, as a result of stroke or other disease, can cause errors in shoulder position to accumulate and propagate to the entire arm. This is why it is a highlight of concern for clinicians and why it is an important point of study. One of the primary causes of impaired shoulder motor control is abnormal mechanical joint impedance, which can be modeled as a 2nd order system consisting of mass, spring and damper. Quantifying shoulder stiffness and damping between healthy and impaired subjects could help improve our collective understanding of how many different neuromuscular diseases impact arm performance. This improved understanding could even lead to better rehabilitation protocols for conditions such as stroke through better identification and targeting of damping dependent spasticity and stiffness dependent hypertonicity. Despite its importance, there is a fundamental knowledge gap in the understanding of shoulder impedance, mainly due to a lack of appropriate characterization tools. Therefore, in order to better quantify shoulder stiffness and damping, a novel low-inertia shoulder exoskeleton is introduced in this work. The device was developed using a newly pioneered parallel actuated robot architecture specifically designed to interface with complex biological joints like the shoulder, hip, wrist and ankle. In addition to presenting the kinematics and dynamics of the shoulder exoskeleton, a series of validation experiments are performed on a human shoulder mock-up to quantify its ability to estimate known impedance properties. Finally, some preliminary data from human experiments is provided to demonstrate the devices ability to collect the measurements needed to estimate shoulder stiffness and damping while worn by a subject.

ACKNOWLEDGEMENTS

Throughout my PhD studies, I received incredible support from my friends, family, mentors and colleagues. Without their encouragement and guidance, this achievement would not have been possible. I would like to take a moment to acknowledge those that meant so much to my success.

First I would like to thank my parents, Anne and Gary Hunt, for encouraging me to pursue an advance degree. They have been an incredible source of support and guidance for which I am extremely grateful. I would also like to thank my girlfriend, Sarah Pfitzner, and her parents, Fariba and Martin Pfitzner, for there kindness, caring and continuous support throughout my research work.

Finally, I would like to express my sincere gratitude and thanks to my PhD advisor, mentor and friend, Dr. Hyunglae Lee, for giving me the opportunity to perform research under his supervision. His integrity, sincerity and work ethic have deeply inspired me. He has taught me the proper methodology to carry out my research and to present the findings as clearly as possible. It was a great privilege and honor to work and study under his guidance.

TABLE OF CONTENTS

Chapter 1

INTRODUCTION

The neuromuscular properties of the human body, determined by the collective behaviors of bones, joints, muscles, nerves and receptors, are responsible for static posture and dynamic movement. These properties can be quantitatively described by mechanical impedance, a fundamental property of the human neuromuscular system in interaction with the physical world [1]–[3]. Characterizing mechanical impedance and its underlying mechanisms, including intrinsic and reflexive impedances, is an important field of study that has significance for a variety of applications. Two examples that are of particular interest to the authors include:

1. **Medical:** characterizing abnormal mechanical impedance associated with neuropathies or neuromuscular autoimmune conditions to assist clinicians in the development of new rehabilitation protocols that more accurately target patient impairment.

2. **Military/Industrial:** characterizing normal mechanical impedance would allow for the development of exoskeleton devices that rely on cooperative human-robot critical stability interaction to provide highly responsive performance.

Efforts to quantify mechanical impedance and its components (e.g., stiffness, damping, reflex gain) of major joints such as the elbow [4], ankle [5]–[7], and wrist [4], [8] have been made prior. Each study utilized a different exoskeleton characterization device designed specifically to interface with the joint of interest. These devices work by applying position/angle (or force/torque) perturbations to the accompanying limb segment/joint and measuring the corresponding force/torque (or position/angle) response.

More complex joints with a large range of motion and high torque output, like the shoulder, are yet to be thoroughly investigated. This is largely due to the lack of exoskeleton characterization tools capable of both interfacing with and manipulating the shoulder joint effectively. This includes the ability to rapidly perturb the limb in multiple directions during both static posture and dynamic movement. This is important, as mechanical impedance has an intrinsic and reflexive components that occur during the first 20 ms and 20-100 ms of an applied external perturbation, respectively [9], [10]. Therefore, the limb needs to be reasonably displaced during this period to characterize intrinsic and reflexive responses and separate their contribution from that of voluntary response. This can be difficult, primarily due to high robot inertia.

Most shoulder exoskeleton robots utilize a serial type architecture that works to bridge the glenohumeral joint using a chain of motors and linkages [11]. The moment arm associated with these linkages has the inherent disadvantage of amplifying torques applied to the joint by external forces. Furthermore, each motorized joint in the armature must be capable of not only actuating the corresponding human limb, but also able to lift and manipulate the motors that follow in series. This requires larger motors with more inertia, which as previously mentioned, makes executing a rapid perturbation difficult.

One solution to this problem is to use a parallel actuated architecture instead. Parallel actuation has several inherent properties that make it ideal for characterizing the neuromuscular properties including joint mechanical impedance. These include low end effector inertia, high end effector acceleration and high potential stiffness [12]–[15]. These advantages are in part why neuromuscular property characterization tools like the AnkleBot, [16], Rice Wrist [17] and Manus [18] all utilize parallel architectures.

The rest of this document focuses on the design, development and validation of different parallel actuated shoulder exoskeleton robots. The following chapters are defined by the published works related to this dissertation. Provide next are detailed description of each chapter.

1.1 Overview - Chapter 2

This chapter presents a five degree-of-freedom (DoF) low inertia shoulder exoskeleton. This device is comprised of two novel technologies. The first is 3-DoF spherical parallel manipulator (SPM), which was developed using a new method of parallel manipulator design. This method involves mechanically coupling certain DoF of each independently actuated linkage of the parallel manipulator in order to constrain the kinematics of the entire system. The second is a 2-DoF passive slip interface used to couple the user upper arm to the SPM. This slip interface increases system mobility and prevents joint misalignment caused by the translational motion of the user's glenohumeral joint from introducing mechanical interference. An experiment to validate the kinematics of the SPM was performed using motion capture. The results of this experiment validated the SPMs forward and inverse kinematic solutions through an Euler angle comparison of the actual and command orientations. A computational slip model was created to quantify the passive slip interface response for different conditions of joint misalignment. In addition to offering a low inertia solution for the rehabilitation or augmentation of the human shoulder, this device demonstrates a new method of motion coupling, which can be used to impose kinematic constraints on a wide variety of parallel architectures. Furthermore, the presented device demonstrates a passive slip interface that can be used with either parallel or serial robotic systems.

1.2 Overview - Chapter 3

The purpose of this chapter is to optimize the stiffness of a novel parallel-actuated robotic exoskeleton designed to offer a large workspace. This is done in an effort to help provide a solution to the issue wearable parallel actuated robots face regarding a tradeoff between stiffness and workspace. Presented in the form of a shoulder exoskeleton, the device demonstrates a new parallel architecture that can be used for wearable hip, ankle and wrist robots as well. The stiffness of the architecture is dependent on the placement of its actuated substructures. Therefore, it is desirable to place these substructures effectively so as to maximize dynamic performance for any application. In this work, an analytical stiffness model of the device is created and validated experimentally. The model is then used, along with a method of bounded nonlinear multi-objective optimization to configure the parallel actuators so as to maximize stiffness for the entire workspace. Furthermore, it is shown how to use the same technique to optimize the device for a particular task, such as lifting in the sagittal plane.

1.3 Overview - Chapter 4

The purpose of this chapter is to introduce a new parallel actuated exoskeleton architecture that can be used for multiple degree-of-freedom (DoF) biological joints. This is done in an effort to provide a better alternative for the augmentation of these joints than serial actuation. The new design can be described as a type of spherical parallel manipulator (SPM) that utilizes three 4-bar substructures to decouple and control three rotational DoFs. Four variations of the 4-bar spherical parallel manipulator (4B-SPM) are presented in this work. These include a shoulder, hip, wrist, and ankle exoskeleton. Also discussed are three different methods of actuation for the 4B-SPM which can be implemented depending on dynamic performance requirements. This work could assist in the advancement of a future generation of parallel actuated exoskeletons that are more effective than their contemporary serial actuated counterparts.

1.4 Overview - Chapter 5

The purpose of this chapter is to introduce a newly developed exoskeleton robot designed to characterize the neuromuscular properties of the shoulder, including intrinsic and reflexive mechanisms, during static posture and dynamic movement in a 3-dimensional space. Quantitative characterization of these properties requires fast perturbation (¿100/s) to separate their contribution from that of voluntary mechanism. Understanding these properties of the shoulder control could assist in the rehabilitation or enhancement of upper limb performance during physical human-robot interaction. The device can be described as a new type of spherical parallel manipulator (SPM) that utilizes three 4-bar (4B) substructures to decouple and control roll, pitch and yaw of the shoulder. By utilizing a parallel architecture, the 4B-SPM exoskeleton has the advantage of high acceleration, fast enough to satisfy the speed requirement for the characterization of distinct neuromuscular properties of the shoulder. In this work, the prototype is presented, along with an evaluation of its position accuracy and step response tracking capabilities. The development and preliminary testing of the 4B-SPM exoskeleton presented in this work demonstrates its potential to be a useful tool for studying the neuromuscular mechanisms of the shoulder joint.

1.5 Overview - Chapter 6

The purpose of this work is to optimize the rigid or compliant behavior of a new type of parallel-actuated robot architecture developed for exoskeleton robot applications. This is done in an effort to provide those that utilize the architecture with the means to maximize, minimize, or simply adjust its stiffness property so as to optimize it for particular tasks, such as augmented lifting or impact absorption. This research even provides the means to produce non-homogeneous stiffness properties for applications that may require non-homogeneous dynamic behavior. In this work, the new architecture is demonstrated in the form of a shoulder exoskeleton. An analytical stiffness model for the shoulder exoskeleton is created and validated experimentally. The model is then used, along with a method of bounded nonlinear multi-objective optimization to configure the parallel substructures for desired rigidity, compliance or nonhomogeneous stiffness behavior. The stiffness model and its optimization can be applied beyond the shoulder to any embodiment of the new parallel architecture, including the hip, wrist and ankle robot applications.

1.6 Overview - Chapter 7

The purpose of this work is to demonstrate that the 4B-SPM shoulder exoskeleton developed previously is capable of accurately estimating the neuromuscular properties of the human shoulder. To do this, the device is tested using a shoulder mock-up that has stiffness, damping and inertia. The stiffness and inertia of the mock-up can be controlled by attaching springs and masses with known properties to it. Estimating these properties accurately using torque and position sensors allows for an evaluation of the device's ability to estimate human shoulder stiffness, damping and inertia. This work also includes some preliminary testing with a human subject.

Chapter 2

A NOVEL SHOULDER EXOSKELETON ROBOT USING PARALLEL ACTUATION AND A PASSIVE SLIP INTERFACE

2.1 Introduction

A parallel manipulator (Merlet, 2012) is a robotic mechanism that uses multiple actuated parallel linkages to synergistically manipulate the motion of its end-effector. The architecture of these devices can vary considerably, but usually consists of between two and six rotational or linear actuators, which couple a mobile platform to a stationary base. In comparison to the more common serial chain manipulator, parallel manipulators can offer better end-effector performance in terms of precision, velocity, and torque generation (Merlet, 2012; Taghirad, 2013; Gogu, 2008). Parallel manipulators also tend to exhibit lower effective inertia than serial chain manipulators (Gogu, 2008; Khatib, 1988). Furthermore, it is possible to design a parallel manipulator such that it does not occupy its center of rotation. This unique combination of advantages, inherent to parallel manipulation, suggests that this type of robotic architecture would be suitable for exoskeleton limb applications.

Parallel manipulators have been used for several exoskeleton applications. Prior works include wearable wrist (Gupta *et al.*, 2008), ankle (Roy *et al.*, 2007) and shoulder (Klein *et al.*, 2010) devices. All of these demonstrate different types of parallel architecture. The RiceWrist (Gupta *et al.*, 2008) uses a 3-RPS (revolute-prismatic-spherical) manipulator with an additional serial revolute joint to generate four degrees-of-freedom (DoF) that includes the rotation of the forearm, wrist height and 2-DoF in rotation of the end-effector platform. The Anklebot (Roy *et al.*, 2007) uses a 2-SPS-1S (spherical-prismatic-spherical, spherical) manipulator that consists of spherical joints and prismatic actuation in conjunction with the biological joint to achieve spherical motion. The shoulder exoskeleton BONES (Klein *et al.*, 2010) uses a RRPS (revolute-revolute-prismatic-spherical) manipulator to decouple and control three rotational DoF. Because all of these devices generate spherical motion through parallel actuation, they can further be categorized as spherical parallel manipulators (SPMs).

The prior works (Gupta *et al.*, 2008; Roy *et al.*, 2007) focus on biological joints that can be modeled as either having purely rotational or spherical motion. Although this simplifying assumption is a good approximation for these joints, it has demonstrated inaccuracy for more complex joints like the shoulder. Rotational motion of the shoulder's clavical and scapula results in translational motion of the glenohumeral joint (Veeger, 2000; Harryman *et al.*, 1990). Therefore the humerus of the upper arm actually has both rotational and translational motion. This has been realized by previous works (Haninger *et al.*, 2014; Carignan *et al.*, 2005; Jung and Bae, 2014; Mihelj *et al.*, 2007; Schiele and Visentin, 2003) whom have all built serial actuated shoulder exoskeletons to more accurately emulate the shoulder's motion by incorporating translational DoF into their designs. However, the choice of using serial actuation has the inherent disadvantages of low stiffness, high inertia, and positioning errors that are accumulated and amplified from base to end-effector.

A solution for emulating the complex rotational and translational motion of the shoulder might be to use a parallel manipulator with a higher degree of actuation. A possibility would be the six linear actuator hexapod design known as the Gough-Stewart (GS) platform (Gao *et al.*, 2005). This device has control over all 6-DoF of its platform and exhibits good stiffness characteristics, making it ideal for high precision and high load applications. However, the GS platform has limited workspace.

This is largely in part to mechanical interference between the device's many parallel linkages. Designing a GS platform with the same range of motion as the shoulder would be difficult (Jiang and Gosselin, 2009; Dasgupta and Mruthyunjaya, 2000). In addition, the argument could be made that a fully actuated 6-DoF system is an overly complicated solution to address the relatively small degree of translational motion of the shoulder.

An alternative to using a more complicated 4, 5 or 6-DoF controlled parallel manipulator is to use a 3-DoF SPM with an integrated passive slip interface. Allowing slip to occur between user and device could be used to alleviate mechanical interference associated with joint misalignment. This mechanical interference could otherwise induce force on the user and may introduce errors in the parallel manipulator kinematics (Pons, 2010). The use of passive slip also simplifies the control scheme of the parallel manipulator, since the degree of joint misalignment no longer needs to be quantified and accounted for. Slip interfaces have been utilized in the works (Jarrassé and Morel, 2012; Vitiello *et al.*, 2013; Cempini *et al.*, 2013), both of which have identified it as a viable means of preventing mechanical interference.

With the exception of BONES, incorporating slip into current SPM designs would be difficult for a shoulder exoskeleton application. The RRPS architecture used with BONES could be modified to include a slip mechanism. However, BONES uses four linear actuators to control the 3-DoF of the shoulder, whereas other SPM architectures have shown that it is possible to achieve 3-DoF control with only three actuators (Gan *et al.*, 2015). The 2-SPS design in (Roy *et al.*, 2007) uses the biological joint as part of the kinematic solution and will not work with slip. One SPM possibility would be the 3-RRR (rotational-rotational-rotational) "Agile Eye" parallel manipulator. This device uses three rotary actuators and curved linkages to decouple and control the three rotational DoF (Gan *et al.*, 2015; Tao and An, 2013). However, the 3-RRR's architecture does not interface well with the human shoulder, as its curved linkages pass through the majority of the sphere in which it rotates about. This would cause interference between the user and device. Another SPM possibility would be the 3-UPU (universal-prismatic-universal) “Spherical Wrist” parallel manipulator. This SPM consists of three parallel linear actuators which decouple and control the three rotational DoF (Gan *et al.*, 2015; Di Gregorio, 2003). The use of only three linear actuators introduces minimal mechanical interference and results a large workspace compared to other SPMs (Saltaren *et al.*, 2007). Additionally, the 3-UPU design is compact, which is advantageous for mobile applications. However, the 3-UPU has been shown to exhibit poor stiffness characteristics, which makes it impractical for real world use (Walter *et al.*, 2009).

In order to address this lack of compatibility with current SPMs and the proposed method of slip, a novel parallel manipulator has been developed. This parallel manipulator shares the SPS characteristic of spherical platform mounting joints and the 3-UPU characteristic of universal base mounting joints, but uses a novel method of coupling certain motions of each actuator independently in order to produce a device with a single kinematic solution.

The rest of this paper presents this novel SPM design along with the discussed slip mechanism for handling translational motion of the shoulder. The sections are organized as follows: Section 2 details the design of the SPM and slip mechanism. Section 3 details the results of an experiment to validate the kinematics and workspace. Finally, Section 4 concludes the paper with a discussion and summary of the contribution.

2.2 Methods

2.2.1 Design Overview

The developed SPM is presented in Fig. 2.1. The device weighs 5.4 kg, excluding batteries and off-board controller. It consists of three parallel linear actuators connected to a shoulder piece coupled to the user. Each actuator has 3-DoF. Two of the DoF are rotational (roll and pitch) and one is translational (stroke). The roll of each actuator is defined to rotate about the vector connecting the actuator's base mounting point to the center of rotation of the user's shoulder. The roll is not directly constrained, but rather set by the synergistic movements of all three actuators. The pitch and length of each actuator are mechanically coupled such that the workspace is a spherical surface centered about the user's shoulder. Each actuator is connected to the shoulder piece by a 3-DoF tie-rod joint. The shoulder piece is connected to the user's arm by a 2-DoF passive slip joint that allows for 1-DoF of rotational motion and 1-DoF of translational motion. The rotational DoF prevents undesired torques from being applied to the user's arm during the rolling action of the exoskeleton shoulder. The translational DoF allows slip to occur between the user and the device. The base mounts of each actuator are situated in close proximity to the user's back. However, placement of the base mounts are flexible and only limited by physical constraints, such as mechanical interference. Several viable alternative mounting configurations are shown in Fig. 2.2.

2.2.2 Actuator Motion Coupling

One of the primary features of this SPM is that it uses the novel method of motion coupling to produce a device with a single kinematic solution. This method involves coupling certain DoF of each actuator independently in order to constrain

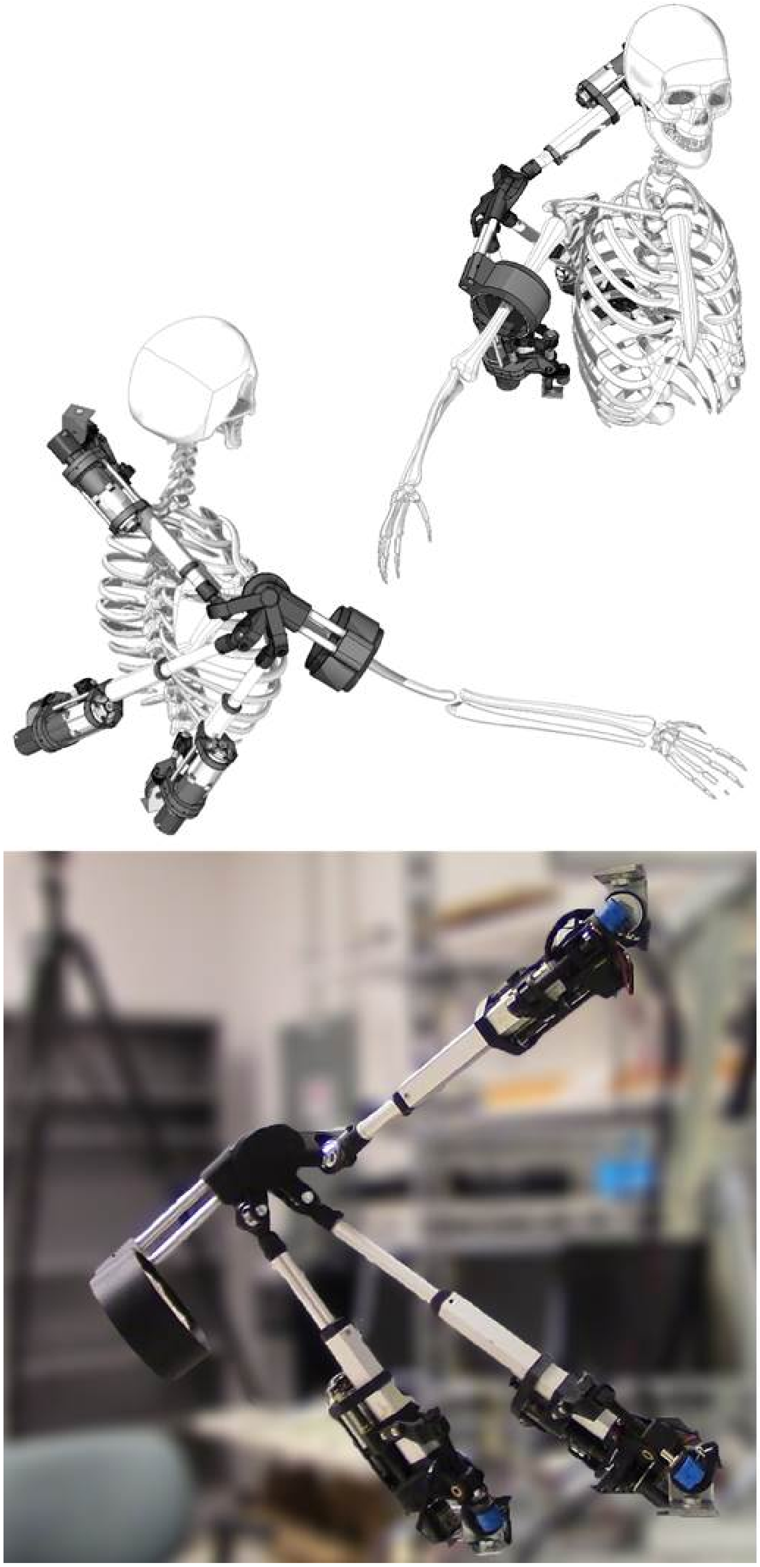

Figure 2.1: The SPM design. Conceptual model illustrating interface with user (top). Prototype (bottom)

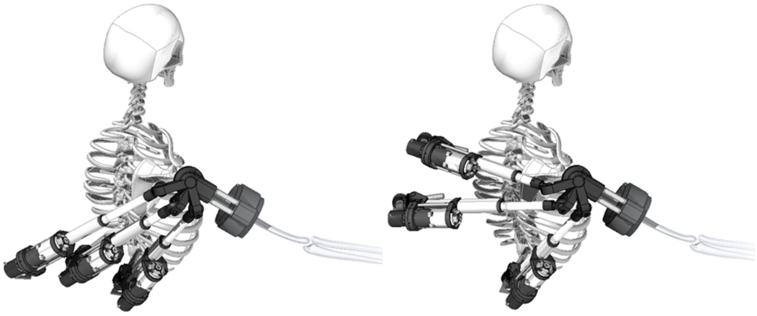

Figure 2.2: Examples of alternative base mount configurations

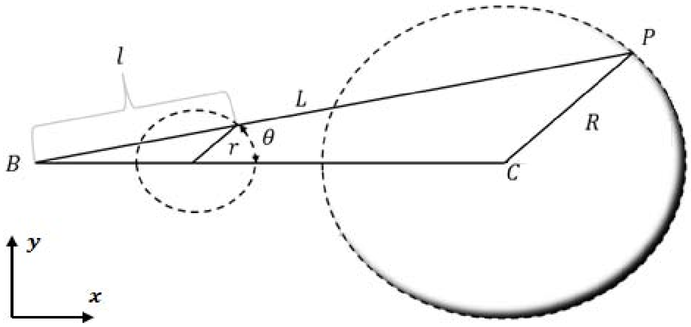

Figure 2.3: Actuator pitch and stroke coupling using similar triangle relation

the multiple kinematic solutions of the non-coupled system to a single solution for the coupled system. For this SPM, the pitch angle θ and length vector $\overline{L}$ of each independent actuator are coupled such that all possible kinematic solutions lie on a sphere centered about the user's shoulder vector $\overline{C}$. With reference to Fig. 2.3, the desired θ is:

$$\theta = atan2(L_y, L_x) \tag{2.1}$$

In order to achieve this required θ angle, a linear slider mounted near the base vector $\overline{B}$ of the actuator is used. This slider controls the position of armature vector $\overline{r}$ along $\overline{L}$ and is driven by the same motor that drives $\overline{L}$, but with a different gearing ratio. Instead of solving the nonlinear Eq. (2.1) for θ, it is possible to solve for the slider distance vector $\overline{l}$ along $\overline{L}$, which is described by a similar triangle relationship between $\overline{B}$, $\overline{C}$, and the platform mount vector $\overline{P}$. This same relationship can also be

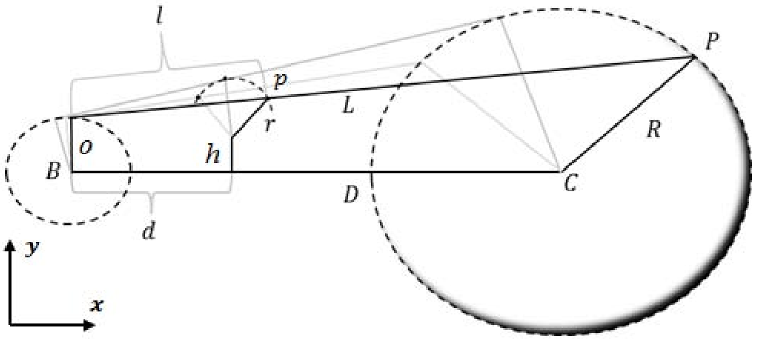

Figure 2.4: Actuator pitch and stroke coupling with offsets r' and d' to avoid mechanical interference

expressed in scalar terms as:

$$\|\bar{l}\| = \frac{\|\overline{L}\|\|\overline{r}\|}{\|\overline{R}\|} \tag{2.2}$$

In practice however, it was found that the similar triangle relationship between lrd and LRD is difficult to maintain. An offset vector $\overline{o}$ from $\overline{B}$ is necessary to avoid mechanical interference. As shown in Fig. 4, the existence of $\overline{o}$ also introduces an offset vector $\overline{h}$ between $\overline{r}$ and $\overline{d}$. Solutions for $\overline{r}$, $\overline{h}$, and $\overline{d}$ can be found by fitting an arc to three slider positions $\overline{p}$ that correspond to three arbitrary values of $\overline{L}$ that exist on the desired spherical workspace. The center of the arc represents the position $\overline{d} + \overline{h}$ and the arc radius represents $\overline{r}$. To construct the arc, the vector components o_x, o_y, L_x, and L_y must first be solved. This can be achieved by the following system of vector and trigonometric equations with relation to the known terms $\|\overline{o}\|$, $\overline{D}$ and $\overline{R}$:

$$\overline{o} + \overline{L} = \overline{D} + \overline{R} \tag{2.3}$$

$$\|\overline{o}\|^2 = o_x^2 + o_y^2 \tag{2.4}$$

$$\|\overline{o}\|^2 + L_x^2 + L_y^2 = (R_x + D_x)^2 + (R_y + D_y)^2 \tag{2.5}$$

Where Eq. (2.3) is the vector relation of $\overline{D}$ and $\overline{R}$ to $\overline{o}$ and $\overline{L}$. The trigonometric Eq. (2.4)-(2.5) relate the known magnitude $\|\overline{o}\|$ and the right angle relation of $\overline{o}$ and $\overline{L}$ to the unknown vectors components of $\overline{o}$ and $\overline{L}$.

With the components of $\overline{L}$ and $\overline{o}$ known, it is possible to solve for the slider distance vector $\overline{l}$ along $\overline{L}$, which is necessary in order to determine the slider position vector $\overline{p}$ with respect to $\overline{B}$. The vector $\overline{l}$ is a function of the collinear vector $\overline{L}$ and the design choices of slider offset l_o from $\overline{o}$, gear ratio w, and retracted actuator length L_o. This relationship can be described by:

$$\overline{l} = w(\overline{L} - L_o\overline{u}) + l_o\overline{u} \tag{2.6}$$

where

$$\overline{u} = \frac{\overline{L}}{\|\overline{L}\|} \tag{2.7}$$

The slider position $\overline{p}$ expressed as a vector from $\overline{B}$ is:

$$\overline{p} = \overline{l} + \overline{o} \tag{2.8}$$

Given three slider position vectors $\overline{p}_1$, $\overline{p}_2$, and $\overline{p}_3$ which correspond to three arbitrary actuator lengths $\overline{L}_1$, $\overline{L}_2$, and $\overline{L}_3$ respectively, which exist on the spherical workspace, it is now possible to construct the arc and solve for $\overline{r}$, $\overline{h}$ and $\overline{d}$.

One of the motion coupled actuators is shown in Fig. 2.5. Each actuator has position feedback sensors to enable closed-loop control. The stroke length of the top two actuators is 152.42 mm and the bottom actuator is 101.62 mm. These lengths were chosen such that the workspace of the device would be approximately one octant of a sphere. Each actuator has been configured such that the device operates on a spherical surface at a radius of $\|\overline{R}\| = 95.17$ mm from the center of rotation of the

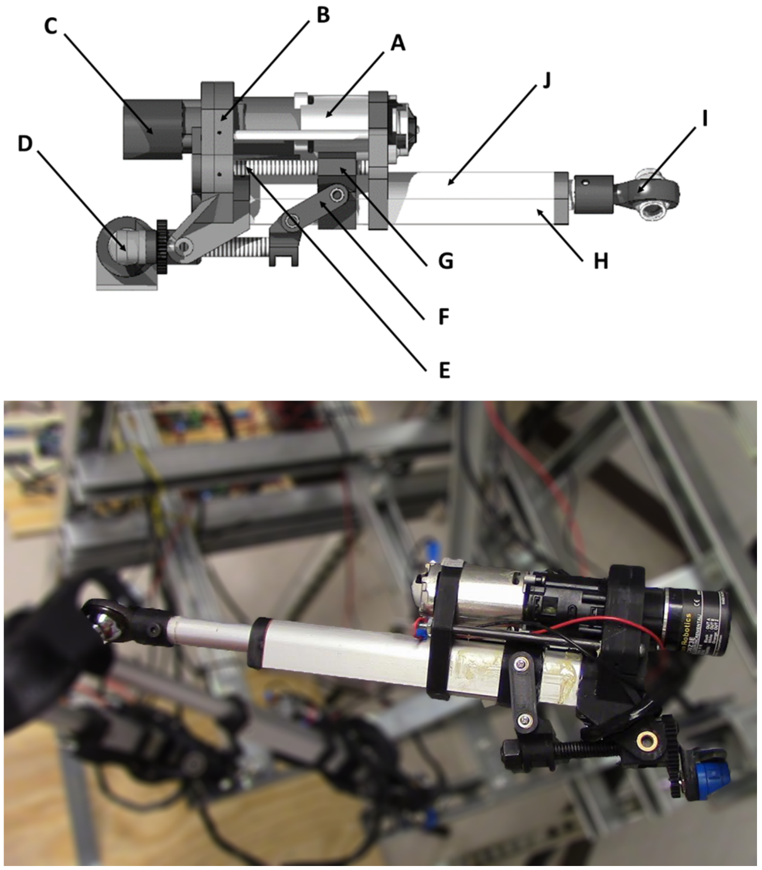

Figure 2.5: Motion coupled actuator. Conceptual model (top) with the following components: A) Motor, B) Custom gearbox, C) Pitch/Stroke encoder, D) Roll measurement potentiometer, E) Wormscrew, F) Pitch/Stroke coupling linkage, G) Pitch control slider, H) Enclosed limit switches, I) Tie rod joint, J) Enclosed powerscrew and slider for linear actuation. Developed prototype (bottom)

user's shoulder. This radius was determined through measurement of the shoulder center of rotation to the outer surface of the lateral and posterior deltoids of three adult male subjects.

2.2.3 Inverse Kinematics

For the global frame defined in Fig. 2.6, the inverse kinematic solution can be determined by first defining the local frame vector $\overline{x}'$ to be collinear to the user's desired arm direction. The vector $\overline{x}'$ can be further described by the inclination angle

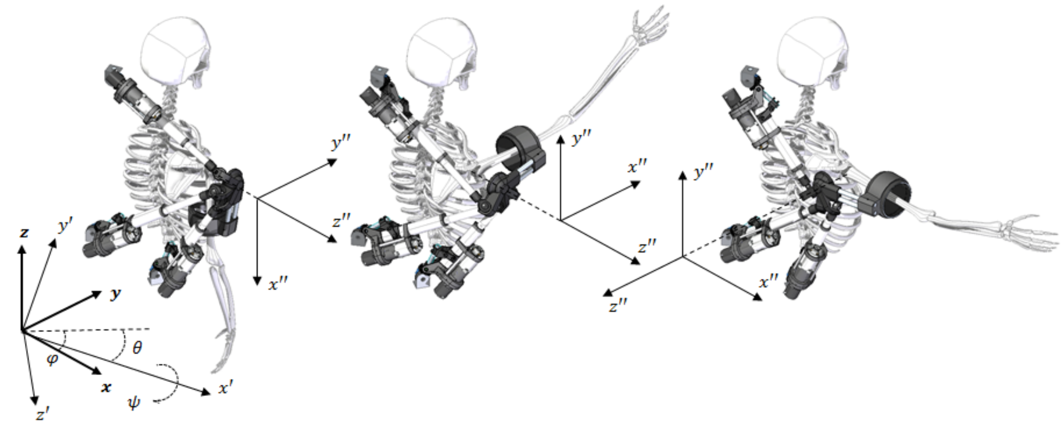

Figure 2.6: Chosen exoskeleton shoulder orientation for given arm directions

θ and azimuth angle ϕ, which are defined in Fig. 2.6. The initial orientation of the local vector $\overline{z}'$ can be expressed as the cross products of $\overline{x}'$ and the global vector $\overline{z}$. The local vector $\overline{y}'$ is the cross product of $\overline{z}'$ and $\overline{x}'$. It is necessary to multiply this initial set of orientation vectors $\mathbf{R}'$ by a rotation matrix $\mathbf{R_x}$ about $\overline{x}'$ in order to keep the shoulder within the workspace of the three linear actuators. Hence the new rotation matrix is:

$$\mathbf{R}'' = \mathbf{R}'\mathbf{R_x} \tag{2.9}$$

where

$$\mathbf{R}' = \begin{bmatrix} x'_x & y'_x & z'_x \\ x'_y & y'_y & z'_y \\ x'_z & y'_z & z'_z \end{bmatrix} \tag{2.10}$$

$$\mathbf{R_x} = \begin{bmatrix} 1 & 0 & 0 \\ 0 & \cos\psi & -\sin\psi \\ 0 & \sin\psi & \cos\psi \end{bmatrix} \tag{2.11}$$

The angle ψ in Eq. 2.11 represents the angle of rotation about $\overline{x}'$. Finding ψ, which determines $\mathbf{R_x}$, is done by first identifying a set of key orientations that define the workspace. For this device, approximately one octant of a sphere is a decidedly sufficient workspace to demonstrate proof-of-concept. The chosen orientation matrices at arm rest $\mathbf{R_r''}$ ($\theta = -90°$, $\phi = 90°$ or $\theta = -90°$, $\phi = 0°$), arm flexion $\mathbf{R_f''}$ ($\theta = 0°$, $\phi = 90°$), and arm abduction $\mathbf{R_a''}$ ($\theta = 0°$, $\phi = 0°$) of the shoulder piece for the three corners of the octant are shown in Fig. 2.6. For these orientations, Eq. 2.9 becomes:

$$\mathbf{R_r''} = \begin{bmatrix} 0 & 0 & 1 \\ 0 & 1 & 0 \\ -1 & 0 & 0 \end{bmatrix} = \begin{bmatrix} 0 & 0 & 1 \\ 0 & 1 & 0 \\ -1 & 0 & 0 \end{bmatrix} \begin{bmatrix} 1 & 0 & 0 \\ 0 & 1 & 0 \\ 0 & 0 & 1 \end{bmatrix} \tag{2.12}$$

or

$$\mathbf{R_r''} = \begin{bmatrix} 0 & 0 & 1 \\ 0 & 1 & 0 \\ -1 & 0 & 0 \end{bmatrix} = \begin{bmatrix} 0 & 1 & 0 \\ 0 & 0 & -1 \\ -1 & 0 & 0 \end{bmatrix} \begin{bmatrix} 1 & 0 & 0 \\ 0 & 0 & 1 \\ 0 & -1 & 0 \end{bmatrix} \tag{2.13}$$

and

$$\mathbf{R_f''} = \begin{bmatrix} 0 & 0 & 1 \\ 1 & 0 & 0 \\ 0 & 1 & 0 \end{bmatrix} = \begin{bmatrix} 0 & 0 & 1 \\ 1 & 0 & 0 \\ 0 & 1 & 0 \end{bmatrix} \begin{bmatrix} 1 & 0 & 0 \\ 0 & 1 & 0 \\ 0 & 0 & 1 \end{bmatrix} \tag{2.14}$$

$$\mathbf{R_a''} = \begin{bmatrix} 1 & 0 & 0 \\ 0 & 0 & -1 \\ 0 & 1 & 0 \end{bmatrix} = \begin{bmatrix} 1 & 0 & 0 \\ 0 & 0 & -1 \\ 0 & 1 & 0 \end{bmatrix} \begin{bmatrix} 1 & 0 & 0 \\ 0 & 1 & 0 \\ 0 & 0 & 1 \end{bmatrix} \tag{2.15}$$

It is important to note that the orientation of $\mathbf{R}'$ in Eq. (2.12)-(2.13) cannot be achieved, since $\overline{z}' = \overline{x}' \times \overline{z}$. However, for the purpose of solving for ψ, $\mathbf{R_r}$ can be assumed to reach this orientation. In practice, only a solution infinitesimally close to this orientation can be achieved. For $\mathbf{R_x}$ in Eq. (2.12)-(2.15), $\psi = 0°$, $-90°$, $0°$, and $0°$, respectively. Given ψ and the corresponding θ and ϕ, it is possible to derive a general relation using a multivariable sinusoidal fit which defines ψ for the entire workspace. The function ψ of θ and ϕ is described by:

$$\psi = \sin(\theta)\left(\frac{\pi}{2} - \phi\right) \tag{2.16}$$

With a known orientation $\mathbf{R}''$ and a chosen radius of operation R, a chain of transformation matrices can then be used to describe the position of any point on the exoskeleton shoulder. For the location of an arbitrary mounting point described by $\overline{P}$ with respect to the local exoskeleton shoulder frame at R from the center of rotation, this transformation matrix $\mathbf{T}$ becomes:

$$\mathbf{T} = \begin{bmatrix} R''_{1x} & R''_{2x} & R''_{3x} & R''_{3x}R \\ R''_{1y} & R''_{2y} & R''_{3y} & R''_{3y}R \\ R''_{1z} & R''_{2z} & R''_{3z} & R''_{3z}R \\ 0 & 0 & 0 & 1 \end{bmatrix} \begin{bmatrix} 1 & 0 & 0 & P_x \\ 0 & 1 & 0 & P_y \\ 0 & 0 & 1 & P_z \\ 0 & 0 & 0 & 1 \end{bmatrix} \tag{2.17}$$

With the location of base mounting point $\overline{D}$ known and the platform mounts described by translational components of $\mathbf{T}$ known, the length of each actuator L_i is the Euclidean distance between its respective mounting points:

$$\|\overline{L_i}\| = \sqrt{(T_{14_i} - D_{x_i})^2 + (T_{24_i} - D_{y_i})^2 + (T_{34_i} - D_{z_i})^2} \tag{2.18}$$

2.2.4 Forward Kinematics

The forward kinematics of this SPM are solved by using position feedback sensors. Each actuator is equipped with an encoder (Karlsson Robotics E6C2), having a resolution of 1024 pulses/rotation, to record the coupled pitch and stroke length. The roll of each actuator is measured using a 10K ohm potentiometer (Bourns 3590S). The endpoint of each actuator is found from both angles and the stroke length. The position and orientation of the platform is found from the three actuator endpoints.

2.2.5 Slip Mechanism

The slip mechanism, used in this shoulder exoskeleton for preventing the adverse effects of joint misalignment, consists of a passive cuff joint with one translational DoF and one rotational DoF. The internal cuff of this joint has a compliant padded interior which is designed to stay in contact with the user's upper arm. The external cuff is connected to the shoulder exoskeleton. When joint misalignment between the center of rotation of the user's glenohumeral joint and the center of rotation of the shoulder exoskeleton occurs, the internal cuff translates within the external cuff as shown in Fig. 2.7. In addition to translational slip S, joint misalignment will effect the orthogonal relationship between the cross-section of the external/internal cuff and the user's arm. This cuff misalignment angle ω is shown in Fig. 2.7. The compliance of the internal cuff's padding allows for a degree of angular misalignment to occur without harm to the user or device. The internal cuff used in this prototype permits 3 cm of diametral padding deformation. The maximum angular misalignment is a function of this allowable deformation and of the user's arm diameter.

The joint misalignment vector $\overline{v}_{mis}$ can occur in any direction. However, the maximum translational slip S_{max} will always occur when user's arm direction vector $\overline{v}_{user}$ is collinear to $\overline{v}_{mis}$, for which $\|\overline{S}_{max}\| = \|\overline{v}_{mis}\|$. This case of maximum slip is exemplified in Fig. 2.7 for which horizontal joint misalignment has occurred and the user arm is at a 90° abduction angle from the resting position. The maximum cuff misalignment angle ω_{max} is also shown in Fig. 2.7 and occurs at the resting position when $\overline{v}_{mis}$ is orthogonal to $\overline{v}_{user}$.

This case of maximum cuff misalignment is also shown in the Fig. 2.7 example and occurs when the arm is at rest, for which $\overline{v}_{mis} \perp \overline{v}_{user}$. Both $\overline{S}_{max}$ and ω_{max} have rotational symmetry about $\overline{v}_{mis}$ and therefore any arbitrary plane about $\overline{v}_{mis}$ can be examined to determine $\overline{S}_{max}$ and ω_{max}. With reference to Fig. 2.8, $\overline{S}_{max}$ and ω_{max} are solved by first projecting the components of the $\overline{v}_{mis}$ into the plane comprised of $\overline{v}_{mis}$, $\overline{v}_{user \perp mis}$, and $\overline{v}_{user \parallel mis}$. Using the collinear relation between $\overline{v}_{user}$ and $\overline{S}$ and the vector relation between $\overline{v}_{user}$, $\overline{v}_{mis}$ and the shoulder exoskeleton arm vector $\overline{v}_{exo}$, $\overline{S}$ can be solved by the following system:

$$\|\overline{v}_{exo}\|^2 = (v_{mis\,xy} + S_{xy} - v_{user\,xy})^2 + (v_{mis\,z} + S_z - v_{user\,z})^2 \tag{2.19}$$

$$\frac{S_{xy}}{S_z} = \frac{v_{user\,xy}}{v_{user\,z}} \tag{2.20}$$

Of the two possible solution sets, the correct set will match the sign notation of the components of $\overline{v}_{user}$. With $\overline{S}$ known, ω is expressed as the angle between $\overline{v}_{user}$ and $\overline{v}_{exo}$, where $\overline{v}_{exo} = \overline{v}_{mis} + \overline{v}_{user} - \overline{S}$.

2.2.6 Control System

To operate the shoulder exoskeleton, a keyboard control scheme running on an off-board PC for high-level control was used. The user commands the θ and ϕ angles in 5° increments using the arrow keys within a Matlab interface. The Matlab script solves the forward and inverse kinematics based on the user's desired position and sends new position and velocity commands via serial communication to a microcontroller (Arduino Mega 2560). This microcontroller then relays the position commands to a set of corresponding PID motion controllers (Kangaroo 2x Motion Controller), which are connected to a set of motor drivers (SyRen 10A Regenerative Motor Driver). Each motion controller was in a feedback loop with its respective actuator's encoder and

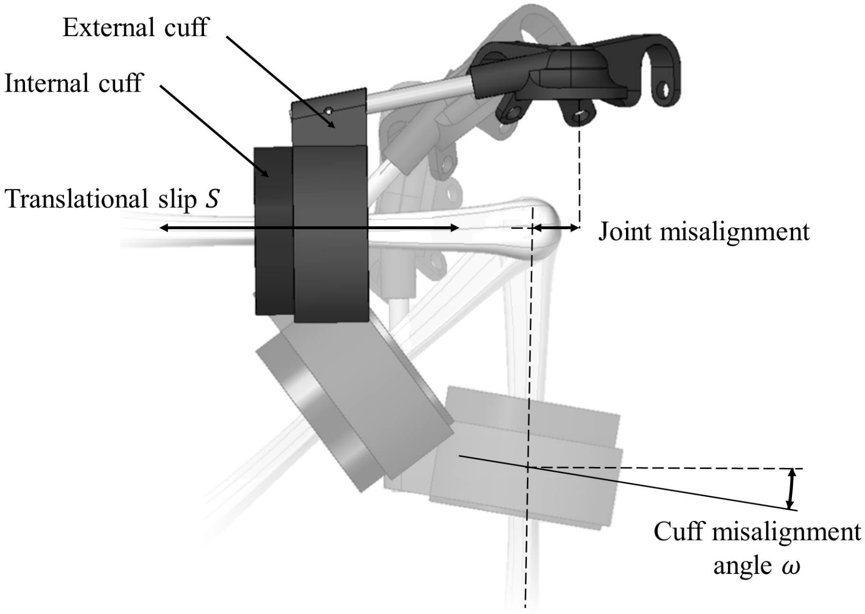

Figure 2.7: Upper arm slip mechanism for joint misalignment

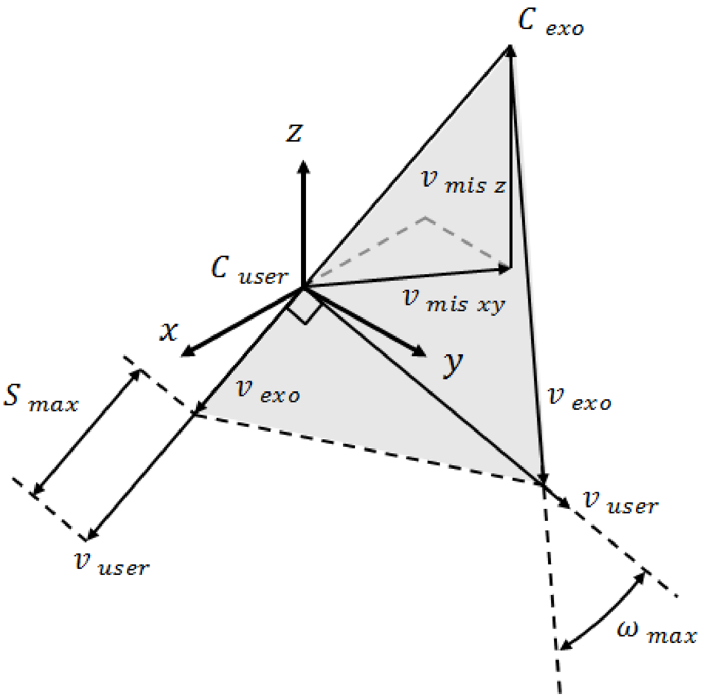

Figure 2.8: Upper arm slip mechanism with joint misalignment in 3D space

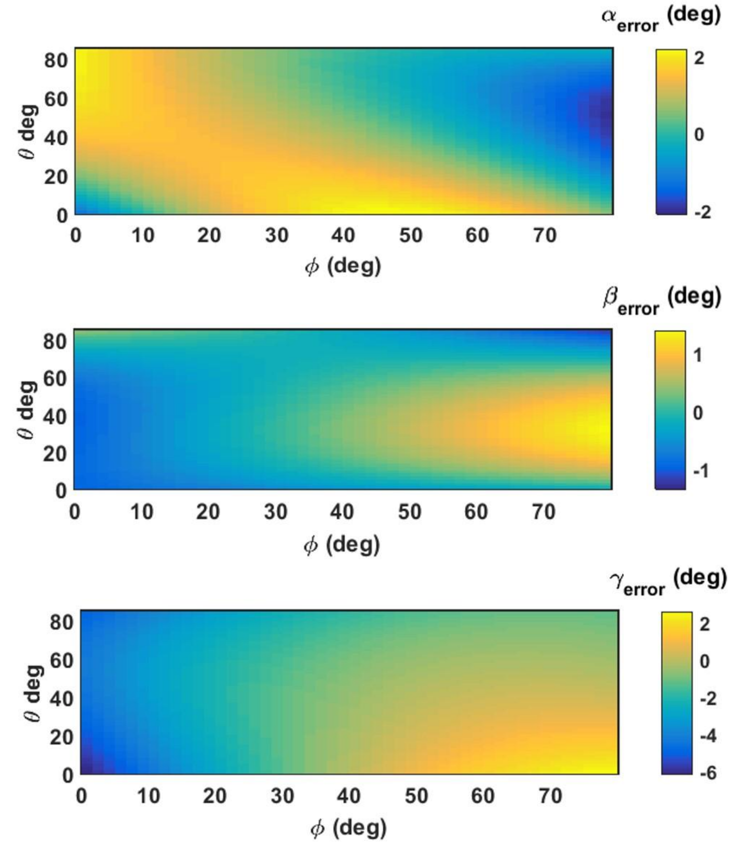

Figure 2.9: Error between the actual and commanded shoulder orientation expressed using the z-x-z euler angles α, β, and γ, respectively

limit switches. Once the desired positions are met, a secondary feedback loop alerts the Matlab-based controller that the motion controller is ready to execute the next set of user commands.

2.3 Results

2.3.1 SPM Kinematics

To validate the kinematics, we conducted a preliminary experiment using VICON motion capture. Markers were placed on the shoulder piece and tracked by a set of four motion capture cameras throughout a grid trajectory that varied both θ and ϕ in 5° increments. The range of θ and ϕ were determined experimentally and the conservative choice of 0° $\leq \theta \leq -85°$ and 0° $\leq \phi \leq 80°$ was used for the experiment in order to ensure that a joint limit would not be reached. Both θ and ϕ are functional to the placement and maximum stroke length of each actuator. Adjusting either of these parameters will effect the workspace. The placed markers were then used to reconstruct the local frame, which was compared to the commanded orientation at each grid point. The comparison was done using z-x-z Euler angles. The difference between each set of angles with respect to the corresponding θ and ϕ angles is presented in Fig. 2.9 for each Euler angle. The results showed mean Euler angle errors of $\alpha_{mean} = 1.01°$, $\beta_{mean} = 0.46°$, and $\gamma_{mean} = 1.87°$. The variance of the Euler angles were calculated to be 1.18°, 0.3°, and 3.46° for α, β, and γ, respectively.

2.3.2 Slip Mechanism

To quantify the translation slip S and the cuff angular misalignment ω, a computational slip model was constructed. The model uses the joint misalignment vector $\overline{v}_{mis}$, the user's arm direction vector $\overline{v}_{user}$, and a zero cuff position at 166 mm from the center of rotation as inputs. In this model, the convention chosen is that θ exists in quadrant III (+x,+y) of the plane and that positive joint misalignment exists in quadrant I (-x,-y). The model results in Fig. 2.10 and Fig. 2.11 show S_{max} and ω_{max}, respectively, across a complete 90° degree variation of θ. It can be observed from Fig. 2.10 that S_{max} is minimized for planar joint misalignment when the joint misalignment vector is in the opposing direction to $\overline{v}_{user}$ at $\theta = -45°$. In Fig. 2.11, it can be observed that ω_{max} is minimized for planar joint misalignment when $\overline{v}_{mis}$ is collinear to $\overline{v}_{user}$ at $\theta = -45°$.

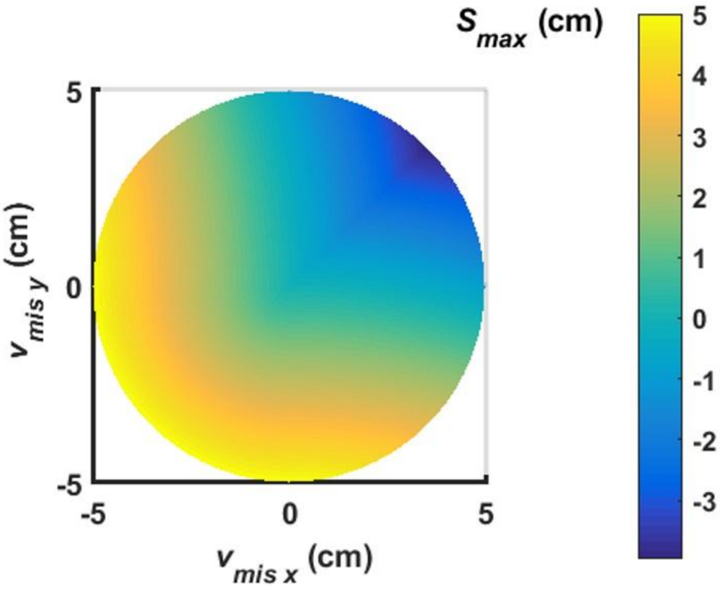

Figure 2.10: Maximum translation slip S_{max} of the cuff for given planar misalignment v_{mis}

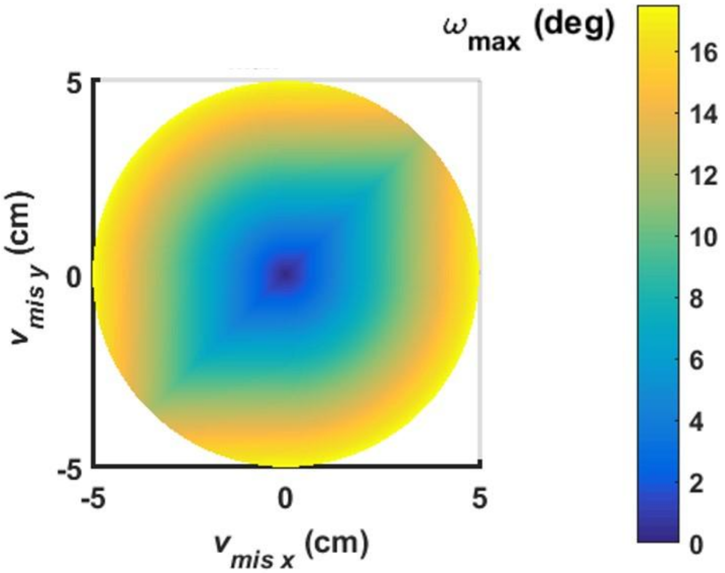

Figure 2.11: Maximum cuff misalignment angle ω_{max} for given planar misalignment v_{mis}

2.4 Discussion

This paper presented a novel 5-DoF shoulder exoskeleton using parallel actuation and an integrated passive slip interface. By using a parallel architecture, our system offers a low inertia solution to limb actuation, which is important with regards to energy cost and the performance of wearable devices. We also presented the method of motion coupling that was used to develop this new type of SPM with a single kinematic solution. This method could be applied to other parallel or serial actuated architectures in order to further constrain motion. Finally, this paper discusses how the use of a slip interface can be used for negating the adverse effects of joint misalignment and how it allows the presented SPM in particular to be used to emulate the complex motion of the human shoulder. It is important to note that this idea of allowing mechanical slip could be extended to include the rest of the arm as well. For a full arm exoskeleton, a secondary slip mechanism would be necessary after the elbow joint.

An experiment was performed to validate the kinematics of the SPM using motion capture. This experiment showed mean Euler angle errors of 1.01°, 0.46°, and 1.87° for α, β, and γ, respectively. Contribution of error includes compliance of 3D printed materials used in the construction of the actuators, low machining tolerances associated with in-house fabrication, and a placement tolerance of 3 mm for the base mounting brackets. Additionally, a computational model to simulate the maximum translation slip S and the cuff misalignment angle ω was created. This model demonstrated the values of S and ω expected for up to 5 cm of joint misalignment.

Apart from being a novel device, this shoulder exoskeleton could be utilized for either rehabilitation or augmentation. In its current keyboard control setup, it could be used for forms of upper limb rehabilitation that are sensitive to the effects of joint misalignment. In regards to assistive applications, this device could be mounted to an electric wheelchair to help those with upper limb impairments. Another application would be to integrate proximity sensors or piezoelectric foam into the arm cuff in order to allow for a different control method targeted at augmentation for industrial or military purposes.

Chapter 3

OPTIMIZING STIFFNESS OF A NOVEL PARALLEL-ACTUATED ROBOTIC SHOULDER EXOSKELETON FOR A DESIRED TASK OR WORKSPACE

In the field of exoskeleton robotics, the close-loop architecture of parallel manipulation offers many advantages over open-loop serial chain manipulation. While the comparatively simple kinematics and large workspace of the serial manipulator gave rise to its popularity, the parallel manipulator offers low end-effector inertia, high acceleration, high position accuracy, and the potential for high stiffness (Merlet, 2012; Taghirad, 2013; Li and Bone, 2001). In addition, certain parallel manipulators such as the 3-SPS (spherical-prismatic-spherical) (Alici and Shirinzadeh, 2004) and 3-RRR (revolute- revolute- revolute) (Wu *et al.*, 2011) designs can operate without occupying their center of rotation, which is particularly useful when interfacing with biological joints such as the shoulder, hip, wrist and ankle with multiple degrees-of-freedom (DoF).

Parallel manipulators have been used before for several different exoskeleton applications. Prior works include wearable wrist (Gupta *et al.*, 2008), ankle (Roy *et al.*, 2009) and shoulder (Klein *et al.*, 2010) devices. All of these demonstrate different types of parallel architecture. The RiceWrist (Gupta *et al.*, 2008) uses a 3-RPS (revolute-prismatic-spherical) manipulator with an additional serial revolute joint to generate 4-DoF. These DoF include the rotation of the forearm, wrist height and 2-DoF in rotation of the end-effector platform. The Anklebot (Roy *et al.*, 2009) uses a 2-SPS-1S (spherical-prismatic-spherical, spherical) manipulator that consists of spherical joints and prismatic actuation in conjunction with the biological joint to achieve spherical motion. The shoulder exoskeleton BONES (Klein *et al.*, 2010) uses a RRPS (revolute-revolute-prismatic-spherical) manipulator to decouple and control three rotational DoF. Because all of these architectures, along with the previously mentioned 3-SPS and 3-RRR, generate spherical motion through parallel actuation, they can further be categorized as spherical parallel manipulators.

Spherical parallel manipulators (SPMs) typically offer a larger workspace than higher DoF parallel architectures (Walter *et al.*, 2009; Gosselin and Angeles, 1989). This is because they require fewer actuated substructures and therefore experience less mechanical interference between substructures. However, this also means they have fewer active DoF, which normally results in a drop in stiffness performance (Jiang and Gosselin, 2009; Gosselin, 1990; El-Khasawneh and Ferreira, 1999). This can be problematic, particularly for augmentative exoskeleton systems, which must maintain rigidity under heavy loading in order to function effectively.

In an effort to improve the workspace/stiffness tradeoff of SPMs, the authors have introduced a new method of parallel architecture design in previous work (Hunt *et al.*, 2017). The presented method involves coupling specific motions of each independent parallel substructure in order to increase the number of active DoF, which works to both constrain the kinematics and increase stiffness of the entire structure. This method was demonstrated by applying it to the design of a novel shoulder exoskeleton. Both the kinematics and workspace of the prototype developed were solved and experimentally verified in previous work (Hunt *et al.*, 2017).

One advantage of the new parallel architecture introduced in (Hunt *et al.*, 2017) is the flexibility of actuator placement. The three substructures that comprise the device can be placed in any position about a center point. Choosing this placement is critical, as the stiffness of the device was found to be highly dependent on the configuration of these substructures. For this reason, it is desirable to place these substructures effectively so as to maximize dynamic performance. Optimization techniques can be employed to maximize stiffness across an entire workspace or even for particular task, such as lifting in the sagittal plane.

The development of a stiffness optimization model would not only allow the stiffness of the shoulder exoskeleton to be maximized for a desired task or workspace, but it would also allow the architecture to be optimized for other joints as well. For example, this could include stair climbing for a hip device or running for an ankle device. Because of the significance that such a tool would have on the potential application of the novel parallel architecture described, this optimization problem is the focus of this work.

The rest of this paper presents the steps taken to optimize the stiffness of the exoskeleton shoulder for a desired task or workspace. The sections are organized as follows: Section II provides (1) a brief overview of the shoulder exoskeleton design, (2) the model used to characterize stiffness, (3) the experimental setup to validate the stiffness model and (4) the optimization techniques used to maximize stiffness. Section III details (1) the results of the stiffness model validation experiment and (2) the optimal actuator placement to maximize stiffness in the sagittal plane and for an entire workspace. Finally, Section IV concludes the paper with a discussion and summary of the contribution.

3.1 Methods

3.1.1 Design Overview

The developed shoulder exoskeleton is presented in Fig. 1. A simulation created to illustrate its design and operation can be found at https://youtu.be/vm9iL-SyoS8. The mobile shoulder piece depicted has three decoupled rotational DoF centered about the convergence point C. This point is assumed to be the center of rotation of the user's shoulder as well. However, due to possible translational motion of the user's

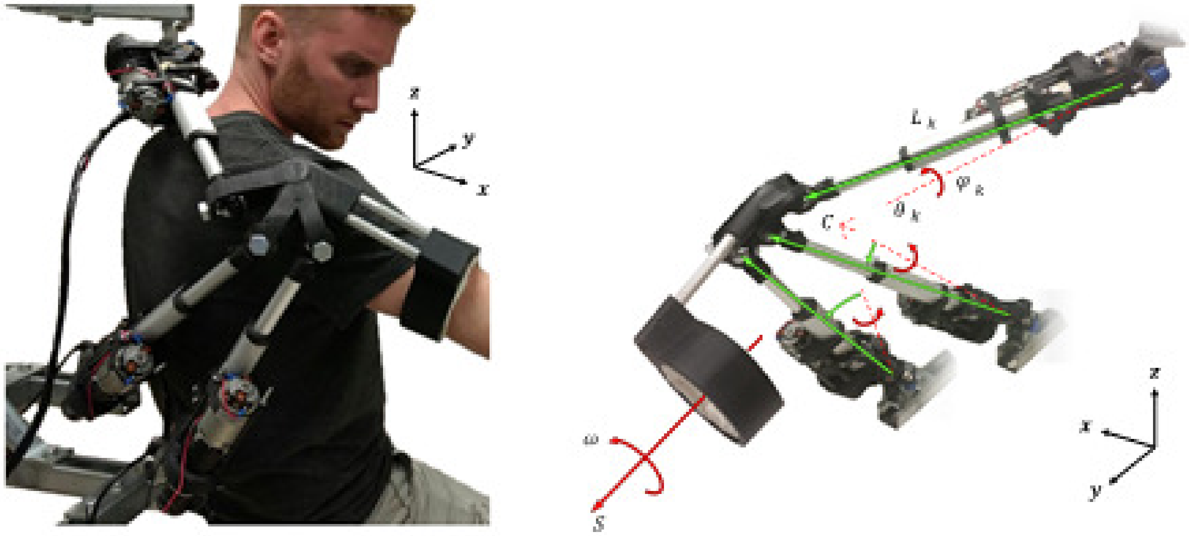

Figure 3.1: Implementation of the parallel actuated wearable robotic joint in a shoulder exoskeleton application. Shown on left is the interface of the actual prototype with a user. Shown on right is the devices architecture with the active (green) and passive (red) joints illustrated. The convergence point C represents the center of rotation for all three DoF of the devices shoulder piece. The variables ω and S represent the inner cuff rotation and translation, respectively. The variables θ_k, φ_k and L_k represent the pitch, roll, and linear stroke of each actuator substructure k, respectively.

shoulder joint, there may be an error between C and the actual center of rotation C'. To alleviate possible mechanical interference generated by the position error between C and C', a slip mechanism is integrated into the cuff of the device. The cuff, which acts as an interface between user and device, is positioned approximately midway on the user's upper arm. The cuff consists of two concentric open cylinders. The inner cylinder is padded with compliant foam and contacts the user's arm. The outer cylinder is connected to mobile shoulder piece by aluminum tubing. When joint misalignment between the user and device occurs, the inner cylinder will translate within the outer cylinder.

The spherical motion of the shoulder piece is accomplished by using three linear actuator substructures. Each substructure k has three DoF: pitch θ_k, roll φ_k and linear stroke L_k. The pitch and linear stroke of each substructure are mechanically coupled in order to achieve an arc motion of the substructure end effector. The method of coupling is a mechanical slider geared to the linear stroke and connected to an armature which adjusts the pitch of the actuator to a corresponding stroke length. This mechanism is detailed in Fig 2. By adjusting key variables of the motion coupling mechanism, such as slider speed and/or armature length, it is possible to adjust the radius and curvature of the substructure end effector motion. This may be necessary to avoid mechanical interference between the device and large or small users. In the current configuration, the arc is set to a constant radius of 9.5 cm. This radius was determined through measurement of the outer surface of the lateral and posterior deltoids to the approximate center of shoulder rotation of three adult male subjects. The roll of each substructure is not directly constrained, but rather set by the synergistic motion of all three substructures. Each actuated substructure is connected to the mobile shoulder piece using a 3-DoF tie rod joint.

Each actuator substructure was built using a linear actuator (FA-PO-35, Firgelli, WA). The top two actuators have a stroke length of 15.2 cm and the bottom actuator has a stroke of 10.2 cm. Each actuator was stripped of its stock motor and gearbox and modified to include a drill motor (393111-01, DeWalt, WI), custom gearbox, motion coupling mechanism, and feedback sensors. The coupled pitch angle and linear stroke length of each actuator are measured using an encoder (E6C2, Karlsson Robotics, FL) with a resolution of 1024 pulses/rotation. The roll is measured using a 10K ohm potentiometer (3590S, Bourns, CA). For testing purposes, each actuator substructure is mounted to a stationary frame. For the configuration and global frame orientation shown in Fig. 1, the Cartesian location of the top, middle and bottom mounting point with respect to C is $[-33, -10, 19]^T$ cm, $[-28, -17, -20]^T$ cm and $[-10, -12, -24]^T$ cm, respectively.

To operate the exoskeleton, a keyboard control scheme running on an off-board

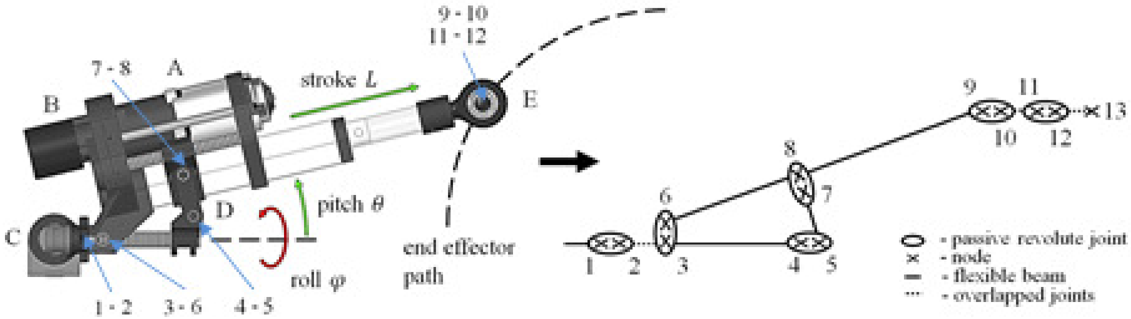

Figure 3.2: : Shown on left is one of the three actuated substructures with its active (green) and passive (red) DoF depicted. Key components are as follows: A) motor, B) pitch and stroke feedback encoder, C) roll feedback potentiometer, D) motion coupling mechanism with actuated slider and pitch control arm, E) 3-Dof platform mounting joint. Shown on right is the actuated substructure equivalent nodal diagram.

PC was used. A Matlab (Mathworks, MA) script was developed to map arrow keys to the elevation and azimuth of the shoulder piece. The program receives feedback from the onboard sensors via serial communication with a microcontroller (Mega 2560, Arduino, Italy) along with user input and uses it to solve the forward and inverse kinematics. Given an elevation and azimuth, the program determines the optimal roll angle of the shoulder piece about the user arm axis in order to keep it within the stroke length of all three actuators. Since the user does not have control over the roll angle of the shoulder, the passive cuff rotational DoF has been incorporated into the design in order to prevent an undesired torque from being applied to the user's arm. For a given desired shoulder orientation, actuator position and velocity commands are sent from the off-board PC through the Arduino microcontroller to a set of three PID motion controllers (0-KANGAROO2, Dimension Engineering, OH). Each PID controller is connected in loop with a 10 A motor driver (0-SYREN10, Dimension Engineering, OH).

Additional details regarding the design are provided in the prior work (Hunt *et al.*, 2017). This reference also provides an analysis of the kinematics and workspace, which have been excluded here for brevity.

3.1.2 Stiffness Model

In order to rapidly characterize the stiffness of the shoulder exoskeleton for different mounting point configurations and end effector orientations, an analytical model was created to calculate stiffness at the center of the shoulder piece. The model was developed using a matrix structural analysis method and closely follows the work of (Deblaise *et al.*, 2006). For brevity, the reader will be referred back to this prior work for some of the more derivative or expansive steps required in the development of this model. With the model, it is possible to generate the theoretical translational and rotational stiffness ellipsoids for different configurations and orientations in order to establish a basis for comparison.

To begin, each actuated substructure k $(k = 1,\ 2,\ 3)$ is deconstructed into nodes that correspond to characteristic points. Shown in Fig. 2 are the node locations for each actuator. The nodes are linked by either a flexible beam or passive revolute joint. It should be noted that beams must be modelled as flexible, since even minor beam deflections can have an impact on end effector stiffness. Each beam n is fixed at its ends by one or two nodes, depending on its location in the substructure. Each beam is therefore represented by either a 6x6 or the 12x12 beam stiffness matrix $\boldsymbol{K}_{n,k}$ as defined in Euler–Bernoulli beam theory. Before these beam stiffness matrices $\boldsymbol{K}_{n,k}$ can be assembled into one stiffness matrix $\boldsymbol{K}_{T,k}$, each must be multiplied by a matrix $\boldsymbol{P}_{n,k}$ comprised of rotation sub matrices $\boldsymbol{R}_{n,k}$, which describe $\boldsymbol{K}_{n,k}$ with respect to the global frame. The rotation of $\boldsymbol{K}_{n,k}$ by $\boldsymbol{P}_{n,k}$ is given by

$$\boldsymbol{K'}_{n,k} = \boldsymbol{P}_{n,k}{}^{-1}\boldsymbol{K}_{n,k}\boldsymbol{P}_{n,k} \tag{3.1}$$

where $\boldsymbol{P}_{n,k} = \begin{bmatrix} \boldsymbol{R}_{n,k} & 0 & \cdots \\ 0 & \boldsymbol{R}_{n,k} & \cdots \\ \vdots & \vdots & \ddots \end{bmatrix}$

The dimension of $\boldsymbol{P}_{n,k}$ is determined by the dimension of $\boldsymbol{K}_{n,k}$. The rotated stiffness matrices $\boldsymbol{K'}_{n,k}$ can then be used to construct $\boldsymbol{K}_{T,k}$ in accordance with the stiffness matrix assembly technique described in (Deblaise *et al.*, 2006; Hughes, 2012).

The matrix $\boldsymbol{K}_{T,k}$ describes the stiffness of the substructure before the inclusion of the passive joints. Each passive joint is defined by a matrix $\boldsymbol{A}_{n,k}$ that describes the kinematic relation between adjacent nodes. To define this relation, let $a_{n,k} = [a_x \ a_y \ a_z]^T{}_{n,k}$ be the unit vector which describes the revolute axis of a passive joint composed of two adjacent nodes. The coordinate frame of each node can be constructed using $a_{n,k}$ and the axially vector $b_{n,k}$ of the adjacent beam. The third coordinate frame vector, $c_{n,k}$ can be determined by $c_{n,k} = a_{n,k} \times b_{n,k}$. These coordinate frames of the two adjacent nodes can be related by a rotation about $a_{n,k}$. The vectors of this rotation can be defined as:

$$\boldsymbol{V}_{n,k} = \begin{bmatrix} b'_x & b'_y & b'_z \\ c'_x & c'_y & c'_z \end{bmatrix}_{n,k} \tag{3.2}$$

The complete kinematic relation between the two nodes that describes the passive revolute joint is derived in (Deblaise *et al.*, 2006) and given as:

$$\boldsymbol{A}_{n,k} = \begin{bmatrix} \boldsymbol{I}_{3x3} & \boldsymbol{0}_{3x3} \\ \boldsymbol{0}_{2x3} & V_{n,k} \end{bmatrix} \tag{3.3}$$

The $\boldsymbol{A}_{n,k}$ matrices are assembled into a single kinematic relation matrix $\boldsymbol{A}_{T,k}$ in a similar manner to $\boldsymbol{K}_{T,k}$. The total substructure stiffness matrix, which includes the effects of both the flexible beams and revolute joint, is derived using the minimum

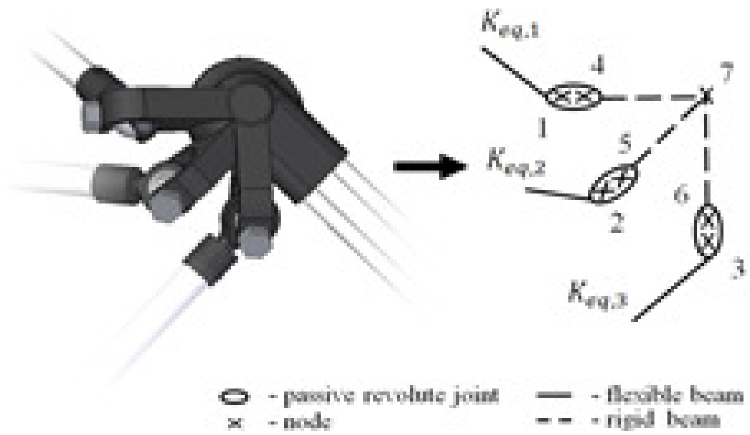

Figure 3.3: Shown on <u>left</u> is the shoulder piece. Shown on <u>right</u> is the shoulder piece equivalent nodal diagram with node 7 acting as the end effector position.

total potential energy principle and given as:

$$\boldsymbol{K}_{G,k} = \begin{bmatrix} \boldsymbol{K}_{T,k} & {\boldsymbol{A}_{T,k}}^T \\ \boldsymbol{A}_{T,k} & \mathbf{0} \end{bmatrix} \tag{3.4}$$

It is possible to calculate the displacement at the last node of each substructure k by permuting $\boldsymbol{K}_{G,k}$ in order to partition the endpoint substructure stiffness matrix $\boldsymbol{K}_{eq,k}$, which describes the last node. To define the stiffness of the entire structure, $\boldsymbol{K}_{eq,k=1,2,3}$ must be assembled to the end effector. The nodal diagram of the end effector is shown in Fig. 3. Since the shoulder piece interconnects all three substructure endpoint nodes and the end effector node, it can no longer be accurately described by Euler–Bernoulli beam theory. Instead, it will be modeled as set of rigid beams with infinite stiffness, which will require the introduction of a new kinematic relation. To start, let $W_n = {[L_x \ L_y \ L_z]_n}^T$ define the vector between two nodes linked by the rigid beam. The corresponding skew-symmetric matrix of this vector is:

$$\widehat{\boldsymbol{L}}_{W_n} = \begin{bmatrix} 0 & -L_z & L_y \\ L_z & 0 & -L_x \\ -L_y & L_x & 0 \end{bmatrix}_n \tag{3.5}$$

The complete kinematic relation between the two nodes that describes the rigid

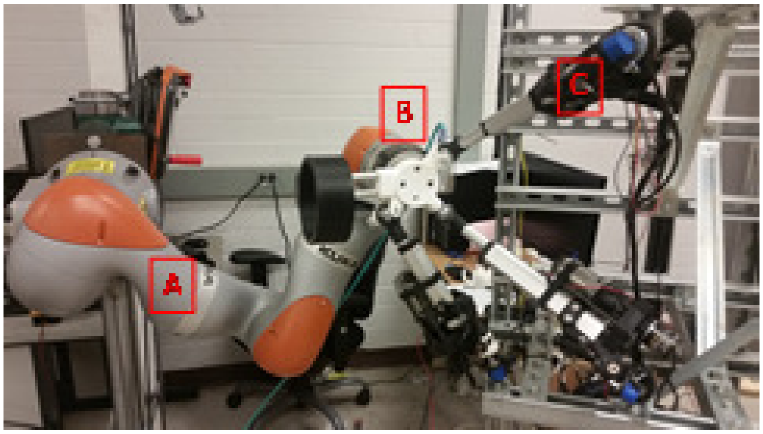

Figure 3.4: Experimental setup for testing stiffness: (A) KUKA robotic arm, (B) ATI force sensor, (C) Exoskeleton shoulder.

beam is derived in [10] and given as:

$$\boldsymbol{B}_n = \begin{bmatrix} \mathbf{0}_{3x3} & \boldsymbol{I}_{3x3} \\ \boldsymbol{I}_{3x3} & \widehat{\boldsymbol{L}}_{W_n} \end{bmatrix} \tag{3.6}$$

With the rigid beam defined, the kinematic relation matrix $\boldsymbol{A}_T$ of the shoulder piece is constructed. The assembly procedure for $\boldsymbol{A}_T$ is the same as it was for $\boldsymbol{A}_{T,k}$, but with the inclusion of $\boldsymbol{B}_n$. Along with $\boldsymbol{A}_T$, the substructure stiffness matrices $\boldsymbol{K}_{eq,k=1,2,3}$ is assembled into a single matrix $\boldsymbol{K}_T$. The assembly technique used to construct $\boldsymbol{K}_T$ is the same used for $\boldsymbol{K}_{T,k}$. The stiffness of the entire shoulder exoskeleton is derived by using minimum total potential energy given as:

$$\boldsymbol{K}_{eq,T} = \begin{bmatrix} \boldsymbol{K}_T & {\boldsymbol{A}_T}^T \\ \boldsymbol{A}_T & \mathbf{0} \end{bmatrix} \tag{3.7}$$

As with $\boldsymbol{K}_{G,k}$, it is possible to calculate the displacement at the end effector by permuting $\boldsymbol{K}_{eq,T}$ in order to partition the equivalent 6x6 end effector stiffness matrix $\boldsymbol{K}_{ee}$, which describes the stiffness at node 7 in Fig. 3.

The matrix $\boldsymbol{K}_{ee}$ can be visualized by its translational and rotational stiffness ellipsoids. As defined in the work of (Mussa-Ivaldi *et al.*, 1985), these ellipsoids are created by first separating $\boldsymbol{K}_{ee}$ into a symmetric component $\boldsymbol{K}_s$ and an antisymmetric component $\boldsymbol{K}_a$. Assume:

$$\boldsymbol{K}_{ee} = \begin{bmatrix} \boldsymbol{K}_{xx} & \boldsymbol{K}_{xy} \\ \boldsymbol{K}_{yx} & \boldsymbol{K}_{yy} \end{bmatrix} \tag{3.8}$$

Then $\boldsymbol{K}_s$ and $\boldsymbol{K}_a$ can be written as:

$$\boldsymbol{K}_s = \begin{bmatrix} \boldsymbol{K}_{xx} & \frac{\boldsymbol{K}_{xy}+\boldsymbol{K}_{yx}}{2} \\ \frac{\boldsymbol{K}_{yx}+\boldsymbol{K}_{xy}}{2} & \boldsymbol{K}_{yy} \end{bmatrix} \tag{3.9}$$

$$\boldsymbol{K}_a = \begin{bmatrix} 0 & \frac{\boldsymbol{K}_{xy}-\boldsymbol{K}_{yx}}{2} \\ \frac{\boldsymbol{K}_{yx}-\boldsymbol{K}_{xy}}{2} & 0 \end{bmatrix} \tag{3.10}$$

where $\boldsymbol{K}_{ee} = \boldsymbol{K}_s + \boldsymbol{K}_a$. The eigenvalues and eigenvectors of the symmetric component $\boldsymbol{K}_s$ can now be used to represent the direction and magnitude of the translational and rotational stiffness matrices. The first three eigenvalues and three eigenvectors pairs correspond to the axes of the translational stiffness ellipsoid, while the last three correspond to the axes of the rotational stiffness ellipsoid.

3.1.3 Stiffness Model Testing

To check the results of the stiffness model, an experiment was performed to compare theoretical stiffness to that of the prototype. A 6-axis force/torque sensor (Delta IP65, ATI, NC) was coupled to the exoskeleton shoulder oriented at 90° flexion in order to measure forces and torques corresponding to displacement. To provide accurate displacement, a 7-DoF robotic arm (LBR iiwa R820, KUKA, Germany) connected to the sensor was used. The shoulder piece used for the model and experiment has a 90° angle between tie-rod mounts, instead of the 45° angle shown in Fig. 2 and Fig. 3. This was done because early testing of the stiffness model suggested that it would produce more homogeneous stiffness ellipsoids. The experimental setup is shown in Fig. 4.

Translational displacements of 3 mm were commanded along +X, +Y and +Z. Rotational displacements of 1.5° where commanded about +X, +Y and +Z. Forces and torques corresponding to displacement were recorded at 1 kHz. The mean force measured over 5 s was used to calculate stiffness. These six measurements about the six DoF were chosen as they can be related by a transformation to each column of the theoretical stiffness matrix. As previously mentioned, this stiffness matrix is a function of the kinematic relation matrix $\boldsymbol{A}_T$. The matrix $\boldsymbol{A}_T$ is very sensitive to change, so if it were not correct, then it would be expected that most, if not all six measurements to be significantly different from the theoretical model.

For the simulation, the flexible beams 3-4 and 6-9 shown in Fig. 2 were modeled as 1045 carbon steel and 2024 aluminum, respectively. The flexible beam 5-7 shown in Fig. 2 and the rigid links 4-7, 5-7 and 6-7 shown in Fig. 3 were modeled as ABS plastic. All critical dimensions used in the simulation match those of the prototype.

3.1.4 Stiffness Optimization

In order to maximize stiffness over a predetermined workspace, the placement of each actuator needs to be determined through optimization. Given that this is a bounded nonlinear multi-objective (rotation and translation) optimization problem, a genetic algorithm was implemented to determine the best actuator placement for a specified orientation. Matlab's Optimization Toolbox was used for this. The genetic algorithm function (ga) was given the stiffness ellipsoid volumes as negative values to minimize, thus maximizing the positive volumes. While there are potentially many optimization criteria to chose from, maximizing the ellipsoid volume was chosen because (1) maximum volume should encourage more spherical or homogeneous solutions, since more spherical ellipsoids will contain greater volume, and (2) it is a simple approach that takes into account the stiffness of all three ellipsoid axes. Possible solutions were restricted to the region ($-0.75 < X < -0.2$, $-0.75 < Y < -0.2$, $-0.75 < Z < -0.2$) m corresponding to the reference frame shown in Fig. 1 with origin C. This region was chosen so that the actuators would be positioned behind the user at a comfortable distance.

The workspace of the shoulder piece and cuff were bounded by the octant (+X, +Y, -Z) shown in Fig.1 with origin C, which can also be defined by the three arm orientations: 90° flexion, 90° abduction, and at rest. Incremental 10° changes in inclination and azimuth of the shoulder piece across the entire workspace produces a point cloud of best solutions for each actuator base mount. The virtual center of each point cloud is taken as the generalized optimal solution for the corresponding workspace.

In addition to optimizing stiffness for the entire workspace, it is possible to optimize stiffness for a particular task, such as lifting in the sagittal plane. To do this, the shoulder piece was incremented in 5° intervals between the arm at rest and 90° flexion. Similar to optimizing for the entire workspace, the point cloud of best solutions generated for each actuator are used to find the corresponding virtual centers for each actuator and thus the generalized best solution.

3.2 Results

3.2.1 Stiffness Model Testing

A comparison of the theoretical and measured stiffness is shown in Fig. 5. For translational stiffness, the mean error along the +X, +Y, and +Z axes is 6.24% with a standard deviation of 3.79. For rotational stiffness, the mean error about +X, +Y,

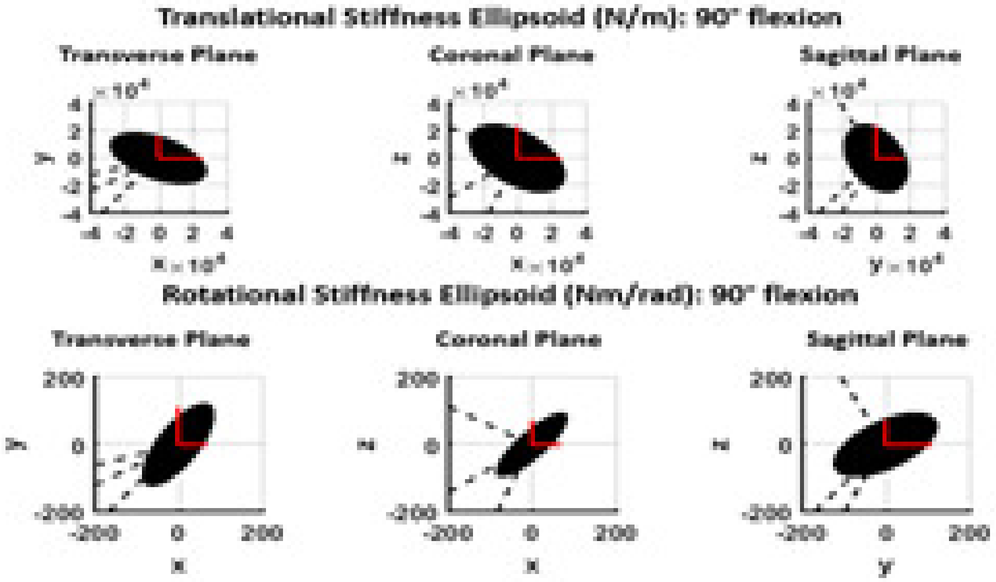

Figure 3.5: Projections of the theoretical stiffness ellipsoid (black), measured axis stiffness (red) and actuator orientations for 90° flexion (dotted black).

and +Z axes is 12.33%, with a standard deviation of 6.55. While some error does exist, it should be noted that the size and shape of the theoretical model suggests that it provides a reasonable approximation of stiffness.

The exact source of this error is unknown, however it is speculated that there are two major contributing factors, both related to the stiffness assemble matrix $\boldsymbol{K}_T$. The first is that the model treats all components to have homogeneous elasticity and shear properties. This may not be accurate for the printed plastics used, due to the layered and honeycombed architecture inherent to 3D printing.

Second, any misalignment between the roll axis of each actuator and the center of rotation C shown in Fig. 1 will produce increased resistance to applied torque. These roll axes were positioned by hand using tooling with a tolerance of 0.5°, which may in part explain the differences seen between theoretical and experimental rotation stiffness.

3.2.2 Stiffness Optimization

For the workspace described by the octant (+X,+Y,-Z) shown in Fig.1, the actuator mounting point configuration to optimize overall stiffness is shown in Fig. 6A as a point

cloud of best solutions. These solutions were found in 10° intervals between arm at rest, 90° flexion and 90° abduction for the entire workspace. The virtual center of each point cloud for the top, middle and bottom actuator, respectively, are $A_t =$ [-0.5277,-0.3020, 0.1502]^T m, $A_m =$[-0.3961, -0.3018,-0.0554]^T m and $A_b =$[-0.3139, -0.5389, -0.4793]^T m. To help visualize this result, Fig. 6B shows where the optimal mounting point configuration is with respect to the user. Finally, in order to give a sense of the stiffness expected for the optimal mounting point configuration, Fig. 6C shows the corresponding generalized translational and rotational stiffness ellipsoids. These ellipsoids represent the average stiffness found in 10° intervals between arm at rest, 90° flexion and 90° abduction for the entire workspace. Presented in a similar form to the previous result, the optimal solution for the sagittal plane is shown in Fig. 7A as a point cloud of best solutions. Solutions were found at 5° intervals between arm at rest and 90° flexion for the sagittal plane. The virtual center of each point cloud for the top, middle and bottom actuator, respectively, are $A_t =$ [-0.5183,-0.1524, 0.1581]^T m, $A_m =$ [-0.2905, -0.3831,-0.211]^T m and $A_b =$ [-0.1262, -0.5369, -0.4711]^T m. As before, Fig. 7B shows where the optimal mounting point configuration is with respect to the user and Fig 7C shows the generalized stiffness ellipsoids corresponding to the point cloud of best solutions.

It should be noted that, while Fig. 6 and Fig. 7 represent the best solutions for the entire workspace and sagittal plane, respectively, they do not consider certain real world factors, such as mechanical interference. In these cases the results were

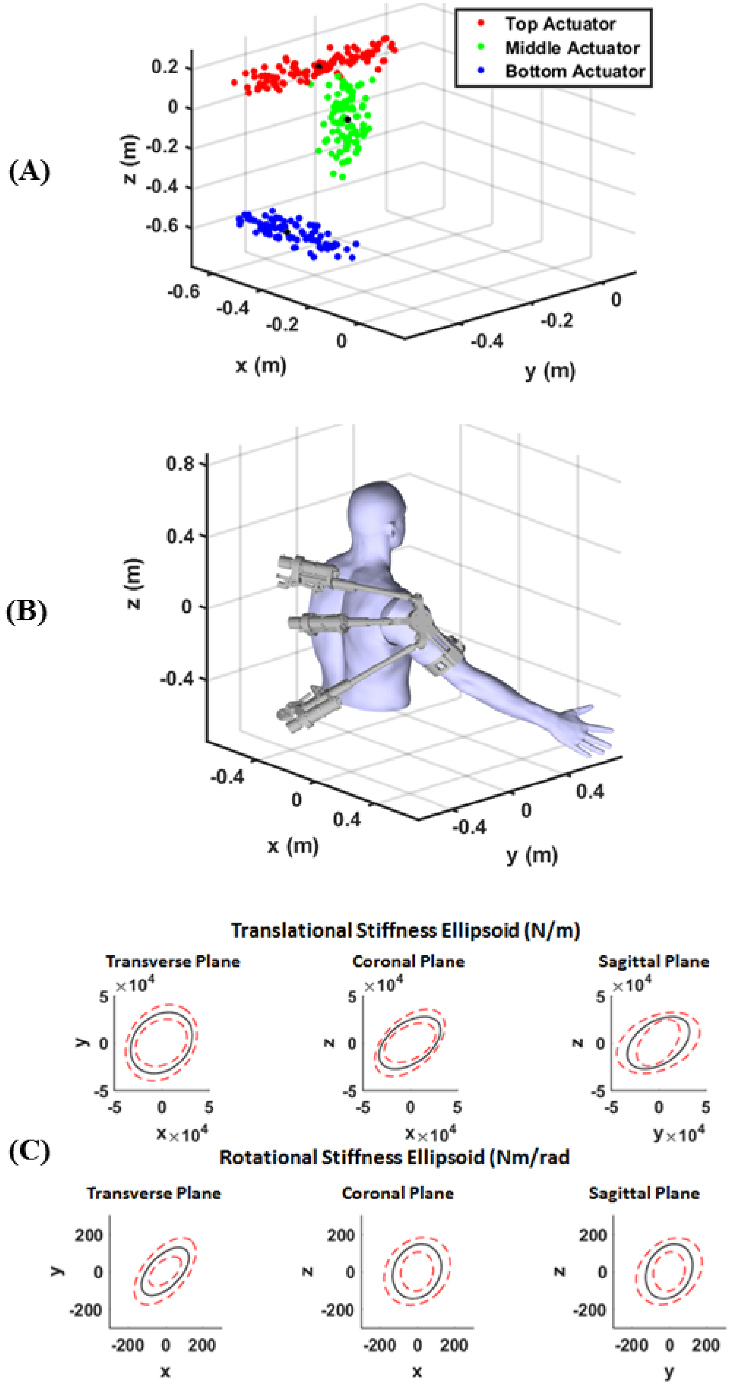

Figure 3.6: (A) Point clouds representing the actuator mounting point positions corresponding to optimized stiffness for the entire workspace. Solutions are found at 10° intervals between arm at rest, 90° flexion and 90° abduction. The virtual center of each cloud is marked by a black dot. (B) Depiction of where the optimal mounting point configuration is with respect to the user. (C) Shows the generalized translational and rotational stiffness ellipsoid (black) along with the standard deviation (dotted red) for the configuration shown in Fig. 6B for movement through the entire workspace.

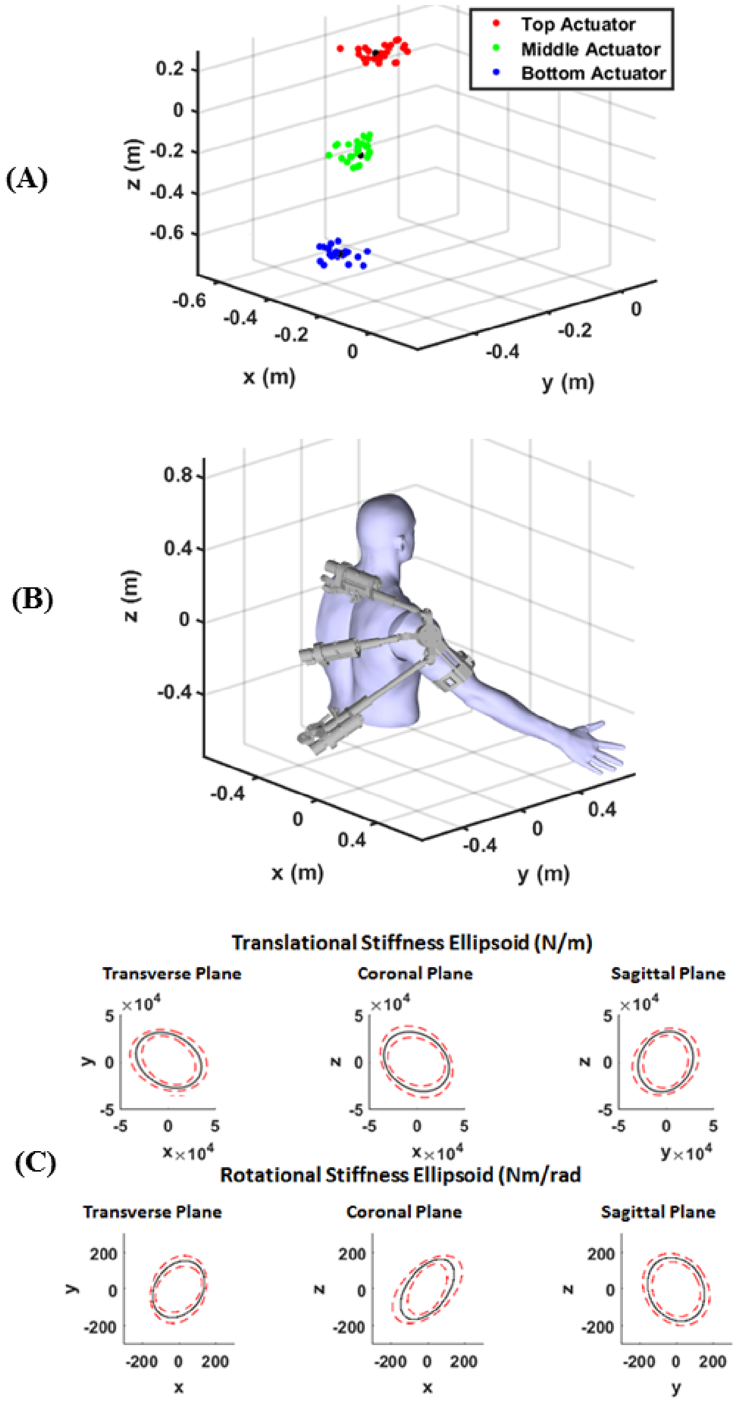

Figure 3.7: (A) Point clouds representing the actuator mounting point positions corresponding to optimized stiffness for the sagittal plane. Solutions are found at 5° intervals between arm at rest and 90° flexion. The virtual center of each cloud is marked by a black dot (B) Depiction of where the mounting point configuration is with respect to the user. (C) Shows the generalized translational and rotational stiffness ellipsoid (black) along with the standard deviation (dotted red) for the configuration shown in Fig. 7B for movement in the sagittal plane only.

somewhat fortunate, because the virtual center of each point cloud is not unreasonably close to the adjacent solution(s). Therefore, mechanical interference between the actuators will not occur for the workspace defined. However, this could change if the desired workspace or task were to change.

3.3 Discussion

This work presented here was motivated by the need for wearable robotic architectures that are capable of matching the workspace of a user while maintaining a high operational stiffness. Because of limitations in the stiffness or workspace of previous designs, the authors developed a novel parallel architecture specifically intended for interface with complex biological joints. Demonstrated in the form of a shoulder exoskeleton, the authors identify here the techniques needed to optimize the stiffness of the device in order to more effectively perform a desired task or operate in a given workspace.

The results of this paper detail a theoretical stiffness model for the novel parallel actuated shoulder exoskeleton presented, along with an experiment to validate the model. Errors of 6.24% and 12.33% for translational and rotational stiffness, respectively, were reported. Considering possible sources of errors in the stiffness model described in the Section III. A, the model still proved to be a reliable approximation of stiffness.

Using this model, along with a bounded nonlinear multi-objective optimization technique, it was shown how to configure the actuated substructures of the device so as to maximize stiffness in a given workspace. The workspace demonstrated here was equal to one octant of a sphere and defined by the three arm orientations: 90° flexion, 90° abduction, and at rest. In a similar manner, it was also shown how to maximize stiffness for certain motions within this workspace. This was demonstrated by maximizing stiffness in the sagittal plane for a lifting task. Both the results for the entire workspace and sagittal plane provided reasonable solutions with respect to real word concerns, such as mechanical interference.

The main contribution of this work is in the detailing of how the stiffness model of a novel parallel actuated shoulder exoskeleton can be used, along with optimization techniques, to maximize the device's stiffness for a particular task or workspace. Additionally, because the architecture of the device can be applied to other spherical joints like the hip, wrist and ankle, it means the stiffness model can be applied to these joints as well. Therefore, future exoskeletons using this architecture could have the stiffness of many joints optimized for overall performance or for specific tasks, such as lifting, stair climbing or running.

Chapter 4

A NEW PARALLEL ACTUATED ARCHITECTURE FOR EXOSKELETON APPLICATIONS INVOLVING MULTIPLE DEGREE-OF-FREEDOM BIOLOGICAL JOINTS

4.1 Introduction

The majority of exoskeleton robotic devices utilize a serial chain architecture of actuated joints and linkages to accomplish a desired task (Craig, 2005). Such designs may in part be bio-inspired by our own anatomy of bones and ligaments, and therefore might seem a logical choice for mirroring or augmenting our own movements. While this rationale holds for simple one degree-of-freedom (DoF) joints like the elbow and knee, it does not for multiple DoF ball and socket joints like the shoulder, hip, wrist and ankle. Unlike 1-DoF biological joints that can share an axis of rotation with a corresponding artificial joint, ball and socket joints operate about a center of rotation that cannot be shared in an anatomically similar manner. Therefore, in order for a serial actuated exoskeleton to interface with a ball and socket joint, its design must diverge from our own anatomy.

The most common solution to augment the motion of a ball and socket joint with serial actuation is to use a multiple linkage robotic armature. The armature works to bridge the ball and socket joint by connecting the structures on either side. While this approach works from a kinematic standpoint, it can be problematic from a dynamic one. In order to bridge a 3-DoF ball and socket joint using a serial armature, the armature must contain at least three joints and two linkages. The moment arm associated with these linkages has the inherent disadvantage of amplifying torques applied to the joint by external forces. Furthermore, each motorized joint in the armature must be capable of not only actuating the corresponding human limb, but also able to lift and manipulate the joints that follow in series. This requires larger motors that consume more energy.

Despite its problems, serial actuation is still arguably the most popular solution for emulating ball and socket joint motion. It has been utilized extensively in exoskeleton robotics with several notable examples including the XOS by Sarcos/Ratheon, HAL by CyberDyne (Bogue, 2009), Body Extender by Perceptual Robotics Laboratory (Marcheschi *et al.*, 2011), HULC by Ekso Bionics (Young and Ferris, 2017), and H-Wex by Hyundai (Toxiri *et al.*, 2018). It could be contended that the popularity of using serial actuation for the purpose augmenting ball and socket joint motion is not the result of ideal performance, but rather a lack of viable alternatives.

When considering alternatives to the conventional use of serial actuation to augment ball and socket joint motion, parallel actuation may come to mind. A parallel architecture can offer many benefits over a serial one. Below is a list of the most prominent advantages of parallel actuation that are relevant to exoskeleton robotics.

1. *Short moment arm:* The end effector of a parallel actuated system has a considerably shorter moment arm than that of a serial system with comparable DoF (Hunt, 1983; Stechert *et al.*, 2006). This can help reduce the resultant torque applied at a joint by external forces.

2. *Low end effector inertia:* Parallel actuated systems have a low center of mass, which results in low end effector inertia (Hunt, 1983; Stechert *et al.*, 2006). This can reduce energy cost during operation and is an important consideration from a mobility perspective.

3. *High end effector acceleration:* As a result of low end effector inertia, parallel

actuated systems are typically capable of high end effector acceleration (Hunt, 1983; Stechert *et al.*, 2006). This can be advantageous for high performance augmentative applications.

4. *Minimal positioning error*: Unlike serial actuated systems, which have position errors that accumulate and amplify from base to end effector, parallel systems work to attenuate errors found in one or more linkages through cooperative end effector control (Hunt, 1983; Stechert *et al.*, 2006; Merlet, 2006).

5. *High potential stiffness:* The multiple mounting point locations on both the mobile platform and stationary base of a parallel system can lead to high mechanical stiffness (Hunt, 1983; Stechert *et al.*, 2006; Gosselin, 1990; Pashkevich *et al.*, 2009). However, this result is highly dependent on both the parallel architecture type and degree of actuation chosen.

6. *May not occupy center of rotation:* Parallel actuated systems can be designed to rotate about a point without occupying it (Stechert *et al.*, 2006; Gosselin and Lavoie, 1993). This has important application when interfaced with ball and socket joints like the shoulder, hip, wrist, and ankle.

Several exoskeleton robotic devices have incorporated parallel actuation in prior work. A few notable examples include the RiceWrist (Gupta *et al.*, 2008) and the MR-SoftWrist (Erwin *et al.*, 2015), both of which utilize a three revolute–prismatic–spherical (3-RPS) architecture (Kim and Tsai, 2002) and the Anklebot (Roy *et al.*, 2009), which uses a two spherical–prismatic–spherical (2-SPS) architecture (Alici and Shirinzadeh, 2004). These robot architectures have been used quite successfully to study certain properties of the human neuromuscular system (Pehlivan *et al.*, 2014; Kong and Gosselin, 2004). However, these robots require the human joint to be used in the closed-form kinematic solution. This is not ideal for certain augmentation applications where dangerously high forces could be transmitted through the system and thus the user.

Despite a few examples of its use, parallel actuation has not yet been widely adopted in the field of exoskeleton robotics. The primary reason for this is that parallel actuated architectures that do not include the human joint as part of the closed form kinematic solution are disadvantaged by a relatively small workspace when compared to serial actuation. This can make it difficult to meet the design requirements of many applications. This limitation is largely a result of mechanical interference between the parallel actuated linkages (Stechert *et al.*, 2006). A good example of this interference can be observed in the 6-DoF Stewart-Gough platform with its six parallel actuators (Tsai and Joshi, 2000).

One method of achieving a larger workspace with parallel actuation is to utilize an architecture that contains fewer parallel linkages and thus less mechanical interference. Such architectures are typically designed to operate with either purely translational or rotational motion and are commonly referred to as translational parallel manipulators (TPM) and spherical parallel manipulators (SPM), respectively (Gosselin and Lavoie, 1993; Kong and Gosselin, 2004). In the case of a ball and socket joint that only requires spherical motion, the use of an SPM is possible. Several SPM architectures have been proposed over the years, with the most common being the Three Universal Parallel Universal (3-UPU) (Walter *et al.*, 2009) and the Three Rotational Rotational Rotational (3-RRR) (Wu *et al.*, 2011). Both of these designs have three decoupled rotational DoF and do not occupy the center of rotation. Therefore, either design could theoretically be used for a exoskeleton robotic application. However, both have been found to have limitations. The 3-UPU, though sound from a kinematic standpoint, has been shown to have poor dynamic performance as a result of a high number of passive DoF (Walter *et al.*, 2009). The 3-RRR, while also not ideal from a dynamic standpoint (Wu *et al.*, 2011), has the additional problem of its curved linkages passing through the majority of the spherical workspace. This makes mechanical interference with the limb a concern.

Limitations with current SPM architectures available led the authors to develop the first SPM specifically intended for exoskeleton robotics in prior work (Hunt *et al.*, 2017). The principal concept of this early design was to minimize the number of parallel substructures while maximizing the number of active DoF in order to maintain good dynamic performance. This was done through a new technique the authors developed call Modular Motion Coupling. This technique involved the use of a specially designed gearbox with one input and multiple outputs connected to each parallel substructure. The multiple outputs would be used to actively control multiple DoF of each substructure dependently. With more active DoF, dynamic performance overall would be improved while still maintaining a large workspace. A prototype of the design was developed to validate its kinematics and investigate its dynamic behavior.

Building and testing this new parallel architecture helped identify two issues with it. First, the need for a complex gearbox with two different specifically geared outputs was found to be significantly more expensive than a traditional gearbox. This limits the design's adoptability from an economic standpoint. Second, while the design was able to provide good dynamic performance along the DoF that were actively controlled, the passive roll DoF of each substructure was not directly actuated, but instead determined by the synergistic motion of all three substructures and proved susceptible to positioning error under load. While likely not an issue for low force tasks, this result could be problematic for high force augmentative applications.

In an effort to resolve the issues with the author's prior work, a novel SPM was developed and is presented in this work. The two driving design principles of this new architecture are affordability and fully active DoF control of all substructures so as to provide good dynamic performance. The design varies from any other SPM, including the author's prior work, through its utilization of multiple four bar linkages as part of a greater mechanism to generate spherical motion. Therefore, the design will be referred to in this work by the acronym 4B-SPM.

The rest of this paper focuses on the 4B-SPM architecture and its potential application for exoskeleton robotics. Section II begins with an overview of the 4B-SPM design, followed by an analysis of its forward and inverse kinematics. Techniques to actuate all DoF of each substructure in order to improve dynamic performance are also introduced. Lastly, a cooperative control strategy is discussed that allows the 4B-SPM to operate with highly flexible joints, like the shoulder and hip, without experiencing mechanical interference between operator and device. Section III demonstrates four different 4B-SPM exoskeleton simulations that establish both the range of application and validate the kinematic methods describe in Section II. These simulations include an ankle, hip, wrist and shoulder exoskeleton robot. Also included in Section III is a case study, in which the development of a shoulder exoskeleton is considered in order to discuss the real world cost and feasibility of the 4B-SPM. Finally, Section IV concludes the paper with a discussion of the results and a summary of contribution.

4.2 Methods

4.2.1 Overview of the 4B-SPM Architecture

The architecture of the 4B-SPM is shown in Fig. 1. The design consists of three actuated substructures that couple a stationary base to a mobile platform. The mobile platform has three independent rotational DoF and operates tangential to the spherical workspace shown in Fig. 1. Each substructure is comprised of a 4-bar mechanism connected to a grounded revolute joint at its base. The axes of the grounded joints are designed to intersect at a desired point in space. This point represents the center of rotation of the mobile platform. The top linkage in each 4-bar mechanism is extended to reach the mobile platform. Each top linkage is coupled to the mobile platform using a 3-DoF spherical joint. Depending on the dynamic performance requirements, three versions of the 4B-SPM that use different actuation methods are presented. These include the three revolute actuator version presented in Fig. 1, along with a six revolute actuator version and a three revolute two prismatic actuator version discussed in Section II-D. While all three architecture share similar kinematic solutions, each has advantages and disadvantages. The three revolute actuator version presented first is the simplest and thus most economic, but is susceptible to low torque output in certain configurations. Therefore, this architecture is not ideal for high load applications. The two alternate designs discussed are more complicated, but offer benefits that include more homogenous torque output and/or higher stiffness. More details regarding the dynamic advantages of these two architectures are provided in Section II-D.

4.2.2 Forward Kinematics

In order to implement practical control of the 4B-SPM, its forward kinematics must be solved so that any differences between commanded and actual position can be mitigated using a closed-loop controller. Solving the forward kinematics require a unique solution to exist for a given set of commands. A singular kinematic solution was shown to exist for the author's prior SPM design that functioned using the same number of substructures with the same number of active and passive DoF (Hunt *et al.*, 2017). Therefore, the 4B-SPM can be classified under the same category of

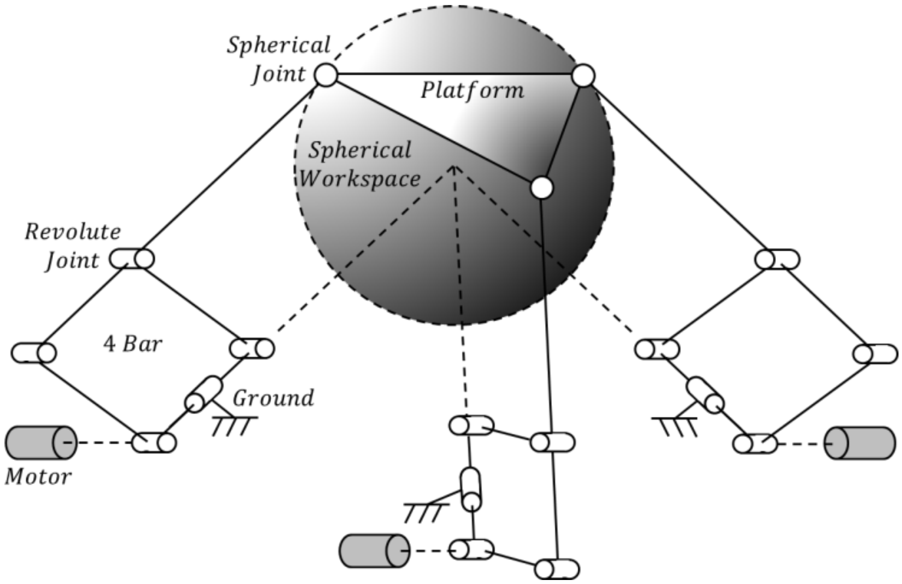

Figure 4.1: Architecture of the 4B-SPM. The design consists of three substructures, each comprised of a 4-bar linkage connected to a grounded revolute joint. The top linkage in each 4-bar mechanism is extended to reach a mobile platform. Each top linkage is coupled to the mobile platform using a spherical joint. The mobile platform is capable of spherical motion about the point in which the axes of all three grounded revolute joints intersect.

SPM and is subject to the same mobility.

As with many parallel architectures, the forward kinematics of the 4B-SPM are not observable using only actuator feedback (Lee and Shah, 1988). Instead, it is necessary to integrate additional sensors into each 4-bar substructure so that the roll, in addition to the pitch, can be directly measured. By knowing the roll and pitch of each substructure, the corresponding end points (i.e., platform mounts) shown in Fig. 2 can be determined. This is most easily done by first realizing that the platform mount vector $\overline{P}_i$ that originates at the global origin frame at the center of the spherical workspace is equal to the 4-bar linkage vector $\overline{C}_i$. This is because $\overline{P}_i$ is not a physical linkage and consequently its magnitude and direction are dictated by the parallel vector $\overline{C}_i$. Therefore, if the pitch $_i$ and roll $_i$ sensors of a given substructure are zeroed with respect to the global frame, then the resulting spherical coordinates $(\left|\overline{C}_i\right|, _i, _i)$ of $\overline{C}_i$ can be directly converted into the Cartesian coordinates

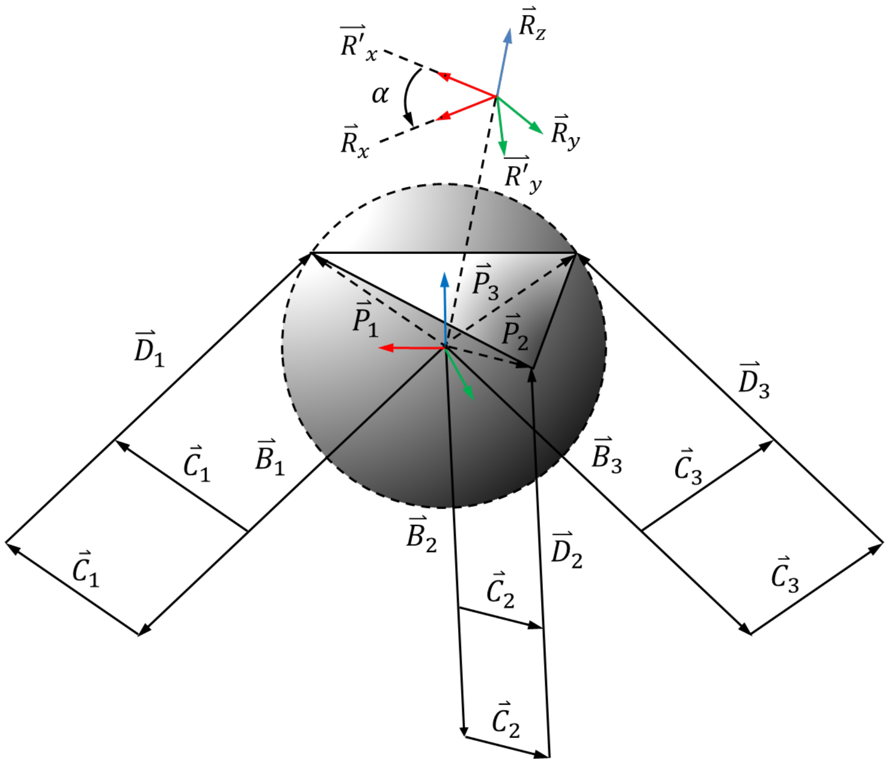

Figure 4.2: Vector representation of the 4B-SPM. All vectors originate at the origin, but are drawn in a configuration similar to Fig. 1 to help the reader identify what each vector represents. The global origin frame is denoted by the RGB (xyz) frame shown at the center of the spherical workspace.

(x_i, y_i, z_i) of platform mount $\overline{P}_i$.

Once the three platform mounts $\overline{P}_{1,2,3}$ are identified, they can be used to generate a transformation matrix $\boldsymbol{T}$ that describes the position $\overline{P}_c$ and orientation $\boldsymbol{R}$ of the platform at its centroid. Referring again to Fig. 2, the transformation matrix $\boldsymbol{T}$ can be obtained by first considering the platform orientation component $\boldsymbol{R}$. The 3x3 matrix $\boldsymbol{R}$ can be determined by first generating an intermediate rotation matrix $\boldsymbol{R'}$ that is dependent only on the position of the platform mounts $\overline{P}_{1,2,3}$ and does not consider the desired XY planar orientation needed to align the local platform frame with the direction of a user limb. Assume that matrix $\boldsymbol{R'}$ is orientated as shown in Fig. 2, then $\boldsymbol{R'}$ can be calculated as follows:

$$\boldsymbol{R'} = [\overline{R}'_x \ \overline{R}'_y \ \overline{R}'_z] \tag{4.1}$$

where

$$\overline{R}'_z = \frac{(\overline{P}_2 - \overline{P}_1) \times (\overline{P}_3 - \overline{P}_1)}{\left|(\overline{P}_2 - \overline{P}_1) \times (\overline{P}_3 - \overline{P}_1)\right|} \tag{4.2}$$

$$\overline{R}'_y = \frac{\overline{R}'_z \times \overline{P}_1}{\left|\overline{R}'_z \times \overline{P}_1\right|} \tag{4.3}$$

$$\overline{R}'_x = \overline{R}'_y \times \overline{R}'_z \tag{4.4}$$

If $\boldsymbol{R'}$ is assumed to not have the same desired XY planar alignment as $\boldsymbol{R}$, then it must be multiplied by the rotation matrix $\boldsymbol{R}_z$ about the z-axis, such that:

$$\boldsymbol{R} = \boldsymbol{R}_z \boldsymbol{R'} \tag{4.5}$$

where

$$\boldsymbol{R}_z = \begin{bmatrix} \cos(\alpha) & -\sin(\alpha) & 0 \\ \sin(\alpha) & \cos(\alpha) & 0 \\ 0 & 0 & 1 \end{bmatrix} \tag{4.6}$$

The angle α is taken to be measured from the axis $\overline{R}'_x$ as shown in Fig. 2. The direction of the new axis $\overline{R}_x$ is intended to be aligned with the user limb. Therefore, α is dependent on the particular geometric design of the mobile platform.

With the rotation matrix $\boldsymbol{R}$ of the platform known, the only component of transformation $\boldsymbol{T}$ left to determine is platform translation. If the translation $\overline{P}_c$ of the platform is taken to be its centroid, then calculating $\overline{P}_c$ is a simple matter of finding the mean vector described by $\overline{P}_{1,2,3}$, which is:

$$\overline{P}_c = \frac{1}{3}\sum_{i=1}^{3}\overline{P}_i \tag{4.7}$$

With both the rotation and translation of the platform known, the complete transformation matrix $\boldsymbol{T}$ that describes the platform position and orientation as a function of the three platform mounts $\overline{P}_{1,2,3}$, with respect to the global frame, can be written as:

$$\boldsymbol{T} = \begin{bmatrix} \boldsymbol{R} & \overline{P}_c \\ \overline{0}_{1x3} & 1 \end{bmatrix} \tag{4.8}$$

To clarify the components of the transformation matrix $\boldsymbol{T}$, $\overline{0}_{n\ x\ m}$ represents a zero vector comprised of n rows and m columns, $\boldsymbol{R}$ represents the desired 3x3 platform rotation matrix and $\overline{P}_c$ represents the calculated 3x1 platform centroid vector.

4.2.3 Inverse Kinematics

The second kinematic operation that must be considered in order to implement effective control over the 4B-SPM is its inverse solution. For this operation, the rotation matrix $\boldsymbol{R}$ of the platform is given and the substructure pitch and roll angles are to be calculated. As with the forward kinematics, identifying the mounting point positions should be considered a first step toward obtaining the substructure pitch angles. To find $\overline{P}_{1,2,3}$ that correspond to the commanded $\boldsymbol{R}$, a series of transformations are used. These transformations in order are: (7.1) rotational transformation $\boldsymbol{T_1}$ from the global frame orientation to the mobile platform orientation$\boldsymbol{R}$, (3.2) translational transformation $\boldsymbol{T_2}$ from the center of rotation to the platform centroid at radius r, (6.2) translational transformation $\boldsymbol{T_{3,i}}$ from the mobile platform centroid to the platform mounting point position. Therefore, the transformation matrix that describes the position of each platform mount $\boldsymbol{T_{p,i}}$ as a function of the platform orientation $\boldsymbol{R}$, platform centroid radius of operation r, and the distance from the platform centroid to the platform mounting points $\overline{p}_i$ can be expressed as:

$$\boldsymbol{T_{p,i}} = \boldsymbol{T_1 T_2 T_{3,i}} \tag{4.9}$$

where

$$\boldsymbol{T_1} = \begin{bmatrix} \boldsymbol{R} & \overline{0}_{3x1} \\ \overline{0}_{1x3} & 1 \end{bmatrix} \tag{4.10}$$

$$\boldsymbol{T_2} = \begin{bmatrix} & 0 \\ \boldsymbol{I} & 0 \\ & r \\ \overline{0}_{1x3} & 1 \end{bmatrix} \tag{4.11}$$

$$\boldsymbol{T_{3,i}} = \begin{bmatrix} \boldsymbol{I} & \overline{p}_i \\ \overline{0}_{1x3} & 1 \end{bmatrix} \tag{4.12}$$

Here, $\boldsymbol{I}$ represents a 3x3 identity matrix and $\overline{0}_{n\ x\ m}$ represents a zero vector comprised of n rows and m columns. The platform mounts $\overline{P}_{1,2,3}$ with respect to the origin are given as the translational component of the transformation $\boldsymbol{T_{p,i}}$. The platform centroid radius of operation is given as r. The pitch β_i and roll γ_i angles of a given substructure i can be identified using $\overline{P}_i$, $\overline{B}_i$ and the global reference frame vector $\overline{z}$ such that:

$$\beta_i = acos\frac{\overline{P}_i \bullet \overline{B}_i}{|\overline{P}_i| \bullet |\overline{B}_i|} \tag{4.13}$$

$$\gamma_i = acos\frac{(\overline{B}_i \times \overline{z}) \bullet (\overline{B}_i \times \overline{P}_i)}{|\overline{B}_i \times \overline{z}| \bullet |\overline{B}_i \times \overline{P}_i|} \tag{4.14}$$

It should be noted that since Eq. 13 and Eq. 14 utilize a dot product operation, the sign of each angle is undetermined. Therefore, it is important to observe the location of $\overline{P}_i$ so that the correct sign convention can be applied.

4.2.4 Roll Actuation of the 4B-SPM Substructures to Improve Dynamic Performance

Many SPM designs have been shown to have sound kinematics, but do not function well under real world conditions. The reason for this is that certain DoF of a given SPM may not be directly actuated, but instead are determined by the synergistic motion of its substructures (Walter *et al.*, 2009; Liu *et al.*, 2000). This is problematic, because certain substructure orientations may produce low torques or forces along the DoF that are not directly actuated. In the case of the 4B-SPM, this is potentially the roll DoF of each substructure. Thus, for certain applications where high loading is a possibility, it may be necessary to actuate the roll DoF of each substructure in a more direct way in order to produce a more homogeneous output torque. Here, two methods to do so are discussed.

D1. Roll actuation using three revolute motors

The simplest and most direct method of actuating the 4B-SPM substructure roll is to actuate each ground revolute joint as shown in Fig. 3. Thus, for this version of the 4B-SPM, both pitch angle $_i$ and the roll angle $_i$ found in Section II-C would be directly controlled. This method of roll actuation would, in effect, produce three simple serial architectures. Each of the serial architectures has its own independent singular kinematic solution, but share the same coupled solution described in Section II-A and II-B.

While the addition of three revolute motors works to actuate roll, it also brings the total motor count to six. This may raise questions as to whether a more traditional

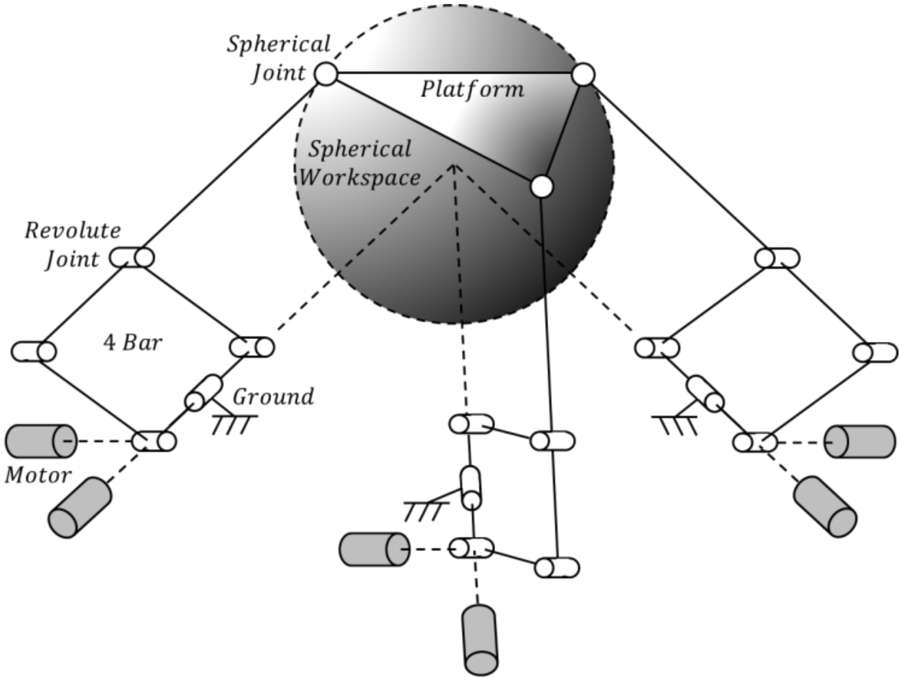

Figure 4.3: Method of substructure roll actuation by the addition of three motors. Each of the three motor are fixed to the ground and coupled to the roll axis of each respective 4 bar mechanism.

six actuator parallel architecture, such as the Stewart Platform (i.e., hexapod) could be used instead of the 4B-SPM. The answer to this goes back to the workspace limitations. Because the 4B-SPM has only three substructures instead of six, it encounters less mechanical interference between substructures and therefore affords a larger spherical workspace.

D2. Roll actuation using two interconnecting motorized linkages

A second approach to roll actuation is to include linkages between substructures 1-2 and 2-3 as shown in Fig. 4. By connecting one end of a linkage to a motorized slider mounted on one of the two corresponding substructures, it is possible to adjust the linkage position such that it does not violate the kinematic solution found in Section II. This approach has a two advantages. First, it only requires two additional motors instead of three. Second, because the linkage is mounted away from the roll axis of each substructure, it helps to further reduce deflection. On the other hand, the

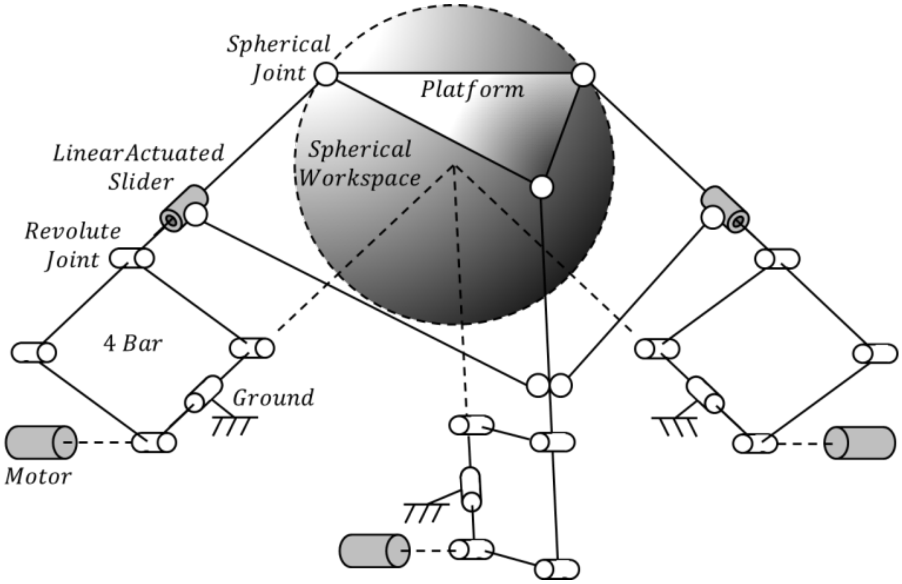

Figure 4.4: Method of substructure roll actuation by the addition of two linear actuated sliders. The sliders are positioned on the outermost substructure with each coupled to the central substructure using interconnecting linkages mounted with spherical joints on either end.

use of motorized sliders makes this approach more complex from a design standpoint than the three and six motor configurations described in Section A and Section D1, respectively.

To find the slider positions that comply with the kinematic solution found in Section II, a system of equations must be solved in a simultaneous manner. Referring to Fig. 5, consider the system:

$$\overline{B}_1 + \overline{C}_1 + k_1\overline{D}_1 \ + \overline{L}_1 = \ \overline{B}_2 + \overline{C}_2 + k_2\overline{D}_2 \tag{4.15}$$

Here, k_1 and k_2 are scalars of the corresponding D vectors such that $k_i\overline{D}_i < \overline{D}_i$. Assume the slider is placed along $\overline{D}_1$, then $k_1\overline{D}_1$ describes the position of the slider and $k_2\overline{D}_2$ is a fixed position along $\overline{D}_2$. The position of $k_2\overline{D}_2$ is a design choice and therefore known. The vectors $\overline{B}_1$ $\overline{C}_1$ and $\overline{D}_1$ are also known from Section II. The unknown terms are k_1 and the interconnecting linkage vector $\overline{L}_1$. Thus, from Eq. 15, we have three equations and four unknowns. The design choice of magnitude of $\overline{L}_1$

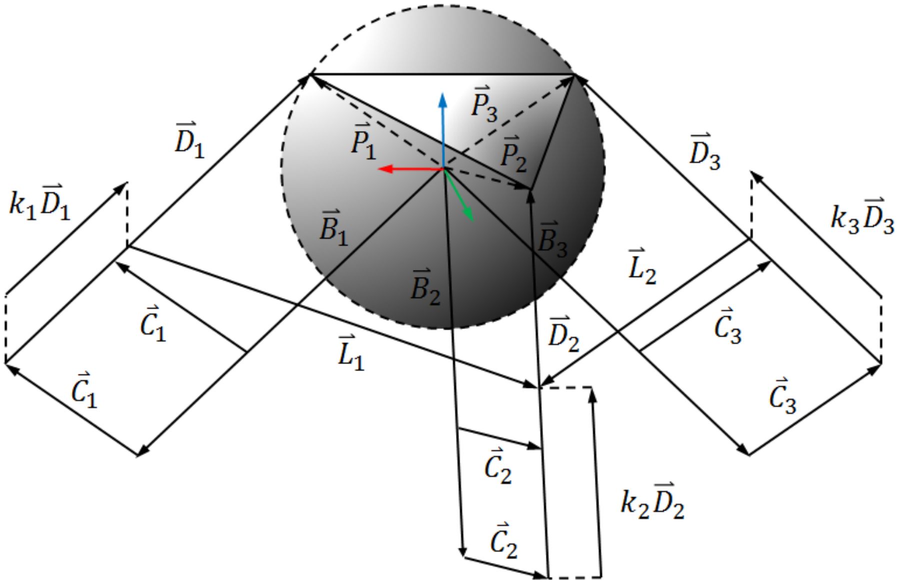

Figure 4.5: Vector representation of the 4B-SPM with the inclusion of two linear actuated sliders and two interconnecting linkages.

must be made before the unknowns can be determines, such that:

$$\left|\overline{L}_1\right|^2 = {L_{1,x}}^2 + {L_{1,y}}^2 + {L_{1,z}}^2 \tag{4.16}$$

By solving Eq. 15 and Eq. 16 simultaneously, it is possible to identify the slider position k_1 that complies with the kinematic solution given in Section II. In a similar manner, k_3 can be determined by choosing k_2 to remain fixed.

4.2.5 Cooperative Control Method to Improve Effective Workspace

As mentioned in the Introduction, one of the disadvantages of parallel manipulation is limited workspace. Although the 4B-SPM architecture presented here provides one of the largest known spherical workspaces, it can still have difficulty matching the range of motion of a highly flexible joint, such as the shoulder or hip. Depending on the task, the mechanical limits of the 4B-SPM may be reached before that of the human joint. One method for increasing workspace is control the roll axis of the

4B-SPM such that the mobile platform is always rolling back toward the center of the workspace, thus mitigating mechanical interference that occurs near its boundaries. With this method, the human can maintain control of both pitch and yaw of the limb while a controller determines the optimal roll for a given desired position. This method is referred to as cooperative control and is presented here. It should be noted that this new method shares some techniques with a similar method that the authors developed in a prior work (Hunt *et al.*, 2017).

The cooperative control technique discussed here involves allocating one of the three DoF of the 4B-SPM to the robot controller. This is done so that the robot controller can determine the solution to this DoF so as to keep the 4B-SPM within its workspace while still following the 2-DoF commands sent by the operator. To better understand this idea, the shoulder will be used as an example moving forward. The shoulder arguably has the greatest range of motion of any joint in the body and therefore is an ideal candidate for such a technique.

For the example of a shoulder exoskeleton, the operator would control the inclination and azimuth of the arm, while the robot would control the roll of the shoulder plate (i.e., mobile platform) in order to keep the 4B-SPM from hitting a mechanical limit. This allows for greater range of motion with the 4B-SPM, but the division of control has a drawback. Allowing the robot control of the shoulder plate roll limits operator ability to reach a desired position with a particular roll orientation of the arm. Therefore, for the device to remain effective, a 1-DoF revolute joint interface between the human operator and the 4B-SPM must be added. This joint could be passive or active depending on the application.

One novel method of determining the roll solution of the shoulder plate is presented here. For this method, the roll of the shoulder plate is considered as a function of the inclination and azimuth of the arm. From Section II, the rotation matrix $\boldsymbol{R}$ that defines the orientation of the platform can be described by a set of three Euler angles. These three angles will be defined as the azimuth φ, inclination θ, and roll ψ of the arm. Therefore, using the global coordinate frame shown in Fig. 2, the matrix $\boldsymbol{R}$ can be defined as:

$$\boldsymbol{R} = \boldsymbol{R_z R_y R_x} \tag{4.17}$$

where

$$\boldsymbol{R}_z = \begin{bmatrix} \cos(\varphi) & -\sin(\varphi) & 0 \\ \sin(\varphi) & \cos(\varphi) & 0 \\ 0 & 0 & 1 \end{bmatrix} \tag{4.18}$$

$$\boldsymbol{R}_y = \begin{bmatrix} \cos(\theta) & 0 & \sin(\theta) \\ 0 & 1 & 0 \\ -\sin(\theta) & 0 & \cos(\theta) \end{bmatrix} \tag{4.19}$$

$$\boldsymbol{R}_x = \begin{bmatrix} 1 & 0 & 0 \\ 0 & \cos(\psi) & -\sin(\psi) \\ 0 & \sin(\psi) & \cos(\psi) \end{bmatrix} \tag{4.20}$$

The matrices $\boldsymbol{R_z}$ and $\boldsymbol{R_y}$ are functions of φ and θ, respectively, and therefore are determined by the operator. To determine the shoulder plate roll matrix $\boldsymbol{R_x}$, it is necessary to consider how one would desire the shoulder plate to move. For example, Fig. 6 shows a set of shoulder plate orientations $\boldsymbol{R}$ selected for a particular range of motion defined by arm at rest, 90° flexion, and 90° abduction. Each of these arm directions has a corresponding roll matrix $\boldsymbol{R_x}$ associated with it. Since $\boldsymbol{R_y}$, $\boldsymbol{R_z}$, and $\boldsymbol{R}$ are known, the roll matrix $\boldsymbol{R_x}$ can be determined by:

$$\boldsymbol{R_x} = \boldsymbol{R_y}^{\boldsymbol{-1}}\boldsymbol{R_z}^{\boldsymbol{-1}}\boldsymbol{R} \tag{4.21}$$

The angle ψ that defines $\boldsymbol{R_x}$ can be determined by comparing similar terms between Eq. 20 and Eq. 21. Now, with all the Euler angles known, it is possible to choose a function for ψ that describes its solution for any location within the desired range of motion. The chosen solution must not only satisfy the three boundary solutions already known, but also take into consideration whether the desired roll motion between boundary solutions should be linear, sinusoidal, etc. For example, assume linear roll motion between points is desired, then the function ψ that also satisfies the boundary solutions can be expressed as:

$$\psi = \frac{2\theta\varphi}{\pi} - \theta + \frac{\pi}{2} \qquad rad/s \tag{4.22}$$

Therefore, the Euler angle ψ that describes the shoulder plate roll is a linear function of the desired azimuth and inclination Euler angles φ and θ as determined by the operator. This relation satisfies the three rotation matrices shown in Fig. 6. As a result, it should be noted that since Eq. 22 was developed using the desired workspace boundary orientations in Fig. 6, it is only applicable for that set orientations. For example, consider the alternative case where the desired shoulder plate orientation for 90° abduction were above rather than behind the shoulder, then a new function for ψ would need to be developed using this new rotation matrix, along with the other two shown in Fig. 6.

4.3 Results

4.3.1 Kinematics

To demonstrate the versatility and kinematics of the 4B-SPM, a series of exoskeleton simulations created using Matlab (MathWorks, MA) are presented. These include an ankle, a wrist, a hip, and a shoulder exoskeleton. For each simulation, both

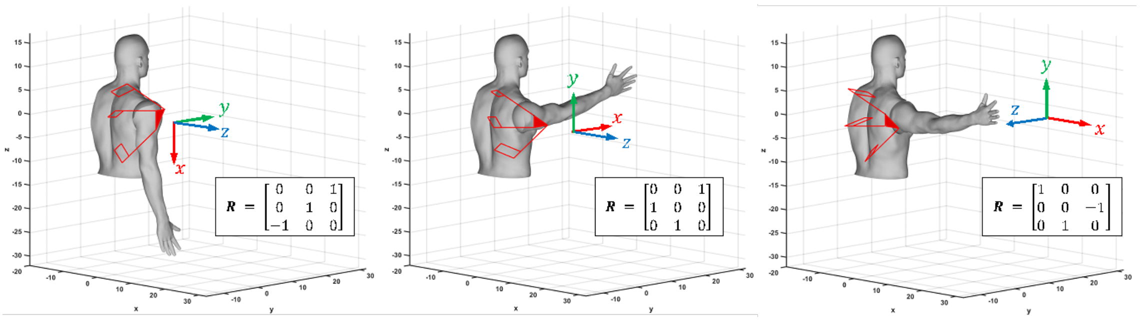

Figure 4.6: Desired shoulder plate orientations corresponding to the three boundary arm configurations that define the workspace. These include: (A) arm at rest ($\varphi = 0$, $\theta = \pi/2$, and $\psi = 0$ or $\varphi = \pi/2$, $\theta = \pi/2$, and $\psi = \pi/2$), (B) 90° flexion ($\varphi = \pi/2$, $\theta = 0$, and $\psi = \pi/2$), and (C) 90° abduction ($\varphi = 0$, $\theta = 0$, and $\psi = \pi/2$). For each arm configuration, the corresponding rotation matrix of the shoulder plate with respect to the global frame is shown.

methods of roll actuation described in Section II-D are demonstrated. Additionally included for the shoulder exoskeleton is the cooperative control technique discussed in Section II-E. Each simulation shows the 4B-SPM linkages as red lines and the mobile platform as a red plane defined by the three mounting points. It should be noted that for a real device, the mobile platform would likely represent a shoulder plate for the shoulder, a rigid cuff for the hip, a shoe for the ankle, and a glove for the wrist. One final aspect of these simulations to be aware of is that since placement of both the base mounts and platform mounts are flexible, each simulation only demonstrate one possible configuration of the 4B-SPM. The configurations shown were chosen because each interfaces well with the anatomy of the corresponding joint while still reaching the desired workspace.

4.3.2 Ankle Exoskeleton:

A 4B-SPM ankle robot is shown in Fig. 7. A simulation of its kinematics for both roll actuation methods described in Section II-D is shown in Extension 1. In the video, the ankle range of motion is shown with bounds of 45° planter flexion, 15° dorsiflexion, 20° inversion, 20° eversion, 20° pronation, and 20° supination. These bounds were chosen to approximately match accumulative average range of motion data (Hoffman, 2006), but could be changed if needed. In this configuration, the base mounts are positioned about the tibia bone and the mobile platform mounts are positioned atop the front and back of the foot. Depending on the application, the mobile platform may be taken as a shoe and the stationary base as either part of a greater exoskeleton or possibly a knee orthosis brace.

4.3.3 Wrist Exoskeleton:

The 4B-SPM wrist robot is shown in Fig. 8. A simulation of its kinematics for both roll actuation methods described in Section II-D is shown in Extension 2. In the video, the wrist range of motion is shown with bounds of 65° flexion, 65° extension, 75° pronation, 75° supination, 20° ulnar deviation, and 20° radial deviation. These bounds were chosen to approximately match accumulative average range of motion data (Schiele and Van Der Helm, 2006), but could be changed if needed. In this configuration, the base mounts are positioned about the forearm and the mobile platform mounts are positioned on the back of the hand opposite the palm. Depending on the application, the mobile platform could be taken as a partially rigid glove and the stationary base as either part of a greater exoskeleton or possibly an elbow orthosis brace.

4.3.4 Hip Exoskeleton:

The 4B-SPM hip robot is shown in Fig. 9. A simulation of its kinematics for both roll actuation methods described in Section II-D is shown in Extension 3. In the video, the hip range of motion is bounded by the three operator leg configurations of 90° flexion, 30° abduction, and at rest. These bounds were chosen to approximately match accumulative average range of motion data Schiele and Van Der Helm (2006),

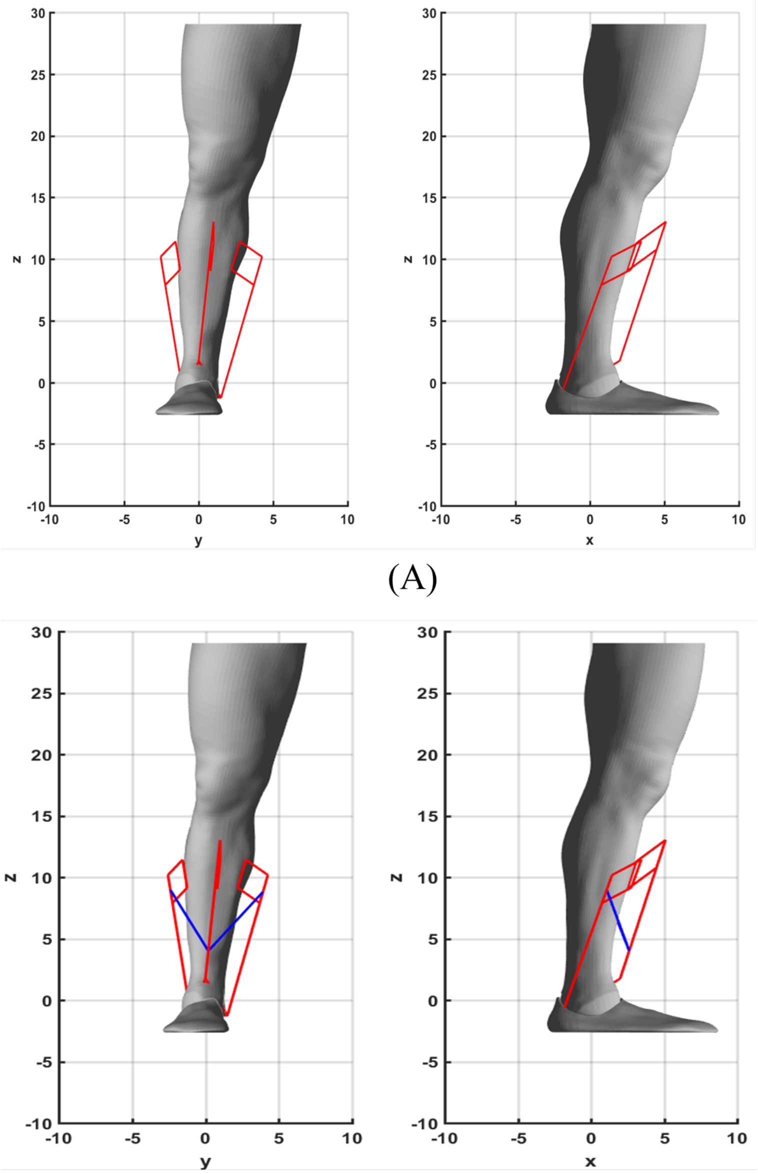

(A)

(B)

Figure 4.7: 4B-SPM ankle exoskeleton. (A) Shows the 4B-SPM architecture used for three or six revolute motors as described in Section II A and Section II D1, respectively. (B) Shows the 4B-SPM architecture used for three revolute motors and two linear actuators as described in Section II D2. The interconnecting linkages that slide up and down the outermost substructures via linear actuation are shown in blue to help distinguish them from the rest of the 4B-SPM.

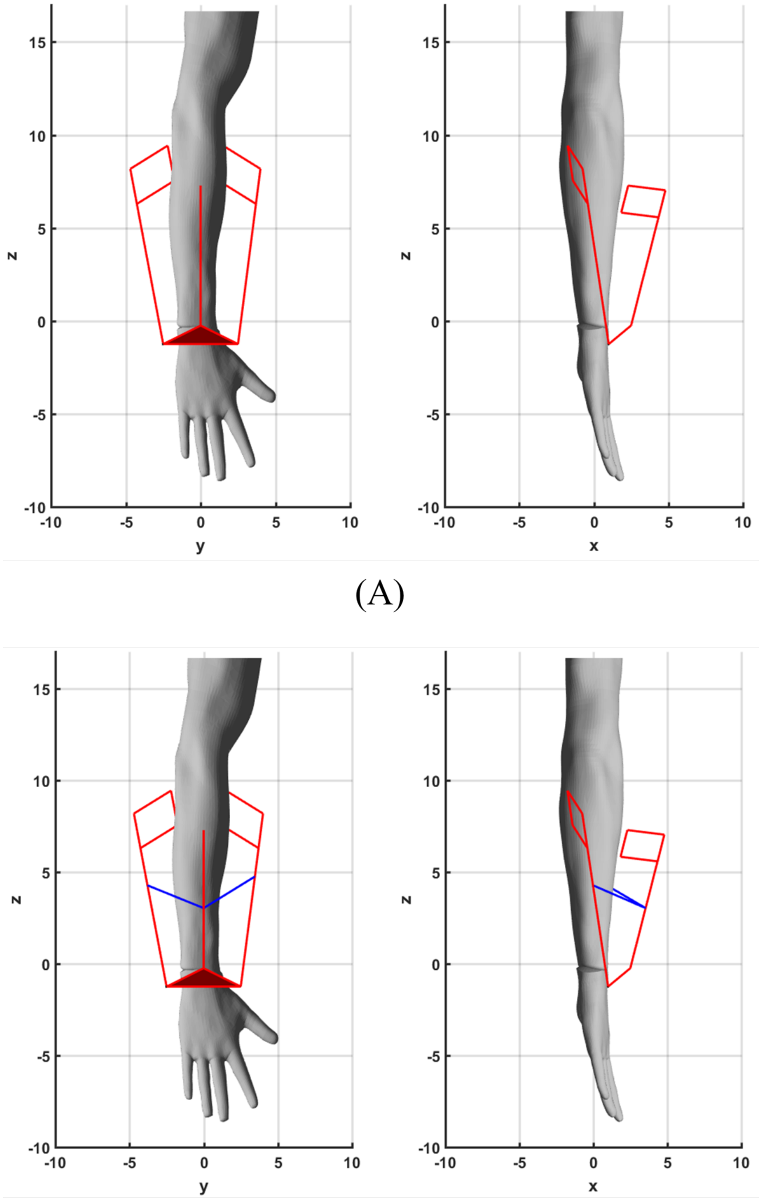

(A)

(B)

Figure 4.8: 4B-SPM wrist exoskeleton. (A) Shows the 4B-SPM architecture used for three or six revolute motors as described in Section II A and Section II D1, respectively. (B) Shows the 4B-SPM architecture used for three revolute motors and two linear actuators as described in Section II D2. The interconnecting linkages that slide up and down the outermost substructures via linear actuation are shown in blue to help distinguish them from the rest of the 4B-SPM.

but could be changed if needed. In this configuration, the base mounts are positioned about the waist and the mobile platform mounts are positioned about the femur. Depending on the application, the mobile platform could be taken as a cuff about the upper leg and the stationary base as either part of a greater exoskeleton or possibly a partially rigid vest.

4.3.5 Shoulder Exoskeleton:

The 4B-SPM shoulder robot is shown in Fig. 10. A simulation of its kinematics for both roll actuation methods described in Section II-D using the cooperative control technique for improving effective workspace discussed in Section II-E is shown in Extension 4. To help demonstrate the importance of cooperative control for large range of motion joints, Extension 5 shows what happens when it is not implemented for the shoulder exoskeleton. In these videos, the shoulder range of motion is bounded by the three operator arm configurations of 90° flexion, 90° abduction, and at rest. While the range of human shoulder motion on average exceed these bounds Schiele and Van Der Helm (2006), this workspace is sufficient to demonstrate both the architecture's potential application for a shoulder exoskeleton device and the cooperative control techniques descripted in Section II-E. The range of motion could be increased by utilizing bounded nonlinear multi-objective optimization to configure the parallel substructures so as to maximize the workspace [33]. In this configuration, the base mounts are positioned behind the operator and the mobile platform mounts are positioned on a shoulder plate. Depending on the application, the stationary base could be taken as either part of a greater exoskeleton or possibly an electric wheel chair.

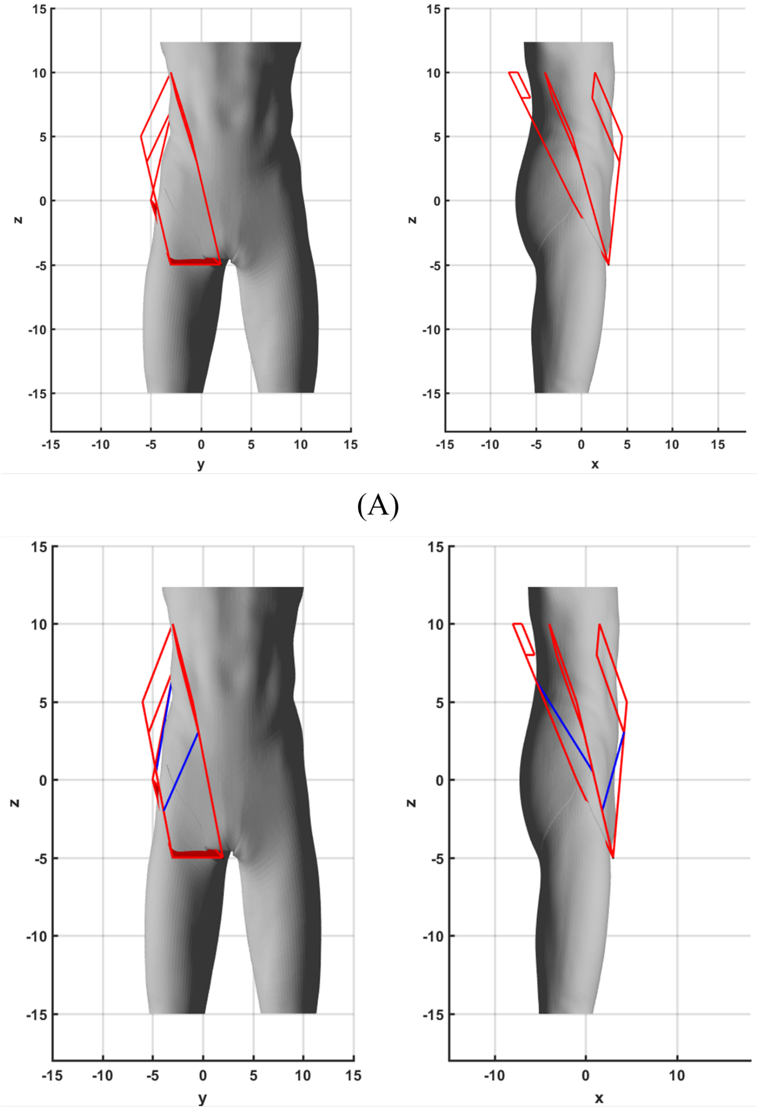

(A)

(B)

Figure 4.9: 4B-SPM hip exoskeleton. (A) Shows the 4B-SPM architecture used for three or six revolute motors as described in Section II A and Section II D1, respectively. (B) Shows the 4B-SPM architecture used for three revolute motors and two linear actuators as described in Section II D2. The interconnecting linkages that slide up and down the outermost substructures via linear actuation are shown in blue to help distinguish them from the rest of the 4B-SPM.

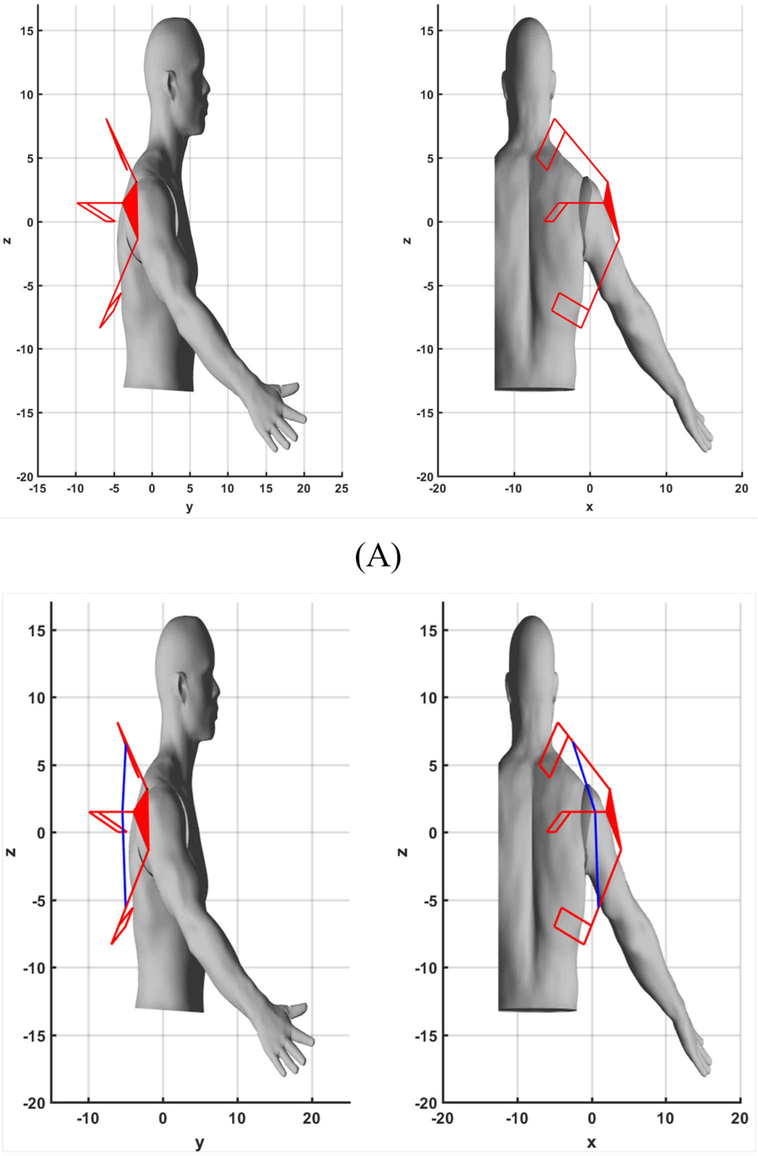

(A)

(B)

Figure 4.10: 4B-SPM shoulder exoskeleton. (A) Shows the 4B-SPM architecture used for three or six revolute motors as described in Section II A and Section II D1, respectively. (B) Shows the 4B-SPM architecture used for three revolute motors and two linear actuators as described in Section II D2. The interconnecting linkages that slide up and down the outermost substructures via linear actuation are shown in blue to help distinguish them from the rest of the 4B-SPM.

4.3.6 Case Study: 4B-SPM Shoulder Exoskeleton Design and Development Considerations

In order to have the opportunity to discuss 4B-SPM exoskeleton design aspects such as cost feasibility, material selection and control methods, a case study is performed here. The objective of this case study is to demonstrate viability of the 4B-SPM architecture through a dialogue regarding aspects critical to its development. A 4B-SPM shoulder exoskeleton was chosen as the subject of this case study. The shoulder was chosen because its complexity relative to the hip, wrist and ankle would suggest that the design methods involved could likely be extrapolated and applied to these simpler joints as well. For this case study, the device is assumed to not be part of a greater exoskeleton system, but instead mounted to a support structure, such as a stationary frame or electric wheel chair.

For this case study, the roll actuation method described in Section-II D1 was chosen in order to provide good dynamic performance. This method was selected because the top linkage connecting each four bar mechanism to the shoulder plate is relatively short for the chosen actuator configuration and therefore does not lend itself well to the roll actuation method described in Section-II D2.

The 4B-SPM shoulder exoskeleton for this case study is shown in Fig. 11, 12. The design consists of three substructures, each equipped with two Dynamixel MX-106R smart servo motors (Robotis, South Korea) with the actuated roll configuration shown in Fig. 3. Each four bar mechanism is built using a combination of rod end bolts, threaded rod, ball bearings, and 6061 aluminum tubing. Each four bar mechanism is coupled to a shoulder plate constructed from 6061 aluminum using a ball joint rod end. The position and orientation of each substructure is held fixed with respect to one another through the use of static Stewart-Gough platforms (SSGP) built using threaded rod and ball joint rod ends. The use of SSGPs is an affordable positioning solution that also offers high stiffness and the ability to alter the substructure configuration if desired. A third SSGP (not shown in Fig. 11, 12) is used to rigidly connect the shoulder exoskeleton to a stationary support frame. It should be noted that the use of SSGP is only one possible solution for the positioning of each actuated substructure. Alternatively, a single piece of custom fabricated material with mounts to connect the three substructures could be used.

It is important to mention not only where the actuated substructures are positioned, but how they are positioned. Proper alignment of the actuated substructures is important. If all substructures do not rotate about the same center of rotation, then the workspace would be ellipsoidal instead of spherical. Additionally, mechanical stress due to misalignment will occur. Two methods to ensure proper alignment of the substructures have been considered: (7.1) With a CAD rendition of the desired 4B-SPM, the designer could extend rods along the roll axis of each substructure and intersect them at the center of rotation. These rods could be encapsulated about the center of rotation by a cubic structure. By subtracting the rod geometry from the cubic geometry, the designer would be left with a part that could be used to orient all three substructures. This cubic part could be 3D printed or fabricated out of more robust materials. The designer would only need to fix temporary rods along the axis of rotation of each substructure to intersect the cubic part during installation of the SSGPs. (3.2) As previously mentioned, one alternative to SSGPs would be to use a single piece of custom fabricated material with mounts to connect the three substructures. If this option were used, then the designer would only need a CAD rendition of the desired 4B-SPM with known substructure mounting locations to design and commission a single piece component that would ensure that the roll axis of each substructure intersects at the same point.

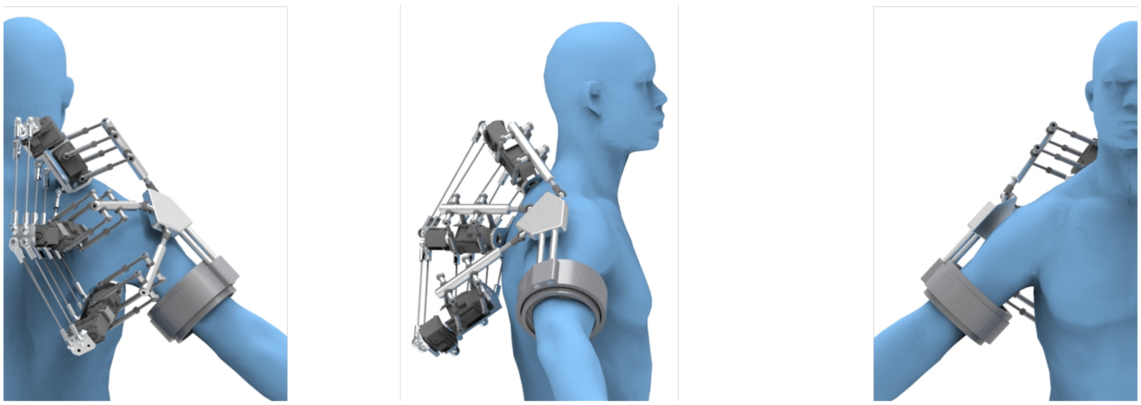

Figure 4.11: 4B-SPM shoulder exoskeleton with a six motor configuration. Shown is a back, side and front view of the device.

To couple the shoulder plate to the operator, a cuff positioned at the upper arm is used. As briefly mentioned in Section II-E, in order for cooperative control techniques that improve the effective workspace of the shoulder exoskeleton to be applied, an additional DoF must be added at the cuff. This is accomplished by constructing the cuff from two concentric tubes. The outer tube is connected to the shoulder exoskeleton and the inner tube is positioned around the upper arm with a padded interface between operator and cuff, as shown in Fig. 11, 12. Not only does this design permit the rotational 1-DoF required for cooperative control, but it also allows 1-DoF of minor translational slip motion between the cuffs. This slip is critical to preventing possible joint misalignment between the operator and shoulder exoskeleton from applying dangerously high force to the human shoulder joint (Cempini *et al.*, 2013; Stienen *et al.*, 2009). More details regarding this slip mechanism can be found in the authors' prior work (Hunt *et al.*, 2017) where it was first introduced.

While the cost of the 4B-SPM will vary depending on design choices such as the servos or the controller used, this case study demonstrates the majority of the parallel substructure components can be purchased off-the-shelf and therefore do not invoke high fabrication costs. In addition to this, as discussed in the Introduction, parallel actuation has the inherent ability to rectify positioning errors. This means that

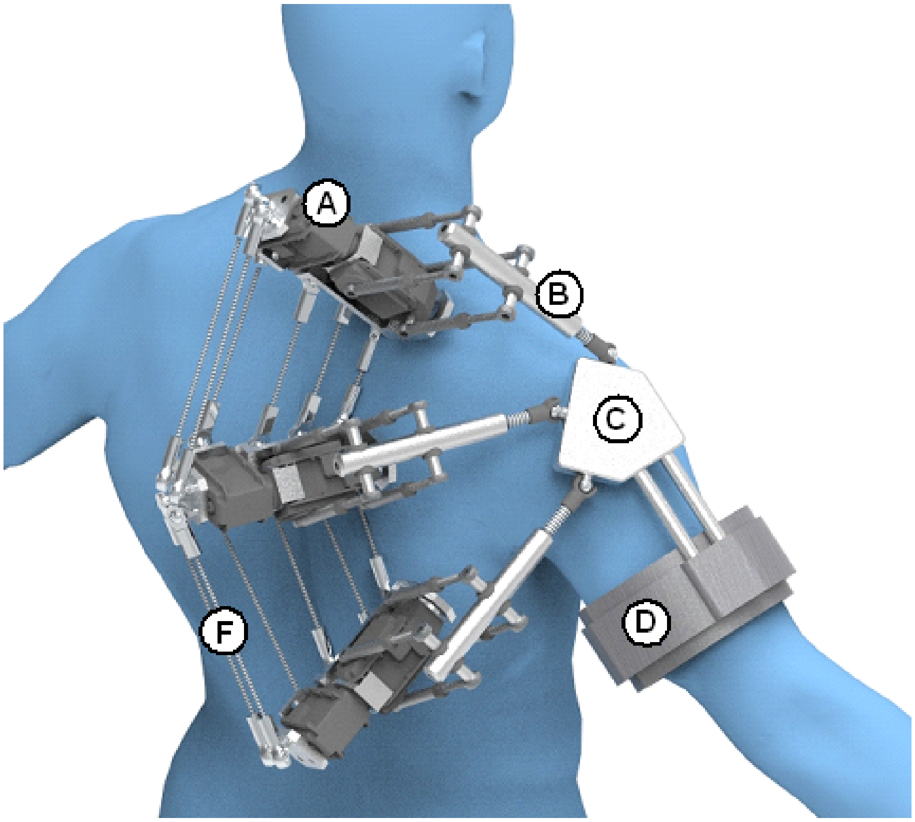

Figure 4.12: 4B-SPM shoulder exoskeleton with a six motor configuration as described in Section D1. With this configuration, each of the three substructures consists of two motors: one for the pitch of the four bar mechanism and one for the roll. Noteworthy components are as follows: (A) Revolute motor. (B) Four bar mechanism. (C) Shoulder Plate. (D) Arm cuff with one translational and one rotational passive DoF. (F) Static Stewart- Gough platform for rigid positioning of adjacent actuated substructures.

cheaper, lower tolerance sensors and components can be used without a significant impact on position accuracy. So even if the six motor 4B-SPM configuration is chosen for high dynamic performance, the architecture may still prove to be more affordable than a serial actuated shoulder exoskeleton with a comparable 3-DoF.

To operate the shoulder exoskeleton, an admittance control scheme (Glosser and Newman, 1994; Hogan, 1988) that utilizes force feedback from the cuff could be used to determine user commands in terms of position. These commands could be sent to the motors using a Dynamixel CM-700 (Robotis, South Korea) motion controller.

Force feedback could be measured using an array of piezoresistive force sensors placed between the inner and outer cuff to capture both the magnitude and direction of the contact force vector. This vector could be converted to angles φ and θ in order to calculate the desired operator command rotations $\boldsymbol{R_z}$ and $\boldsymbol{R_y}$ described in Section II-E.

Finally, a comment regarding the dynamic performance of this 4B-SPM shoulder exoskeleton. Even without a complete dynamic model for this particular actuator configuration, the output torque can still be estimated within a given range. It should be noted that a torque estimate is only possible for the six motor configuration shown in Fig. 3 and used for this case study. This is because each substructure of the parallel system is fully actuated and thus can operate independently as a 2-DoF serial manipulator. The torque output of a 2-DoF serial manipulator is well understood and is easily calculate based on the motor outputs. Therefore, estimates of static output torque for three 2-DoF serial manipulators operating synchronously can be given. Each MX-106R servo has a rated stall torque of 10 Nm. Therefore, if each servo were fully engaged, $\sim$60 Nm of torque output would be expected for the static case. However, most shoulder plate orientations will not utilize all six servos fully at once. As shown Section-II C, operation is possible with only three servos. Therefore, depending on the commanded shoulder plate motion, operating torques can be approximated to be between $\sim$30 and $\sim$60 Nm of output at the shoulder for the static case. If conversely, three motors were used, then the approximated torque output would be between $\sim$0 and $\sim$30 Nm of static torque output. The occurrence of $\sim$0 Nm torque output for certain shoulder configurations can be mitigated by carefully considering the placement of each actuator or by constraining the workspace.

4.4 Discussion

The development of the 4B-SPM was motivated by the need for a exoskeleton robotic architecture that can operate effectively with complex ball and socket joints like the shoulder, hip, wrist, and ankle. Conventionally, these spherical joints have been augmented using serial actuation as it can offer a large workspace. However this approach requires the use of a long serial moment arm that in turn results poor dynamic performance. Not only does the unique architecture of the 4B-SPM provide a short moment arm while still maintaining a large workspace, but its use of multiple mounting points and fully active DoF offers some of the dynamic advantages inherent to parallel actuation.

In this work, an analysis of the 4B-SPM forward and inverse kinematics was performed, along with multiple methods of actuation that can be implemented depending on dynamic performance requirements. These actuation types include a three revolute actuator, a six revolute actuator, and a three revolute two prismatic actuator version of the 4B-SPM. Also discussed is a technique of cooperative control that allows the 4B-SPM a greater effective workspace by preventing mechanical interference between the device and operator from occurring.

The results of this paper detail four example exoskeleton types that could be built using the 4B-SPM. These include a shoulder, hip, wrist, and ankle device. Each was designed to match the approximate range of motion of the respective joints. Video simulations of each exoskeleton were included in this work. Also included in all four simulations were the different methods of roll actuation to improve dynamic performance. Furthermore, for the shoulder simulation, the cooperative control technique discussed in Section II-E was demonstrated.

The four embodiments of the 4B-SPM presented in this work help to establish its versatility as a result of flexible placement of the actuator mounting points. This versatility means the 4B-SPM substructures could be positioned to not only accommodate the human anatomy, but also aspects of a greater exoskeleton system as well. Therefore, certain design decisions such as placement of a power source, life support, and onboard sensors could be made before 4B-SPM substructure placement is considered.

In conclusion of this work, the 4B-SPM can be realized as a viable parallel actuated design that allows for the augmentation complex biologicals joints like the shoulder, hip, wrist, and ankle. With advantages such as a short moment arm, low inertia, and rigidity associated with parallel structures, the 4B-SPM can be considered a viable alternative to the traditional use of serial actuation to the same end. Along with other architectures such as the Stewart-Gough platform, which has been suggested to be an effective solution for augmenting torso movement (Park *et al.*, 2015), the 4B-SPM could assist in the development of a future series of parallel actuated exoskeletons that are more effective than their contemporary serial counterparts.

Chapter 5

DEVELOPMENT OF A LOW INERTIA PARALLEL ACTUATED SHOULDER EXOSKELETON ROBOT FOR THE CHARACTERIZATION OF NEUROMUSCULAR PROPERTY DURING STATIC POSTURE AND DYNAMIC MOVEMENT

5.1 Introduction

The neuromuscular properties of the human body, determined by the collective behaviors of bones, joints, muscles, nerves and receptors, are responsible for static posture and dynamic movement. These properties can be quantitatively described by mechanical impedance, a fundamental property of the human neuromuscular system in interaction with the physical world (Burdet *et al.*, 2001; Hogan, 1985; Perreault *et al.*, 1999). Characterizing mechanical impedance and its underlying mechanisms, including intrinsic and reflexive impedances, is an important field of study that has significance for a variety of applications. Two examples that are of particular interest to the authors include:

1. **Medical:** characterizing abnormal mechanical impedance associated with neuropathies or neuromuscular autoimmune conditions to assist clinicians in the development of new rehabilitation protocols that more accurately target patient impairment.
2. **Military/Industrial:** characterizing normal mechanical impedance would allow for the development of exoskeleton devices that rely on cooperative human-robot critical stability interaction to provide highly responsive performance.

Efforts to quantify mechanical impedance and its components (e.g., stiffness, damping, reflex gain) of major joints such as the elbow (Popescu *et al.*, 2003), ankle (Lee *et al.*, 2011; Lee and Hogan, 2015; Kearney *et al.*, 1997), and wrist (Pando *et al.*, 2014) have been made prior. Each study utilized a different exoskeleton characterization device designed specifically to interface with the joint of interest. These devices work by applying position/angle (or force/torque) perturbations to the accompanying limb segment/joint and measuring the corresponding force/torque (or position/angle) response.

More complex joints with a large range of motion and high torque output, like the shoulder, are yet to be thoroughly investigated. This is largely due to the lack of exoskeleton characterization tools capable of both interfacing with and manipulating the shoulder joint effectively. This includes the ability to rapidly perturb the limb in multiple directions during both static posture and dynamic movement. This is important, as mechanical impedance has an intrinsic and reflexive components that occur during the first 20 ms and 20-100 ms of an applied external perturbation, respectively (Ito *et al.*, 2004; Kurtzer *et al.*, 2008). Therefore, the limb needs to be reasonably displaced during this period to characterize intrinsic and reflexive responses and separate their contribution from that of voluntary response. This can be difficult, primarily due to high robot inertia.

Most shoulder exoskeleton robots utilize a serial type architecture that works to bridge the glenohumeral joint using a chain of motors and linkages (Zhang and Nelson, 2011). The moment arm associated with these linkages has the inherent disadvantage of amplifying torques applied to the joint by external forces. Furthermore, each motorized joint in the armature must be capable of not only actuating the corresponding human limb, but also able to lift and manipulate the motors that follow in series. This requires larger motors with more inertia, which as previously mentioned, makes executing a rapid perturbation difficult.

One solution to this problem is to use a parallel actuated architecture instead. Parallel actuation has several inherent properties that make it ideal for characterizing the neuromuscular properties including joint mechanical impedance. These include low end effector inertia, high end effector acceleration and high potential stiffness (Hunt, 1983; Merlet, 2012; Pashkevich *et al.*, 2009; Gosselin, 1990). These advantages are in part why neuromuscular property characterization tools like the AnkleBot, (Roy *et al.*, 2009), Rice Wrist (Gupta *et al.*, 2008) and Manus (Hogan *et al.*, 1992) all utilize parallel architectures.

In an effort to develop a shoulder exoskeleton robot with high acceleration in order to characterize the neuromuscular properties of the shoulder, the authors recently introduced a new type of parallel architecture specifically designed to interface with multiple degree-of-freedom (DoF) biological joints. The architecture can be described as a type spherical parallel manipulator (SPM) that utilizes three 4-bar (4B) substructures to move a mobile platform about a fixed point. A kinematic solution to the 4B-SPM architecture was proposed by the authors in a prior work (Hunt and Lee, 2018).

In this work, a shoulder exoskeleton prototype that utilizes the 4B-SPM architecture is presented. In addition to providing a new research platform for shoulder studies, this work is meant to show the viability of the 4B-SPM architecture. This could lead to its use for other spherical joint applications, such as the wrist, hip and ankle.

The rest of this paper focuses on the design, development and validation of the 4B-SPM shoulder exoskeleton robot. Section II begins with a detailed description of the prototype, complete with a video demonstration of its operation. This is followed by discussion of the setup and parameters of position accuracy and step response tracking experiments. Section III presents the results of the two experiments. Finally, Section IV concludes the paper with discussion of the results and a summary of contribution.

5.2 Methods

5.2.1 A. Prototype Overview

The 4B-SPM shoulder exoskeleton prototype is presented in Fig. 1. A video demonstrating its kinematics can be found here: https://youtu.be/ZsSo4RxwrwU. The design consists of three actuated substructures that couple a stationary base to a mobile ABS shoulder plate. Each substructure is comprised of two Dynamixel MX-106R Servos (Robotis, South Korea) and one aluminum/steel 4-bar mechanism. The first servo of each substructure is fixed to the stationary base and works to actuate the roll of the second servo in series and its corresponding 4-bar mechanism. The second servo of each substructure works to actuate the pitch of the attached 4-bar mechanism. The three axes for the three fixed servos intersect at a singular point in space that represents the center of rotation for the shoulder plate. The top linkage in each 4-bar mechanism is extended to reach a shoulder plate, which operates spherically about the center of rotation. Each top linkage is coupled to the shoulder plate using a 3-DoF universal joint. The shoulder plate is connected to an upper arm cuff using a pair of embedded aluminum tubes. The prototype as described is shown in Fig. 2 with labels that highlight key components. The substructure architecture as described is shown in Fig. 3.

For ideal operation, the center of rotation of the human shoulder and exoskeleton would exist at the same point. However, because the human shoulder can translate as well as rotate, perfect alignment cannot be assumed. Therefore, to resolve this issue, the inner aluminum ring of the cuff has both a passive translational and rotational

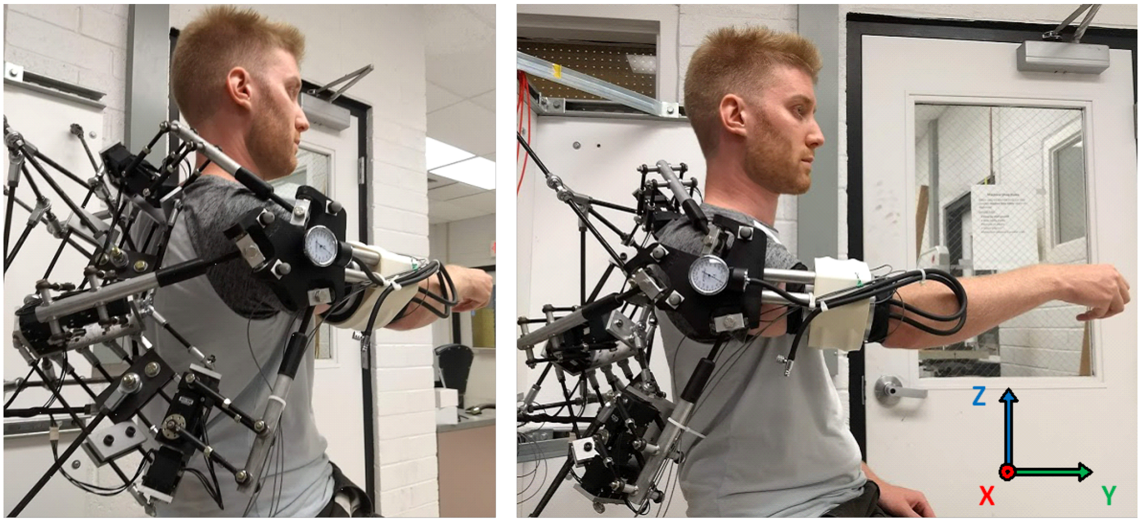

Figure 5.1: 4B-SPM shoulder exoskeleton mounted to a stationary platform with a human subject in the seated position. This orientation is taken to be the zero pitch, yaw and roll position of the shoulder piece.

DoF along the arm. In the event that joint misalignment occurs, the inner ring will slip to prevent discomfort to the user. This slip mechanism was first introduced in the authors' prior work (Hunt *et al.*, 2017). A diagram of the slip mechanism is provided in Fig. 4.

The arm cuff of the exoskeleton contains four LLB300 Subminiature Load Cells (Futek, California). Each load cell is positioned between steel disks that are embedded within inner and outer ABS holding rings. The ABS rings are positioned between inner and outer aluminum rings for rigidity. The inner aluminum ring holds a blood pressure cuff that can be inflated to ensure proper contact between user and exoskeleton. All of these components are encapsulated by an ABS outer shell that connects the arm cuff to the shoulder plate aluminum tubing. The arm cuff as described is shown in Fig. 5 with labels that highlight key components.

To control the exoskeleton, desired roll, pitch and yaw Euler angle commands for the shoulder plate are translated into servo rotations using the 4B-SPM kinematic model (Hunt and Lee, 2018). The model runs on nearby PC that sends position

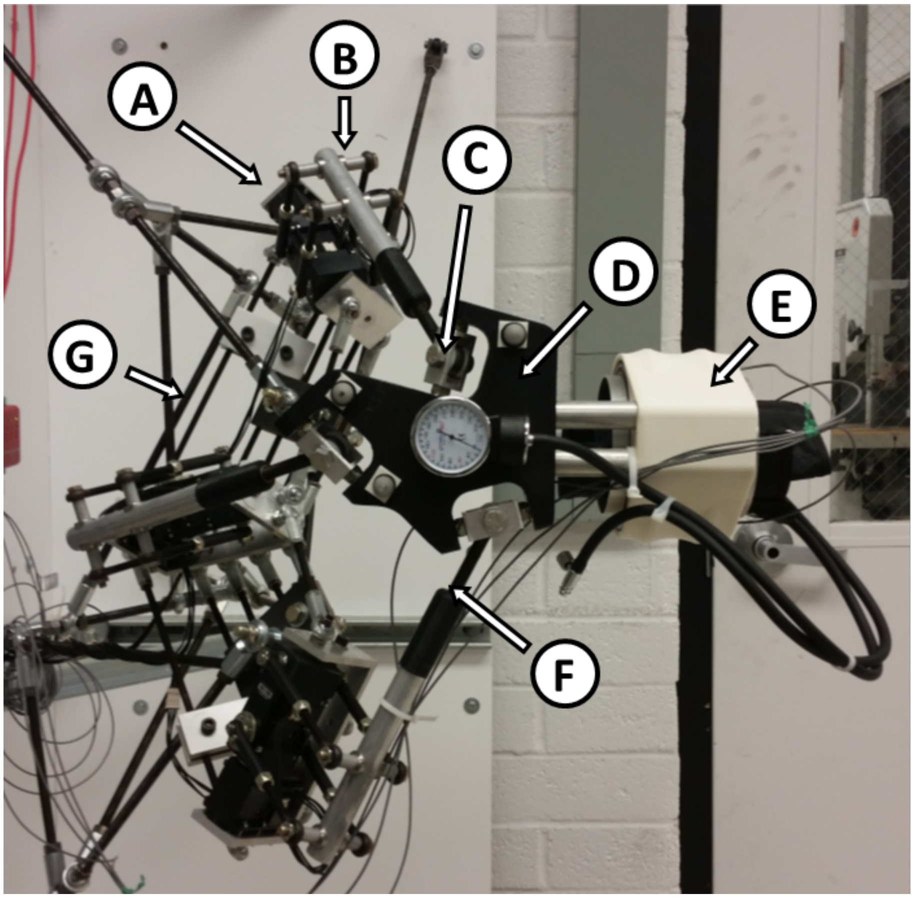

Figure 5.2: 4B-SPM shoulder exoskeleton: (A) dual servo substructure, (B) 4-bar mechanism arm, (C) universal joint, (D) mobile shoulder piece, (E) arm cuff, (F) revolute joint, (G) stationary mounting structure.

commands to a CM-700 Servo Controller (Robotis, South Korea) at 100 Hz. This controller is in turn connected to the six servo motors. This setup is shown in Fig. 6. While the current prototype utilizes position control, it should be noted that the embedded load cells in the cuff would permit an admittance control scheme to be used instead if needed.

While any set of Euler angle commands could be sent to the 4B-SPM shoulder exoskeleton, it is important that the operator avoid mechanical interference that might occur if the workspace is overextended. In prior work, it was demonstrated that the practical workspace of any 4B-SPM device could be increased by utilizing a function

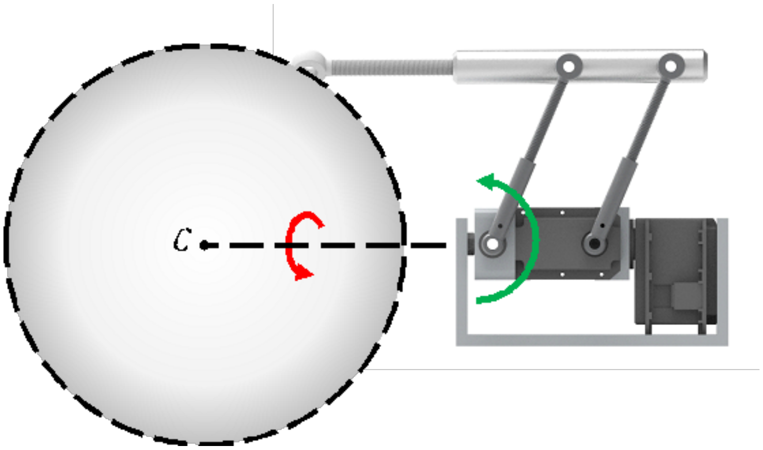

Figure 5.3: 4B-SPM actuated substructure. Each substructure is comprised of two servo motors that control the roll (red) and pitch (green) of a four-bar mechanism. The end effector of the four-bar mechanism operates on the surface a sphere centered at C. By connecting three of these substructures end effectors to a shoulder piece, it is possible to have that shoulder piece rotate about C with a singular define kinematic solution.

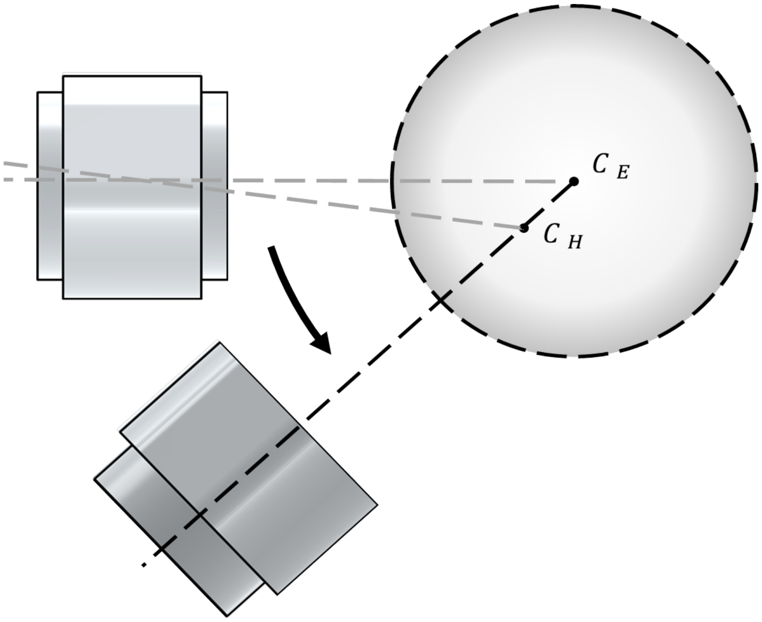

Figure 5.4: diagram showing how the arm cuff slip mechanism translates when the shoulder exoskeleton center of rotation C_E and humen shoulder center of rotation C_H are not aligned.

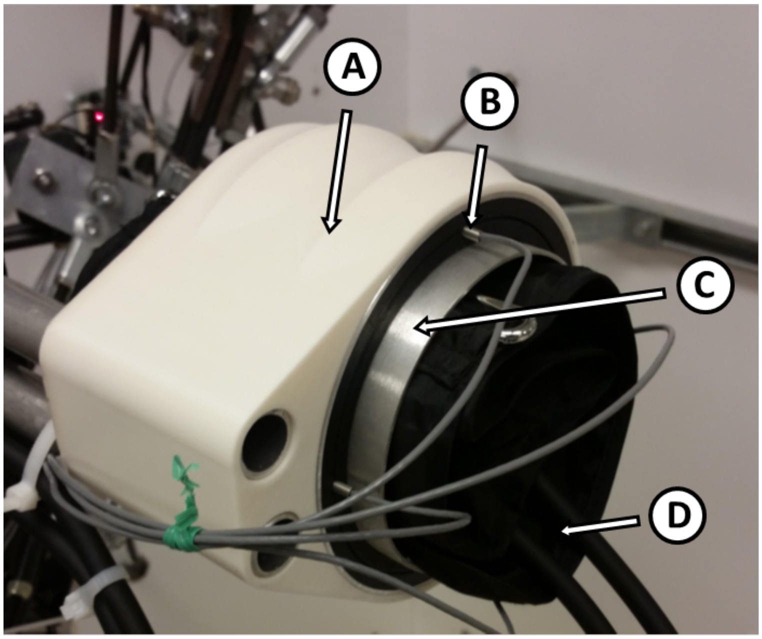

Figure 5.5: Arm cuff: (A) external casing, (B) embedded load cell, (C) 2-DoF slip ring, (D) blood pressure cuff.

that determine roll of the mobile platform given a commanded pitch and yaw to avoid mechanical interference (Hunt and Lee, 2018). For the 4B-SPM shoulder exoskeleton, this function would ensure that the shoulder plate always rolls back toward the center of the workspace as the pitch and yaw approach their respective limits. This was demonstrated in the video provided. It should be noted that this cooperative control technique is made possible by the previously mentioned passive roll DoF at the cuff that permits the shoulder plate to rotate freely without harming the operator. If a particular study requires the actuation of the roll DoF of the shoulder, then the passive roll DoF at the cuff can be locked and the roll of the shoulder plate actuated as normal.

B. Shoulder Plate Design

The design of the shoulder plate is a critical factor in determining the performance the 4B-SPM exoskeleton. Careful placement of the three mounting points on

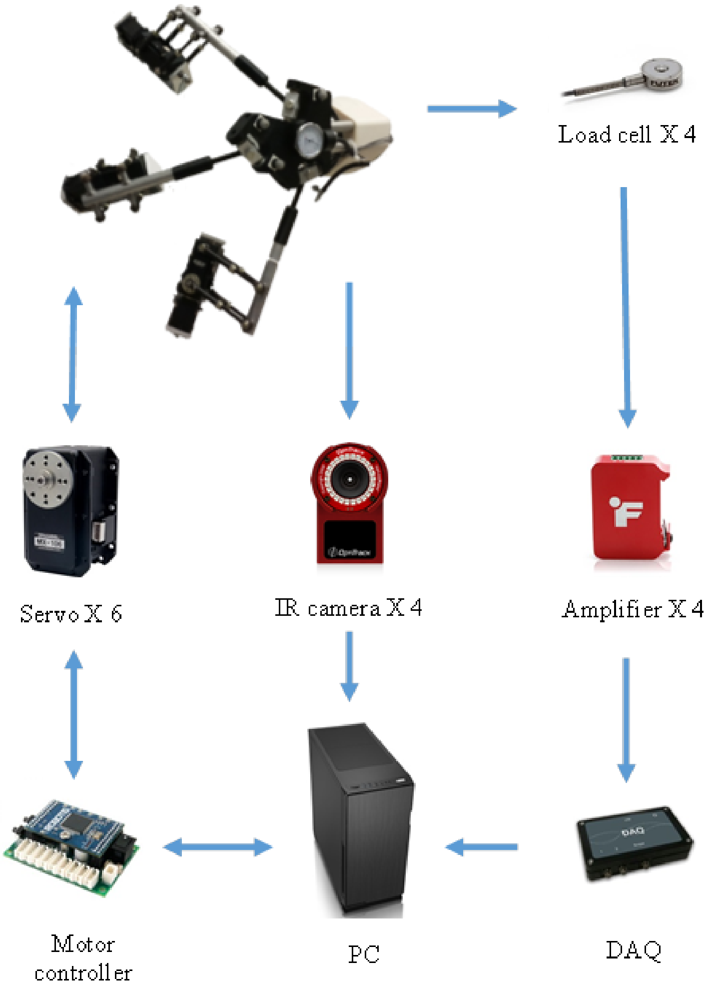

Figure 5.6: Hardware setup showing the open loop (single arrow) and closed loop (double arrow) processes. The hardware includes: six Dynamixel MX-106R Servos (Robotis, South Korea), one CM-700 Servo Controller (Robotis, South Korea), four LLB300 Subminiature Load Cells (Futek, California) four IAA100 Analog Amplifiers (Futek, California), custom DAQ and PC. For the experiments performed in Section II-B, four Flex 3 IR Cameras (OptiTrack, Oregon) are used to confirm the shoulder piece Euler angles.

the shoulder plate can mitigate mechanical interference between the substructures during motion, resulting in a large permissible workspace. In addition, mounting point placement can improve overall 4B-SPM stiffness as well. Increasing the spacing between the mounting points increases the distance between each substructure end effector and the center of rotation of the shoulder plate. This results in improved stiffness as each substructure has a longer moment arm to resist applied torque.

Several contrasting shoulder plate designs are provided in Fig. 7 to demonstrate how the workspace can be varied. Shown in Fig. 7A is the primary shoulder plate used in this work as it provided a good balance between stiffness and workspace. Shown in Fig. 7B is alternate design to Fig. 7A that utilizes the same mounting point locations, but rotates the entire workspace 65° by changing the fixed orientation of the arm cuff relative to the shoulder plate. Shown in Fig. 8C is another alternate design to Fig. 7A that utilizes that same fixed orientation of the arm cuff relative to the shoulder plate, but utilizes a different set of mounting point locations to give a similar, yet slightly larger workspace. A video of the 4B-SPM with the shoulder plate shown in Fig. 7C can be found here: https://youtu.be/KtbHZuGzHuU.

Increasing the shoulder plate stiffness of the 4B-SPM exoskeleton while still maintaining a large workspace can be done through optimization techniques. One such method for optimizing the stiffness of a parallel actuated SPM was detailed in a prior work by the authors for a similar robot architecture. This method involved applying a genetic algorithm to an analytical robot stiffness model created using a matrix structural analysis (Hunt *et al.*, 2018).

5.2.2 C. Experimental Setup and Protocols

To evaluate the 4B-SPM shoulder exoskeleton's performance, two experiments were performed. These include a quantification of position error and response time.

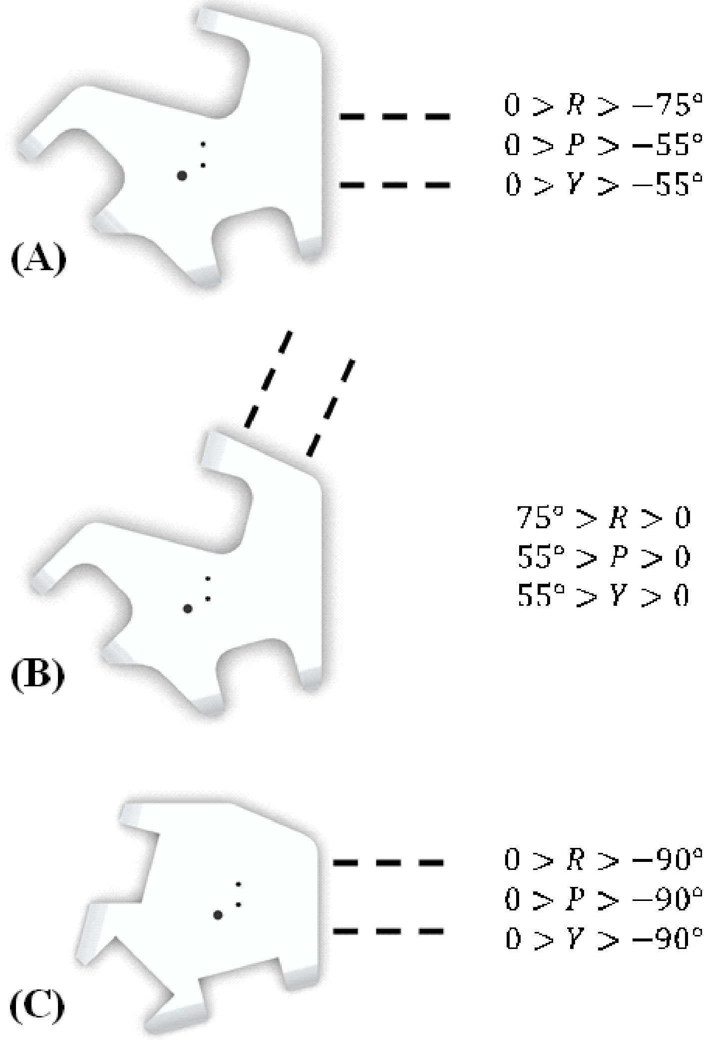

Figure 5.7: Various shoulder piece designs with corresponding roll (R), pitch (P), yaw (Y) workspaces. (A) Current shoulder piece with tested workspace. (B) Alternate shoulder piece design with same mounting point locations as (A), but with a different cuff position, so as to apply a 65° rotation to the workspace. (C) Alternate shoulder piece design with different mounting point locations than (A), but with the same cuff position, so as to give a similar yet slightly larger workspace.

To conduct these tests, accurate Euler Angle measurements of the 4B-SPM shoulder plate are needed. To measure the Euler Angles, four Flex 3 infrared (IR) Cameras (OptiTrack, Oregon) cameras operating at 100 Hz were used. These cameras track three IR markers placed on the shoulder plate to recreate its rotation matrix. These markers can be seen in Fig. 1-2. It should be noted that, while the prototype does already have feedback of the shoulder plate position via the six servo encoders and a forward kinematic model (Hunt and Lee, 2018), the decision was made to not rely on this feedback until these initial evaluation tests are complete. Details of the two performance experiments are as follows:

1. **Shoulder Plate Tracking:** To check for possible mechanical interference and positioning errors due to misalignment of the three actuated substructures during hand assembly, a position tracking experiment was performed. This was done by comparing the Euler angle input and measured values of the shoulder plate shown in Fig. 7A. To perform this test, the shoulder exoskeleton was first positioned at the 0° pitch, yaw and roll orientation shown in Fig. 1. The roll, pitch and yaw of the shoulder plate were varied from 0 to -75°, -55° and -55°, respectively. This matches the motion shown in the video link provided in II-A. As previously mentioned, a larger workspace or an entirely different workspace is possible if desired. The scale and position of the workspace are primarily dependent on the design of the shoulder plate [19]. To show this, Experiment 1 was repeated with the shoulder plate shown in Fig. 7C. The roll, pitch and yaw for this second shoulder plate were varied from 0 to -90°, -90° and -90°, respectively.

2. **Step Response Tracking:** to benchmark the 4B-SPM shoulder exoskeleton response time, a step input was applied along multiple directions. To perform

this test, the shoulder exoskeleton was positioned at the 0° pitch, yaw and roll orientation, as shown in Fig. 1. A 10° step perturbation was commanded along the shoulder plate pitch and yaw. The measured and input pitch and yaw angles were then compared against the commanded values to evaluate rise time of the 4B-SPM shoulder exoskeleton under these conditions. The rise time definition of 10% to 90% of its steady value was used. To ensure that the results are not position dependent, the test was repeated with the second shoulder position of 0° pitch, -45° yaw and 0° roll.

5.3 Results

The results of the shoulder plate tracking test using the shoulder plate given in Fig. 7A are shown in Fig. 8. The experiment showed average roll, pitch and yaw errors during motion of 1.12°, 1.15° and 1.56°, respectively. The standard deviation of the roll pitch and yaw angles were 0.75°, 0.53° and 1.19°, respectively. Similarly, the results of the shoulder plate tracking test using the shoulder plate given in Fig. 7C are shown in Fig. 9. This second test showed average roll, pitch and yaw errors during motion of 1.18°, 1.23° and 1.81°, respectively. The standard deviation of the roll pitch and yaw angles were 0.77°, 0.85° and 1.72°, respectively.

Some Euler Angle errors were expected for the shoulder plate tracking experiment, since the manufacturing and assembly of the device was done by hand with limited tooling. Most likely this error is due to misalignment of the substructures, which results in the three roll axes to not intersect preciously at a single point. This causes the shoulder plate to rotate about an ellipsoid instead of a perfect sphere. Another cause of potential error is part tolerance. Many of the components were machined or 3D printed in house, which could contribute to a buildup of position errors. Proper CNC components with high tolerance could likely resolve any errors in position. How-

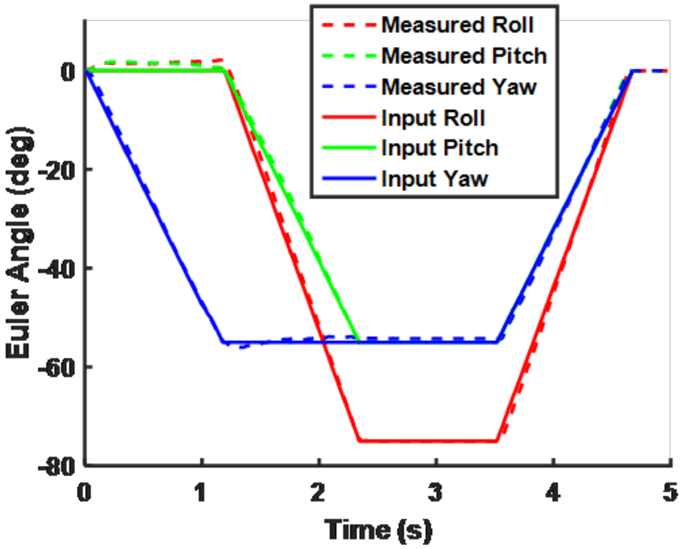

Figure 5.8: Euler angles of the 4B-SPM shoulder plate shown in Fig. 7A as it moves throughout the workspace.

ever, this is why it is important to use a 3D motion capture system to measure the shoulder plate position during neuromuscular property characterization studies, since a high degree of accuracy is required to perform these tests. The motion capture system reports high Euler Angle accuracy, regardless of prototype position errors or deflection that may be cause by physical human-robot interaction.

The results of the step response tracking experiment for the 4B-SPM in a 0° pitch, yaw and roll orientation are shown in Fig. 10. The experiment showed a rise time of ∼70 ms to a ∼10° step displacement along both pitch and yaw. To confirm that these results are not position depended, the second shoulder position of 0° pitch, -45° yaw and 0° roll was tested. These results are shown in Fig. 11. Slight variations in the step response amplitude along different directions are observed. This can be explained by the results of the first experiment. The rise times are consistent across all four step responses.

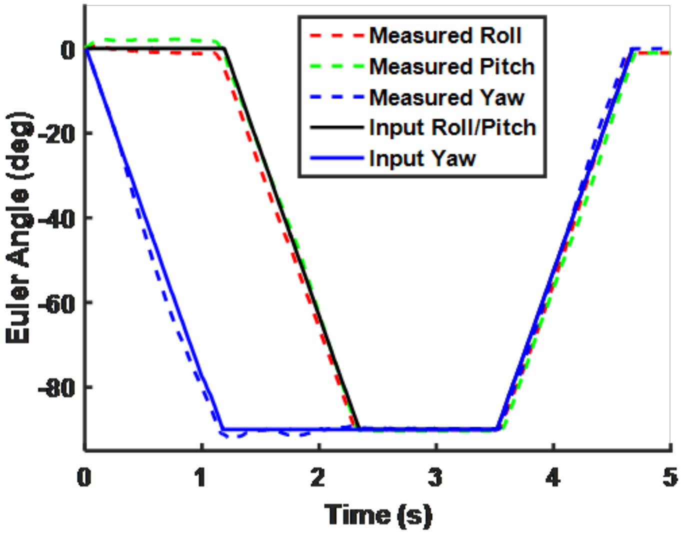

Figure 5.9: Euler angles of the 4B-SPM shoulder plate shown in Fig. 7C as it moves throughout the workspace.

5.4 Discussion

The development of the low inertia 4B-SPM shoulder exoskeleton was motivated by the need for a highly responsive device that could be used to characterize the neuromuscular properties of the shoulder during static posture and dynamic movement. This includes the ability to quantify the intrinsic and reflexive responses of the shoulder. In this work, a prototype 4B-SPM shoulder exoskeleton is presented for the first time. A video of its operation is shown, along with a complete description of its architecture, hardware and controls.

Two preliminary experiments were performed in this work. The first was to evaluate the device's performance by tracking its shoulder plate positional accuracy across a given workspace. This test was performed for two different shoulder plates to demonstrate that the workspace is dependent on the shoulder plate design. The results showed that the overall kinematic model used for the 4B-SPM exoskeleton is correct, though some minor errors due to part tolerances issues and substructure

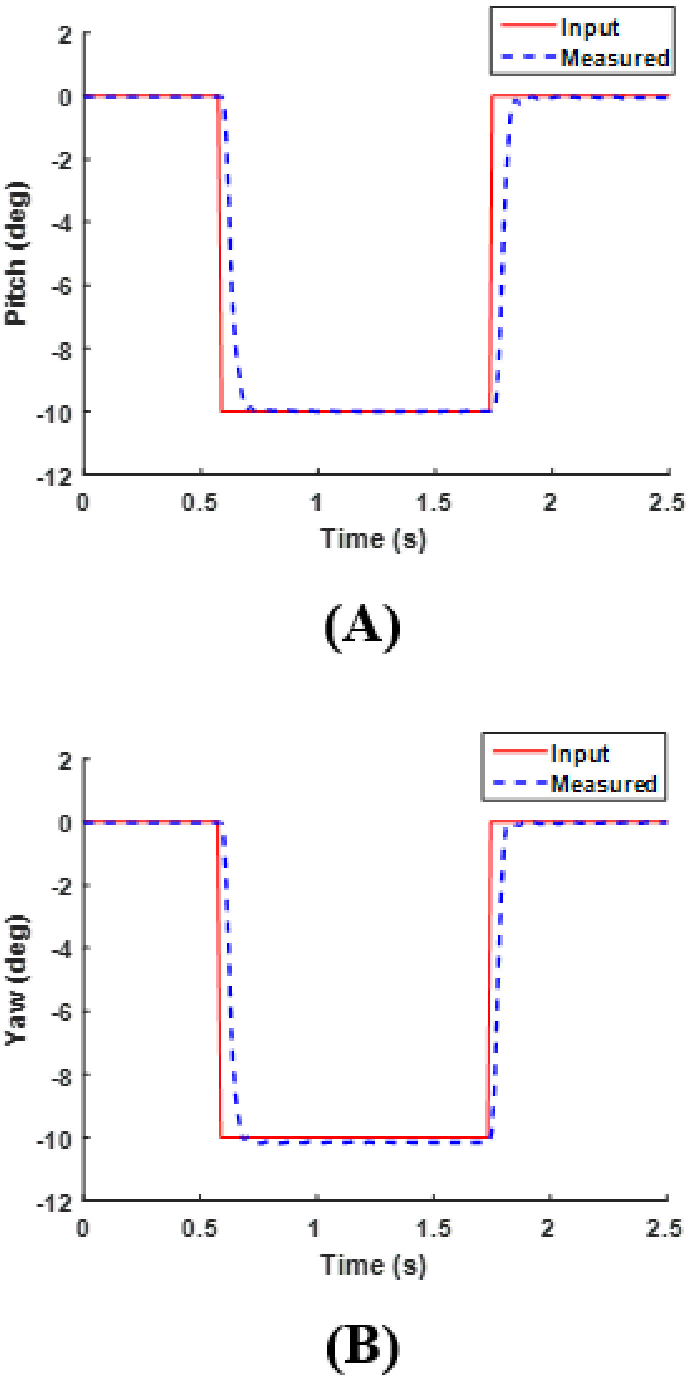

Figure 5.10: 4B-SPM shoulder exoskeleton response at shoulder position of 0° pitch, 0° yaw and 0° roll to: (A) 10° pitch angle step input, (B) 10° yaw angle step input

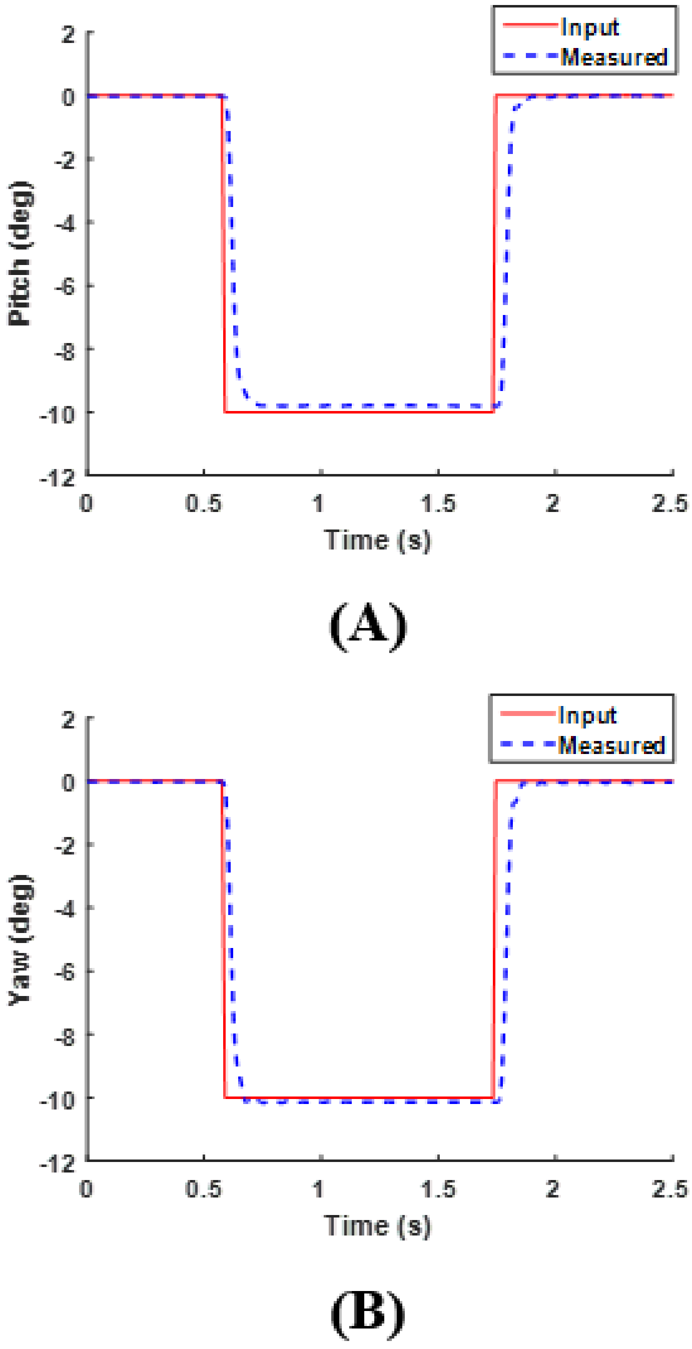

Figure 5.11: 4B-SPM shoulder exoskeleton response at the shoulder position of 0° pitch pitch, 45° pitch yaw and 0° pitch roll to: (A) 10° pitch pitch angle step input, (B) 10° pitch yaw angle step input.

misalignment were identified. This means for upper limb studies requiring less than 1° Euler angle accuracy of the shoulder, the 4B-SPM shoulder exoskeleton's onboard encoders should not be solely relied on for position feedback. Instead, an off-board 3D position tracking system should be used in conjunction with on-board feedback. Precise machining and assembly of the 4B-SPM exoskeleton would eliminate the need for a secondary feedback mechanism. Ultimately though, for the purposes of characterizing the neuromuscular properties of the shoulder, using a secondary source of feedback is not an issue.

The second experiment performed was a test of the 4B-SPM response to a step input. The experiment benchmarked the device's ability to perturb ~10° in ~70 ms. This exceeds the initial target speed of 100°/s, which would suggest that 4B-SPM response time should be sufficient for many types of dynamic upper limb studies.

Most shoulder exoskeletons do not report response time to a step input, possibly because most are not designed for rapid perturbations. Therefore, a direct comparison between the 4B-SPM performance and that of current state-of-the-art shoulder exoskeletons is not easily made. However, it should be noted that the motors used for the 4B-SPM were relatively small compared to most shoulder exoskeletons, yet the target of >100°/s speed was still achieved. This suggests that the end effector speed of the 4B-SPM shoulder exoskeleton could greatly exceed that of a serial actuated shoulder exoskeleton for matched motor specifications.

In conclusion of this work, the 4B-SPM shoulder exoskeleton presented shows promising potential to be a useful tool for the characterization of neuromuscular shoulder properties. From this work, a comprehensive study to map the mechanical impedance of the shoulder workspace for both static posture and dynamic movement is to follow.

Chapter 6

OPTIMIZING THE RIGID OR COMPLIANT BEHAVIOR OF A NOVEL PARALLEL-ACTUATED ARCHITECTURE FOR EXOSKELETON ROBOT APPLICATIONS

6.1 Introduction

In the field of exoskeleton robotics, parallel actuation can offer many advantages over more commonly used serial actuation. Despite having complex kinematics and a typically small workspace, parallel actuation has numerous useful properties including low end-effector inertia, high acceleration, high position accuracy, and the potential for high stiffness (Merlet, 2012; Taghirad, 2013; Li and Bone, 2001). Furthermore, certain types of parallel architectures, such as the 3-SPS (spherical-prismatic-spherical) (Alici and Shirinzadeh, 2004), 3-RRR (revolute- revolute-revolute) (Wu *et al.*, 2011) and 3-UPU (universal-prismatic-universal) (Di Gregorio, 2003), can operate without occupying the center of rotation, which is particularly useful when interfacing with multiple degrees-of-freedom (DoF) biological joints such as the ankle, hip, shoulder and wrist. Parallel actuation has been utilized for a number of exoskeleton applications. These include devices for the wrist, ankle, hip and shoulder. The wrist exoskeleton RiceWrist (Gupta *et al.*, 2008), uses a 3-RPS (revolute-prismatic-spherical) architecture with an additional serial revolute joint to generate 4-DoF. These DoF include the rotation of the forearm, wrist height and 2-DoF in rotation of the end-effector platform. Since the introduction of the RiceWrist, several other exoskeleton research prototypes have adopted the 3-RPS architecture (Fan and Yin, 2009; Nurahmi *et al.*, 2017). The ankle exoskeleton Anklebot (Roy *et al.*, 2009) uses a

2-SPS-1S (spherical-prismatic-spherical, spherical) manipulator in conjunction with the ankle joint to achieve semi-spherical motion. The shoulder exoskeleton BONES (Klein *et al.*, 2010) uses a RRPS (revolute-revolute-prismatic-spherical) manipulator to achieve spherical motion. Because all of these architectures, along with the previously mentioned 3-SPS, 3-RRR and 3-UPU, generate spherical motion through parallel actuation, they can further be categorized as spherical parallel manipulators Spherical parallel manipulators (SPMs) are the most popular choice for exoskeleton applications, primarily because they offer a greater workspace than parallel architectures with a high degree of actuation, like the Stewart-Gough Platform (Stewart, 1965). This is a result of SPMs typically having two to three actuated substructures instead of the four, five or six of typical of higher DoF parallel manipulators. This means that SPMs have less mechanical interference between substructures. However, fewer active DoF also means that SPMs typically have lower stiffness performance than higher active DoF parallel manipulators (Walter *et al.*, 2009; Gosselin and Angeles, 1989; Jiang and Gosselin, 2009). This can be problematic, particularly for augmentative exoskeleton systems that require high rigidity. In order to improve the workspace/stiffness tradeoff of SPMs, the authors introduced a new type of SPM architecture (Hunt *et al.*, 2017). The architecture utilizes a new design method that the authors refer to as modular motion coupling. The method involves coupling multiple DoF of each actuated substructure in order to maintain a high level of actuation while still maintaining a relatively low number of substructures. The authors developed a shoulder exoskeleton prototype that utilized this new architecture and performed a stiffness analysis on it (Hunt *et al.*, 2018). Many approaches to analyzing the stiffness of parallel manipulators have been proposed over the years. One popular method utilizes the Jacobian matrix to calculate the stiffness matrix (Gosselin, 1990). While this method provides a reasonable approximation of stiffness, it does not take into account linkage flexibility, which is critical for an accurate end-effector stiffness estimate. Another method utilizes strain energy to develop a model of stiffness (Yan *et al.*, 2016). While promising, this strain energy method is quite new and therefore less proven than other solutions. Additional methods include a lumped parameter approach (Pashkevich *et al.*, 2009) and a more traditional FEA approach (El-Khasawneh and Ferreira, 1999). After considering each of these, the authors opted for a different method that utilized matrix structural analysis techniques that have been used extensively in civil engineering and have been proven to provide accurate estimates of end-effector stiffness for parallel manipulators with both passive and active DoF and flexible linkages (Deblaise *et al.*, 2006). The results of the stiffness analysis identified some non-homogeneous stiffness behavior for certain end-effector orientations. This was determined to be a result of each substructure not having an actuated roll DoF. In addition, this SPM architecture was non-backdrivable, which limited its number of practical applications. Having identified these limitations, the authors developed a second-generation SPM that resolved these issues (Hunt and Lee, 2018, 2019). The second-generation SPM developed by the authors utilized a system of 4-bar (4B) mechanisms to rotate a mobile platform about a center point. The advantage of this new 4B-SPM design is that the 4-bar system achieves similar arc motion to the previous design while utilizing a far more simplistic construction and maintaining back-drivability. Furthermore, the 4B-SPM utilizes three additional motors to actuate the roll DoF of each substructure, eliminating the primary issues of the previous design mentioned above. An additional property of the 4B-SPM architecture is flexibility of actuator placement. The three substructures that comprise the device can be placed in any position about a center point. Placement is critical, as the stiffness of the 4B-SPM will be highly dependent on the configuration chosen. Therefore, a stiffness model with substructure placement as an input and end effector stiffness as an output would be useful for achieving desired dynamic behavior. Several examples of this include:

1. Maximizing stiffness for applications such as lifting or crush protection.
2. Maximizing compliance for applications requiring a high degree of unpredictable human-robot interaction or collision protection.
3. Designing custom non-homogeneous stiffness ellipsoids for applications that may require non-homogeneous dynamic behavior.

With a stiffness model, the 4B-SPM could have widespread application for exoskeleton devices, as it has been shown to (1) interface well the shoulder, hip, wrist and ankle, (2) not require any complex mechanical components, (3) have very flexible actuator placement, and (4) not require the human joint for a singular kinematic solution (Hunt and Lee, 2018). For this reason, a 4B-SPM stiffness model is developed and presented in this work. It should be noted that, as previously mentioned, the authors have developed stiffness models for past parallel architectures. However, the ability of the 4B-SPM to interface well with different biological joints, along with its economic design, makes it a major improvement over past parallel architectures development by the authors. Therefore, a separate stiffness analysis of this architecture is justified as it would offer other researchers and members of the robotics community a complete and flexible parallel actuated solution that could be customized to fit many different exoskeleton design requirements. The rest of this paper presents the steps taken to optimize the rigid or compliant behavior of the 4B-SPM for a given workspace. The sections are organized as follows: Section II includes (1) a brief overview of the of the 4B-SPM architecture, (2) the model used to characterize stiffness, (3) the experimental setup to validate the stiffness model, and (4) the optimization techniques used to maximize the rigid, compliant or nonhomogeneous stiffness behavior of the 4B-SPM. Section III details (1) the results of the stiffness model validation experiment and (2) the optimal actuator placement for maximum rigid, compliant or nonhomogeneous stiffness behavior. Finally, Section IV concludes the paper with a discussion and summary of the contribution.

6.2 Methods

6.2.1 A. 4B-SPM Design Overview

The previously developed 4B-SPM architecture is presented in Fig. 1 (Hunt and Lee, 2018). The 4B-SPM uses three parallelogram 4-bar substructures. Each substructure has two actuated DoF: pitch and roll. The roll DoF axis of each substructure intersects with the others at a singular point which represents the virtual center of a spherical workspace. The top linkage in each 4-bar substructure is extended to reach a mobile platform that moves tangential to the spherical workspace. Each top linkage is coupled to the mobile platform using a spherical joint. Shown in Fig. 2 are four different embodiments of the 4B-SPM architecture that the authors have developed kinematic models for (Hunt and Lee, 2018). In preparation for the dynamic analysis performed in this work, the authors developed a shoulder exoskeleton prototype of the 4B-SPM architecture (Hunt and Lee, 2019). This prototype is shown in Fig. 3. A video of the shoulder exoskeleton is included as an attachment to this work.

6.2.2 B. 4B-SPM Stiffness Model

For the purpose of determining end effector stiffness of the 4B-SPM for different substructure configurations, an analytical model was created. The model is based off of a matrix structural analysis method commonly used for calculating stiffness

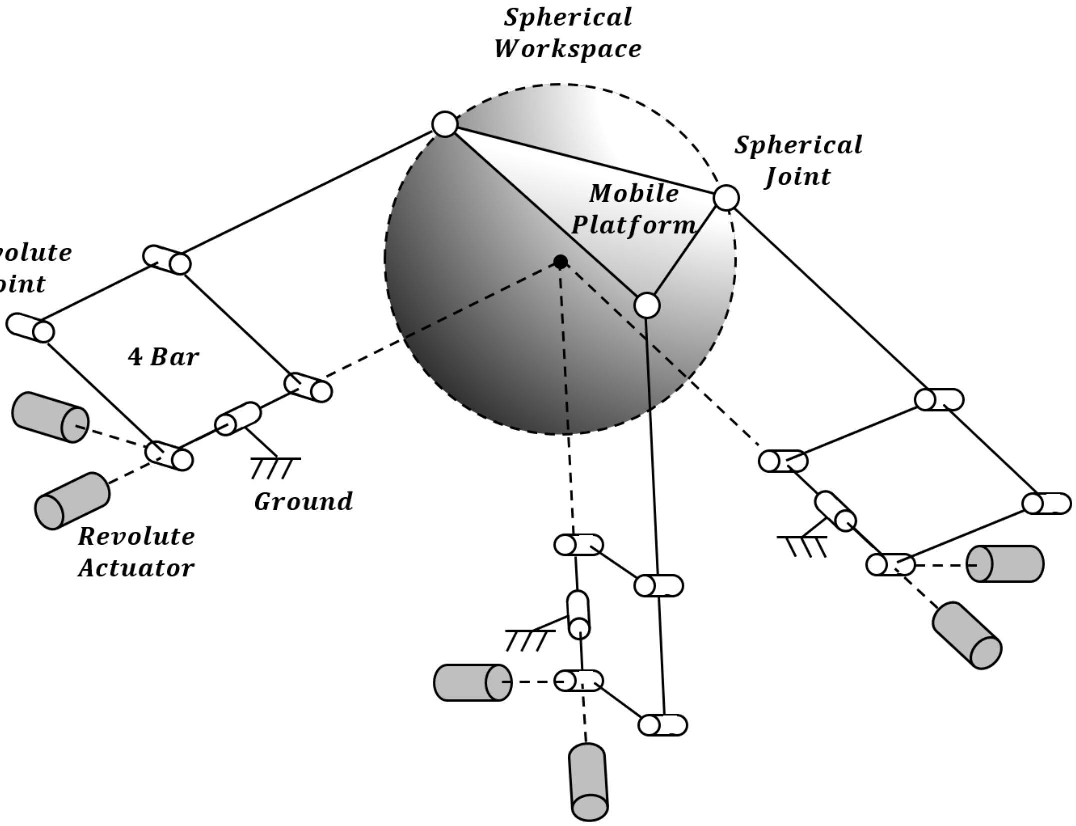

Figure 6.1: 4-Bar Spherical Parallel Manipulator (4B-SPM) architecture. The 4B-SPM uses three parallelogram 4-bar substructures. Each substructure has two actuated DoF: pitch and roll. The roll DoF axis of each substructure intersects with the others at a singular point which represents the virtual center of a spherical workspace. The top linkage in each 4-bar substructure is extended to reach a mobile platform that moves tangential to the spherical workspace. Each top linkage is coupled to the mobile platform using a spherical joint.

of complex truss networks typically found in bridges. The concept of applying this method to parallel manipulators was first introduced by Dominique Deblaise (Deblaise *et al.*, 2006). For brevity, the reader will be referred back to Deblaises prior work for some of the more derivative or expansive steps required in the development of this model. With the model, it is possible to generate the end effector rotational stiffness ellipsoids that will govern how the 4B-SPM responds to externally applied torques. To start, each actuated substructure k (k=1,2,3) is represented by a nodal system that corresponds to characteristic points. Shown in Fig. 4 are the node locations

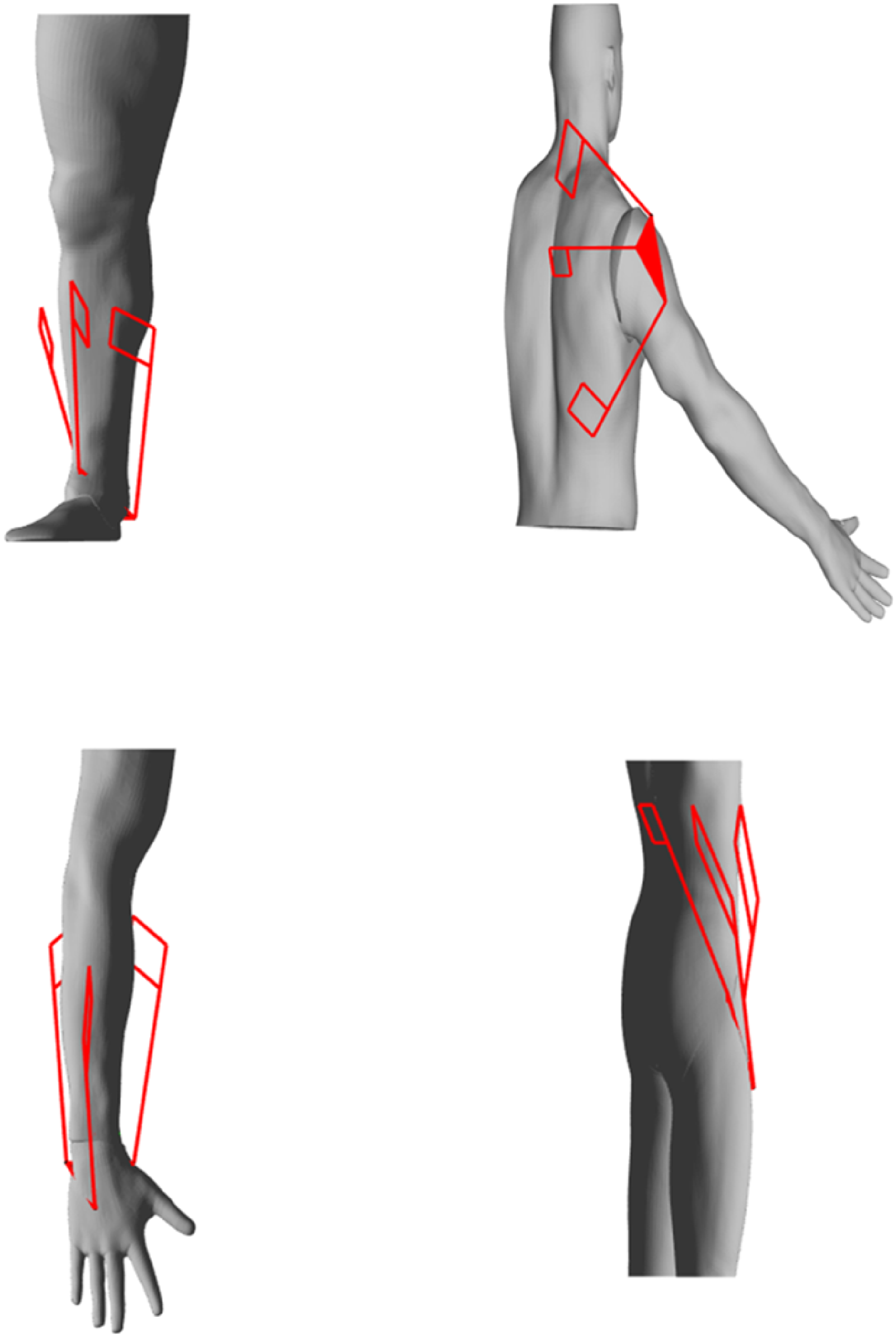

Figure 6.2: Four embodiments of the 4B-SPM architecture for which the authors have solved the kinematics for include: ankle, shoulder, wrist and hip exoskeletons.

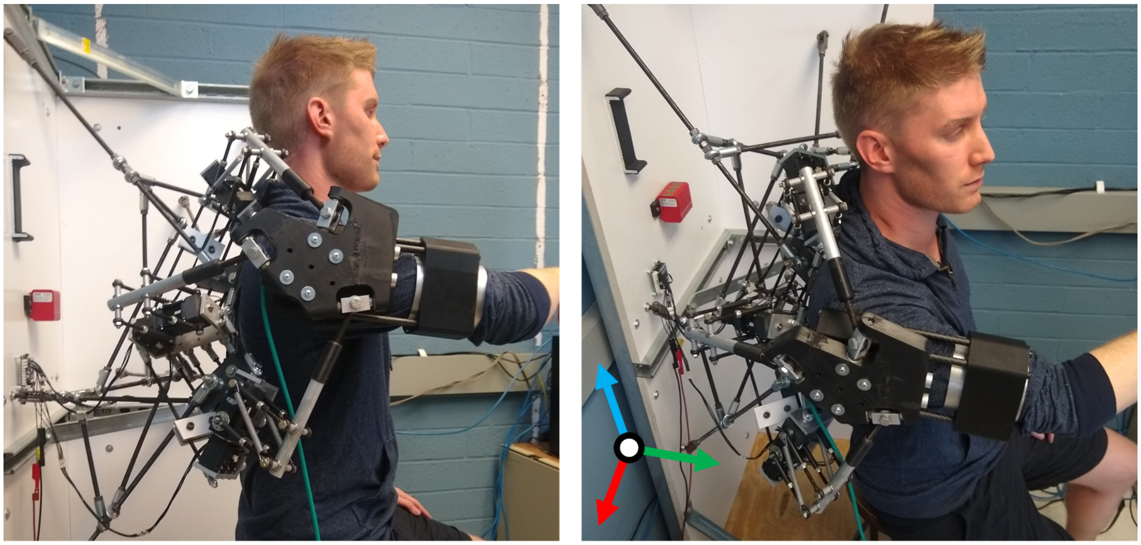

Figure 6.3: 4B-SPM shoulder exoskeleton prototype mounted to a stationary platform with a human subject in the seated position. The subject is coupled to the device through the use of an upper arm cuff. To maintain good contact between the subject and device, a blood pressure cuff is used at the contact point. The pitch, roll and yaw axes are represented by the orthogonal red, green and blue axes, respectively.

for each substructure. It should be noted that a simplification has been made to the nodal diagram with regards to the 4-bar mechanism. In the prototype shown in Fig. 3, there are actually four parallel vertical bars connecting the top and bottom linkage of the 4-bar mechanism, whereas the nodal diagram shown in Fig. 4 reduces this down to two. This is done to simplify the analysis and is justified by the fact that only one of the four parallel vertical bars is actually connected to the servo motor and therefore grounded, similar to Fig. 4. Thus, pitch and roll stiffness of the substructure will not be affected by this simplification. The yaw may be slightly affected, although it is not considered to be of the same contributing magnitude to the overall stiffness model as pitch and roll. Nevertheless, to mitigate this error, the authors make an adjustment to the geometric properties of the two vertical bars within the model to more accurately reflect the actual prototype.

The nodes shown in Fig. 4 are coupled by either a flexible beam or passive revolute joint. Each beam n is fixed at its ends by one or two nodes, depending on if the beam

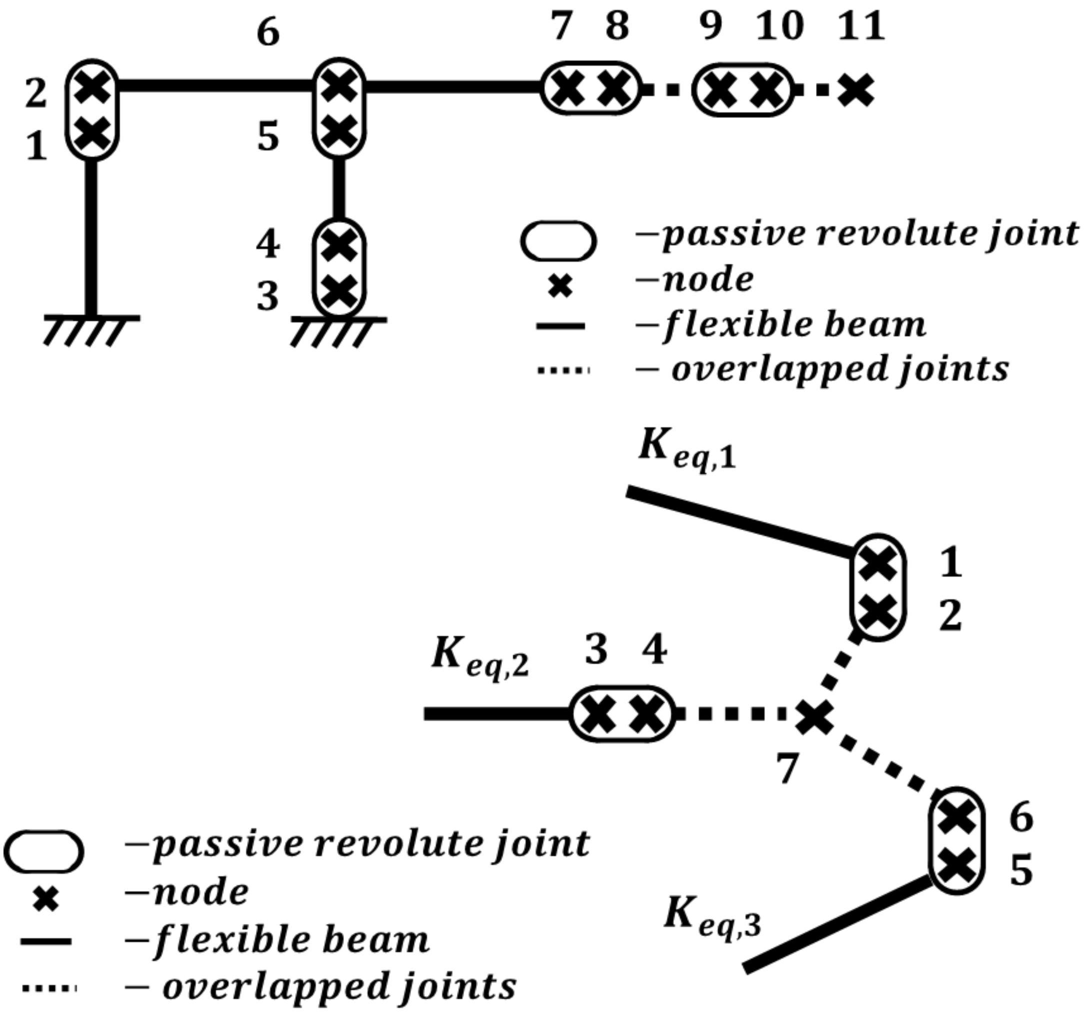

Figure 6.4: (Top) 4-bar substructure equivalent nodal diagram, (Bottom) shoulder plate end effector equivalent nodal diagram.

is considered rigidly fixed at one end. Therefore, each beam is represented by either a 6x6 or the 12x12 beam stiffness matrix $\boldsymbol{K}_{n,k}$ as defined in EulerBernoulli beam theory. Each of these beam stiffness matrices must be oriented through multiplication of matrix $\boldsymbol{P}_{n,k}$ comprised of rotational submatrices $\boldsymbol{R}_{n,k}$ along its diagonal. The rotated beam stiffness matrix $\boldsymbol{K'}_{n,k}$ can be expressed as:

$$\boldsymbol{K'}_{n,k} = \boldsymbol{P}_{n,k}{}^{-1}\boldsymbol{K}_{n,k}\boldsymbol{P}_{n,k} \tag{6.1}$$

Where rotation matrix $\boldsymbol{P}_{n,k}$ can be determined by:

$$\text{where } \boldsymbol{P}_{n,k} = \begin{bmatrix} \boldsymbol{R}_{n,k} & 0 & \cdots \\ 0 & \boldsymbol{R}_{n,k} & \cdots \\ \vdots & \vdots & \ddots \end{bmatrix}$$

The n number of rotated beam stiffness matrices $\boldsymbol{K'}_{n,k}$ can then be assemble into a singular substructure stiffness matrix $\boldsymbol{K}_{T,k}$. This assembly can be done using recognized stiffness matrix assembly methods (Hughes, 2012). The substructure stiffness matrix $\boldsymbol{K}_{T,k}$ represents substructure stiffness before the addition of passive joints shown in Fig. 4. Each passive joint will be defined by a kinematic relationship matrix $\boldsymbol{A}_{n,k}$, which can be expressed as:

$$\boldsymbol{A}_{n,k} = \begin{bmatrix} \boldsymbol{I}_{3x3} & \mathbf{0}_{3x3} \\ \mathbf{0}_{2x3} & V_{n,k} \end{bmatrix} \tag{6.2}$$

Where $r_{n,k}$ is comprised of the rotation matrix vectors orthogonal to the rotation axis unit vector of the passive joint. One of these rotation matrix vectors should also be parallel to the adjacent beam. The $\boldsymbol{A}_{n,k}$ matrices can then be assembled into a singular substructure kinematic matrix $\boldsymbol{A}_{T,k}$, similar to$\boldsymbol{K}_{T,k}$. The kinematically adjusted substructure stiffness matrix, with the inclusion of passive joints, is derived using the minimum total potential energy principle (Deblaise *et al.*, 2006). It can be expressed as:

$$\boldsymbol{K}_{G,k} = \begin{bmatrix} \boldsymbol{K}_{T,k} & \boldsymbol{A}_{T,k}{}^{T} \\ \boldsymbol{A}_{T,k} & \mathbf{0} \end{bmatrix} \tag{6.3}$$

At this point, it is necessary to permutate $\boldsymbol{K}_{G,k}$ in order to move the last node submatrix to the end of the $\boldsymbol{K}_{G,k}$ so that it can be redefined as the endpoint substructure stiffness matrix $\boldsymbol{K}_{eq,k}$. In order to determine the global stiffness of the

4B-SPM architecture, the substructure end point stiffness matrices $\boldsymbol{K}_{eq,k=1,2,3}$ must be assembled to the end effector node 7 shown in Fig 4. The shoulder plate that connects $\boldsymbol{K}_{eq,k=1,2,3}$ is considered rigid and therefore cannot be modelled using EulerBernoulli beam theory. Instead, it will be modeled as series of rigid beams with infinite stiffness. This rigid beam model will be defined by the kinematic relationship matrix $\boldsymbol{B}_n$, which can be expressed as:

$$\boldsymbol{B}_n = \begin{bmatrix} \boldsymbol{0}_{3x3} & \boldsymbol{I}_{3x3} \\ \boldsymbol{I}_{3x3} & \widehat{\boldsymbol{L}}_{W_n} \end{bmatrix} \tag{6.4}$$

Where $\widehat{\boldsymbol{L}}_{W_n}$ is the symmetric skew matrix defined by the rigid beam direction vector $W_n = [L_x \ L_y \ L_z]_n{}^T$. With the kinematic relationship matrix $\boldsymbol{B}_n$ defined, the kinematic relation matrix $\boldsymbol{A}_T$ of the shoulder plate can be constructed in a similar manner to $\boldsymbol{A}_{T,k}$. The shoulder plate stiffness matrix $\boldsymbol{K}_T$. Can also be constructed in a similar to $\boldsymbol{K}_{T,k}$. The kinematically adjusted shoulder plate stiffness matrix, with the inclusion of passive joints and rigid beams, is once again derived using the minimum total potential energy principle:

$$\boldsymbol{K}_{eq,T} = \begin{bmatrix} \boldsymbol{K}_T & \boldsymbol{A}_T{}^T \\ \boldsymbol{A}_T & \boldsymbol{0} \end{bmatrix} \tag{6.5}$$

Similar to $\boldsymbol{K}_{G,k}$, it is necessary to permutate $\boldsymbol{K}_{eq,T}$ in order to move the last node submatrix to the end so that it can be redefined as the 6x6 end-effector stiffness matrix $\boldsymbol{K}_{ee}$, which represents the stiffness at node 7 in Fig. 4. The end-effector stiffness matrix $\boldsymbol{K}_{ee}$ can be visualized by plotting its translational and rotational stiffness ellipsoids. As defined in the work of Mussa-Ivaldi (Mussa-Ivaldi *et al.*, 1985), these ellipsoids are created by first decomposing $\boldsymbol{K}_{ee}$ into its symmetric $\boldsymbol{K}_s$ and an antisymmetric $\boldsymbol{K}_a$ component. Assume that $\boldsymbol{K}_{ee}$ is defined by the following four submatrices:

$$\boldsymbol{K}_{ee} = \begin{bmatrix} \boldsymbol{K}_{xx} & \boldsymbol{K}_{xy} \\ \boldsymbol{K}_{yx} & \boldsymbol{K}_{yy} \end{bmatrix} \tag{6.6}$$

Then $\boldsymbol{K}_s$ and $\boldsymbol{K}_a$ can be written as:

$$\boldsymbol{K}_s = \begin{bmatrix} \boldsymbol{K}_{xx} & \frac{\boldsymbol{K}_{xy}+\boldsymbol{K}_{yx}}{2} \\ \frac{\boldsymbol{K}_{yx}+\boldsymbol{K}_{xy}}{2} & \boldsymbol{K}_{yy} \end{bmatrix} \tag{6.7}$$

$$\boldsymbol{K}_a = \begin{bmatrix} 0 & \frac{\boldsymbol{K}_{xy}-\boldsymbol{K}_{yx}}{2} \\ \frac{\boldsymbol{K}_{yx}-\boldsymbol{K}_{xy}}{2} & 0 \end{bmatrix} \tag{6.8}$$

where $\boldsymbol{K}_{ee} = \boldsymbol{K}_s + \boldsymbol{K}_a$.The first three eigenvalues and eigenvectors of $\boldsymbol{K}_s$ represent the direction and magnitude of the three pairwise perpendicular axes of symmetry for the translational stiffness matrices. The last three correspond to the perpendicular axes of symmetry of the rotational stiffness ellipsoid.

6.2.3 C. 4B-SPM Stiffness Model

An experiment was performed to test the validity of the stiffness model through a comparison of the theoretical 4B-SPM stiffness to that of the prototype. The shoulder exoskeleton was oriented at 90 flexion and coupled to one end of a 6-axis force/torque sensor (Delta IP65, ATI, NC). To provide an accurate displacement of the load cell, a 7-DoF research robotic arm (LBR iiwa R820, KUKA, Germany) was connected to the other end of the sensor. This robot was chosen for its ability to perform these sensitive experiments. In addition to a rated payload that exceeds to forces exerted during these tests, the device has highly repeatable position control (0.015 mm), which is necessary for accurate stiffness estimates (KUKA, 015c). The 7-DoF robotic arm was in turn bolted to a steel structural support column. The experimental setup is shown in Fig. 5.

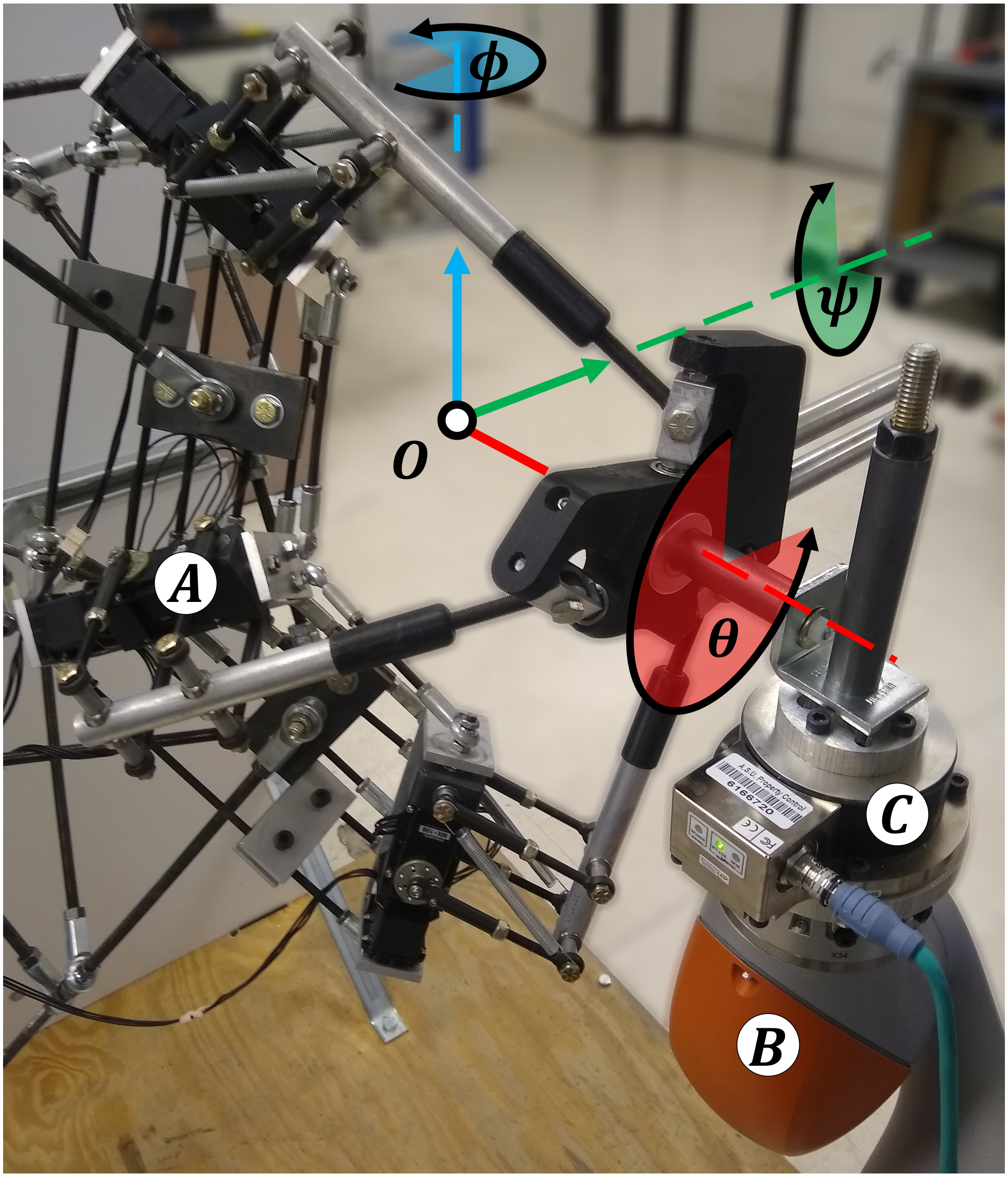

Figure 6.5: Experimental setup for evaluating the 4B-SPM prototype stiffness oriented at 90 flexion. (A) 4B-SPM Shoulder exoskeleton, (B) 7-DoF robotic arm (LBR iiwa R820, KUKA, Germany), (C) 6-axis load cell (Delta IP65, ATI, NC). The shoulder exoskeleton was mechanically coupled to the load cell, which was in turn coupled to the 7-DoF robotic arm. The roll, pitch and yaw angles of the shoulder exoskeleton about its center-of-rotation O are represented , and , respectively.

The roll (), pitch () and yaw () angles of the shoulder exoskeleton were perturbed 3 by the 7-DoF robotic arm. A sinusoidal perturbation profile commanded over 3000 ms was used. The corresponding forces were recorded by the 6-axis load cell at 1 kHz. All the collected measurements were filtered using a zero-phase 2nd order Butterworth filter with a 20 Hz cutoff frequency. With measurements of corresponding displacement and force F, it is possible to calculate the stiffness k of the prototype using $F = k$. Peak displacement and the corresponding force were used for calculating stiffness. It should be noted that the theoretical stiffness model is a function of the kinematic relationship matrix A_T and stiffness matrix K_T. These matrices are sensitive to change, so if it were incorrect, then significant differences from the theoretical stiffness model and prototype would be expected. For the simulation, all flexible beams were modeled as 1045 carbon steel, except for the top linkage that was modeled as 2024 aluminum. This is representative of the materials used for the prototype. All critical dimensions used in the simulation match those of the prototype. The only exception to this was the flexible beam connecting nodes 4 and 5 of the 4-bar mechanism shown in Fig. 4. For the reasons mentioned in the beginning of this Section, the cross-sectional area of this beam was doubled to more accurately reflect the duel beam design used in the prototype.

6.2.4 D. Stiffness Optimization

In order to maximize overall rigidity, compliance, or nonhomogeneous stiffness behavior for a given workspace, the placement of each substructure needs to be optimized. There are a couple of parameters applied to this optimization. First, solutions for each substructure location must be bounded to a practical region were mechanical interference between robot-robot and human-robot cannot occur. After considering the geometry of the human model shown in Fig. 4 and the approximate workspace of the human shoulder, the regions $[-0.3 < x_t < 0.1, -0.4 < y_t < 0,$ $0 < z_t < 0.3]$ m, $[-0.3 < x_m < 0.1,$ $-0.4 < y_m < 0,$ $-0.3 < z_m < 0.1]$ m, and $[-0.4 <$ $x_b < 0.1,$ $-0.4 < y_b < 0,$ $-0.4 < z_b < -0.2]$ m were selected for the top, middle and bottom substructure, respectively, As is convention, the coordinates x-y, y-z and z-x used here represent the transverse, sagittal and coronal planes, respectively . Second, in order to optimize the rigidity or compliance of the 4B-SPM, the stiffness ellipsoid volume equation $O = (43)k_a k_b$ was chosen as the objective function to maximize or minimize, here k_a, k_b and k_c are the orthogonal axes of the ellipsoid. These two parameters make the problem a bounded nonlinear multi-objective (roll, pitch and yaw axes) optimization problem. Because of the multiple parameters, a genetic algorithm was chosen as the optimization method for determining substructure placement. The genetic algorithm attempts to minimize the objective function, so in order to maximize rigidity and compliance, $O = -(43)k_a k_b k_c$ and $O = (43)k_a k_b k_c$ were used, respectively. For maximizing nonhomogeneous stiffness, the objective function $O = -(k_a - k_b - k_c)$ was used, which drives $k_a, k_b 0 and k_c 0$ as the objective function is minimized. In this case, maximizing k_a and minimizing k_b and k_c is the arbitrarily chosen nonhomogeneous behavior. Alternatively, k_b or k_c could also be maximized if desired. For executing the genetic algorithm, Matlabs Optimization Toolbox (Mathworks, MA, USA) was used. The genetic algorithm function (ga) was given the boundary conditions and objective functions stated, along with the stiffness model with shoulder plate orientation as an input and the stiffness ellipsoid as an output. The shoulder plate orientation was varied in 10 along the pitch and yaw Euler angles and bounded by the octant (+x, +y, -z). At each orientation, the genetic algorithm was executed and the optimal substructure mounting points were found. The approach generates a point cloud of best solutions for each substructure mounting location. The mean of these point clouds is taken as the generalized best solution.

6.3 Results

6.3.1 *A. Stiffness Model Testing*

A comparison of the theoretical and mean measured stiffness is shown in Fig. 6 for the shoulder plate orientated at 90 flexion. The mean error along roll-pitch-yaw is 11.8 percent with a standard deviation of 8.4. While error does exist, it should be noted that the size and shape of the theoretical model demonstrates a reasonable approximation of stiffness based on the global axis measurements taken.

Several causes for the error have been identified by the authors: (1) Imperfect intersection of the roll axes for the three substructures. This misalignment could produce increased resistance to applied torque that may contribute to differing stiffness results. This could be corrected with higher manufacturing tolerances. (2) Backlash in the servo motors. This could potentially cause play in the shoulder plate that could affect the stiffness measurements. It should be noted that efforts to minimize backlash were taken by applying minor tension of the three substructures against the shoulder plate equal to the measured backlash of the servos. This minimizes backlash without changing the kinematic solution. (3) Imperfect modeling of the prototypes geometric and material properties. Measurements taken from the prototype and materials utilized vary within tolerance. These tolerances are not accounted for by the theoretical model and are therefore a potential source for minor error. (4) Simplification 4-bar mechanism nodal diagram, as described in Section 2. B.

6.3.2 *B. Stiffness Optimization*

For the octant workspace bounded by the +x, +y, and -z axes defined in Fig. 7, the 4B-SPM substructure configurations to achieve optimal rigid, compliant and non-

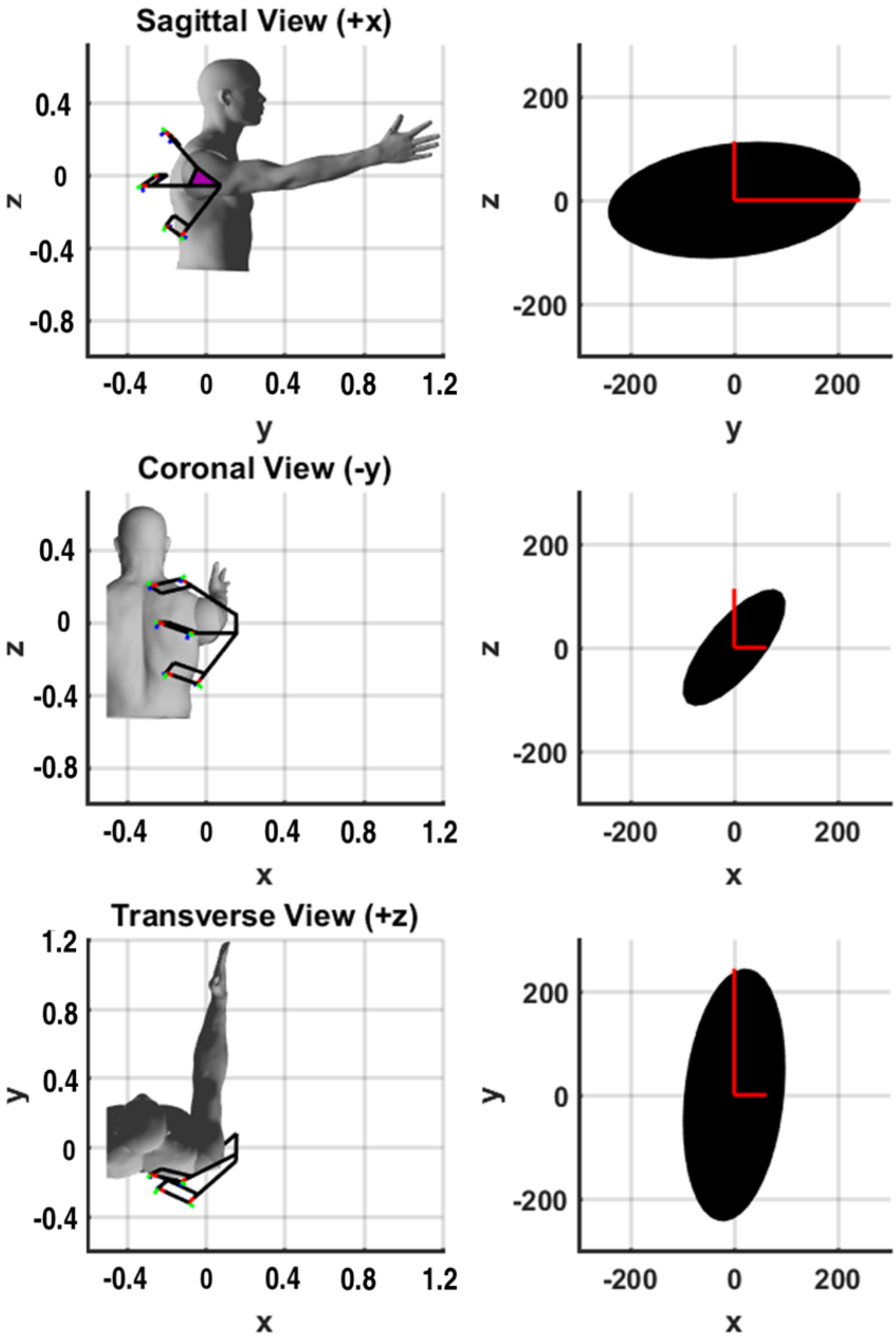

Figure 6.6: Orientation of the shoulder exoskeleton along with projections of the associated theoretical rotational stiffness ellipsoid (Nm/rad) shown in black. The roll, pitch and yaw stiffness measurements are shown in red for contrast. The origin of the frame is at the center-of-rotation of the human shoulder.

homogeneous stiffness behavior were found. The optimal configurations are shown in Fig. 7, along with a point cloud of best solutions for different shoulder plate orientations. These solutions were found at 10 increments along the pitch and yaw Euler angles. The optimal substructure configuration for each result is taken to be the mean location of each substructure point cloud. For optimal rigidity, the virtual center of each point cloud for the top, middle and bottom substructure, respectively, are $A_t = [-0.23,\ -0.16, 0.27]T$ m, $A_m = [-0.27,\ -0.21, 0.02]$ m and $A_b = [-0.21,$ $-0.12, -0.31]T$ m. For optimal compliance, the virtual center of each point cloud for the top, middle and bottom substructure, respectively, are $A_t = [-0.25,\ -0.16, 0.11]T$ m, $A_m = [-0.29,\ -0.23, 0.01]T$ m and $A_b = [-0.28,\ -0.14, -0.24]T$ m. For the optimal nonhomogeneous stiffness behavior, the virtual center of each point cloud for the top, middle and bottom substructure, respectively, are $A_t = [-0.29, -0.24, 0.29]T$ m, $A_m = [-0.29, -0.24, -0.10]T$ m and $A_b = [-0.21, -0.14, -0.26]T$ m. The generalized rotational stiffness ellipsoid that represents the average stiffness across the entire workspace for each solution is shown in Fig. 7 as well. Included with them is the standard deviation for each solution.

The results shown in Fig. 7 help identify a few interesting characteristics of the 4B-SPM. Firstly, a comparison between maximum rigidity and compliance suggests that stiffness is largely dependent on the distances between substructures mounts. This is somewhat intuitive, although the extent of dependency was not clear until now. Another interesting feature identified by these findings is how the rigid and compliant results show fairly symmetric solutions corresponding to relatively homogeneous stiffness ellipsoids. In contrast, the nonhomogeneous stiffness results shown in Fig. 7C correspond to a highly nonsymmetrical substructure mounting point solution. These observations would suggest that symmetry of the 4B-SPM affects its degree of homogeneous stiffness behavior. The results shown in Fig. 7 also provide

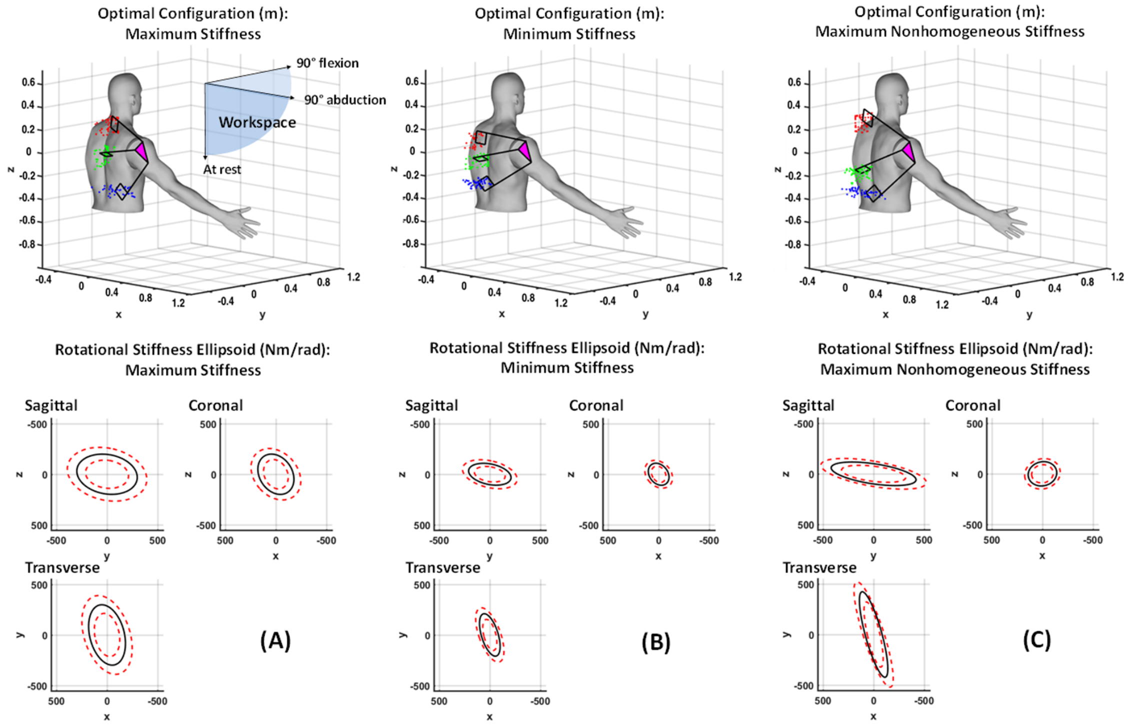

Figure 6.7: (A) Shown at top is the generalized maximum stiffness configuration for the 4B-SPM substructures along with point clouds of the best solutions found throughout the workspace. Shown at bottom are projections of the generalized maximum stiffness ellipsoid. (B) Shown at top is the generalized minimum stiffness configuration for the 4B-SPM substructures along with point clouds of the best solutions found throughout the workspace. Shown at bottom are projections of the generalized minimum stiffness ellipsoid. (C) Shown at top is the generalized maximum desired nonhomogeneous stiffness configuration for the 4B-SPM substructures along with point clouds of the best solutions found throughout the workspace. Shown at bottom are projections of the generalized maximum nonhomogeneous stiffness ellipsoid. For all three figures, the origin of each frame is at the center-of-rotation of the human shoulder.

the opportunity to compare the stiffness of this new 4B-SPM architecture to that of the previous motion-coupled SPM architecture developed by the authors for similar purposes and discussed in the Introduction. In prior work the authors analyzed the rotational stiffness of this motion-coupled design across the same workspace used in this paper for the 4B-SPM (Hunt *et al.*, 2018). For a maximum stiffness configuration, the motion-coupled design had a mean stiffness ellipsoid volume of $6.2210^6 (Nmrad)^3$. In comparison, the 4B-SPM has a mean stiffness ellipsoid volume of $3.2410^7 (Nmrad)^3$

for the maximum stiffness configuration. This increase in stiffness is likely due to (1) the addition of the three revolute actuators that control the roll of each 4B-SPM substructure and (2) the simplified 4-bar design that possess fewer failure modes. Other factors, such as part materials and geometry may also contribute to the increased stiffness.

6.4 Discussion

The work performed for this paper was motivated by the need for exoskeleton architectures that are capable of matching the workspace of a user while exhibiting desired stiffness characteristics. Because of limitations in the stiffness or workspace of typical serial and parallel actuated architectures, the authors developed the new 4B-SPM architecture in prior work that was specifically designed for exoskeleton applications involving complex biological joints like the shoulder, hip, wrist and ankle. Demonstrated in the form of a shoulder exoskeleton, the authors performed a dynamic analysis on the 4B-SPM in order to help validate the derived stiffness model. The model was then used to optimize the 4B-SPM configuration in order to achieve rigid, compliant and nonhomogeneous stiffness behavior. The results of this paper detail a theoretical stiffness model for the 4B-SPM presented, along with an experiment to validate the model. An error between the prototype stiffness and theoretical stiffness of 11.8 percent with a standard deviation of 8.4 was reported. Despite some error, the model still proved to be a reasonable approximation of stiffness. Possible causes for the error are discussed in Section 3. A. The stiffness model was used in conjunction with a bounded nonlinear multi-objective optimization method in order determine the optimal placement of the three actuated substructures to achieve certain dynamic behavior within a given workspace. The workspace was chosen to be one octant of a sphere defined by the three arm orientations: 90 flexion, 90 abduction, and at rest.

For this workspace, the actuator placements for optimal rigid, compliant and certain nonhomogeneous stiffness behavior were demonstrated. The main contribution of this work is providing researchers and members of the robotics community who chose to use the 4B-SPM architecture a means of adjusting its dynamic performance to fit many different exoskeleton applications. To reiterate, there are many reasons to use the 4B-SPM, the primary ones being: (1) interfaces well the shoulder, hip, wrist and ankle; (2) does not require any complex mechanical components; (3) has very flexible actuator placement; and (4) does not require the human joint for a singular kinematic solution. With the addition of the presented stiffness model, future wearable 4B-SPM devices could be optimized for a variety of tasks and applications, such as lifting, jumping, running, crush protection and impact absorption.

Chapter 7

VALIDATING THE 4B-SPM SHOULDER EXOSKELETON FOR CHARACTERIZATION OF NEUROMUSCULAR PROPERTIES

7.1 Introduction

The human shoulder plays an integral role in upper limb motor function. As the basis of arm motion, its performance is vital to the accomplishment of daily tasks. Impaired motor control, as a result of stroke or other disease, can cause errors in shoulder position to accumulate and propagate to the entire arm. This is why it is a highlight of concern for clinicians and why it is an important point of study. One of the primary causes of impaired shoulder motor control is abnormal mechanical joint impedance, which can be modeled as a 2nd order system consisting of mass, spring and damper. Quantifying shoulder stiffness and damping between healthy and impaired subjects could help improve our collective understanding of how many different neuromuscular diseases impact arm performance. This improved understanding could even lead to better rehabilitation protocols for conditions such as stroke through better identification and targeting of damping dependent spasticity and stiffness dependent hypertonicity. Despite its importance, there is a fundamental knowledge gap in the understanding of shoulder impedance, mainly due to a lack of appropriate characterization tools.

Perhaps the most prominent studies that examine shoulder impedance are performed using a single axis servo that attaches to the human arm and can be manually re-positioned to allow for perturbations in either pitch or yaw (Lipps *et al.*, 2015, 2020). While the pioneering research has helped lay the groundwork for shoulder impedance studies, it has limitations inherent to the hardware setup. First, the device has limited work-space, which makes it difficult to test a variety of postures. Second, It does not allow for multi-dimensional (i.e. off-axis) perturbations without changing the entire device's setup. These multidimensional perturbations are necessary to develop a more complete picture of shoulder impedance. Finally, the limited active DoF of the device makes characterization during dynamic movement difficult. Given these limitations, the Authors sought to develop a more flexible robotic solution for shoulder impedance characterization, the result of which is the 4B-SPM shoulder exoskeleton described in Chapters 4-6.

In order to characterize human shoulder mechanical impedance using the 4B-SPM exoskeleton, the device must first be validated. To do this, a set of experiments were performed on the exoskeleton using a shoulder mock-up. These experiments consisted of first attaching different masses and springs with known inertia and stiffness to the mock-up. The mock-up was then perturbed by the exoskeleton while the resultant interaction forces and torques between the exoskeleton and mock-up were measured, along with the position of the mock-up. From these measurements, it is possible to estimate the inertia and stiffness of the attached masses and springs by using a 2nd order system model. In addition to validating the exoskeleton by characterizing masses and springs with known properties, a preliminary human test was performed to show the devices ability to be used by human subjects without issue while collecting all necessary data for impedance estimates.

The rest of this paper describes the efforts made to validate the shoulder exoskeleton for human impedance studies, along with some preliminary results from human testing.The sections are organized as follows: Section II includes (1) hardware setup, (2) inertia and stiffness estimations, (3) mock-up tests, (4) human tests. Section III details (1) the results of the mock-up tests and (2) the results of the human tests.

Finally, Section IV concludes the paper with a discussion and summary of the contribution.

7.2 Methods

7.2.1 Validation Testing: Hardware Setup

A mock-up of the human shoulder was constructed using a piece of 6 mm threaded steel rod attached to a steel tie-rod joint. The tie rod joint was attached at the center-of-rotation of the exoskeleton shoulder using a steel mounting fixture. This point is also the theoretical center-of-rotation of the human operator. The thread rod was secured within the upper arm cuff of the exoskeleton using a fitted wooden block. To test different inertia and stiffness properties, a set of calibrated masses and springs were used. The masses were attached by sliding them over the threaded rod and securing them with nuts and washers. The springs were attached at one end to the mock-up using copper cable. The other end of the springs were fixed to a point on the ceiling or wall using copper cable, such that the springs act orthogonal to the mock-up at the initial position prior to perturbations. This setup is exemplified in Fig. 1-3.

The position of both the exoskeleton and mock-up are tracked using three Bonita 10 (Vicon, Denver USA) IR motion capture cameras operating at 250 Hz and positioned throughout the testing space. The cameras track three markers attached on the exoskeleton and three markers on the mock-up. Each set of three markers allows a rotation matrix to be constructed the represents the orientation of the attached object. The Euler angles used to track the pitch and yaw of mock-up can be deconstructed from its rotation matrix. These angles, along with torque inputs, are used to estimate inertia and stiffness.

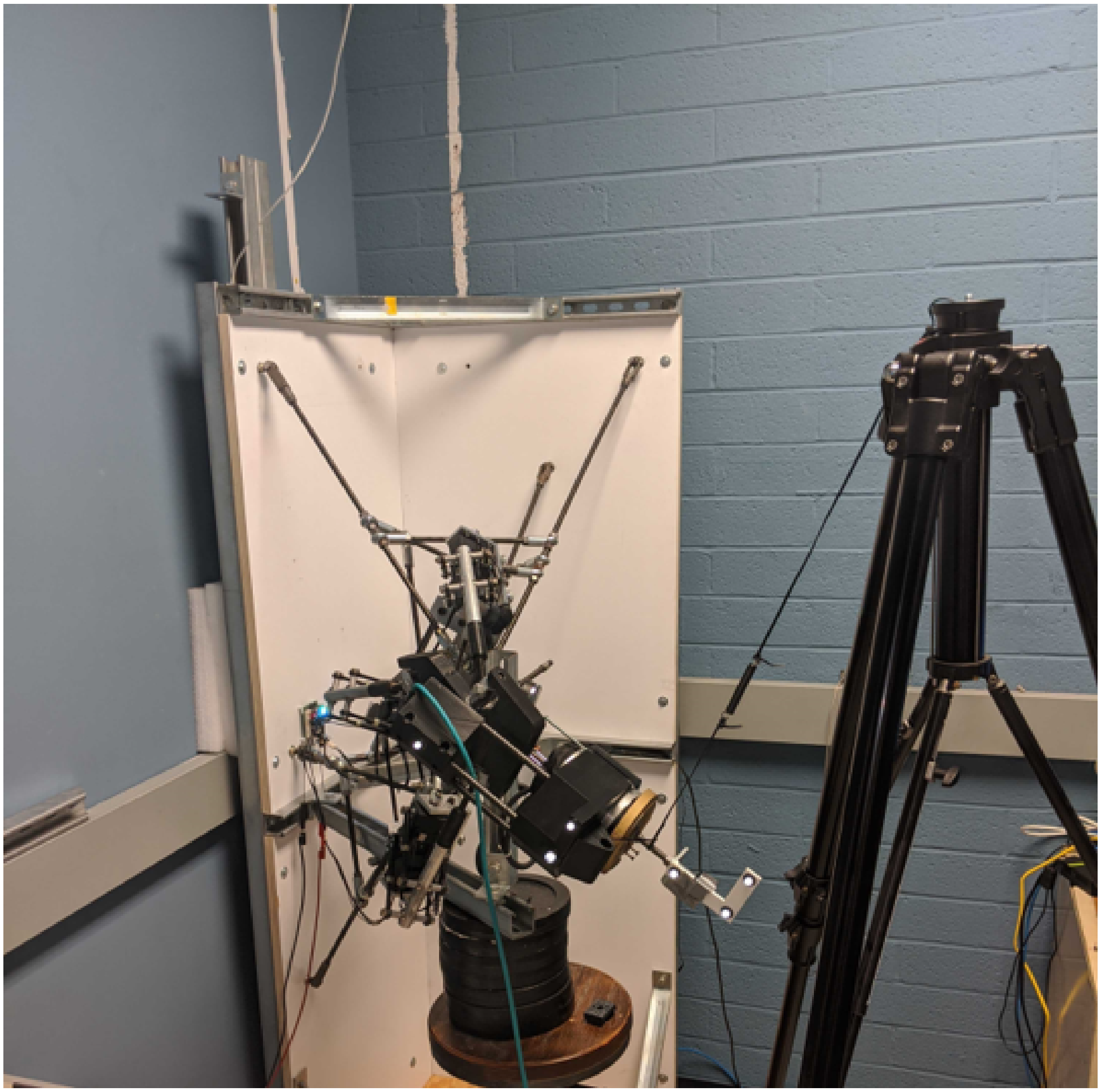

Figure 7.1: Angle 1 - Shown is the shoulder exoskeleton with a mock-up of the human shoulder installed. Attached is a 1 kg mass and a 42.3 Nm/rad spring oriented for testing in the negative pitch direction.

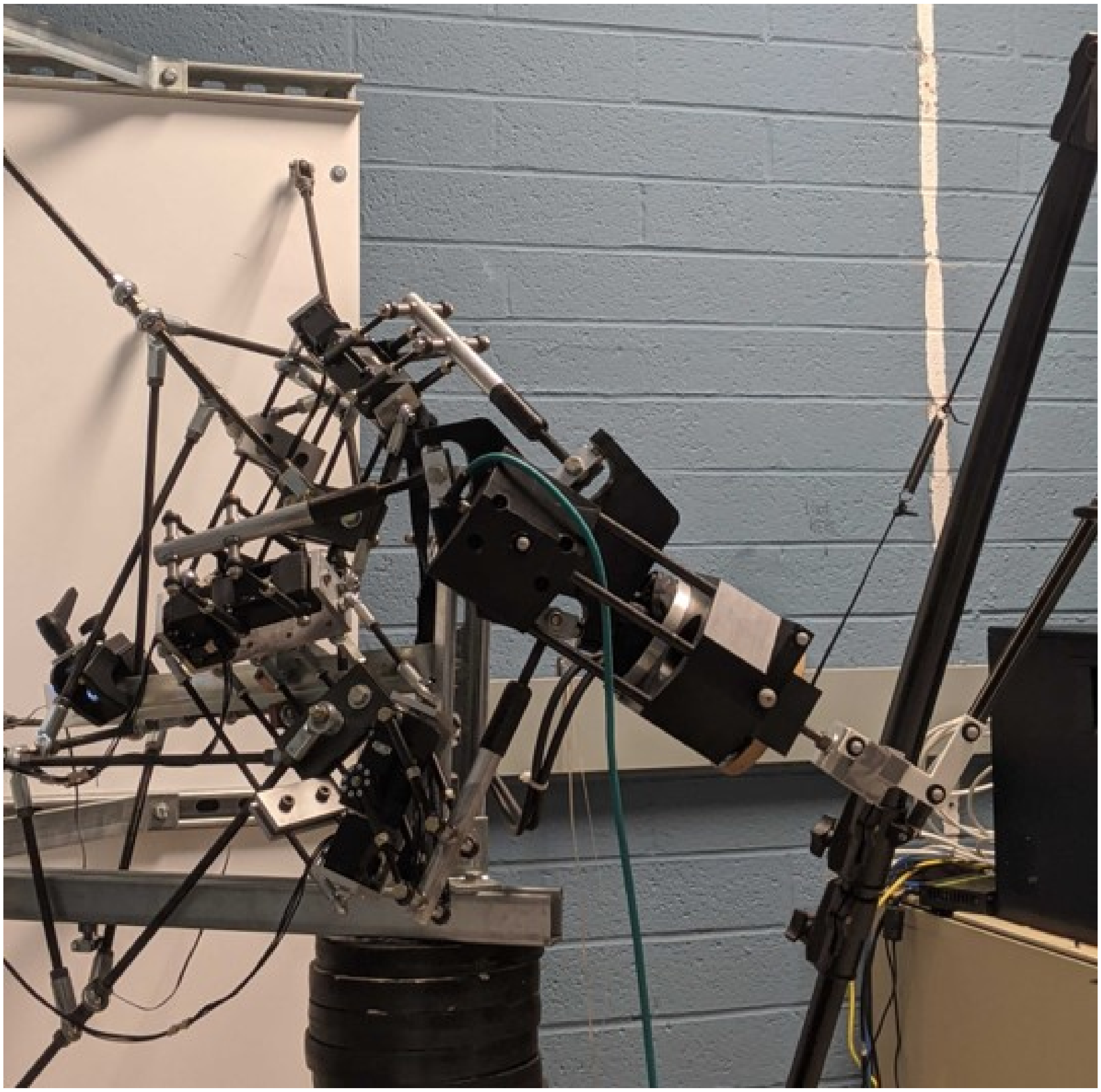

Figure 7.2: Angle 2 - Shown is the shoulder exoskeleton with a mock-up of the human shoulder installed. Attached is a 1 kg mass and a 42.3 Nm/rad spring oriented for testing in the negative pitch direction.

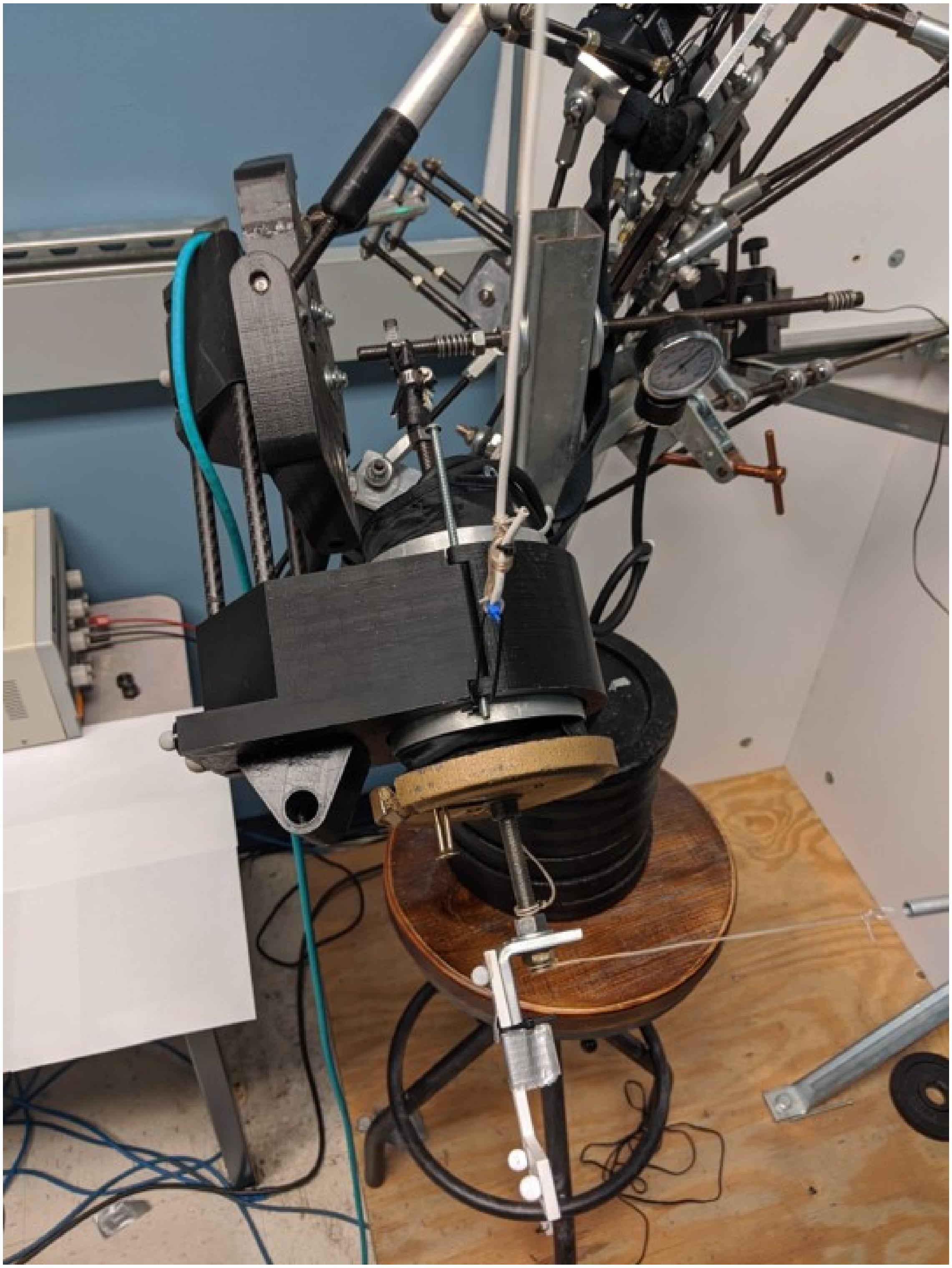

Figure 7.3: Angle 3 - Shown is the shoulder exoskeleton with a mock-up of the human shoulder installed. Attached is a 1 kg mass and a 24.4 Nm/rad spring oriented for testing in the negative yaw direction.

The torques exerted on the exoskeleton by the mock-up are measured using a AXIA 80 EDU (ATI-AI, NC USA) force/torque transducer. This transducer is fixed at one end onto the shoulder plate of the exoskeleton, while the other end is attached to carbon fiber tubing that in turn is connected to the upper arm cuff of the exoskeleton. The pitch and yaw torques as measured by the transducer are used, along the measured pitch and yaw Euler angles mentioned previously, to estimate inertia and stiffness.

7.2.2 Inertia and Stiffness Estimations

Inertia and stiffness of the human arm can be estimated using a 2nd order system model. In this model, inertia, damping and stiffness are represented. These terms can be correlated to position, velocity, acceleration and interaction torque in the following manner:

$$T = I\ddot{\theta} + B\dot{\theta} + K\Delta\theta \tag{7.1}$$

For the experiments conducted, the torque is measured using the force/torque transducer and Euler angle theta is measured from the motion capture setup. Both $\ddot{\theta}$ and $\dot{\theta}$ are derived form theta and the known sampling rate of 250 Hz. The Euler angle difference $\Delta\theta$ is measured relative to theta at the beginning of the perturbation. The inertia I, damping B, and stiffness K are determined using multiple input and multiple out linear (MIMO) regression.

The robot was commanded to perturb in two directions: -pitch and -yaw. These directions were selected as they represent two independent (i.e. decoupled) Euler angles. Demonstrating accurate characterization along these directions is important, as it would suggest that any coupled combination of the two would also yield accurate estimates. A 5th order minimum jerk perturbation profile was used for each direction.

The perturbation had a commanded magnitude of 7 degrees and rise time of 160 ms.

Masses and springs were chosen that reflect inertia and stiffness estimates that would be approximately in the range of what is expected for human subjects, which is between 20-40 Nm/rad in the relaxed state (Lipps *et al.*, 2020). Dampers were not used in these validation experiments. The reason for this is that pure dampers do not exist. Commercially available dampers have stiffness components that are highly nonlinear, therefore characterization of damping using MIMO is not practically done. Furthermore, because position, velocity and acceleration are related by the sample rate, accurate estimates of position dependent stiffness and acceleration dependent inertia would suggest the the related velocity dependent damping would also be accurately estimated. A total of four mass spring conditions were used for each of the two directions: (1) 24.4 Nm/rad with 0 kg add, (2) 24.4 Nm/rad with 1 kg added, (3) 42.3 Nm/rad with 0 kg added, and (4) 42.3 Nm/rad with 1 kg added. Three tests were performed for each of these conditions. Therefore, with two directions, four conditions and three repetitions, the total number of experiments conducted with the mock-up was 24.

The position, velocity, acceleration and torque data is filtered using a 4th-order Butterworth with a 12 Hz cutoff frequency. This cutoff was chosen due to some unidentified noise in the system occurring at 13-14 Hz. An outlier rejection criteria of $2/sigma$ is applied to all filtered trials.

7.2.3 Human Testing

Preliminary human testing with the 4B-SPM shoulder exoskeleton was perform in order to demonstrate the devices ability to collect the measurements needed to estimate shoulder stiffness and damping while worn by a subject. To conduct these experiments, minor modifications had to be made in order to track the position of a human arm instead of the mock-up. A carbon fiber rod with a 3D printed right-angle fixture at its end was secured to the subject's upper arm using tape. Mounted to the printed fixture are the three IR markers previously used to track the position of the mock-up. This setup, which is shown in Fig. 4, allows for the position of the human arm to be tracked during perturbations. To further secure the right-angle to the arm, both were wrap in a blood pressure cuff before being locked into the exoskeleton arm cuff. Once locked to the exoskeleton, the blood pressure cuff was lightly inflated.

The second modification made in order to perform human experiments was the addition of a forearm brace armature. This brace helped the subjects maintain a consistent arm posture throughout the experiment. The brace armature consisted of two 3-DoF joints that were connected by a piece of aluminum tubing. This aluminum tube could also translate within each universal joint. Therefore, the brace armature had a total of 7-DoF. All 7-DoF could be lock in place using a pair of locking handles positioned on the universal joints. At the end of the brace armature was a wrist brace that could be adjusted with straps to fit different subjects. This setup is shown in Fig. 4.

For human testing, a total of 30 perturbations in each of the +- pitch/yaw directions were performed. To prevent the human arm from getting tired, these perturbations were divided into subsets of 10 in each direction, or 40 total. after these 40 perturbations, the subjects were allowed to rest for up to 5 minutes. The same perturbation profile conditions that were used in the mock tests were used in the human tests.

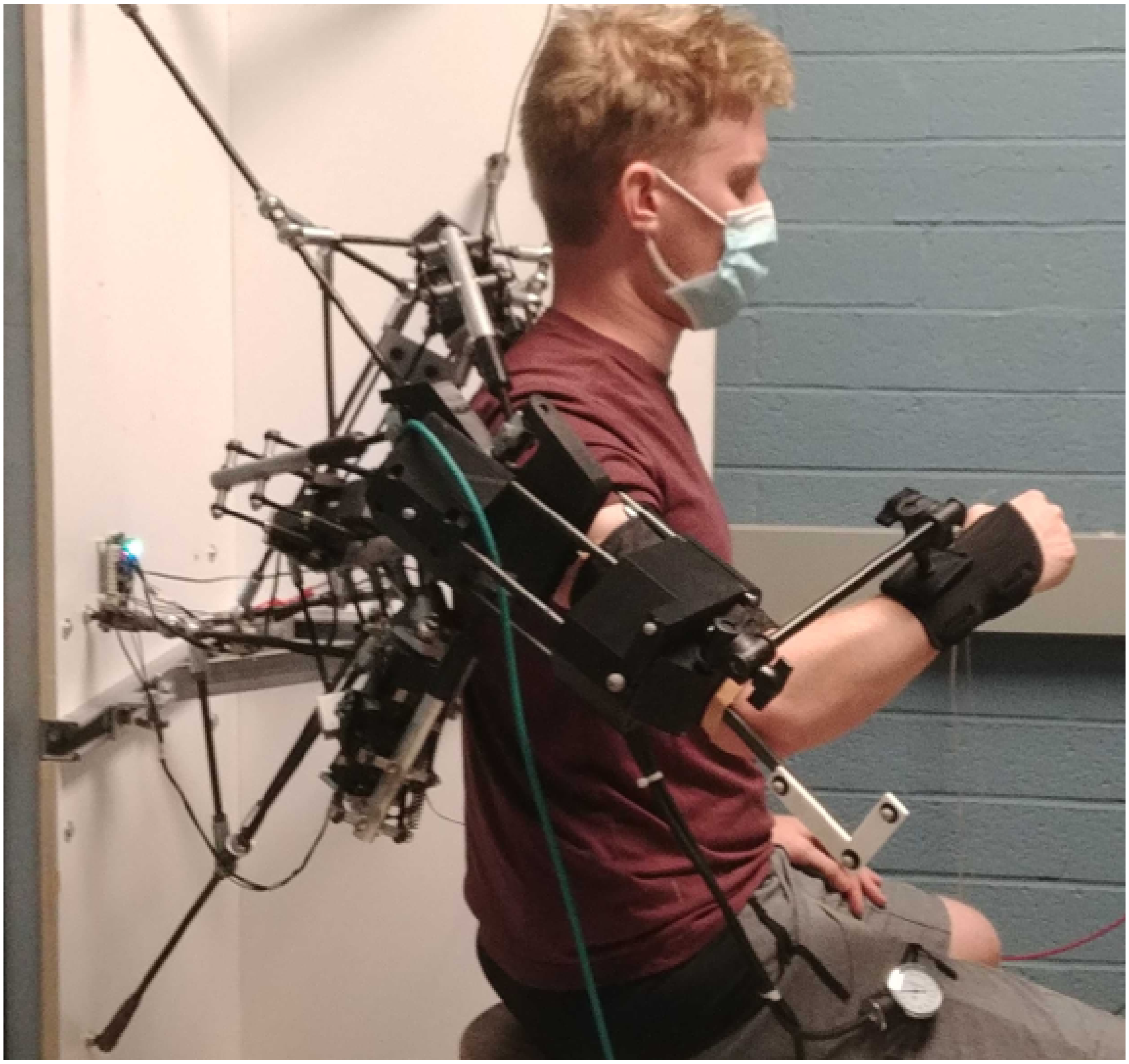

Figure 7.4: Shown is a human subject connected to the 4B-SPM exoskeleton.

7.3 Results

7.3.1 Mock-up Tests

The results of the 24 mock-up tests performed to characterize the performance of the 4B-SPM shoulder exoskeleton are provided in the following figures: Fig. 5-8 show the numerical results of the 24 experiments, Fig 9-32 show the Euler angle position, velocity, acceleration, along with the corresponding measured torque and IBK contribution estimates.

For the pitch direction with a 24.4 Nm/rad spring and 0 kg of added mass, the mean estimates of the 3 experiments for inertia and stiffness were 0.063 kgm^2 (10.47 percent error) and 22.88 Nm/rad (6.22 percent error). For the pitch direction with a 24.4 Nm/rad spring and 1 kg of added mass, the mean estimates of the 3 experiments for inertia and stiffness were 0.133 kgm^2 (1.31 percent error) and 24.12 Nm/rad (1.12 percent error).

For the pitch direction with a 42.3 Nm/rad spring and 0 kg of added mass, the mean estimates of the 3 experiments for inertia and stiffness were 0.067 kgm^2 (4.76 percent error) and 43.79 Nm/rad (3.43 percent error). For the pitch direction with a 42.3 Nm/rad spring and 1 kg of added mass, the mean estimates of the 3 experiments for inertia and stiffness were 0.131 kgm^2 (4.62 percent error) and 41.88 Nm/rad (1.55 percent error).

For the yaw direction with a 24.4 Nm/rad spring and 0 kg of added mass, the mean estimates of the 3 experiments for inertia and stiffness were 0.072 kgm^2 (2.38 percent error) and 23.77 Nm/rad (3.54 percent error). For the yaw direction with a 24.4 Nm/rad spring and 1 kg of added mass, the mean estimates of the 3 experiments for inertia and stiffness were 0.145 kgm^2 (6.08 percent error) and 22.54 Nm/rad (8.83 percent error).

For the yaw direction with a 42.3 Nm/rad spring and 0 kg of added mass, the mean estimates of the 3 experiments for inertia and stiffness were 0.076 kgm^2 (7.14 percent error) and 44.31 Nm/rad (5.37 percent error). For the yaw direction with a 42.3 Nm/rad spring and 1 kg of added mass, the mean estimates of the 3 experiments for inertia and stiffness were 0.159 kgm^2 (16.5 percent error) and 44.11 Nm/rad (6.3 percent error).

It should be noted that the 0.07 kgm^2 estimate of the robot inertia (i.e. no mass added) is based the measured mass of different major components and the relative distance of each component to the center-of-rotation. The robot is however, a complex system, so these inertia calculations may have some error associated with them. However, if instead one examines the difference between 0 kg of mass added and 1 kg of mass added, it can be seen that the measured inertia of 1 kg with a known moment arm is 0.061 kgm^2 for pitch and 0.084 kgm^2. In comparison the calculate inertia of this point-mass is 0.067 kgm^2. This gives confidence that the setup is providing reasonable estimates of inertia.

7.3.2 Human Tests

The results of the human test performed to estimate human shoulder impedance are provided in the following figures: Fig. 33 shows the numerical results of human test, Fig 34-37 show the Euler angle position, velocity, acceleration, along with the corresponding measured torque and IBK contribution estimates.

For the positive yaw direction, the estimated inertia is 0.124 kgm^2 and stiffness is 33.7 Nm/rad. For the positive pitch direction, the estimated inertia is 0.134 kgm^2 and stiffness is 40.8 Nm/rad. For the negative yaw direction, the estimated inertia is 0.14 kgm^2 and stiffness is 29.5 Nm/rad. For the negative pitch direction, the estimated inertia is 0.099 kgm^2 and stiffness is 35.6 Nm/rad.

7.4 Discussion

This chapter has provided the setup and results of an extensive set of tests to validate the 4B-SPM shoulder exoskeleton for human testing. The results of these tests show that the device is capable of estimating stiffness and inertia of a mock-up shoulder for a variety of different mass and spring conditions. This gives confidence that the device will be capable of performing humans tests with a high degree of accuracy.

This chapter also introduces some preliminary results from human testing with the 4B-SPM. This human test was performed to show the devices ability to interface with and collect data on human subjects. While in no way is this early test conclusive of human shoulder impedance, it provides a starting point in terms of experimental protocol that more extensive future tests can benefit from. It also shows the device's ability to provide reasonable impedance estimates that are representative of what is expected, based on current literature (Lipps *et al.*, 2020). One point of note for future experiments, the authors have since developed a torque feedback GUI in order to help reduce the variance during experiments. The subjects are now required to maintain a certain near-zero torque value before a perturbation will occur. This will help improve initial condition consistency across all trials.

This work is an important first step toward characterizing human shoulder impedance for a variety of applications. One such application would be using the 4B-SPM shoulder exoskeleton to develop a model of shoulder impedance for both static posture and dynamic motion of healthily human subjects. This model will then be used as a point of comparison for similar studies conducted with stroke impaired individuals. Quantifying shoulder stiffness and damping between healthy and impaired subjects could help improve our collective understanding of how many different neuromuscular diseases impact arm performance. This improved understanding could even lead to better rehabilitation protocols for stroke and other conditions through better identification and targeting of damping dependent spasticity and stiffness dependent hypertonicity. A second application example would high performance military industrial upper limb exoskeletons. Characterizing normal mechanical impedance would allow for the development of exoskeleton devices that rely on cooperative human-robot critical stability interaction to provide highly responsive performance.

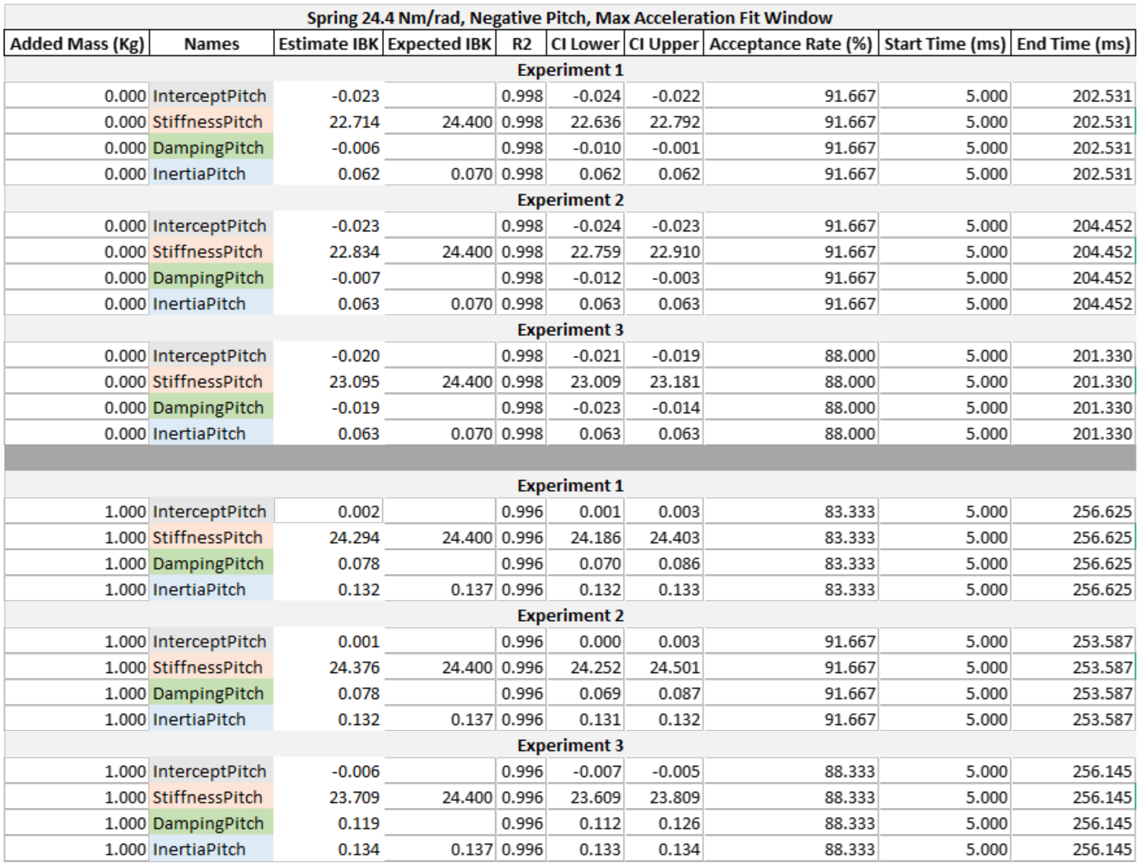

Spring 24.4 Nm/rad, Negative Pitch, Max Acceleration Fit Window									
Added Mass (Kg)	**Names**	**Estimate IBK**	**Expected IBK**	**R2**	**CI Lower**	**CI Upper**	**Acceptance Rate (%)**	**Start Time (ms)**	**End Time (ms)**
				Experiment 1					
0.000	InterceptPitch	-0.023		0.998	-0.024	-0.022	91.667	5.000	202.531
0.000	StiffnessPitch	22.714	24.400	0.998	22.636	22.792	91.667	5.000	202.531
0.000	DampingPitch	-0.006		0.998	-0.010	-0.001	91.667	5.000	202.531
0.000	InertiaPitch	0.062	0.070	0.998	0.062	0.062	91.667	5.000	202.531
				Experiment 2					
0.000	InterceptPitch	-0.023		0.998	-0.024	-0.023	91.667	5.000	204.452
0.000	StiffnessPitch	22.834	24.400	0.998	22.759	22.910	91.667	5.000	204.452
0.000	DampingPitch	-0.007		0.998	-0.012	-0.003	91.667	5.000	204.452
0.000	InertiaPitch	0.063	0.070	0.998	0.063	0.063	91.667	5.000	204.452
				Experiment 3					
0.000	InterceptPitch	-0.020		0.998	-0.021	-0.019	88.000	5.000	201.330
0.000	StiffnessPitch	23.095	24.400	0.998	23.009	23.181	88.000	5.000	201.330
0.000	DampingPitch	-0.019		0.998	-0.023	-0.014	88.000	5.000	201.330
0.000	InertiaPitch	0.063	0.070	0.998	0.063	0.063	88.000	5.000	201.330
				Experiment 1					
1.000	InterceptPitch	0.002		0.996	0.001	0.003	83.333	5.000	256.625
1.000	StiffnessPitch	24.294	24.400	0.996	24.186	24.403	83.333	5.000	256.625
1.000	DampingPitch	0.078		0.996	0.070	0.086	83.333	5.000	256.625
1.000	InertiaPitch	0.132	0.137	0.996	0.132	0.133	83.333	5.000	256.625
				Experiment 2					
1.000	InterceptPitch	0.001		0.996	0.000	0.003	91.667	5.000	253.587
1.000	StiffnessPitch	24.376	24.400	0.996	24.252	24.501	91.667	5.000	253.587
1.000	DampingPitch	0.078		0.996	0.069	0.087	91.667	5.000	253.587
1.000	InertiaPitch	0.132	0.137	0.996	0.131	0.132	91.667	5.000	253.587
				Experiment 3					
1.000	InterceptPitch	-0.006		0.996	-0.007	-0.005	88.333	5.000	256.145
1.000	StiffnessPitch	23.709	24.400	0.996	23.609	23.809	88.333	5.000	256.145
1.000	DampingPitch	0.119		0.996	0.112	0.126	88.333	5.000	256.145
1.000	InertiaPitch	0.134	0.137	0.996	0.133	0.134	88.333	5.000	256.145

Figure 7.5: IBK results for 6 pitch direction perturbations experiments with a 24.4 Nm/rad spring. The first 3 are with 0 kg of added mass. The last 3 are for 1 kg of added mass.

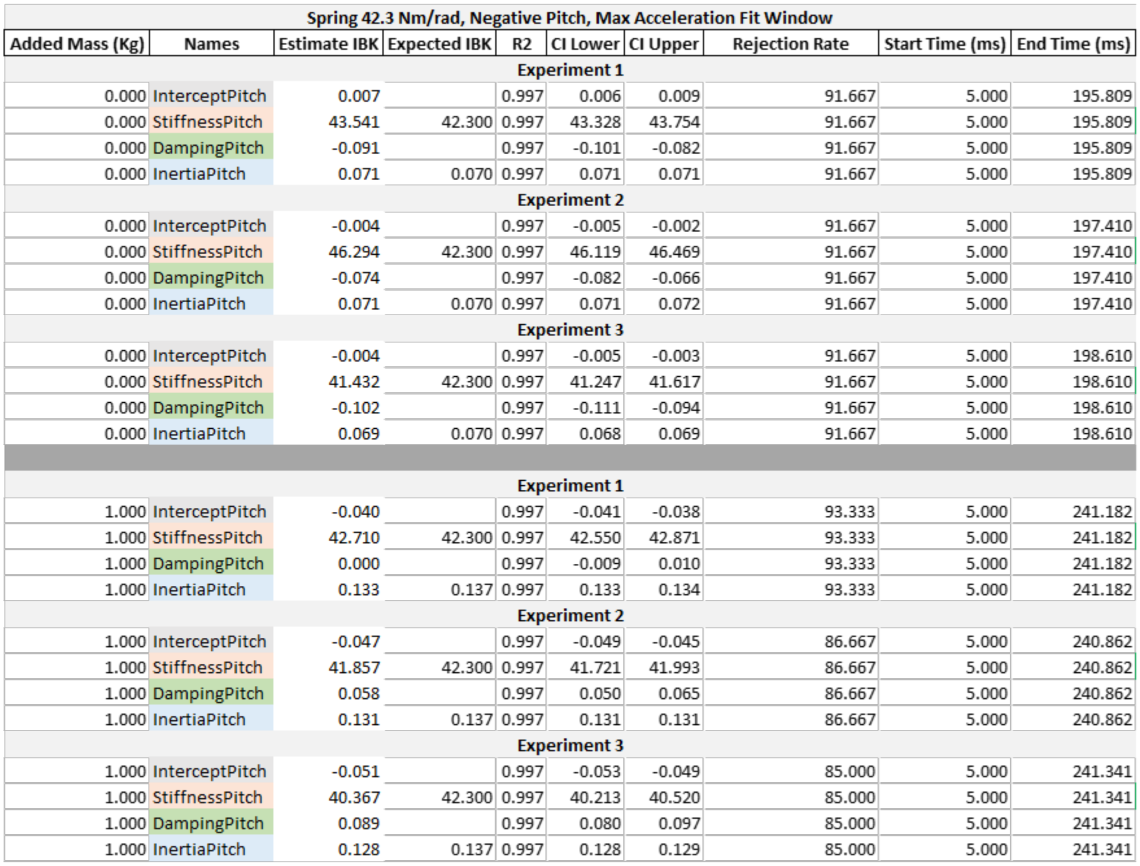

Spring 42.3 Nm/rad, Negative Pitch, Max Acceleration Fit Window

Added Mass (Kg)	Names	Estimate IBK	Expected IBK	R2	CI Lower	CI Upper	Rejection Rate	Start Time (ms)	End Time (ms)
Experiment 1									
0.000	InterceptPitch	0.007		0.997	0.006	0.009	91.667	5.000	195.809
0.000	StiffnessPitch	43.541	42.300	0.997	43.328	43.754	91.667	5.000	195.809
0.000	DampingPitch	-0.091		0.997	-0.101	-0.082	91.667	5.000	195.809
0.000	InertiaPitch	0.071	0.070	0.997	0.071	0.071	91.667	5.000	195.809
Experiment 2									
0.000	InterceptPitch	-0.004		0.997	-0.005	-0.002	91.667	5.000	197.410
0.000	StiffnessPitch	46.294	42.300	0.997	46.119	46.469	91.667	5.000	197.410
0.000	DampingPitch	-0.074		0.997	-0.082	-0.066	91.667	5.000	197.410
0.000	InertiaPitch	0.071	0.070	0.997	0.071	0.072	91.667	5.000	197.410
Experiment 3									
0.000	InterceptPitch	-0.004		0.997	-0.005	-0.003	91.667	5.000	198.610
0.000	StiffnessPitch	41.432	42.300	0.997	41.247	41.617	91.667	5.000	198.610
0.000	DampingPitch	-0.102		0.997	-0.111	-0.094	91.667	5.000	198.610
0.000	InertiaPitch	0.069	0.070	0.997	0.068	0.069	91.667	5.000	198.610
Experiment 1									
1.000	InterceptPitch	-0.040		0.997	-0.041	-0.038	93.333	5.000	241.182
1.000	StiffnessPitch	42.710	42.300	0.997	42.550	42.871	93.333	5.000	241.182
1.000	DampingPitch	0.000		0.997	-0.009	0.010	93.333	5.000	241.182
1.000	InertiaPitch	0.133	0.137	0.997	0.133	0.134	93.333	5.000	241.182
Experiment 2									
1.000	InterceptPitch	-0.047		0.997	-0.049	-0.045	86.667	5.000	240.862
1.000	StiffnessPitch	41.857	42.300	0.997	41.721	41.993	86.667	5.000	240.862
1.000	DampingPitch	0.058		0.997	0.050	0.065	86.667	5.000	240.862
1.000	InertiaPitch	0.131	0.137	0.997	0.131	0.131	86.667	5.000	240.862
Experiment 3									
1.000	InterceptPitch	-0.051		0.997	-0.053	-0.049	85.000	5.000	241.341
1.000	StiffnessPitch	40.367	42.300	0.997	40.213	40.520	85.000	5.000	241.341
1.000	DampingPitch	0.089		0.997	0.080	0.097	85.000	5.000	241.341
1.000	InertiaPitch	0.128	0.137	0.997	0.128	0.129	85.000	5.000	241.341

Figure 7.6: IBK results for 6 pitch direction perturbations experiments with a 42.3 Nm/rad spring. The first 3 are with 0 kg of added mass. The last 3 are for 1 kg of added mass.

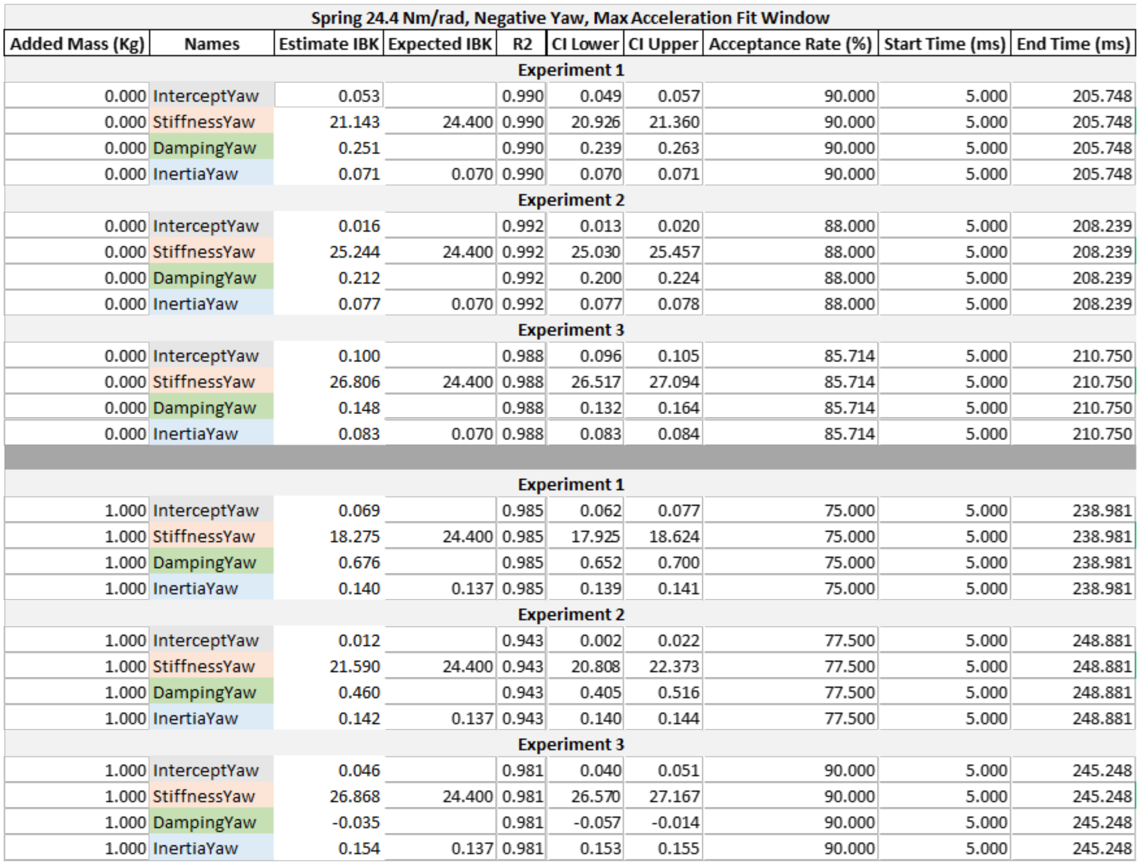

Spring 24.4 Nm/rad, Negative Yaw, Max Acceleration Fit Window

Added Mass (Kg)	Names	Estimate IBK	Expected IBK	R2	CI Lower	CI Upper	Acceptance Rate (%)	Start Time (ms)	End Time (ms)
Experiment 1									
0.000	InterceptYaw	0.053		0.990	0.049	0.057	90.000	5.000	205.748
0.000	StiffnessYaw	21.143	24.400	0.990	20.926	21.360	90.000	5.000	205.748
0.000	DampingYaw	0.251		0.990	0.239	0.263	90.000	5.000	205.748
0.000	InertiaYaw	0.071	0.070	0.990	0.070	0.071	90.000	5.000	205.748
Experiment 2									
0.000	InterceptYaw	0.016		0.992	0.013	0.020	88.000	5.000	208.239
0.000	StiffnessYaw	25.244	24.400	0.992	25.030	25.457	88.000	5.000	208.239
0.000	DampingYaw	0.212		0.992	0.200	0.224	88.000	5.000	208.239
0.000	InertiaYaw	0.077	0.070	0.992	0.077	0.078	88.000	5.000	208.239
Experiment 3									
0.000	InterceptYaw	0.100		0.988	0.096	0.105	85.714	5.000	210.750
0.000	StiffnessYaw	26.806	24.400	0.988	26.517	27.094	85.714	5.000	210.750
0.000	DampingYaw	0.148		0.988	0.132	0.164	85.714	5.000	210.750
0.000	InertiaYaw	0.083	0.070	0.988	0.083	0.084	85.714	5.000	210.750
Experiment 1									
1.000	InterceptYaw	0.069		0.985	0.062	0.077	75.000	5.000	238.981
1.000	StiffnessYaw	18.275	24.400	0.985	17.925	18.624	75.000	5.000	238.981
1.000	DampingYaw	0.676		0.985	0.652	0.700	75.000	5.000	238.981
1.000	InertiaYaw	0.140	0.137	0.985	0.139	0.141	75.000	5.000	238.981
Experiment 2									
1.000	InterceptYaw	0.012		0.943	0.002	0.022	77.500	5.000	248.881
1.000	StiffnessYaw	21.590	24.400	0.943	20.808	22.373	77.500	5.000	248.881
1.000	DampingYaw	0.460		0.943	0.405	0.516	77.500	5.000	248.881
1.000	InertiaYaw	0.142	0.137	0.943	0.140	0.144	77.500	5.000	248.881
Experiment 3									
1.000	InterceptYaw	0.046		0.981	0.040	0.051	90.000	5.000	245.248
1.000	StiffnessYaw	26.868	24.400	0.981	26.570	27.167	90.000	5.000	245.248
1.000	DampingYaw	-0.035		0.981	-0.057	-0.014	90.000	5.000	245.248
1.000	InertiaYaw	0.154	0.137	0.981	0.153	0.155	90.000	5.000	245.248

Figure 7.7: IBK results for 6 yaw direction perturbations experiments with a 24.4 Nm/rad spring. The first 3 are with 0 kg of added mass. The last 3 are for 1 kg of added mass.

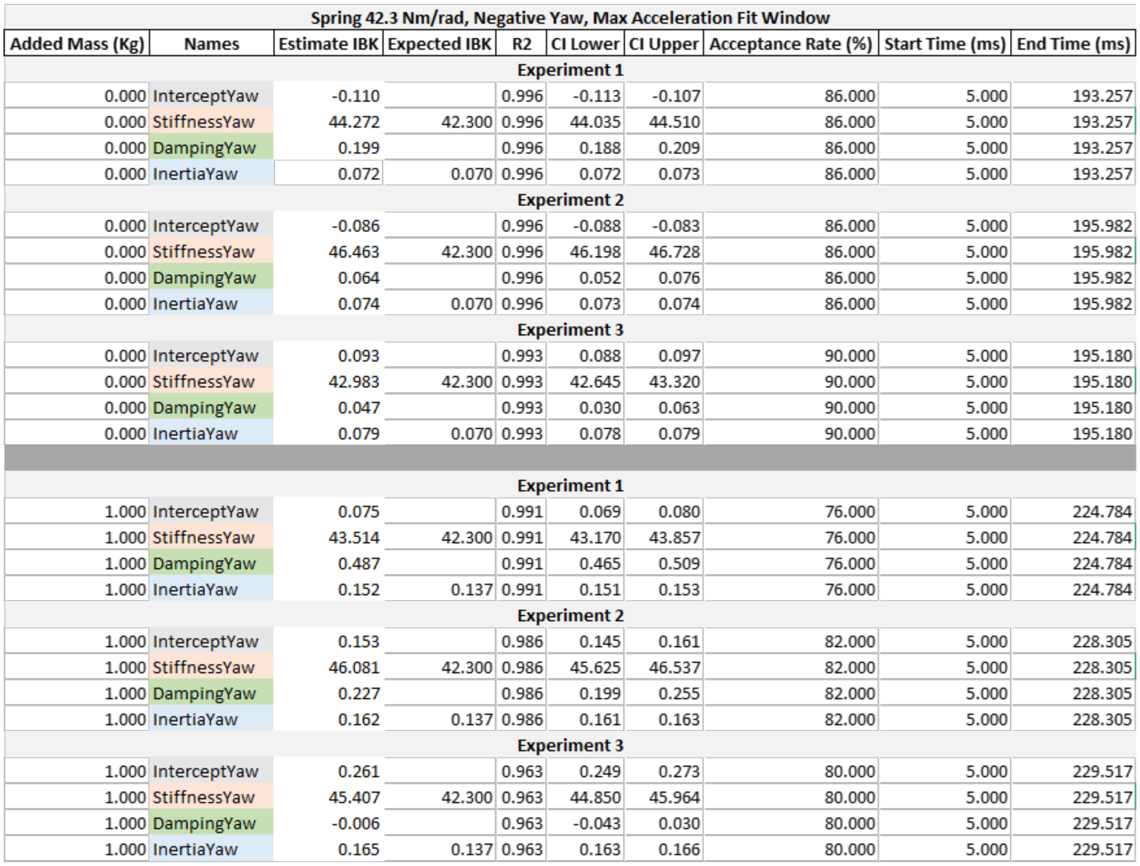

Spring 42.3 Nm/rad, Negative Yaw, Max Acceleration Fit Window

Added Mass (Kg)	Names	Estimate IBK	Expected IBK	R2	CI Lower	CI Upper	Acceptance Rate (%)	Start Time (ms)	End Time (ms)
Experiment 1									
0.000	InterceptYaw	-0.110		0.996	-0.113	-0.107	86.000	5.000	193.257
0.000	StiffnessYaw	44.272	42.300	0.996	44.035	44.510	86.000	5.000	193.257
0.000	DampingYaw	0.199		0.996	0.188	0.209	86.000	5.000	193.257
0.000	InertiaYaw	0.072	0.070	0.996	0.072	0.073	86.000	5.000	193.257
Experiment 2									
0.000	InterceptYaw	-0.086		0.996	-0.088	-0.083	86.000	5.000	195.982
0.000	StiffnessYaw	46.463	42.300	0.996	46.198	46.728	86.000	5.000	195.982
0.000	DampingYaw	0.064		0.996	0.052	0.076	86.000	5.000	195.982
0.000	InertiaYaw	0.074	0.070	0.996	0.073	0.074	86.000	5.000	195.982
Experiment 3									
0.000	InterceptYaw	0.093		0.993	0.088	0.097	90.000	5.000	195.180
0.000	StiffnessYaw	42.983	42.300	0.993	42.645	43.320	90.000	5.000	195.180
0.000	DampingYaw	0.047		0.993	0.030	0.063	90.000	5.000	195.180
0.000	InertiaYaw	0.079	0.070	0.993	0.078	0.079	90.000	5.000	195.180
Experiment 1									
1.000	InterceptYaw	0.075		0.991	0.069	0.080	76.000	5.000	224.784
1.000	StiffnessYaw	43.514	42.300	0.991	43.170	43.857	76.000	5.000	224.784
1.000	DampingYaw	0.487		0.991	0.465	0.509	76.000	5.000	224.784
1.000	InertiaYaw	0.152	0.137	0.991	0.151	0.153	76.000	5.000	224.784
Experiment 2									
1.000	InterceptYaw	0.153		0.986	0.145	0.161	82.000	5.000	228.305
1.000	StiffnessYaw	46.081	42.300	0.986	45.625	46.537	82.000	5.000	228.305
1.000	DampingYaw	0.227		0.986	0.199	0.255	82.000	5.000	228.305
1.000	InertiaYaw	0.162	0.137	0.986	0.161	0.163	82.000	5.000	228.305
Experiment 3									
1.000	InterceptYaw	0.261		0.963	0.249	0.273	80.000	5.000	229.517
1.000	StiffnessYaw	45.407	42.300	0.963	44.850	45.964	80.000	5.000	229.517
1.000	DampingYaw	-0.006		0.963	-0.043	0.030	80.000	5.000	229.517
1.000	InertiaYaw	0.165	0.137	0.963	0.163	0.166	80.000	5.000	229.517

Figure 7.8: IBK results for 6 yaw direction perturbations experiments with a 42.3 Nm/rad spring. The first 3 are with 0 kg of added mass. The last 3 are for 1 kg of added mass.

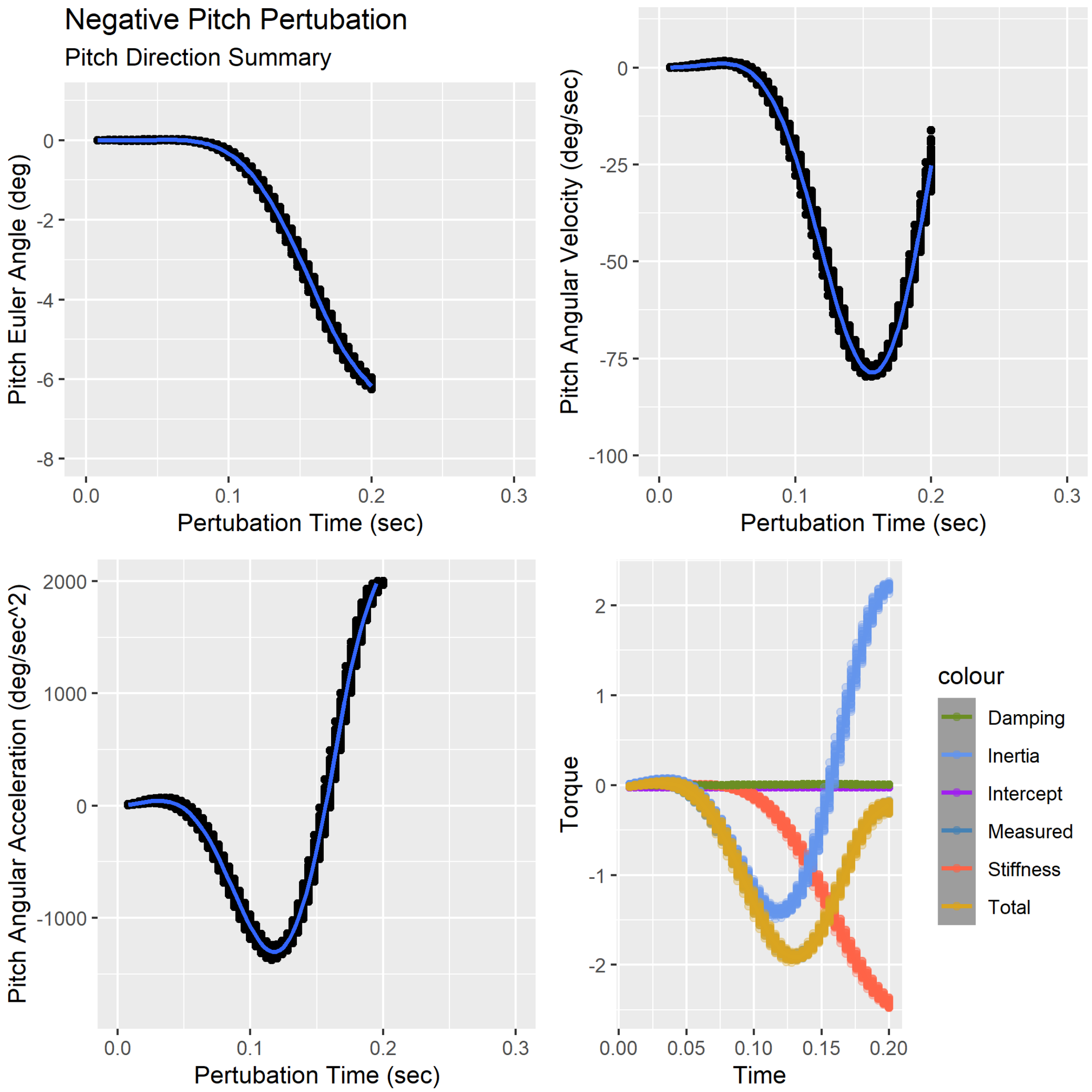

Figure 7.9: Shown are position, velocity, acceleration, corresponding torque and IBK contribution estimates for 24.4 Nm/rad spring, 0 kg of added mass, experiment 1

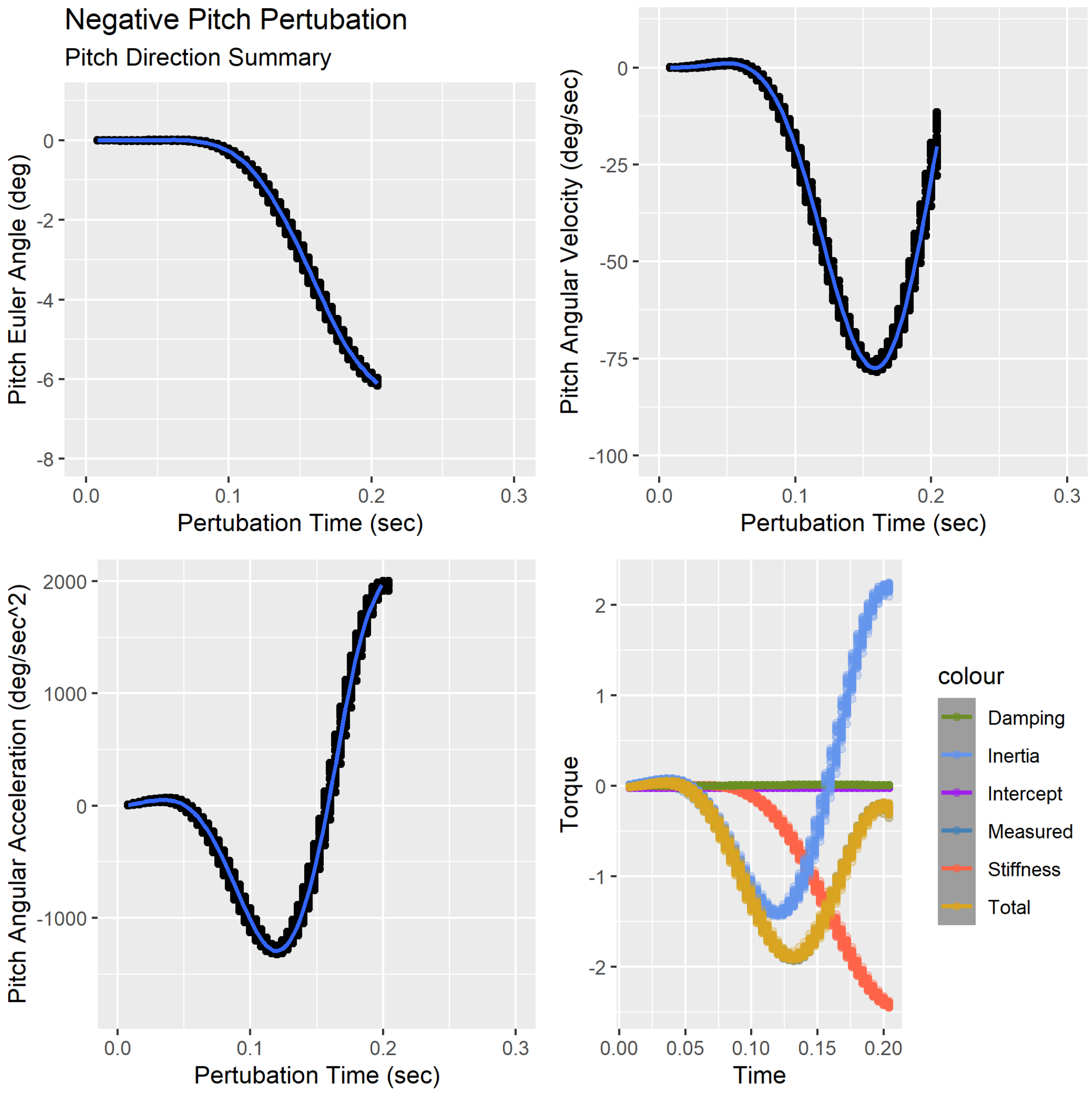

Figure 7.10: Shown are position, velocity, acceleration, corresponding torque and IBK contribution estimates for 24.4 Nm/rad spring, 0 kg of added mass, experiment 2

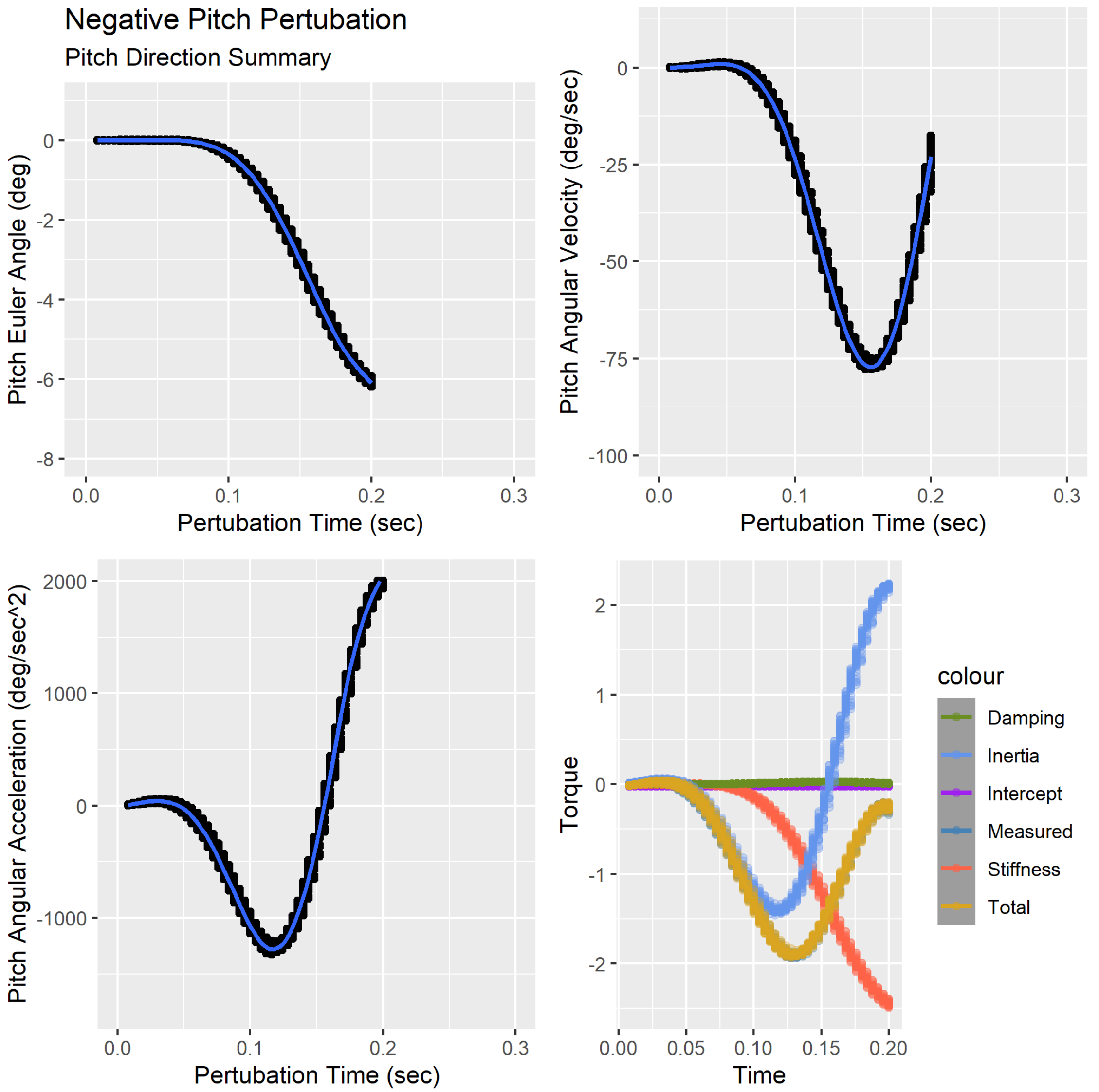

Figure 7.11: Shown are position, velocity, acceleration, corresponding torque and IBK contribution estimates for 24.4 Nm/rad spring, 0 kg of added mass, experiment 3

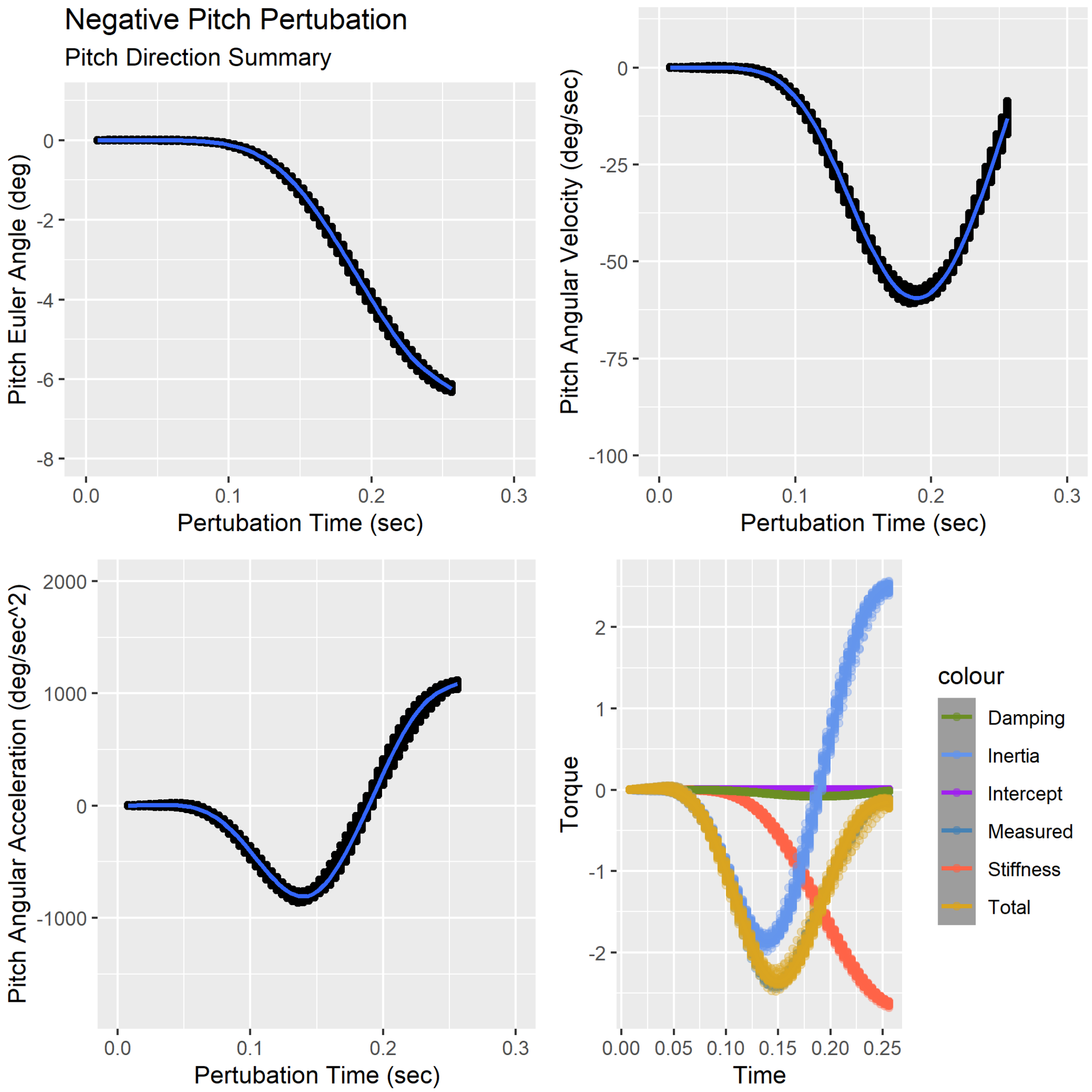

Figure 7.12: Shown are position, velocity, acceleration, corresponding torque and IBK contribution estimates for 24.4 Nm/rad spring, 1 kg of added mass, experiment 1

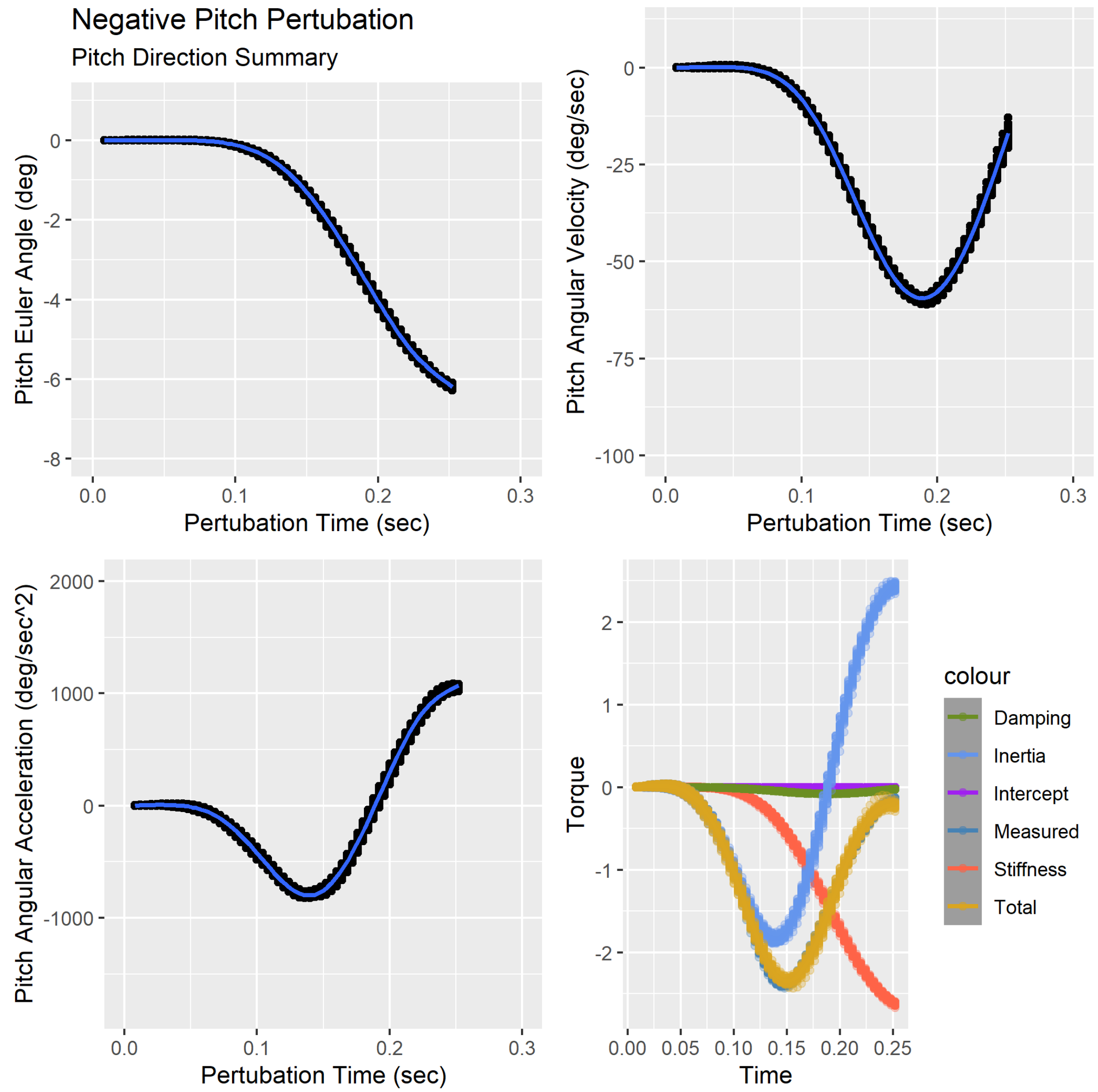

Figure 7.13: Shown are position, velocity, acceleration, corresponding torque and IBK contribution estimates for 24.4 Nm/rad spring, 1 kg of added mass, experiment 2

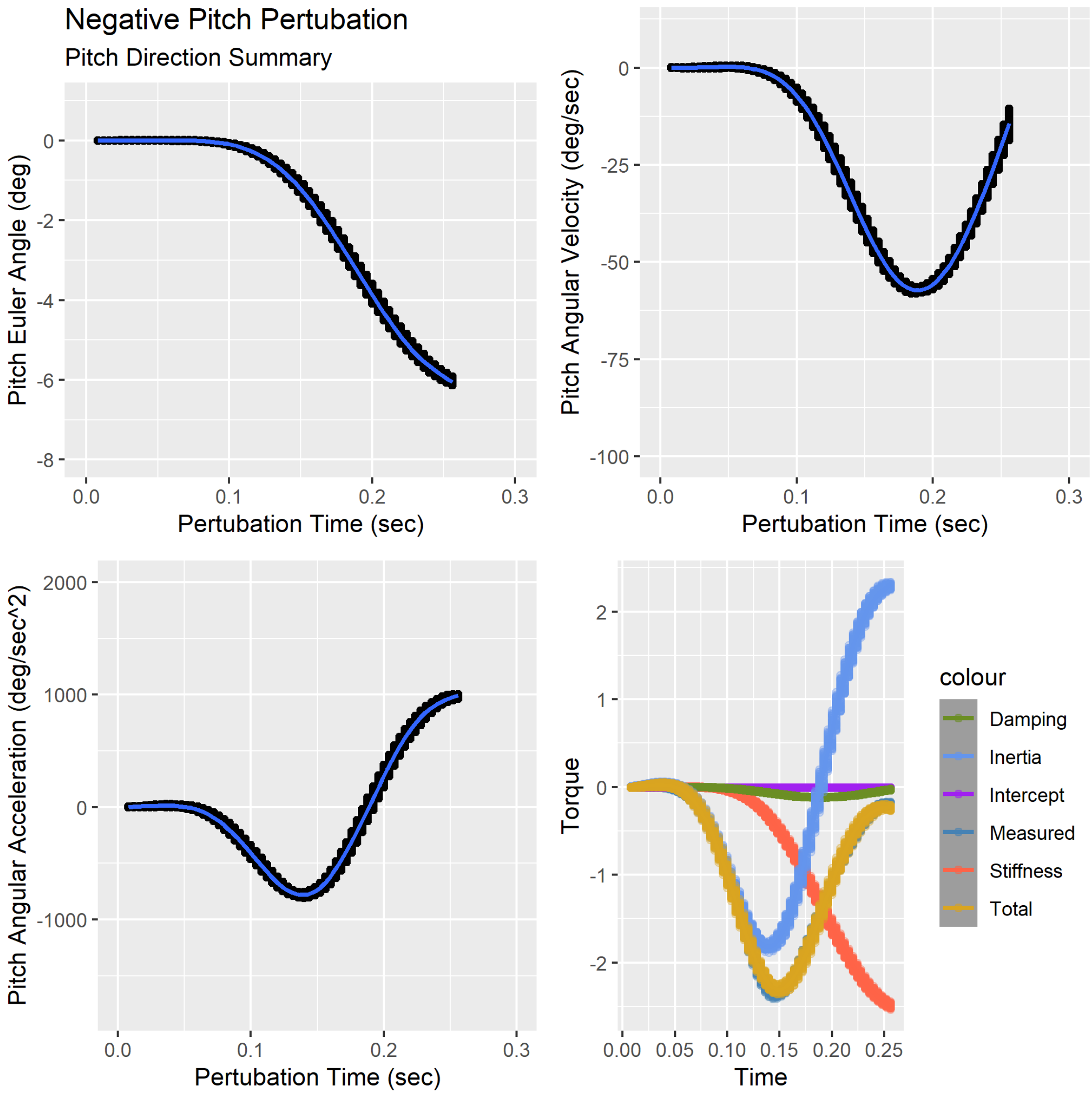

Figure 7.14: Shown are position, velocity, acceleration, corresponding torque and IBK contribution estimates for 24.4 Nm/rad spring, 1 kg of added mass, experiment 3

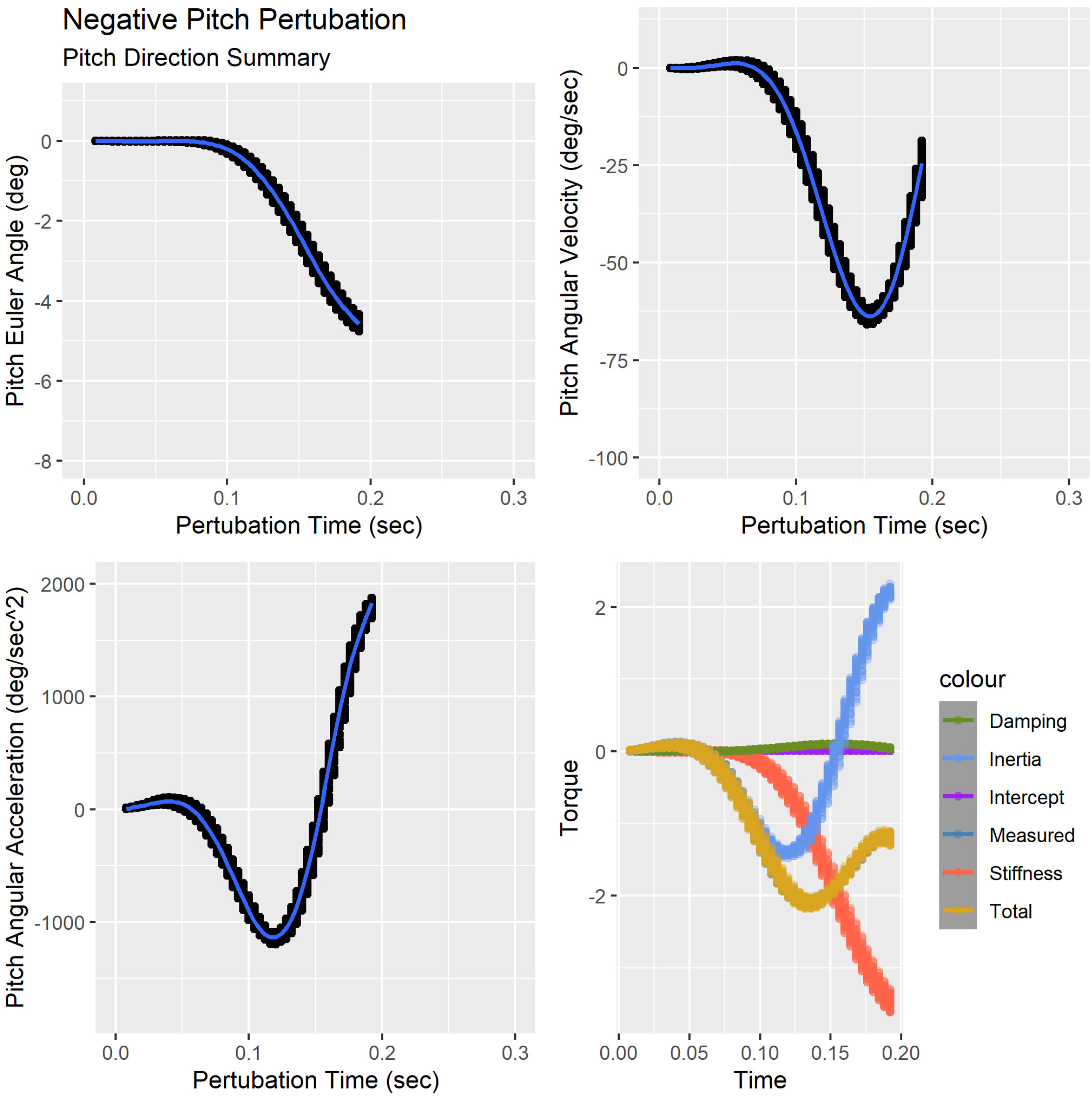

Figure 7.15: Shown are position, velocity, acceleration, corresponding torque and IBK contribution estimates for 42.3 Nm/rad spring, 0 kg of added mass, experiment 1

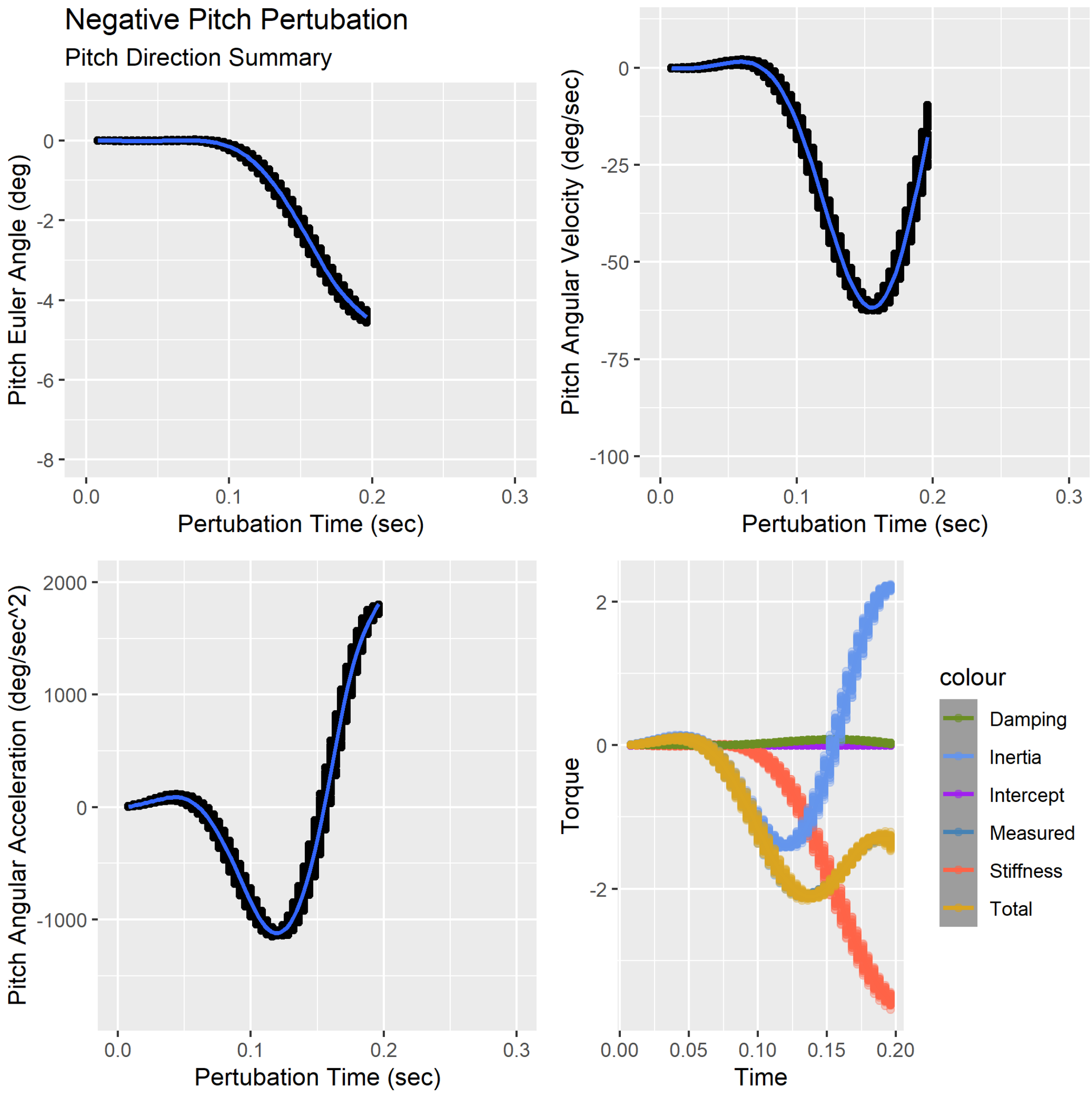

Figure 7.16: Shown are position, velocity, acceleration, corresponding torque and IBK contribution estimates for 42.3 Nm/rad spring, 0 kg of added mass, experiment 2

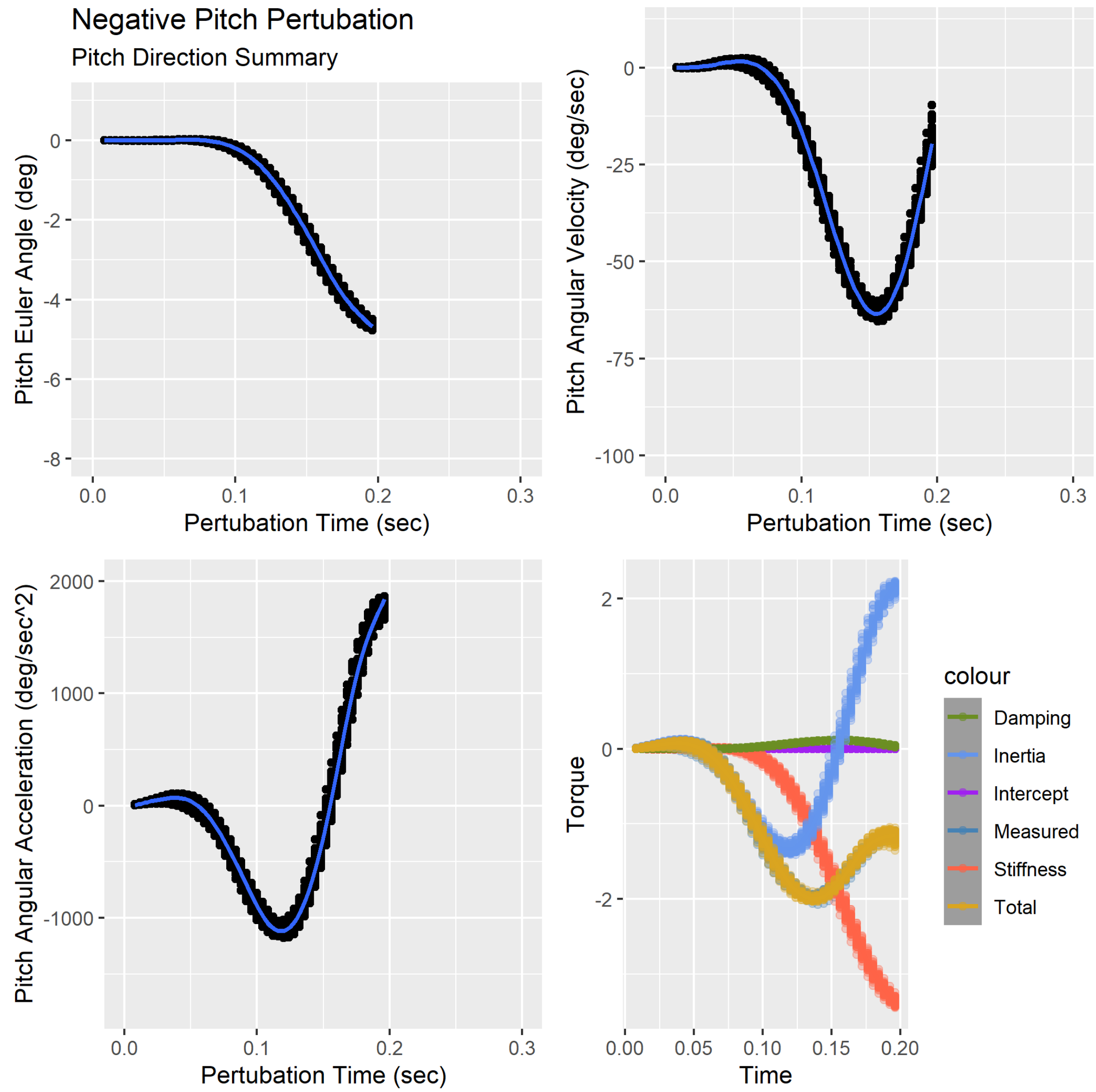

Figure 7.17: Shown are position, velocity, acceleration, corresponding torque and IBK contribution estimates for 42.3 Nm/rad spring, 0 kg of added mass, experiment 3

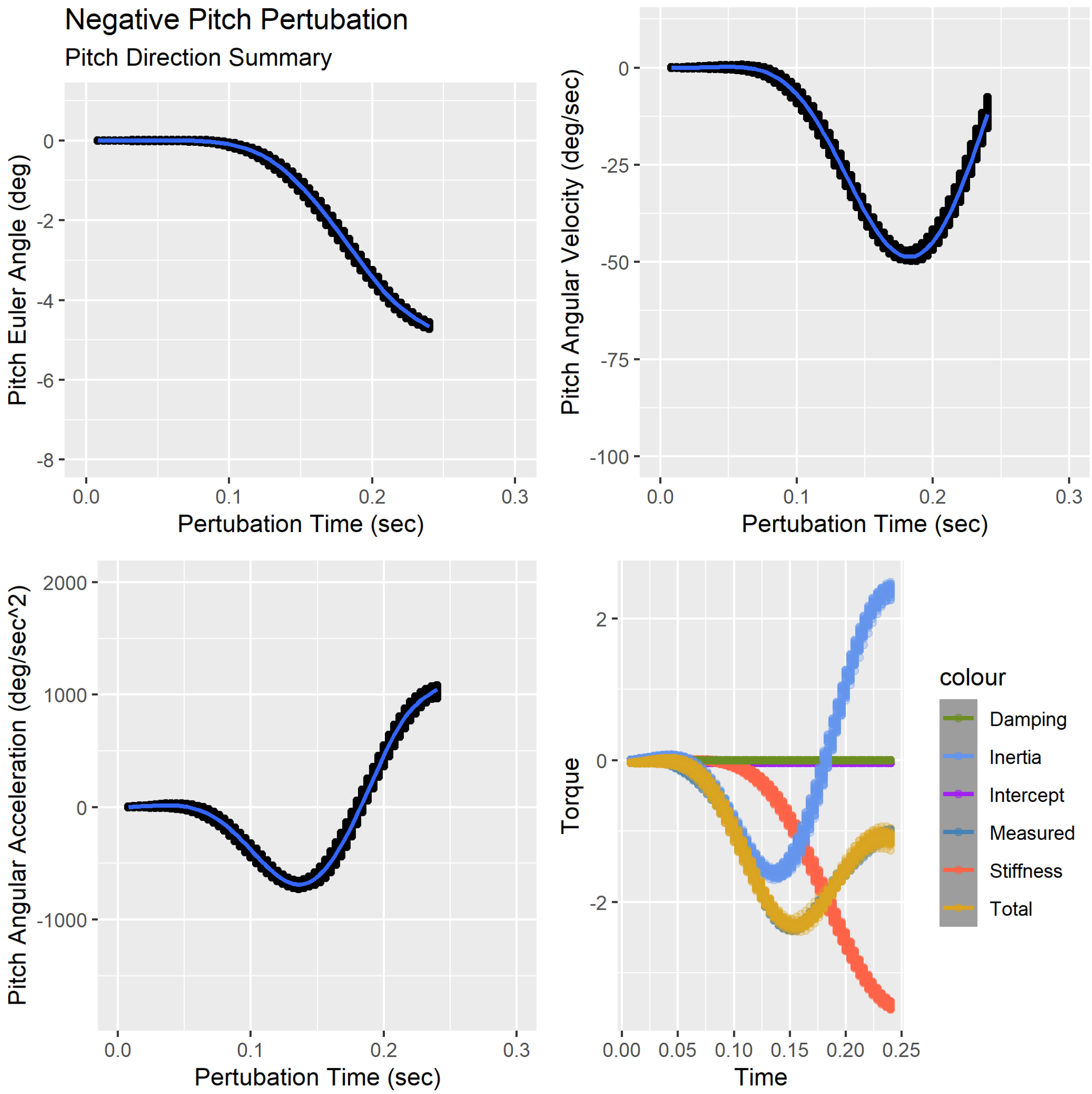

Figure 7.18: Shown are position, velocity, acceleration, corresponding torque and IBK contribution estimates for 42.3 Nm/rad spring, 1 kg of added mass, experiment 1

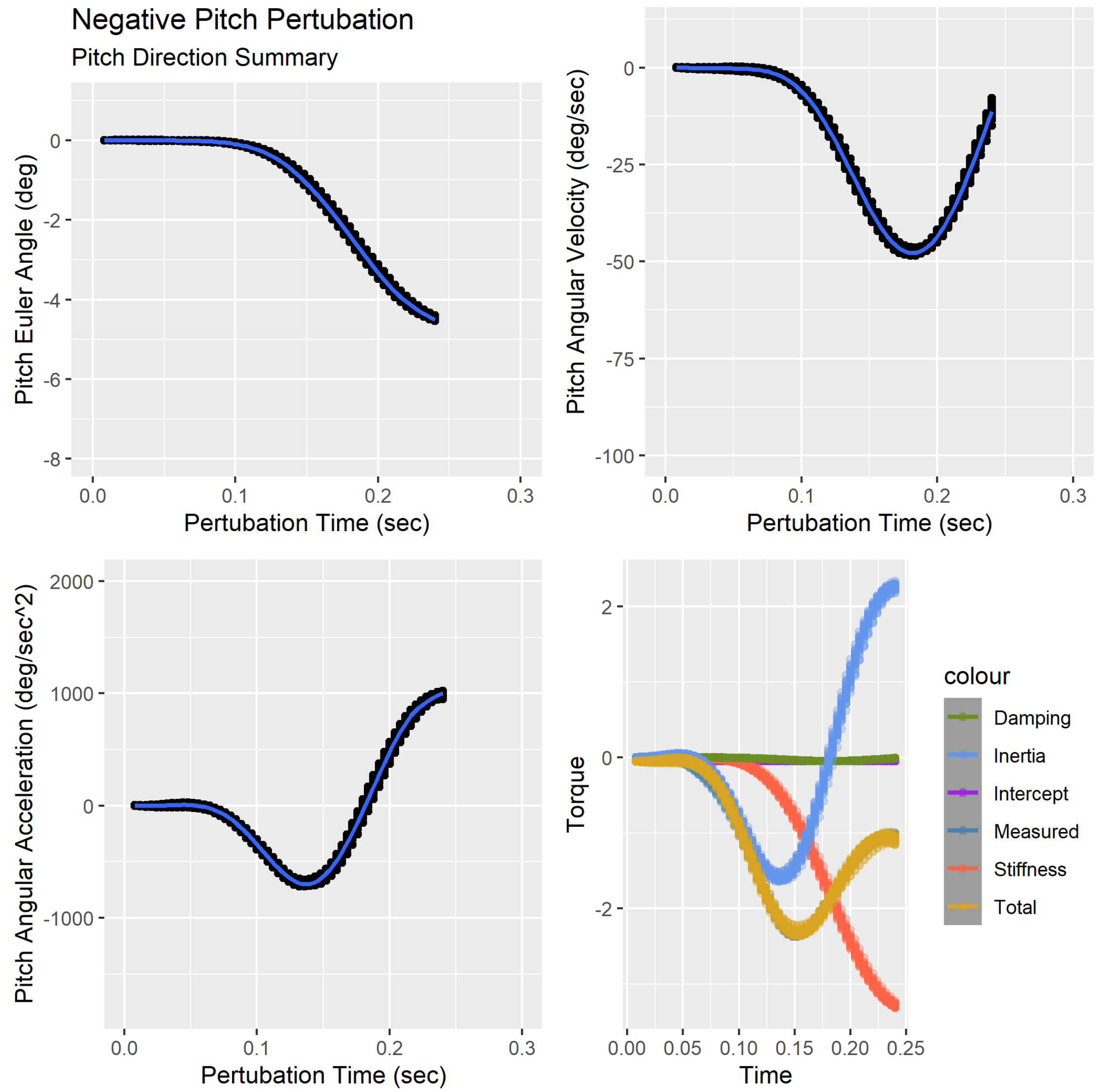

Negative Pitch Pertubation

Pitch Direction Summary

Figure 7.19: Shown are position, velocity, acceleration, corresponding torque and IBK contribution estimates for 42.3 Nm/rad spring, 1 kg of added mass, experiment 2

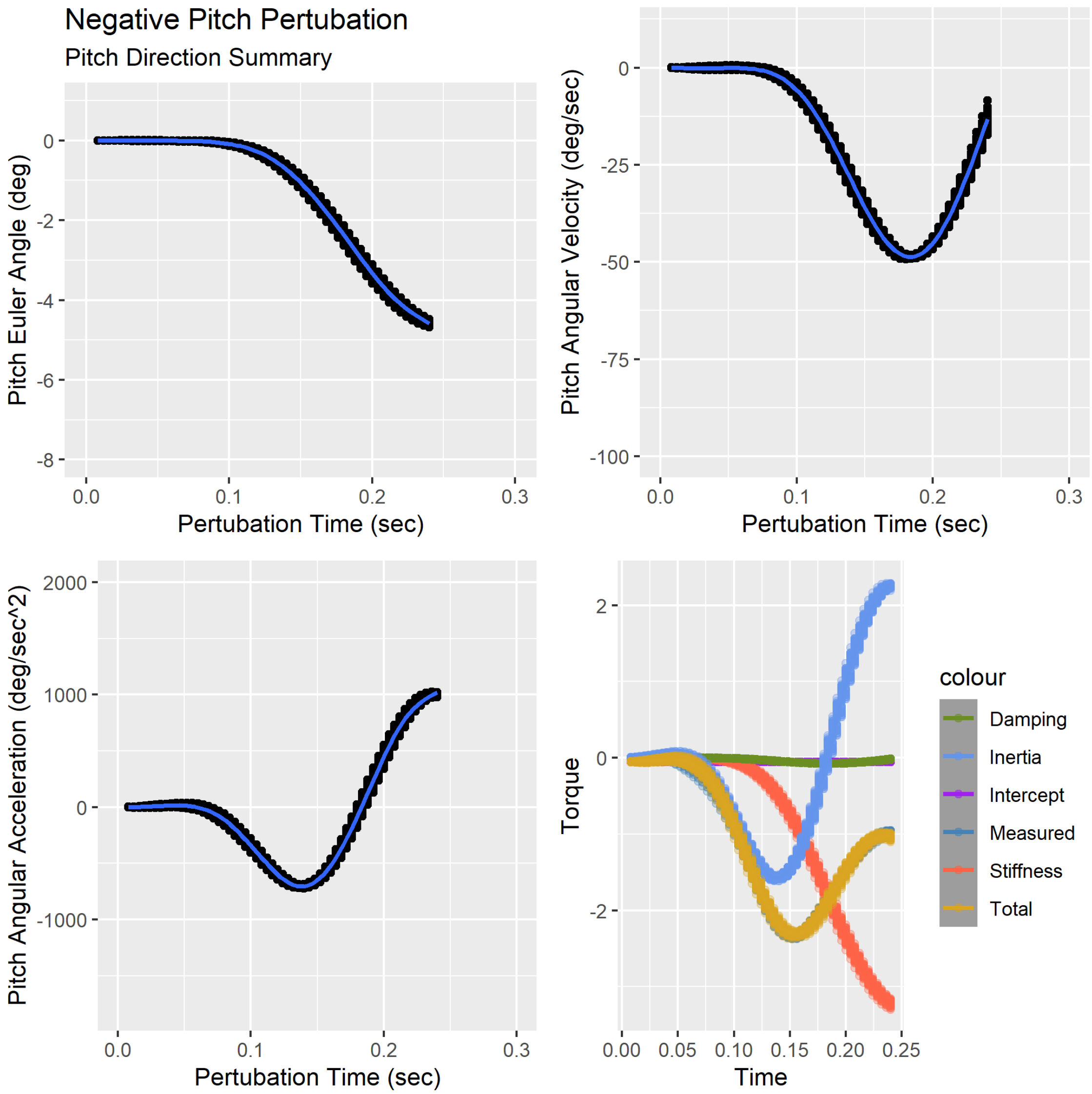

Figure 7.20: Shown are position, velocity, acceleration, corresponding torque and IBK contribution estimates for 42.3 Nm/rad spring, 1 kg of added mass, experiment 3

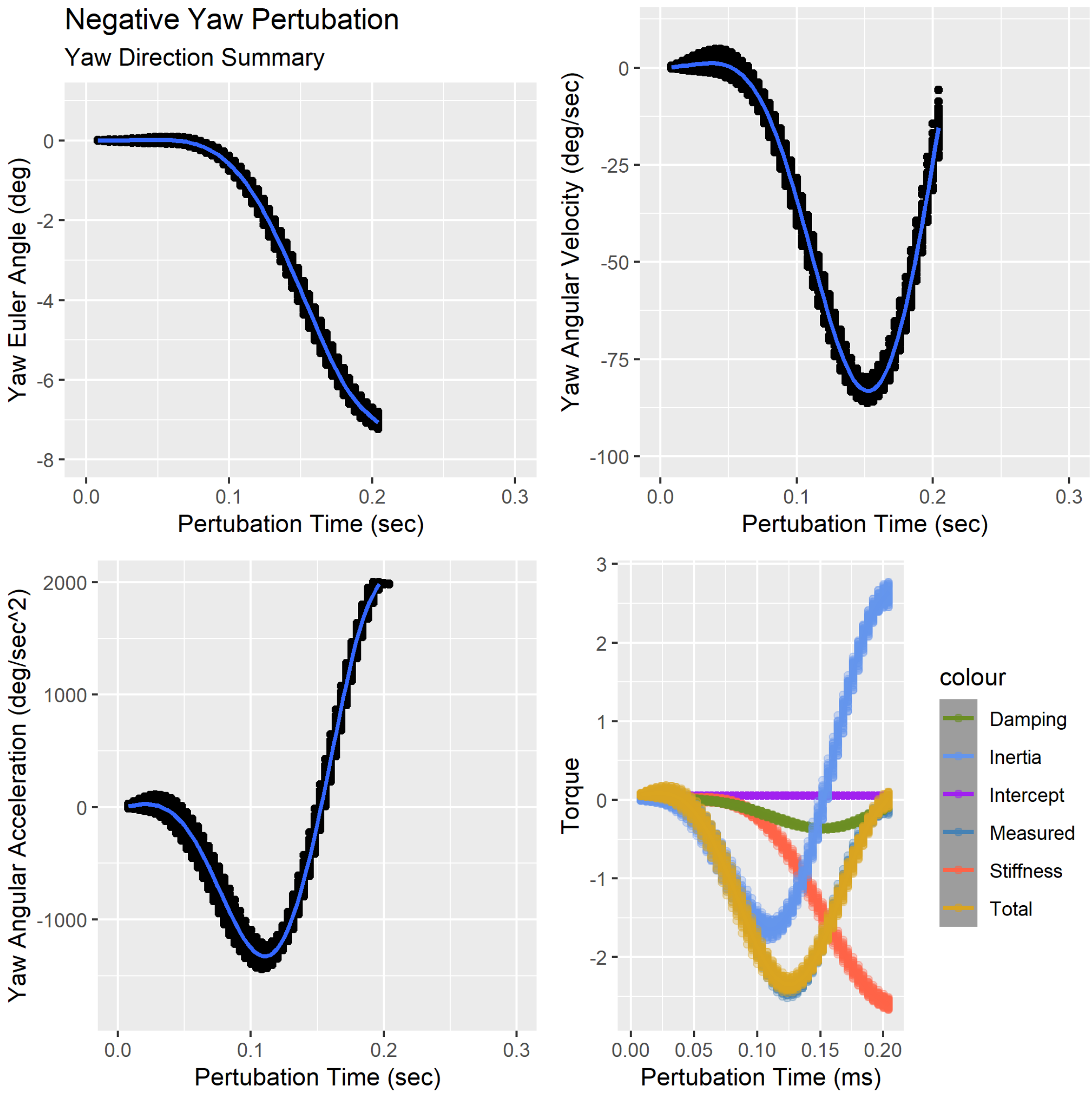

Figure 7.21: Shown are position, velocity, acceleration, corresponding torque and IBK contribution estimates for 24.4 Nm/rad spring, 0 kg of added mass, experiment 1

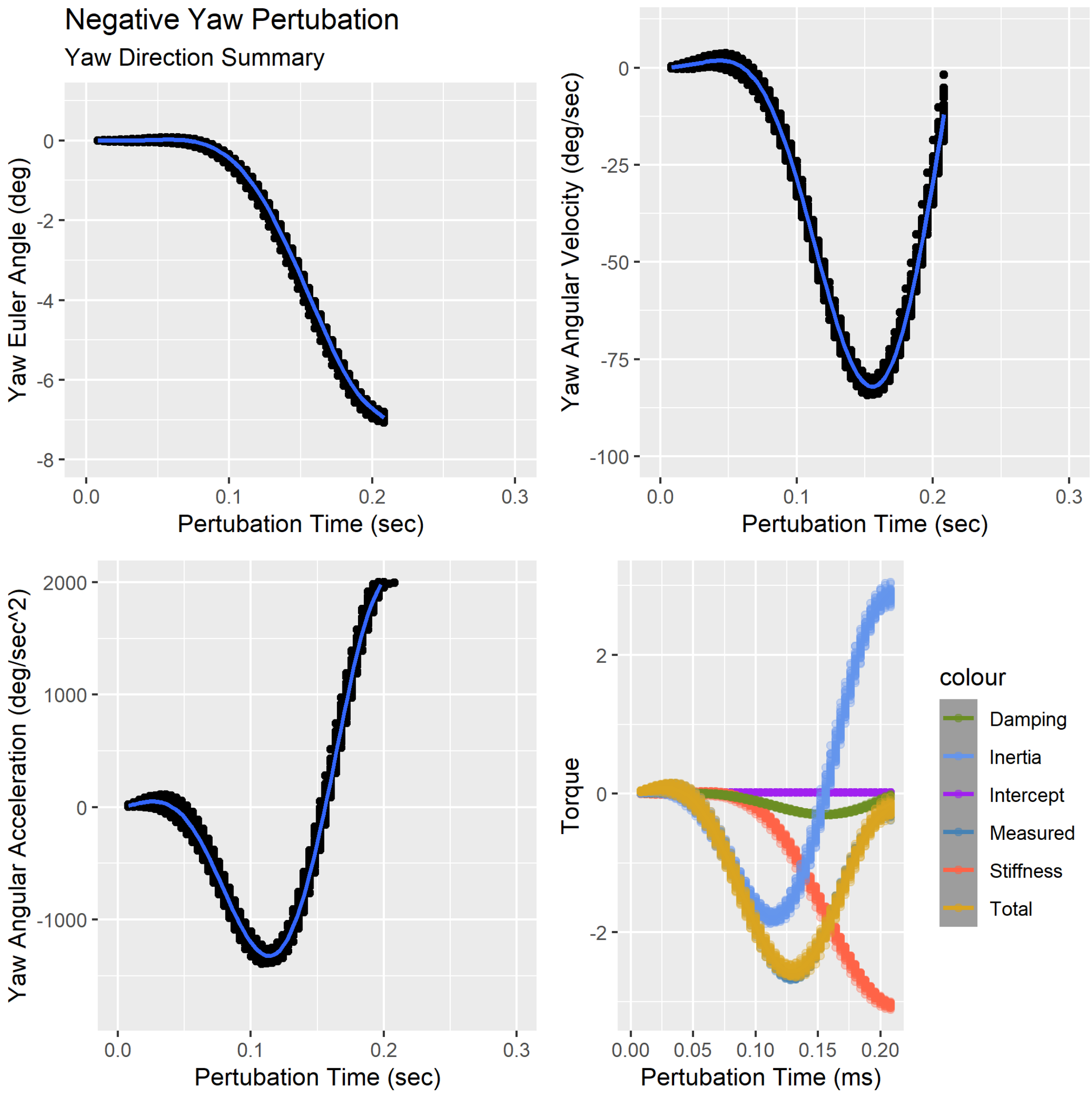

Figure 7.22: Shown are position, velocity, acceleration, corresponding torque and IBK contribution estimates for 24.4 Nm/rad spring, 0 kg of added mass, experiment 2

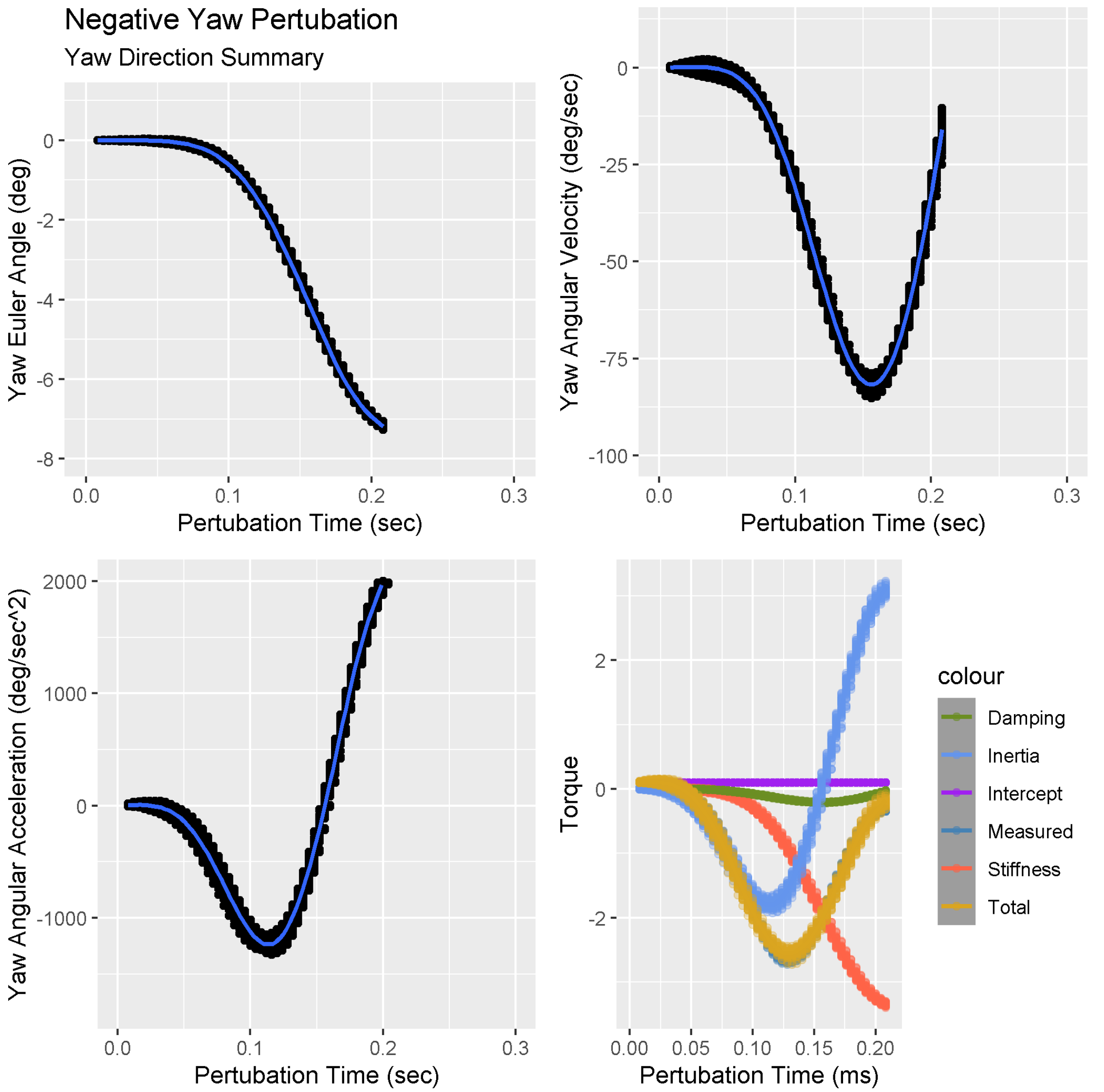

Figure 7.23: Shown are position, velocity, acceleration, corresponding torque and IBK contribution estimates for 24.4 Nm/rad spring, 0 kg of added mass, experiment 3

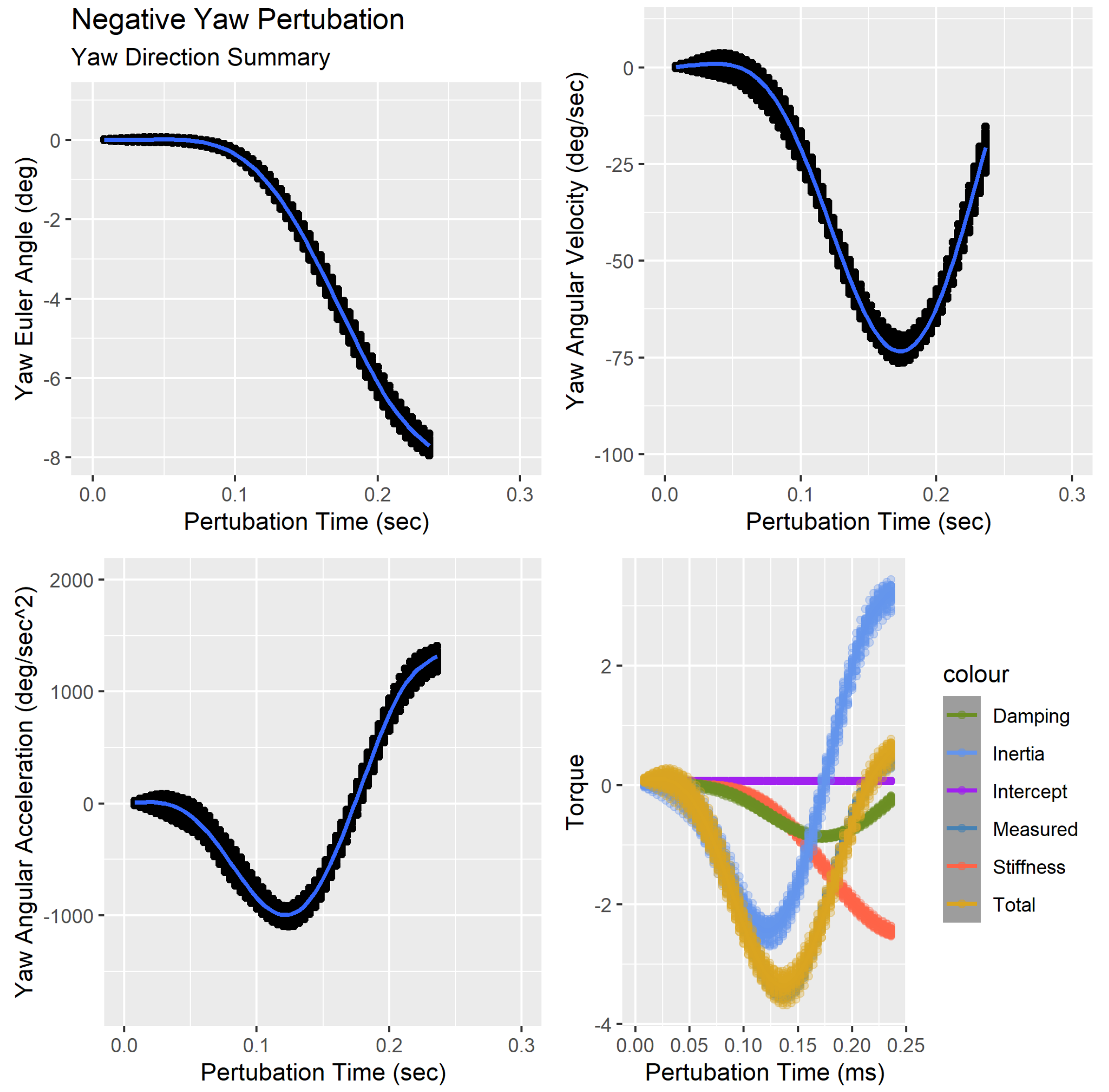

Figure 7.24: Shown are position, velocity, acceleration, corresponding torque and IBK contribution estimates for 24.4 Nm/rad spring, 1 kg of added mass, experiment 1

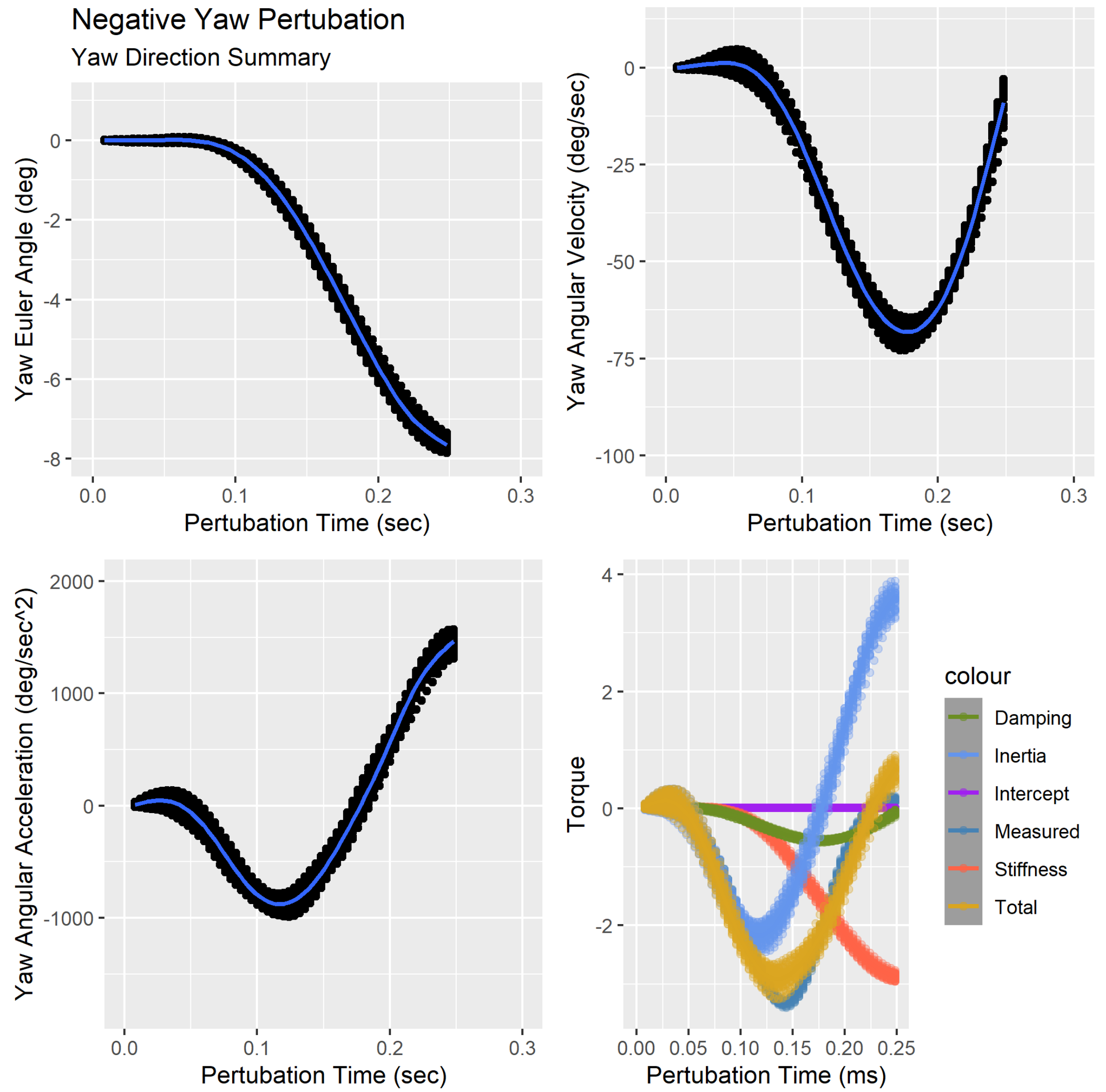

Figure 7.25: Shown are position, velocity, acceleration, corresponding torque and IBK contribution estimates for 24.4 Nm/rad spring, 1 kg of added mass, experiment 2

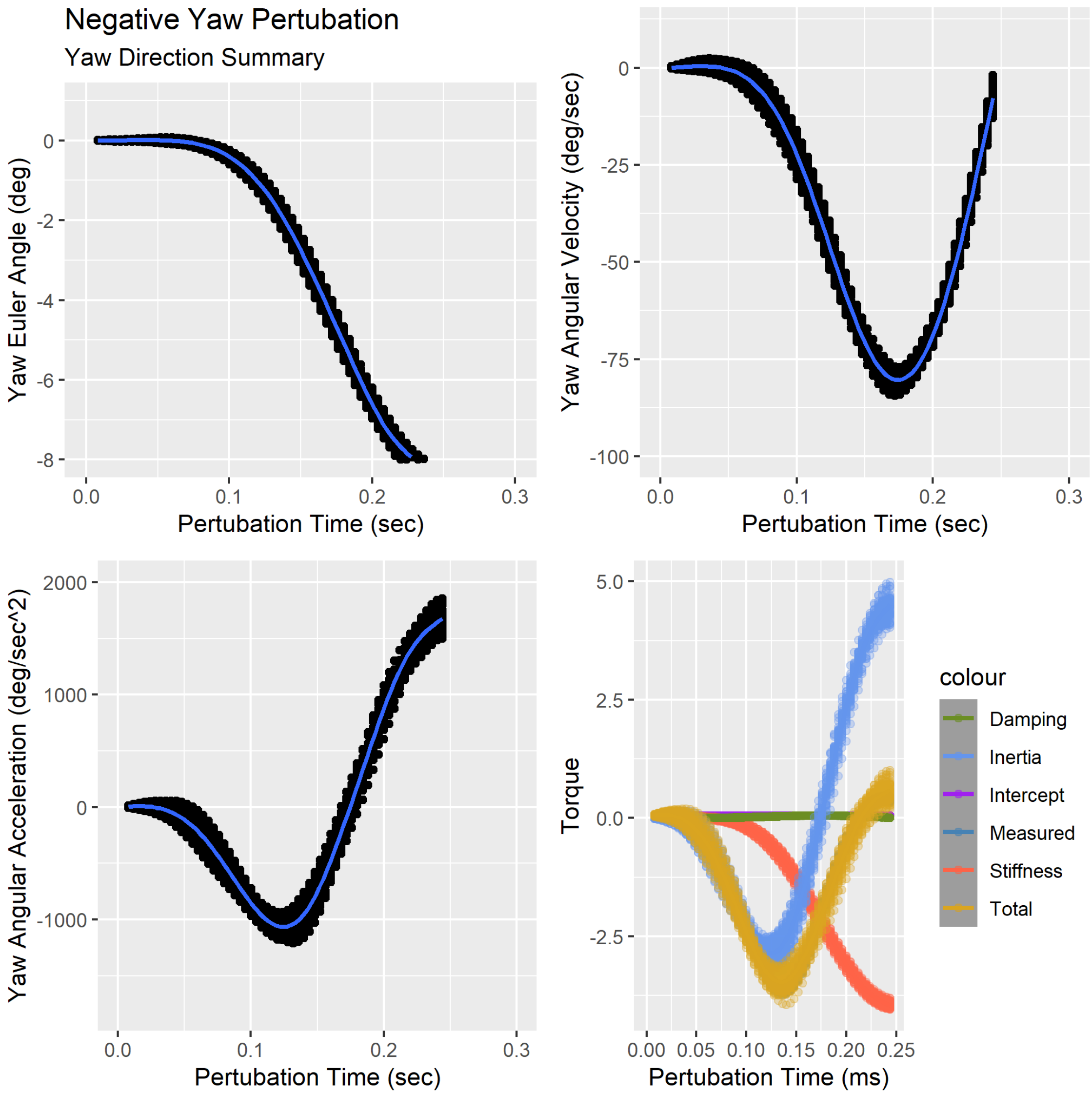

Figure 7.26: Shown are position, velocity, acceleration, corresponding torque and IBK contribution estimates for 24.4 Nm/rad spring, 1 kg of added mass, experiment 3

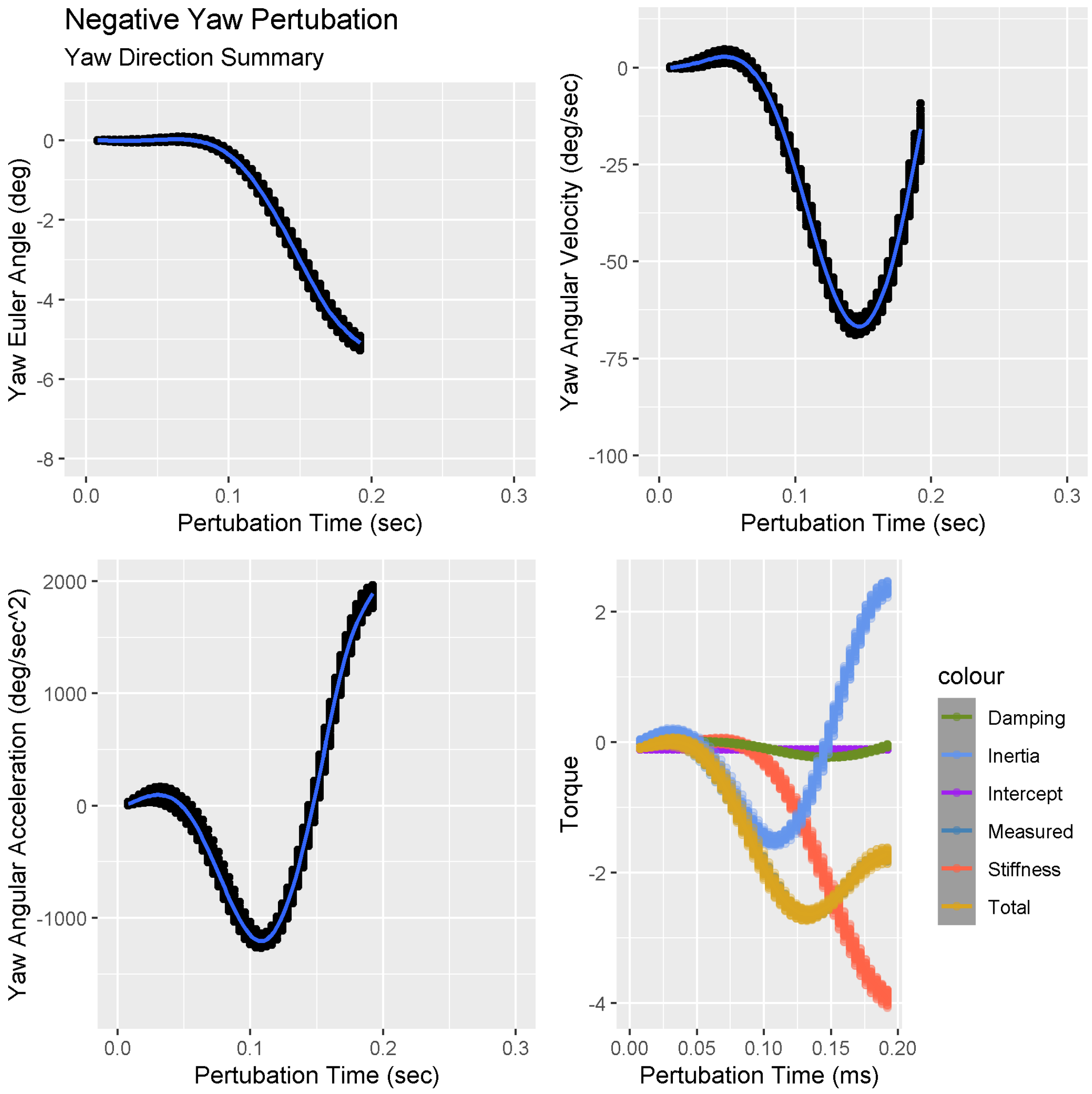

Figure 7.27: Shown are position, velocity, acceleration, corresponding torque and IBK contribution estimates for 42.3 Nm/rad spring, 0 kg of added mass, experiment 1

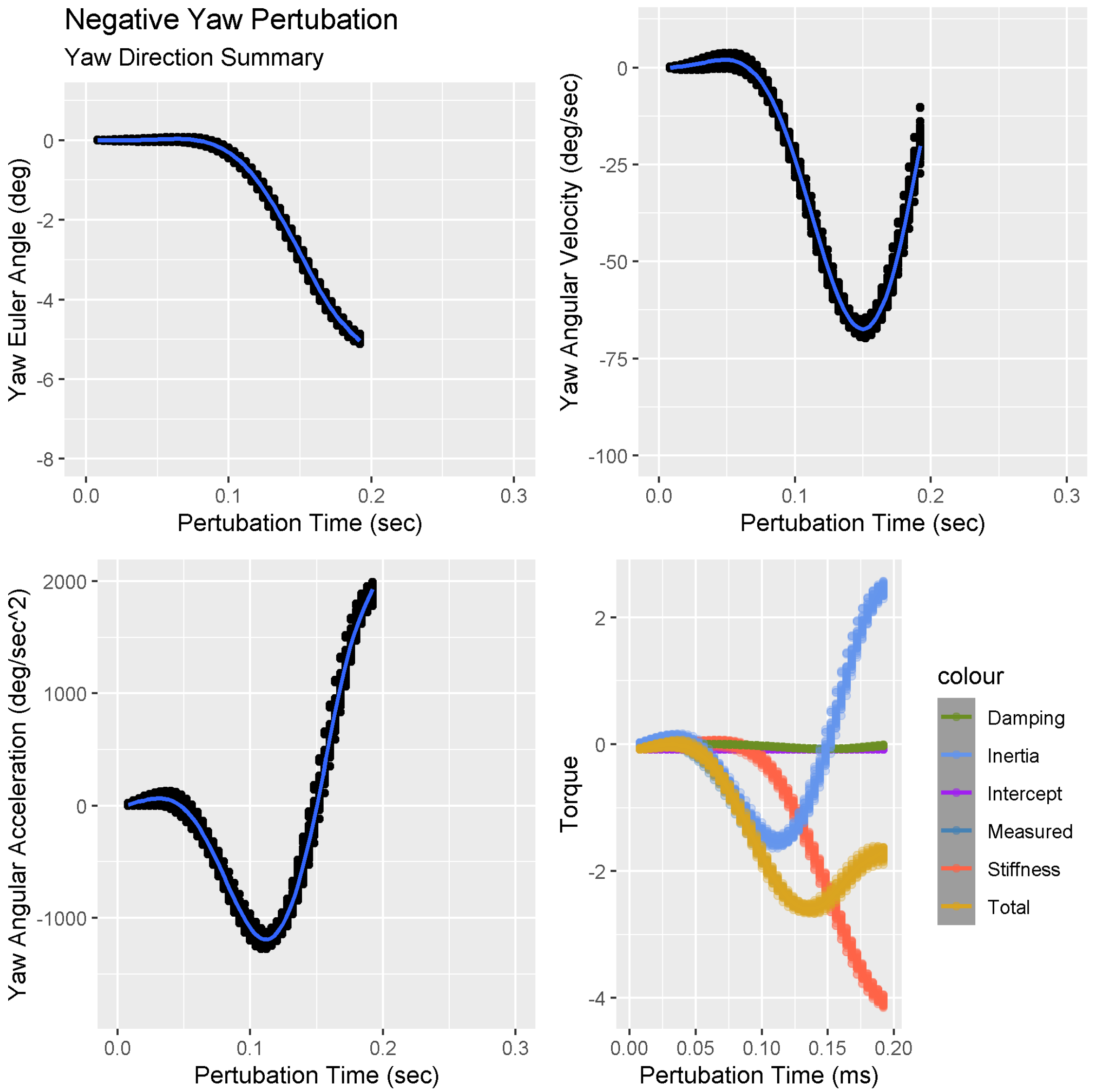

Figure 7.28: Shown are position, velocity, acceleration, corresponding torque and IBK contribution estimates for 42.3 Nm/rad spring, 0 kg of added mass, experiment 2

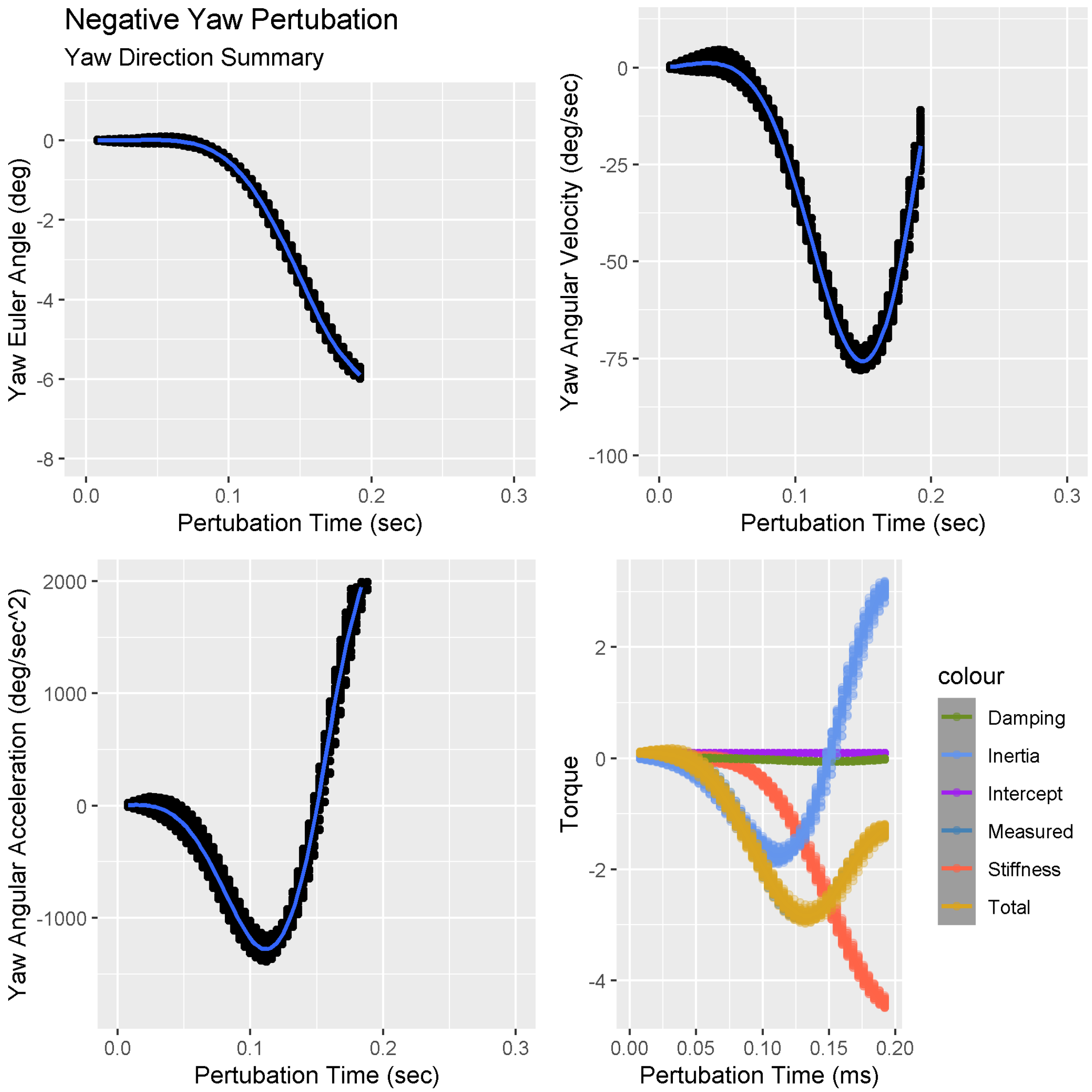

Figure 7.29: Shown are position, velocity, acceleration, corresponding torque and IBK contribution estimates for 42.3 Nm/rad spring, 0 kg of added mass, experiment 3

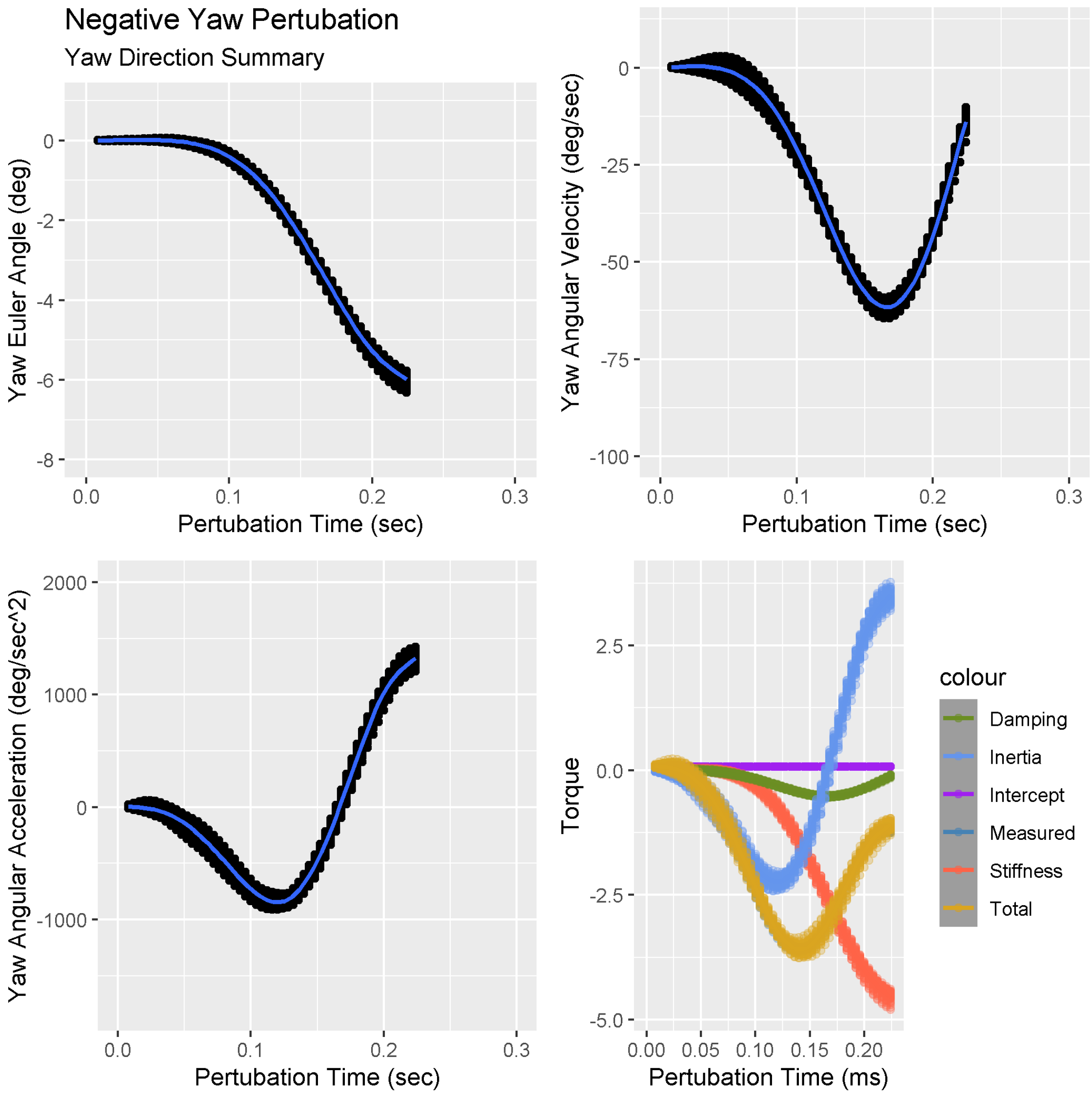

Figure 7.30: Shown are position, velocity, acceleration, corresponding torque and IBK contribution estimates for 42.3 Nm/rad spring, 1 kg of added mass, experiment 1

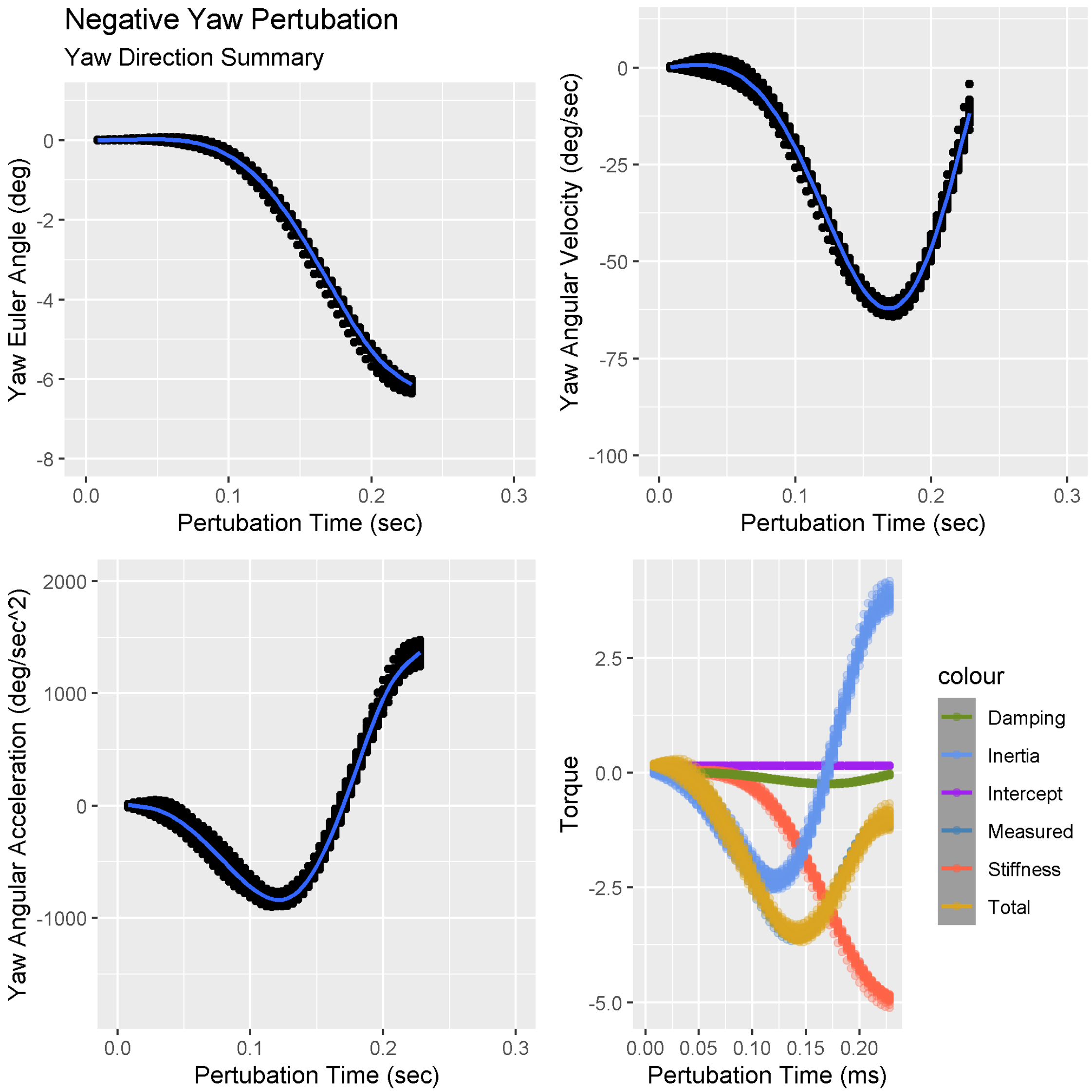

Figure 7.31: Shown are position, velocity, acceleration, corresponding torque and IBK contribution estimates for 42.3 Nm/rad spring, 1 kg of added mass, experiment 2

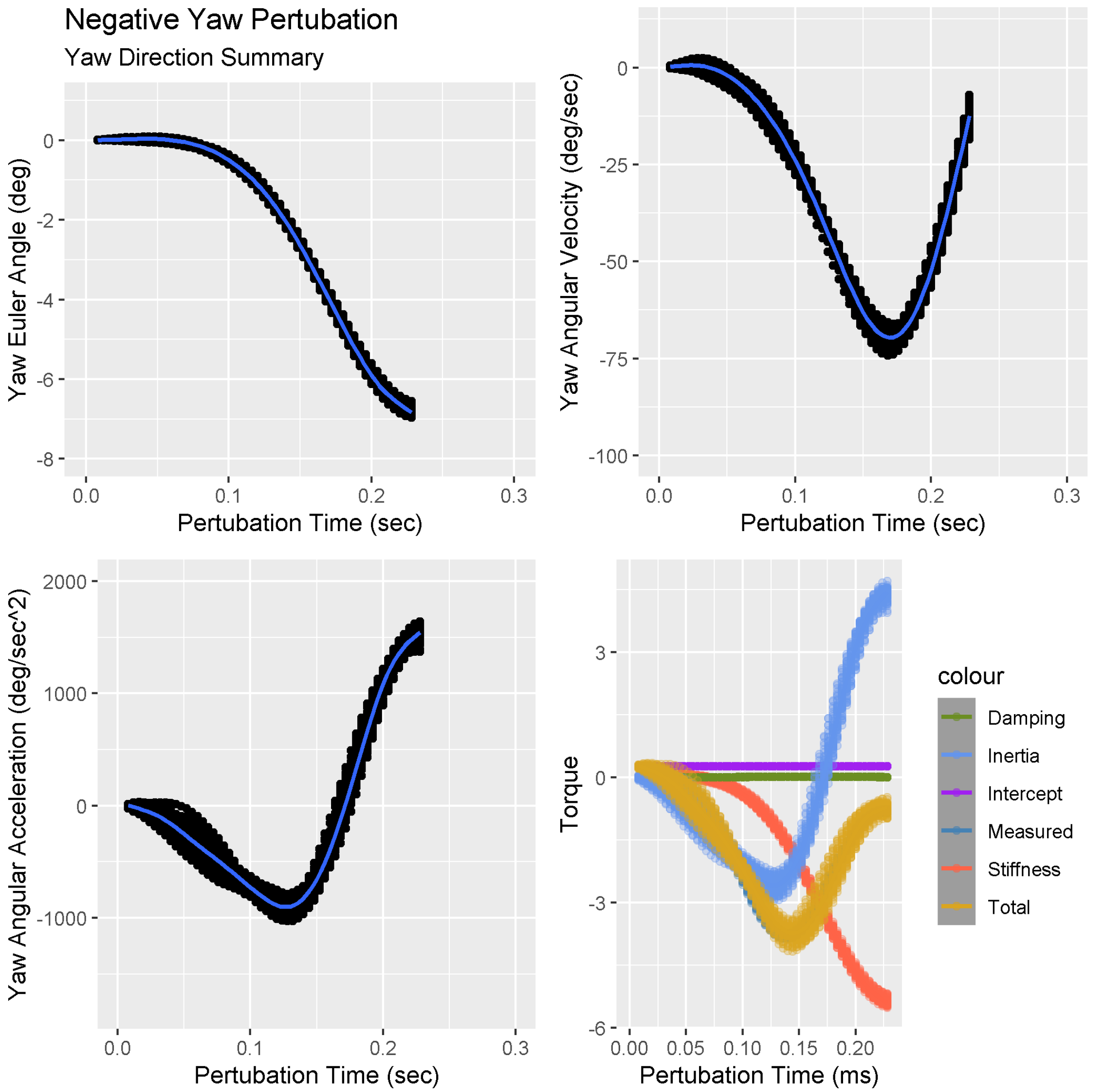
Negative Yaw Pertubation

Yaw Direction Summary

Figure 7.32: Shown are position, velocity, acceleration, corresponding torque and IBK contribution estimates for 42.3 Nm/rad spring, 1 kg of added mass, experiment 3

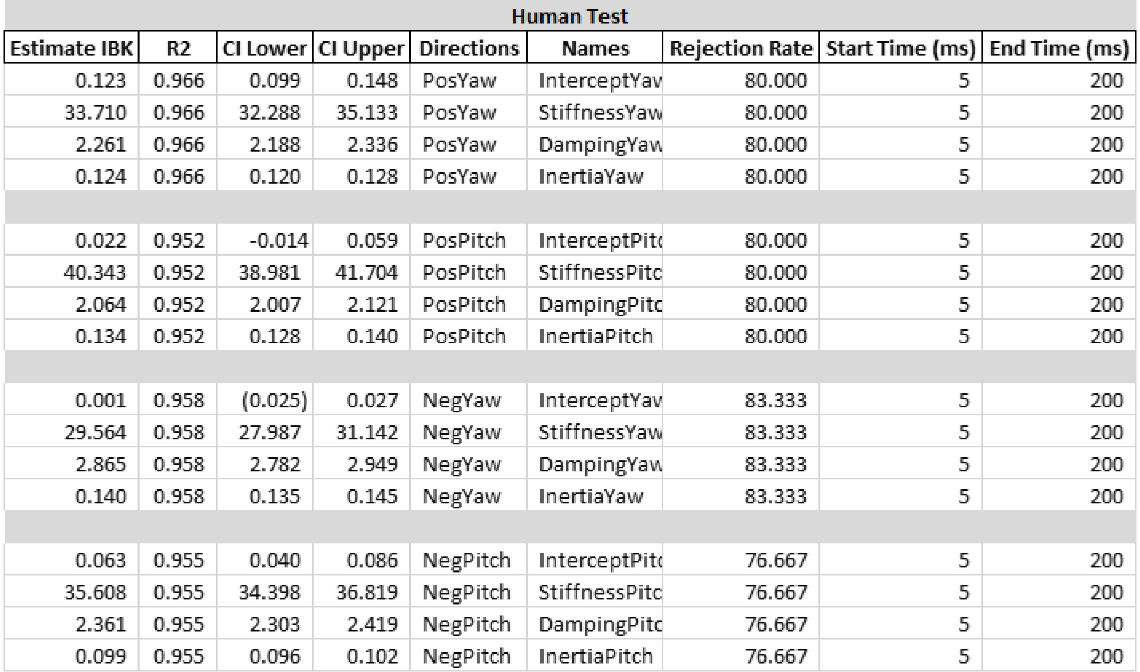

Human Test

Estimate IBK	R2	CI Lower	CI Upper	Directions	Names	Rejection Rate	Start Time (ms)	End Time (ms)
0.123	0.966	0.099	0.148	PosYaw	InterceptYav	80.000	5	200
33.710	0.966	32.288	35.133	PosYaw	StiffnessYaw	80.000	5	200
2.261	0.966	2.188	2.336	PosYaw	DampingYaw	80.000	5	200
0.124	0.966	0.120	0.128	PosYaw	InertiaYaw	80.000	5	200
0.022	0.952	-0.014	0.059	PosPitch	InterceptPit	80.000	5	200
40.343	0.952	38.981	41.704	PosPitch	StiffnessPitc	80.000	5	200
2.064	0.952	2.007	2.121	PosPitch	DampingPitc	80.000	5	200
0.134	0.952	0.128	0.140	PosPitch	InertiaPitch	80.000	5	200
0.001	0.958	(0.025)	0.027	NegYaw	InterceptYav	83.333	5	200
29.564	0.958	27.987	31.142	NegYaw	StiffnessYaw	83.333	5	200
2.865	0.958	2.782	2.949	NegYaw	DampingYaw	83.333	5	200
0.140	0.958	0.135	0.145	NegYaw	InertiaYaw	83.333	5	200
0.063	0.955	0.040	0.086	NegPitch	InterceptPit	76.667	5	200
35.608	0.955	34.398	36.819	NegPitch	StiffnessPitc	76.667	5	200
2.361	0.955	2.303	2.419	NegPitch	DampingPitc	76.667	5	200
0.099	0.955	0.096	0.102	NegPitch	InertiaPitch	76.667	5	200

Figure 7.33: IBK results for the human subject in all four primary directions

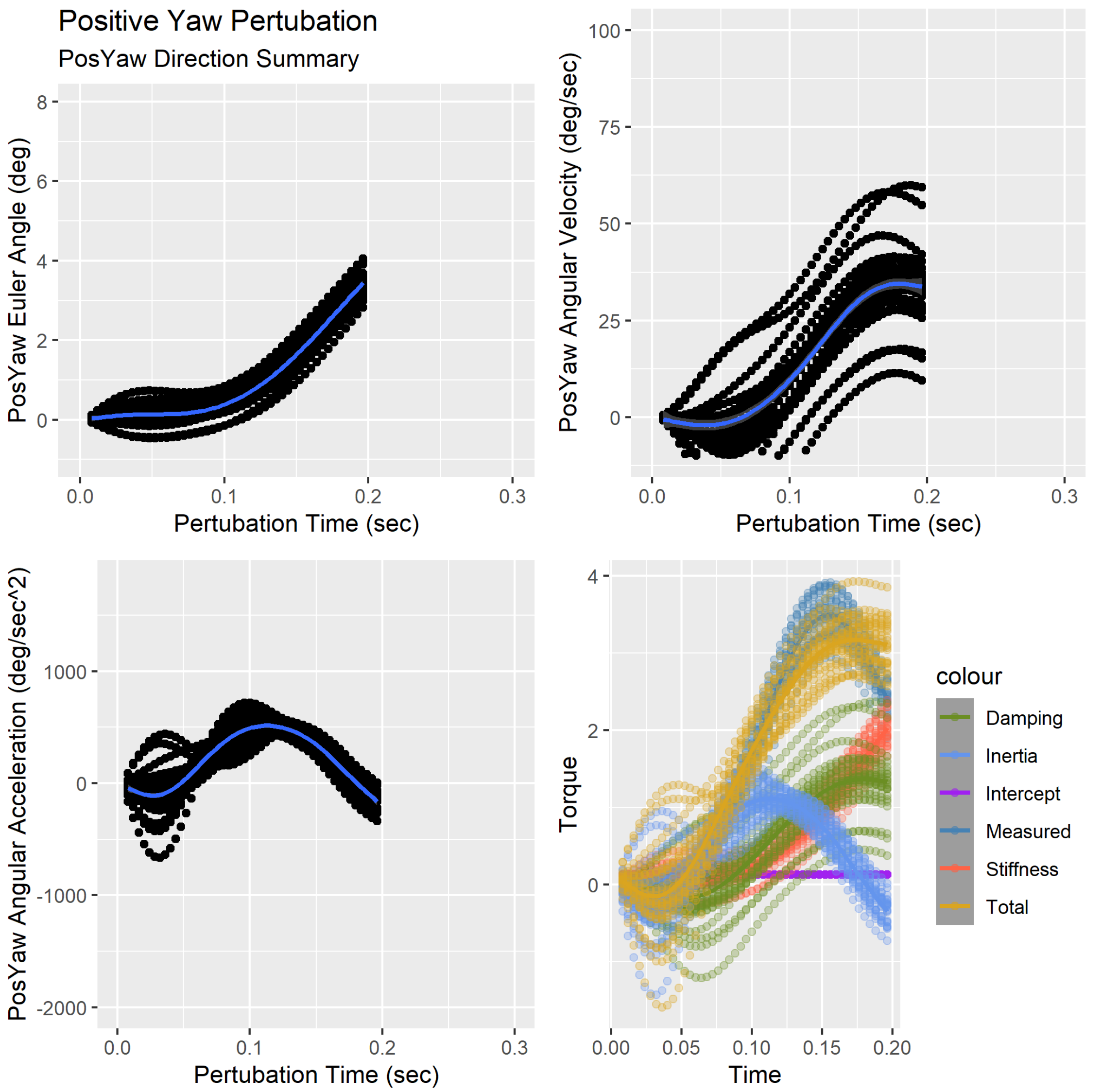

Figure 7.34: Shown are position, velocity, acceleration, corresponding torque and IBK contribution estimates for the human subject in the positive yaw direction.

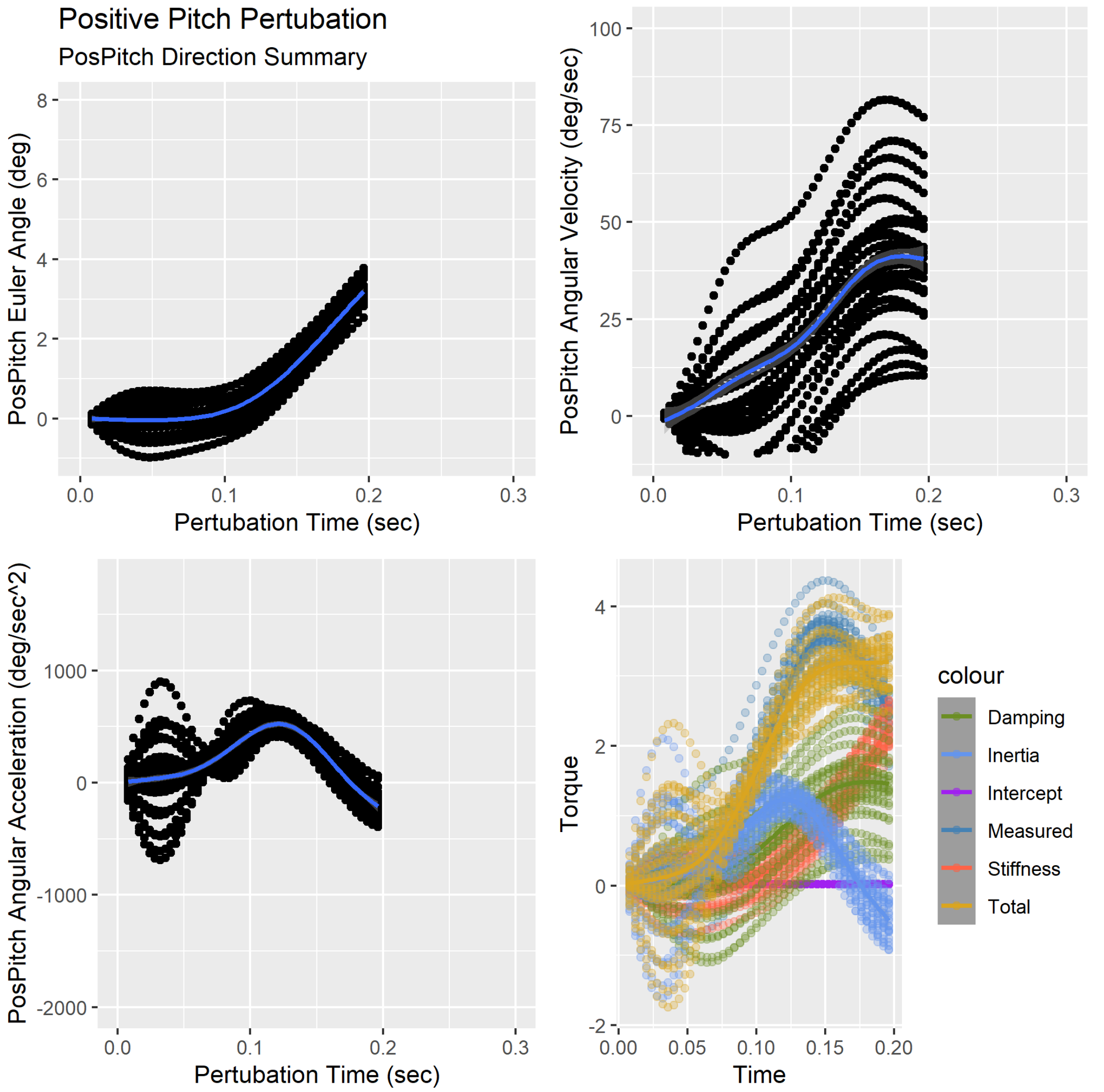

Figure 7.35: Shown are position, velocity, acceleration, corresponding torque and IBK contribution estimates for the human subject in the positive pitch direction.

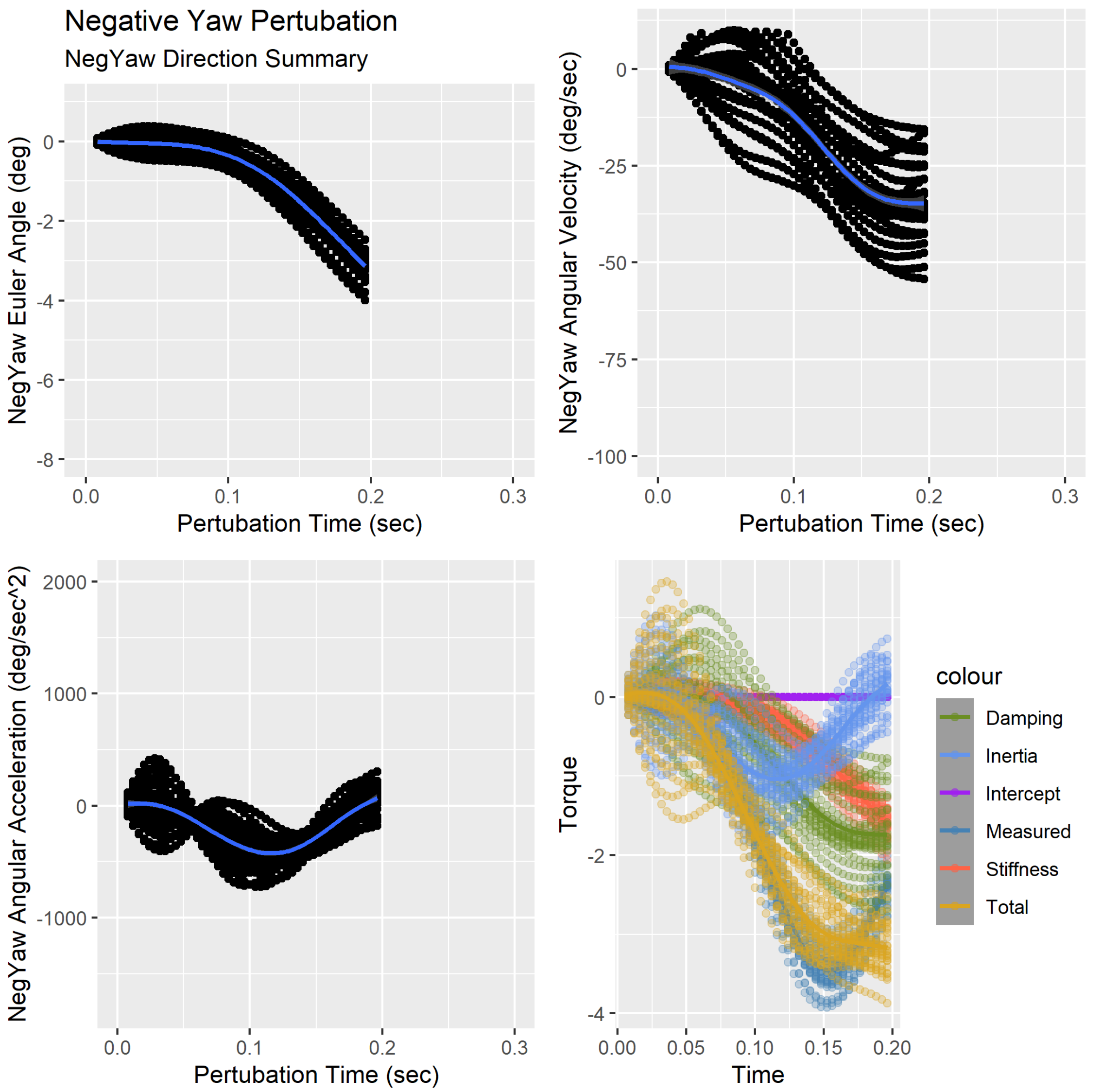

Figure 7.36: Shown are position, velocity, acceleration, corresponding torque and IBK contribution estimates for the human subject in the negative yaw direction.

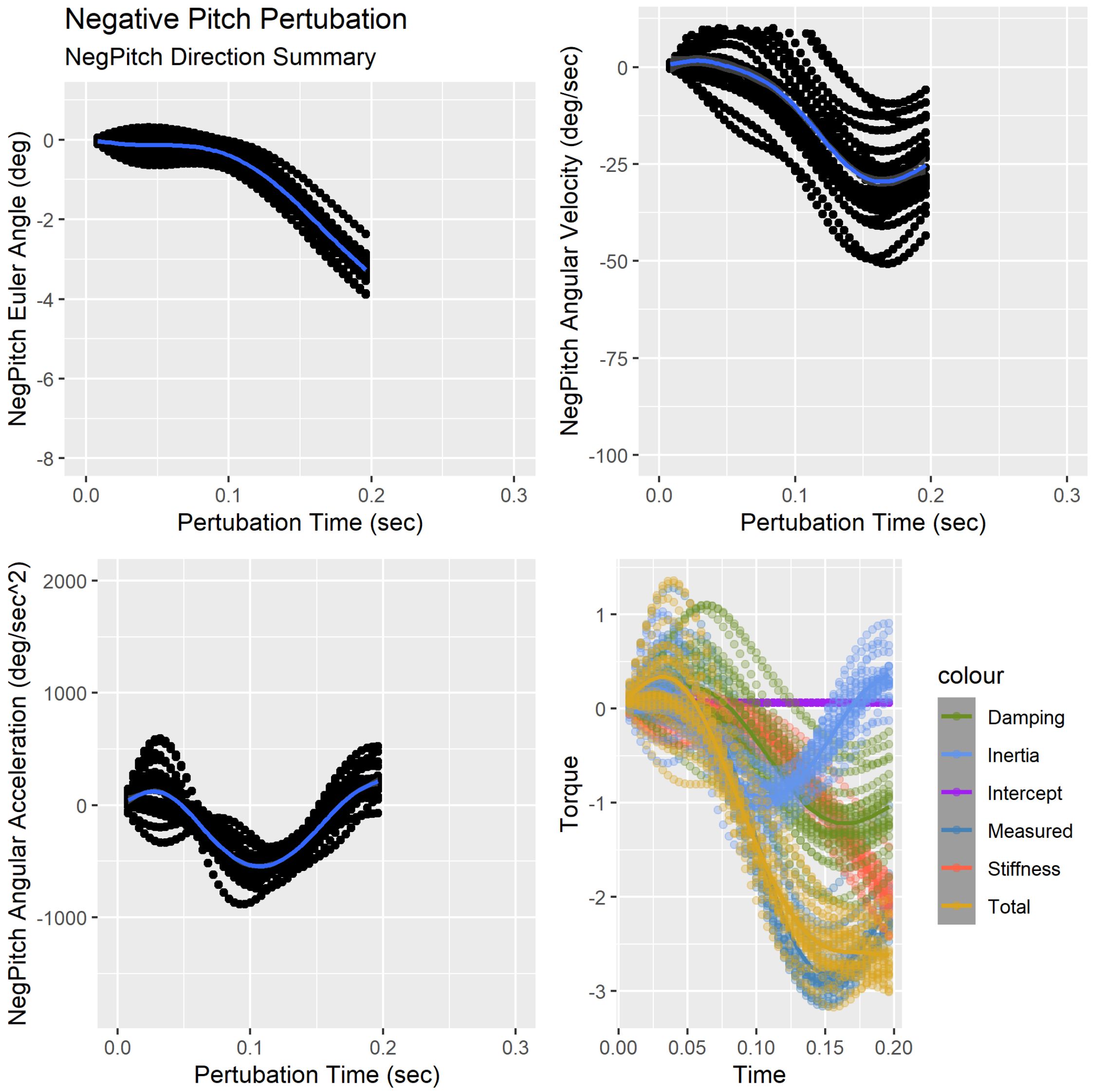

Figure 7.37: Shown are position, velocity, acceleration, corresponding torque and IBK contribution estimates for the human subject in the negative pitch direction.

REFERENCES

Alici, G. and B. Shirinzadeh, “Topology optimisation and singularity analysis of a 3-sps parallel manipulator with a passive constraining spherical joint”, Mechanism and Machine Theory **39**, 2, 215–235 (2004).

Bogue, R., “Exoskeletons and robotic prosthetics: a review of recent developments”, Industrial Robot: An International Journal **36**, 5, 421–427 (2009).

Burdet, E., R. Osu, D. W. Franklin, T. E. Milner and M. Kawato, “The central nervous system stabilizes unstable dynamics by learning optimal impedance”, Nature **414**, 6862, 446 (2001).

Carignan, C., M. Liszka and S. Roderick, “Design of an arm exoskeleton with scapula motion for shoulder rehabilitation”, in “Advanced Robotics, 2005. ICAR’05. Proceedings., 12th International Conference on”, pp. 524–531 (IEEE, 2005).

Cempini, M., S. M. De Rossi, T. Lenzi, N. Vitiello and M. Carrozza, “Self-alignment mechanisms for assistive wearable robots: A kinetostatic compatibility method”, Robotics, IEEE Transactions on **29**, 1, 236–250 (2013).

Craig, J. J., *Introduction to robotics: mechanics and control*, vol. 3 (Pearson/Prentice Hall Upper Saddle River, NJ, USA:, 2005).

Dasgupta, B. and T. Mruthyunjaya, “The stewart platform manipulator: a review”, Mechanism and machine theory **35**, 1, 15–40 (2000).

Deblaise, D., X. Hernot and P. Maurine, “A systematic analytical method for pkm stiffness matrix calculation”, in “Robotics and Automation, 2006. ICRA 2006. Proceedings 2006 IEEE International Conference on”, pp. 4213–4219 (IEEE, 2006).

Di Gregorio, R., “Kinematics of the 3-upu wrist”, Mechanism and machine theory **38**, 3, 253–263 (2003).

El-Khasawneh, B. S. and P. M. Ferreira, “Computation of stiffness and stiffness bounds for parallel link manipulators1”, International Journal of Machine Tools and Manufacture **39**, 2, 321–342 (1999).

Erwin, A., M. K. O’Malley, D. Ress and F. Sergi, “Development, control, and mri-compatibility of the mr-softwrist”, in “Rehabilitation Robotics (ICORR), 2015 IEEE International Conference on”, pp. 187–192 (IEEE, 2015).

Fan, Y. and Y. Yin, “Mechanism design and motion control of a parallel ankle joint for rehabilitation robotic exoskeleton”, in “2009 IEEE International Conference on Robotics and Biomimetics (ROBIO)”, pp. 2527–2532 (IEEE, 2009).

Gan, D., J. S. Dai, J. Dias and L. Seneviratne, “Forward kinematics solution distribution and analytic singularity-free workspace of linear-actuated symmetrical spherical parallel manipulators”, Journal of Mechanisms and Robotics **7**, 4, 041007 (2015).

Gao, X.-S., D. Lei, Q. Liao and G.-F. Zhang, “Generalized stewart-gough platforms and their direct kinematics”, Robotics, IEEE Transactions on **21**, 2, 141–151 (2005).

Glosser, G. D. and W. S. Newman, “The implementation of a natural admittance controller on an industrial manipulator”, in “Robotics and Automation, 1994. Proceedings., 1994 IEEE International Conference on”, pp. 1209–1215 (IEEE, 1994).

Gogu, G., *Structural synthesis of parallel robots* (Springer, 2008).

Gosselin, C., “Stiffness mapping for parallel manipulators”, IEEE Transactions on Robotics and Automation **6**, 3, 377–382 (1990).

Gosselin, C. and J. Angeles, “The optimum kinematic design of a spherical three-degree-of-freedom parallel manipulator”, Journal of mechanisms, transmissions, and automation in design **111**, 2, 202–207 (1989).

Gosselin, C. M. and E. Lavoie, “On the kinematic design of spherical three-degree-of-freedom parallel manipulators”, The International Journal of Robotics Research **12**, 4, 394–402 (1993).

Gupta, A., M. K. O’Malley, V. Patoglu and C. Burgar, “Design, control and performance of ricewrist: A force feedback wrist exoskeleton for rehabilitation and training”, The International Journal of Robotics Research **27**, 2, 233–251 (2008).

Haninger, K., J. Lu, W. Chen and M. Tomizuka, “Kinematic design and analysis for a macaque upper-limb exoskeleton with shoulder joint alignment”, in “Intelligent Robots and Systems (IROS 2014), 2014 IEEE/RSJ International Conference on”, pp. 478–483 (IEEE, 2014).

Harryman, D. T., J. Sidles, J. M. Clark, K. J. McQuade, T. D. Gibb and F. A. Matsen, “Translation of the humeral head on the glenoid with passive glenohumeral motion.”, J Bone Joint Surg Am **72**, 9, 1334–1343 (1990).

Hoffman, J., *Norms for fitness, performance, and health* (Human Kinetics, 2006).

Hogan, N., “Impedance control: An approach to manipulation: Part iiimplementation”, Journal of dynamic systems, measurement, and control **107**, 1, 8–16 (1985).

Hogan, N., “On the stability of manipulators performing contact tasks”, IEEE Journal on Robotics and Automation **4**, 6, 677–686 (1988).

Hogan, N., H. I. Krebs, J. Charnnarong, P. Srikrishna and A. Sharon, "Mit-manus: a workstation for manual therapy and training. i", in "Robot and Human Communication, 1992. Proceedings., IEEE International Workshop on", pp. 161–165 (IEEE, 1992).

Hughes, T. J., *The finite element method: linear static and dynamic finite element analysis* (Courier Corporation, 2012).

Hunt, J., P. Artemiadis and H. Lee, "Optimizing stiffness of a novel parallel-actuated robotic shoulder exoskeleton for a desired task or workspace", in "2018 IEEE International Conference on Robotics and Automation (ICRA)", pp. 6745–6751 (IEEE, 2018).

Hunt, J. and H. Lee, "A new parallel actuated architecture for exoskeleton applications involving multiple degree-of-freedom biological joints", Journal of Mechanisms and Robotics **10**, 5, 051017 (2018).

Hunt, J. and H. Lee, "Development of a low inertia parallel actuated shoulder exoskeleton robot for the characterization of neuromuscular property during static posture and dynamic movement", in "2019 International Conference on Robotics and Automation (ICRA)", pp. 556–562 (IEEE, 2019).

Hunt, J., H. Lee and P. Artemiadis, "A novel shoulder exoskeleton robot using parallel actuation and a passive slip interface", Journal of Mechanisms and Robotics **9**, 1, 011002 (2017).

Hunt, K., "Structural kinematics of in-parallel-actuated robot-arms", Journal of Mechanisms, Transmissions, and Automation in Design **105**, 4, 705–712 (1983).

Ito, T., E. Z. Murano and H. Gomi, “Fast force-generation dynamics of human articulatory muscles”, Journal of applied physiology **96**, 6, 2318–2324 (2004).

Jarrassé, N. and G. Morel, “Connecting a human limb to an exoskeleton”, Robotics, IEEE Transactions on **28**, 3, 697–709 (2012).

Jiang, Q. and C. M. Gosselin, “Determination of the maximal singularity-free orientation workspace for the gough–stewart platform”, Mechanism and Machine Theory **44**, 6, 1281–1293 (2009).

Jung, Y. and J. Bae, “Performance verification of a kinematic prototype 5-dof upper-limb exoskeleton with a tilted and vertically translating shoulder joint”, in “Advanced Intelligent Mechatronics (AIM), 2014 IEEE/ASME International Conference on”, pp. 263–268 (IEEE, 2014).

Kearney, R. E., R. B. Stein and L. Parameswaran, “Identification of intrinsic and reflex contributions to human ankle stiffness dynamics”, IEEE transactions on biomedical engineering **44**, 6, 493–504 (1997).

Khatib, O., “Augmented object and reduced effective inertia in robot systems”, in “American Control Conference, 1988”, pp. 2140–2147 (IEEE, 1988).

Kim, H. S. and L.-W. Tsai, “Kinematic synthesis of spatial 3-rps parallel manipulators”, in “ASME 2002 International Design Engineering Technical Conferences and Computers and Information in Engineering Conference”, pp. 873–880 (American Society of Mechanical Engineers, 2002).

Klein, J., S. Spencer, J. Allington, J. E. Bobrow and D. J. Reinkensmeyer, “Optimization of a parallel shoulder mechanism to achieve a high-force, low-mass, robotic-arm exoskeleton”, IEEE Transactions on Robotics **26**, 4, 710–715 (2010).

Kong, X. and C. M. Gosselin, “Type synthesis of 3-dof translational parallel manipulators based on screw theory”, Journal of mechanical design **126**, 1, 83–92 (2004).

KUKA, R. G., *LBR iiwa 7 R800, LBR iiwa 14 R820 Specification* (KUKA, 2015c).

Kurtzer, I. L., J. A. Pruszynski and S. H. Scott, “Long-latency reflexes of the human arm reflect an internal model of limb dynamics”, Current Biology **18**, 6, 449–453 (2008).

Lee, H., P. Ho, M. A. Rastgaar, H. I. Krebs and N. Hogan, “Multivariable static ankle mechanical impedance with relaxed muscles”, Journal of biomechanics **44**, 10, 1901–1908 (2011).

Lee, H. and N. Hogan, “Time-varying ankle mechanical impedance during human locomotion”, IEEE Transactions on Neural Systems and Rehabilitation Engineering **23**, 5, 755–764 (2015).

Lee, K.-M. and D. K. Shah, “Dynamic analysis of a three-degrees-of-freedom in-parallel actuated manipulator”, IEEE Journal on Robotics and Automation **4**, 3, 361–367 (1988).

Li, Y. and G. M. Bone, “Are parallel manipulators more energy efficient?”, in “Computational Intelligence in Robotics and Automation, 2001. Proceedings 2001 IEEE International Symposium on”, pp. 41–46 (IEEE, 2001).

Lipps, D. B., E. M. Baillargeon, D. Ludvig and E. J. Perreault, “System identification of multidimensional shoulder impedance during volitional contractions”, IFAC-PapersOnLine **48**, 28, 1369–1374 (2015).

Lipps, D. B., E. M. Baillargeon, D. Ludvig and E. J. Perreault, "Quantifying the multidimensional impedance of the shoulder during volitional contractions", Annals of Biomedical Engineering pp. 1–16 (2020).

Liu, X.-J., Z.-L. Jin and F. Gao, "Optimum design of 3-dof spherical parallel manipulators with respect to the conditioning and stiffness indices", Mechanism and machine Theory **35**, 9, 1257–1267 (2000).

Marcheschi, S., F. Salsedo, M. Fontana and M. Bergamasco, "Body extender: whole body exoskeleton for human power augmentation", in "Robotics and Automation (ICRA), 2011 IEEE International Conference on", pp. 611–616 (IEEE, 2011).

Merlet, J.-P., "Jacobian, manipulability, condition number, and accuracy of parallel robots", Journal of Mechanical Design **128**, 1, 199–206 (2006).

Merlet, J.-P., *Parallel robots*, vol. 74 (Springer Science & Business Media, 2012).

Mihelj, M., T. Nef and R. Riener, "Armin ii-7 dof rehabilitation robot: mechanics and kinematics", in "Robotics and Automation, 2007 IEEE International Conference on", pp. 4120–4125 (IEEE, 2007).

Mussa-Ivaldi, F. A., N. Hogan and E. Bizzi, "Neural, mechanical, and geometric factors subserving arm posture in humans", Journal of Neuroscience **5**, 10, 2732–2743 (1985).

Nurahmi, L., M. Solichin, D. Harnany and A. Kurniawan, "Dimension synthesis of 3-rps parallel manipulator with intersecting r-axes for ankle rehabilitation device", in "2017 18th International Conference on Advanced Robotics (ICAR)", pp. 269–274 (IEEE, 2017).

Pando, A. L., H. Lee, W. B. Drake, N. Hogan and S. K. Charles, "Position-dependent characterization of passive wrist stiffness", IEEE Transactions on Biomedical Engineering **61**, 8, 2235–2244 (2014).

Park, J.-H., P. Stegall and S. K. Agrawal, "Dynamic brace for correction of abnormal postures of the human spine", in "Robotics and Automation (ICRA), 2015 IEEE International Conference on", pp. 5922–5927 (IEEE, 2015).

Pashkevich, A., D. Chablat and P. Wenger, "Stiffness analysis of overconstrained parallel manipulators", Mechanism and Machine Theory **44**, 5, 966–982 (2009).

Pehlivan, A. U., F. Sergi, A. Erwin, N. Yozbatiran, G. E. Francisco and M. K. O'Malley, "Design and validation of the ricewrist-s exoskeleton for robotic rehabilitation after incomplete spinal cord injury", Robotica **32**, 8, 1415–1431 (2014).

Perreault, E. J., R. F. Kirsch and A. M. Acosta, "Multiple-input, multiple-output system identification for characterization of limb stiffness dynamics", Biological cybernetics **80**, 5, 327–337 (1999).

Pons, J. L., "Rehabilitation exoskeletal robotics", Engineering in Medicine and Biology Magazine, IEEE **29**, 3, 57–63 (2010).

Popescu, F., J. M. Hidler and W. Z. Rymer, "Elbow impedance during goal-directed movements", Experimental brain research **152**, 1, 17–28 (2003).

Roy, A., H. I. Krebs, S. L. Patterson, T. N. Judkins, I. Khanna, L. W. Forrester, R. M. Macko and N. Hogan, "Measurement of human ankle stiffness using the anklebot", in "Rehabilitation Robotics, 2007. ICORR 2007. IEEE 10th International Conference on", pp. 356–363 (IEEE, 2007).

Roy, A., H. I. Krebs, D. J. Williams, C. T. Bever, L. W. Forrester, R. M. Macko and N. Hogan, “Robot-aided neurorehabilitation: a novel robot for ankle rehabilitation”, IEEE transactions on robotics **25**, 3, 569–582 (2009).

Saltaren, R. J., J. M. Sabater, E. Yime, J. M. Azorin, R. Aracil and N. Garcia, “Performance evaluation of spherical parallel platforms for humanoid robots”, Robotica **25**, 03, 257–267 (2007).

Schiele, A. and F. C. Van Der Helm, “Kinematic design to improve ergonomics in human machine interaction”, IEEE Transactions on Neural Systems and Rehabilitation Engineering **14**, 4, 456–469 (2006).

Schiele, A. and G. Visentin, “The esa human arm exoskeleton for space robotics telepresence”, in “7th International Symposium on Artificial Intelligence, Robotics and Automation in Space”, pp. 19–23 (2003).

Stechert, C., H.-J. Franke and C. Wrege, “Task-based modular configurations for hybrid and redundant parallel robots”, IFAC Proceedings Volumes **39**, 15, 218–223 (2006).

Stewart, D., “A platform with six degrees of freedom”, Proceedings of the institution of mechanical engineers **180**, 1, 371–386 (1965).

Stienen, A. H., E. E. Hekman, F. C. Van Der Helm and H. Van Der Kooij, “Self-aligning exoskeleton axes through decoupling of joint rotations and translations”, IEEE Transactions on Robotics **25**, 3, 628–633 (2009).

Taghirad, H. D., *Parallel robots: mechanics and control* (CRC press, 2013).

Tao, Z. and Q. An, “Interference analysis and workspace optimization of 3-rrr spherical parallel mechanism”, Mechanism and Machine Theory **69**, 62–72 (2013).

Toxiri, S., A. S. Koopman, M. Lazzaroni, J. Ortiz, V. Power, M. P. de Looze, L. O'Sullivan and D. G. Caldwell, "Rationale, implementation and evaluation of assistive strategies for an active back-support exoskeleton", Frontiers in Robotics and AI **5**, 53 (2018).

Tsai, L.-W. and S. Joshi, "Kinematics and optimization of a spatial 3-upu parallel manipulator", Journal of Mechanical Design **122**, 4, 439–446 (2000).

Veeger, H., "The position of the rotation center of the glenohumeral joint", Journal of biomechanics **33**, 12, 1711–1715 (2000).

Vitiello, N., T. Lenzi, S. Roccella, S. M. De Rossi, E. Cattin, F. Giovacchini, F. Vecchi and M. Carrozza, "Neuroexos: A powered elbow exoskeleton for physical rehabilitation", Robotics, IEEE Transactions on **29**, 1, 220–235 (2013).

Walter, D. R., M. L. Husty and M. Pfurner, "A complete kinematic analysis of the snu 3-upu parallel robot", Contemporary Mathematics **496**, 331–347 (2009).

Wu, J., J. Wang and Z. You, "A comparison study on the dynamics of planar 3-dof 4-rrr, 3-rrr and 2-rrr parallel manipulators", Robotics and computer-integrated manufacturing **27**, 1, 150–156 (2011).

Yan, S., S. Ong and A. Nee, "Stiffness analysis of parallelogram-type parallel manipulators using a strain energy method", Robotics and Computer-Integrated Manufacturing **37**, 13–22 (2016).

Young, A. J. and D. P. Ferris, "State of the art and future directions for lower limb robotic exoskeletons", IEEE Transactions on Neural Systems and Rehabilitation Engineering **25**, 2, 171–182 (2017).

Zhang, X. and C. A. Nelson, “Multiple-criteria kinematic optimization for the design of spherical serial mechanisms using genetic algorithms”, Journal of Mechanical Design **133**, 1, 011005 (2011).